UNIVERSITÀ
DEGLI STUDI
DI PADOVA

Head Office: Università degli Studi di Padova

Department of Civil, Environmental and Architectural Engineering (ICEA Dept.)

Ph.D. COURSE IN SCIENCES OF CIVIL, ENVIRONMENTAL AND ARCHITECTURAL ENGINEERING
CURRICULUM: Rischio, vulnerabilità, ambiente, salute e territorio
SERIES: XXXVI

ADVANCES IN HYDRODYNAMIC AND MORPHODYNAMIC MODELLING

Thesis written with the financial contribution of Fondazione Cariparo and Fondazione Ing. A. Gini

Coordinator: Prof. Massimiliano Ferronato
Supervisor: Prof. Daniele Pietro Viero
Co-Supervisor: Prof. Andrea Defina

Ph.D. student : Tommaso Lazzarin

Abstract

The present research focuses on the advanced modelling of complex phenomena of river hydraulics. Modelling river flows has long represented one of the most challenging tasks of fluid dynamics, because river flows are characterized by high Reynolds numbers, by an inherent three-dimensional (3D) nature promoted by the irregular geometry of the physical domain at the micro- and the macro-scale, and by morphodynamic processes that can modify the domain in time. Nevertheless, modelling and understanding river flows has fundamental implications for advancing the knowledge of environmental processes, the design of hydraulic works, the flood prediction, etc.

Nowadays, two-dimensional (2D) depth-averaged hydrodynamic models are common tools in river hydraulics. Though outperforming classical one-dimensional models, 2D models still have limitations, essentially because the vertical velocity component can often play a non-negligible role and pressure is often quite different from hydrostatic one. The first theme of the present research is aimed at enhancing the predictive ability of 2D models by including effects induced by large-scale 3D flow structures. The focus is here on the secondary currents generated by the streamline curvature in river bends. A parametrization of curvature-induced helical flow is included in a 2D hydro- and morpho-dynamic model on flexible grids based on a cartesian frame by means of additional dispersive terms in the Shallow Water Equations. The non-linear saturation effect, which limits the growth of the helical-flow in case of relatively sharp bends, is modelled with a novel, purely 2D approach suitable for real-world applications. The model also accounts for the effects of helical flow on passive tracers mixing and on the bedload transport. Model applications to laboratory tests and to a real river, under fixed and mobile bed conditions, confirmed the validity of the proposed approach, the relevance of accounting for secondary flows in specific cases, and provided guidelines for a proper application of 2D hydrodynamic models to river flows in bends.

Other kinds of geometrical irregularities of the solid boundary, such as macro-roughness elements or built-up structures, produce 3D turbulent structures that require the use of more sophisticated models. In the recent years, advances in numerical techniques and the increase in computational power have promoted the use of eddy-resolving Computational Fluid Dynamics (CFD) models to describe turbulent river flows. Then, the second theme of the present research concerns the application of these models to river flows over complex geometries. The Detached Eddy Simulation (DES) approach is used to simulate turbulent flows in natural beds in the presence of relatively large roughness elements (i.e., freshwater mussels) and structures (i.e., bridges).

Studying the mutual interactions between turbulent flow and mussel shells has important ecological implications because mussels are among the most imperilled fauna, and understanding the flow at the organism scale may be of help for their conservation. The present research is based on the representation of a real gravel-bed to simulate realistic scenarios; indeed, mussels typically live in sand or gravel beds, where the bed roughness plays a role. The analysis moves from the case of flow around an isolated freshwater mussel and extends through considering large arrays of mussels (i.e., mussel beds), to understand the influence of different physical parameters (e.g., number of mussels per unit area, filtering activity, bed roughness, burrowing ratio) on flow, turbulent structures, drag forces on the mussel shells, bed shear stresses, and mixing of clean water exhaled from the mussels siphons.

Finally, the DES approach is used to study the turbulent flow at a real bridge with multiple piers, which is of great importance because bridge failures are often caused by hydraulic-related reasons, such as bed erosion and trapping of floating debris. The DES simulations account for the detailed geometry of the bridge and for the real bathymetry of the riverbed; the Volume of Fluid (VoF) numerical technique is used to track the free-surface. Such simulations overcome the limitations of previous studies that either used turbulence-averaged models (e.g., RANS), or referred to idealized geometrical conditions. The goals include understanding how the flow and the shear stress at the bed are affected by the presence of the bridge, in both the free-surface conditions and in the pressure-flow with deck overtopping. The analysis focuses on the main turbulent coherent structures and their interaction with the riverbed, and allows comparing the results of DES and RANS approaches.

Sommario

Il presente lavoro di ricerca si concentra sulla modellazione avanzata di fenomeni complessi dell'idraulica fluviale. La modellazione delle correnti fluviali ha da sempre rappresentato una sfida impegnativa nell'ambito della fluidodinamica, poiché il moto in tali contesti è spesso caratterizzato da elevati numeri di Reynolds, da una intrinseca natura tridimensionale (3D) enfatizzata dalla geometria irregolare del dominio a diverse scale spaziali e da processi morfodinamici che possono modificare il dominio nel tempo. D'altra parte, modellare le correnti fluviali e comprenderne le caratteristiche salienti in casi complessi ha importanti implicazioni per l'interpretazione dei processi ambientali, per la progettazione di opere in alveo, per la previsione delle piene, ecc.

Al giorno d'oggi, i modelli idrodinamici bidimensionali (2D) mediati sulla verticale sono strumenti di uso comune in vari campi dell'idraulica fluviale. Pur essendo più affidabili e completi dei classici modelli monodimensionali, i modelli 2D hanno limitazioni intrinseche, dovute al fatto che spesso le componenti verticali della velocità determinano effetti non trascurabili sul campo di moto e la distribuzione delle pressioni non sempre è idrostatica. Il primo tema della presente ricerca ha l'obiettivo di migliorare la capacità predittiva dei modelli 2D tenendo conto degli effetti indotti dalle strutture tridimensionali a larga scala. Nello specifico, l'attenzione è rivolta alle correnti secondarie generate dalla curvatura delle linee di corrente nei tratti di canale in curva. Il moto elicoidale che si sviluppa in tali casi è parametrizzato mediante l'introduzione di appositi termini dispersivi nelle equazioni delle onde lunghe in acque basse, implementate in un modello idro- e morfo-dinamico 2D su griglia non strutturata in coordinate cartesiane. Il processo non-lineare di saturazione, che limita lo sviluppo del moto elicoidale in caso di curvature pronunciate, è modellato con un approccio originale puramente 2D, adatto all'applicazione a casi reali. Il modello tiene conto degli effetti che il moto elicoidale in curva esercita anche sul trasporto e la diffusione di traccianti passivi e sul trasporto al fondo di sedimenti. Le applicazioni del modello volte a riprodurre casi studio di laboratorio e di un fiume reale, condotte sia in ipotesi di fondo fisso e sia di fondo mobile, hanno confermato la validità dell'approccio proposto, la rilevanza degli effetti delle correnti secondarie in molte applicazioni e hanno consentito di formulare linee guida per una corretta modellazione bidimensionale di correnti fluviali in tratti curvi.

Altri tipi di irregolarità geometriche dei contorni solidi, come per esempio macro-scabrezze o strutture costruite in alveo, producono strutture turbolente 3D che richiedono l'uso di modelli più sofisticati. Negli ultimi anni, l'introduzione di schemi numerici avanzati e l'aumento della potenza computazionale hanno reso possibile l'utilizzo, anche in ambito fluviale, dei modelli di fluidodinamica computazionale

(CFD). Perciò, il secondo tema di ricerca riguarda l'applicazione di questi modelli per la simulazione di correnti fluviali in presenza di geometrie complesse. L'approccio ibrido DES (Detached Eddy Simulations) è utilizzato nella presente ricerca per lo studio di correnti turbolente in casistiche complesse e irregolari come nel caso di letti fluviali con elementi di macro-scabrezza (es., cozze di acqua dolce) e in presenza di ostacoli in alveo (es., strutture dei ponti). Studiare le mutue interazioni tra i flussi turbolenti e le cozze di acqua dolce ha importanti implicazioni biologiche ed ecologiche in quanto la sopravvivenza di tali molluschi è fortemente compromessa dalle variazioni nell'habitat idrodinamico, e la comprensione delle dinamiche di flusso a scala di organismo può fornire indicazioni utili per la valutazione delle azioni da intraprendere per la loro conservazione. La presente ricerca si basa sulla rappresentazione di un fondo scabro per simulare scenari realistici; infatti, tali molluschi si collocano generalmente su fondi ghiaiosi o sabbiosi, nei quali la scabrezza del fondo risulta importante. Lo studio si sviluppa a partire del caso di flusso attorno ad una cozza isolata, e considera poi il caso di colonie di molluschi. L'analisi, di tipo parametrico, consente di valutare l'influenza di diversi parametri fisici (ad esempio, numero di cozze per unità di area, intensità di filtrazione della cozza, scabrezza del fondo, grado di interrimento) sul campo di moto e sulle strutture turbolente, sulle forze destabilizzanti indotte sul carapace, sugli sforzi al fondo e sul trasporto di un tracciante passivo utilizzato per rappresentare il flusso di acqua filtrata dalla cozza.

Infine, simulazioni con approccio DES sono utilizzate per studiare le correnti fluviali turbolente che si sviluppano in corrispondenza di un ponte con più pile in alveo. L'argomento è di interesse alla luce del fatto che il collasso di ponti è spesso determinato da cause idrauliche, come per esempio l'erosione del fondo e la cattura di materiale galleggiante trasportato dalla corrente. Le simulazioni DES condotte nel presente lavoro tengono conto della geometria del ponte e della reale batimetria del fondo; il metodo Volume of Fluid (VoF) è utilizzato per tracciare la superficie libera. Tale impianto modellistico consente di superare alcune limitazioni che caratterizzano i lavori precedenti, basati sull'uso di modelli mediati sulla turbolenza (e.g., RANS) o su condizioni geometriche idealizzate. Gli obiettivi includono l'analisi del campo di moto e delle sollecitazioni che esso induce sul fondo in termini di sforzi tangenziali a causa della presenza del ponte, sia nel caso di moto a superficie libera, sia nel caso di flusso in pressione con sormonto dell'impalcato. L'analisi si concentra sullo studio delle strutture turbolente coerenti e sulla loro interazione con il letto del fiume e permette inoltre di confrontare tra loro i risultati ottenuti con gli approcci DES e RANS.

Contents

List of Figures

List of Tables

1 Introduction

The use of numerical models has become increasingly widespread during the recent years in the different fields of river hydraulics. Models for hydrodynamic simulations are nowadays the standard tool for the design of civil works, the assessment of hydraulic risk, the prediction of floods, etc. The coupling with sediment transport models also allows for the analysis and prediction of the morphodynamic evolution of river systems.

Numerical modelling of river flows has long represented one of the most challenging tasks in fluid dynamics, given the complexity of these flows compared to others (e.g., in the industrial field). Many are the factors that characterize river flows and make their simulation particularly complex: the large spatial extension of the geometrical domain, the long simulation time and the huge need for computational resources, the presence of high-Reynolds turbulent flows, the free-surface regime, the irregular bathymetry (both at the micro- and at the macro-scale), the presence of obstacles and geometrical singularities, the mobility of riverbeds, etc.

The possibility of representing accurately some of the complex phenomena that characterize river flows is strongly connected with the choice of the model, and hence with its intrinsic level of simplification, with the refinement of the spatial discretization, and, ultimately, with the availability of computational power.

Indeed, numerical models solve approximate and/or reduced versions of the full Navier-Stokes (NS) equations on discrete computational grids. A wealth of methods has been developed and the availability of computational power has been growing at exceptional rates, allowing for more and more detailed solutions of flow fields. However, the availability of computational resources is still a limit, and all the simplified approaches are characterized by peculiar limitations. Earlier models used to simulate river flows were based on reduced-order versions (i.e., 1D and 2D) of the full NS equations, in which flow resistance was accounted for with simplified parametrizations such as uniform flow formulae (e.g., Strickler-Manning or Chezy formulas). Enhanced 2D models now include more complex turbulent models, typically based on the concept of eddy viscosity and Reynolds stresses. Three-dimensional (3D) models, commonly referred to as Computational Fluid Dynamics (CFD) tools, have become increasingly popular in the last decades also in the field of environmental research. Applications to river flows were mainly based on Reynold-Averaged Navier-Stokes (RANS) equations, with the associated issues of choosing suitable turbulence models and to model large enough domains using a sufficiently fine numerical grid. More advances numerical approaches, such as the Large Eddy Simulation (LES) and the hybrid Detached Eddy Simulation (DES), were the subject of some pioneering applications, typically in spatially limited and/or simplified domains.

Accordingly, in the field of fluvial hydraulics there is still the need of developing specific modelling approaches to obtain solutions that are practically useful and sufficiently accurate for given specific problems. Furthermore, testing innovative computational approaches such as the DES in the field of (as real as possible) river flows, is of particular interest as well.

1.1 Enhancing 2D models with the effect of secondary currents

Given their modest computational demand, reduced-order 1D models have been first developed to simulate river flows. They solve the 1D de Saint Venant equations, sometimes neglecting specific terms, on a geometrical domain that is composed of a series of river cross-sections. These models can be used for both steady and unsteady flows, such as flood waves. As a main assumption, water must flow primarily along the streamwise direction, with negligible contributions of the lateral components of velocity. Considering the present availability of computational power, 1D models are extremely fast to run. However, given the strong limitations in reconstructing complex flow fields, 1D models can be used only for simple applications on channels with compact sections where the velocity components in the transversal direction are negligible.

Some of the above limitations can be overcame by using 2D depth-averaged models, based on the 2D shallow water equations (SWEs). Accounting for both planar components of velocity, they can be used to predict water depth and flow velocity in compound sections, over floodplains, and/or in braided rivers. Nowadays, they represent one of the best compromises between accuracy and computational cost in many applications (Shaheed et al., 2021; Uijttewaal, 2014). For simulations at the scale of the river reach, 2D models are reasonably fast so that, with the present availability of computational power, they can used also for large-scale and real-time simulations (Echeverribar et al., 2019; Vacondio et al., 2017, 2014).

However, also 2D models present some important simplifications, which make them not appropriate for representing complex, three-dimensional flow fields with adequate accuracy. The 2D SWEs are derived by means of the Reynolds decomposition to represent turbulence effects, and of depth-averaging that means neglecting the vertical velocity component and assuming a constant vertical profile of the velocity (Bates, 2022). These last simplifications do not always hold in case of natural river flows where different factors, such as the presence of bends, can alter the vertical distribution of the flow velocity. In river bends, the imbalance among the centrifugal acceleration and the pressure gradient leads to the formation of a streamwise-oriented helical flow, which produces non-negligible velocity components in the transversal direction (Falcon, 1984; Johannesson and Parker, 1989a). This helical flow, known also as curvature-induced secondary current, constitutes a large-scale three-dimensional structure that develops progressively along the bend and typically involves the entire cross-section. This secondary flow has a number of consequences on the hydrodynamics and on the transport of passive tracers and bed particles (Dietrich and Smith, 1983; Duan, 2004): increasing the flow resistance, deviating the high-velocity core, enhancing the mixing of

solutes, deflecting the direction of particles transport, shaping the riverbed by eroding the outer bank and accreting the inner bars, etc.

It is then desirable to account for the effects of the helical flows in reduced-order models, to increase their predictive ability still retaining their easiness of use and computational efficiency (Begnudelli et al., 2010). To reach the goal, the typical approach consisted in including these effects by introducing additional dispersive terms in the governing equations (Johannesson and Parker, 1989b; Odgaard, 1986), as a function of the geometry of the bend (e.g., curvature radius, resistance parameters) and of the characteristics of the flow field (e.g., flow velocity, water depth). The research work performed in the last four decades has led to several parameterizations for the intensity of the helical flow, that were mainly thought in the framework of enhanced 1D models. The dispersive terms for curvature-induced secondary flows have been first applied to 2D models with reference to curvilinear boundary-fitted grids, whereas their use in conjunction to more flexible unstructured meshes has been achieved only recently (Begnudelli et al., 2010), showing the need for a number of applicative techniques. Furthermore, most of the parameterizations predict a linear, unbounded growth of the helical flow intensity with the bend curvature; however, it has been shown that a non-linear saturation effect limits of the growth of secondary currents, particularly in (but not limited to) sharp bends (see e.g., Blanckaert and de Vriend, 2003). A 1D model for helical flow saturation has been recently developed (Blanckaert and de Vriend, 2010), but an effective implementation in 2D schemes on unstructured grids was still lacking.

As a last point, from a review of the technical literature, it is not clear when (and where) curvature-induced secondary currents need to be simulated including the dispersive terms in the SWEs, or when accounting for their effects on bedload transport is sufficient to perform reliable morphodynamic simulations.

1.2 3D CFD modelling to investigate complex flows

As already introduced, river flows are generally complex, because of the high Reynolds numbers and the three-dimensional characteristics, induced by the irregular geometry both at the macro-scale (e.g. bends, bottom jumps, interaction with in-stream structures, etc.) and at the scale of wall (micro- and macro-roughness).

While some of the large-scale flow structures (e.g., secondary currents) can be modelled using reduced-order models with proper parametrizations, accurate predictions of the three-dimensional turbulent flows in rivers, as well as their interactions with the bottom, require the use of more complex computational techniques. 3D Computational Fluid Dynamics (CFD) models have been increasingly used to simulate free-surface river flows. While developed primarily for industrial applications, nowadays CFD models represent the state of the art of hydraulic modelling at local scale also in the field of environmental research (Wright and Hargreaves, 2013). They allow to model complex riverine flows, such as those over irregular bathymetries, in channel bends, past large roughness elements, or in-stream structures, etc. However, besides specific skills to setup suitable computational grids, they require also large

computational resources and long time for the simulation. This has limited their diffusion for practical applications in the environmental field (Fischer-Antze et al., 2008). In most cases their use is restricted to the academic research, especially to reproduce idealized conditions at the laboratory scale or the flow in short or simplified natural reaches.

As mentioned, the numerical simulation of turbulent flows has long represented one of the main difficulties in fluid dynamics, as opposed to the case of laminar flows. Evaluating the turbulent motion of free-surface flows is not straightforward because of their complexity and irregularity, and still this represents one of the big fields of research in CFD (Argyropoulos and Markatos, 2015). Turbulence has many implications for river flows, such as momentum transfers, increased friction, mixing of passive tracers, entrainment of bed particles, etc., and accounting for its effect is needed to obtain accurate solutions. Direct Numerical Simulations (DNS) solve the full Navier-Stokes equations and naturally account for turbulence at all relevant spatial and temporal scales. To solve the flow field up to the dissipative scale, DNS require extremely fine grids and huge computational cost, which become soon unfeasible for the Reynolds numbers typical of turbulent geophysical flows (Fröhlich and von Terzi, 2008). Rather than modelling turbulence directly, the first practical solution is modeling the effects of turbulence with models based on the Reynolds-Averaged Navier-Stokes (RANS) equations. Their main assumption is the decomposition of velocities and pressure terms into their mean and fluctuating contributes. The time-averaging of the fluctuating components leads to additional turbulent stresses, which require proper parametrizations (i.e., the closure of turbulence, with a wealth of available approaches such as the well-known k-ε or k-ω models). RANS approaches have long represented the most common way to account for turbulence effects. They are the standard for reduced-order models, but they are also used in 3D models. Although RANS models account for the effect of turbulence, they do not explicitly reproduce the energetic eddies developing in the flow. Large Eddy Simulations (LES) models, instead, have been proposed to model the large-scale eddies in 3D models (Smagorinsky, 1963, see also Rodi et al., 2013). They require a parametrization only for eddies whose length-scale is smaller than the size of the computational grid elements. If the grid is sufficiently refined, eddies smaller than the grid size have been shown to have homogenous characteristics, making their modelling easier with respect to larger-scale eddies. However, in return for the increased precision, these models require more refined grids and larger computational efforts compared to RANS models. In particular, a critical point for LES is that, close to the walls, its computational requirement is close to that of a DNS. As a compromise between RANS and LES approaches, hybrid models have been developed to couple the former in the proximity of solid walls with the latter in the other parts of the physical domain. Such models require a lower computational effort compared to LES models, and include DES (Detached Eddy Simulations) models, which nowadays represent one of the best options for modelling complex river flows (Spalart, 2009).

LES and DES models explicitly characterize the larger-scale turbulent structures, and provide detailed and complete pictures of turbulent flow fields in case of complex

geometrical domains. Thus, they constitute powerful tools for investigations. Though in the academic field LES and DES models has already found application to environmental hydraulics, the application of such models to river flows is still limited for different reasons: the numerical approach is relatively new, the setup of numerical grid requires skills that are not in the background of most of environmental modelers yet, and the need of computational resources becomes challenging when dealing with hydrodynamic studies of natural flows at a large spatial scale.

Despite that, many are the possible applications for the study of the environmental flows, among which one of the most relevant concerns the interplay between flows and geometric singularities at various scales.

1.3 Goals and Outline of the work

The general aim of the present work is to advance hydro- and morpho-dynamic modelling with regards to the representation of some relevant 3D features of the flow fields. The research develops along two main directions.

First, the work deals with the improvement of an existing 2D hydro- and morpho-dynamic model by including effective parametrizations of the curvature-induced secondary currents. The specific goals of this part include:

- developing a model implementation that incorporates different previous formulations and evaluating their performance against data from available laboratory experiments;
- development of a pure 2D model to account for the non-linear saturation mechanism on general unstructured grids, and verification using data available in the literature;
- evaluating the effects of including helical flow dispersive terms in reconstructing the flow field, in predicting the transport of passive tracers, and in modelling the bedload transport;
- assessing the role of secondary currents in equilibrium and non-equilibrium morphodynamic conditions in a real case study, shedding light on the interplay between secondary flow and bed bathymetry (i.e., the so-called topographic steering);
- highlighting the key factors and providing practical guidelines for a proper modelling of river flows in bends using 2D models.

Second, the work deals with the application of eddy resolving CFD simulations (i.e., DES) to describe the turbulent flows in natural streams in presence of large roughness elements (i.e., the shells of freshwater mussels) and of in-stream structures (i.e., bridges). Findings of the present study can be of help also for proper parametrizations in reduced-order models. The main goals of this part include:

- analyzing the flow over isolated, partially-burrowed, freshwater mussels to analyze the role and the interplay of bed roughness, burrowing degree, and filtering activity of the mussels;
- understanding the key features of the fully-developed flow over clusters of partially-burrowed mussels, and how they vary depending on mussel density (i.e., number of mussels per unit area), on bed roughness, and on the filtering activity of the mollusks;
- describing the key features of the free-surface flow and the bed shear stresses at a realistic bridge on a real river bathymetry, highlighting the changes ascribed to the shift from the free-surface regime to the pressurize flow with deck overtopping.

The analysis and the 2D modelling of secondary currents are discussed in Chapter 2 of the present work. The study of the interactions between the turbulent flow and a riverbed with large roughness elements is reported in Chapters 3, which focus on partially-burrowed freshwater mussels. The analysis of the flow field in the presence of in-stream structures is reported in Chapter 4, which deals with a realistic, multi-pier riverine bridge over the real bathymetry. Some conclusions close the thesis.

1.4 References

Argyropoulos, C.D., Markatos, N.C., 2015. Recent advances on the numerical modelling of turbulent flows. Appl. Math. Model. 39, 693–732. https://doi.org/10.1016/j.apm.2014.07.001

Bates, P.D., 2022. Flood Inundation Prediction. Annu. Rev. Fluid Mech. 54, 287–315. https://doi.org/10.1146/annurev-fluid-030121-113138

Begnudelli, L., Valiani, A., Sanders, B.F., 2010. A balanced treatment of secondary currents, turbulence and dispersion in a depth-integrated hydrodynamic and bed deformation model for channel bends. Adv. Water Resour. 33, 17–33. https://doi.org/10.1016/j.advwatres.2009.10.004

Blanckaert, K., de Vriend, H.J., 2003. Nonlinear modeling of mean flow redistribution in curved open channels. Water Resour. Res. 39, 1375. https://doi.org/10.1029/2003WR002068

Blanckaert, K., de Vriend, H.J., 2010. Meander dynamics: A nonlinear model without curvature restrictions for flow in open-channel bends. J. Geophys. Res. Earth Surf. 115, F0401. https://doi.org/10.1029/2009JF001301

Dietrich, W.E., Smith, J.D., 1983. Influence of the point bar on flow through curved channels. Water Resour. Res. 19, 1173–1192. https://doi.org/10.1029/WR019i005p01173

Duan, J.G., 2004. Simulation of Flow and Mass Dispersion in Meandering Channels. J. Hydraul. Eng. 130, 964–976. https://doi.org/10.1061/(ASCE)0733-9429(2004)130:10(964)

Echeverribar, I., Morales-Hernández, M., Brufau, P., García-Navarro, P., 2019. 2D numerical simulation of unsteady flows for large scale floods prediction in real time. Adv. Water Resour. 134, 103444. https://doi.org/10.1016/j.advwatres.2019.103444

Falcon, M., 1984. Secondary Flow in Curved Open Channels. Annu. Rev. Fluid Mech. 16, 179–193. https://doi.org/10.1146/annurev.fl.16.010184.001143

Fischer-Antze, T., Olsen, N.R.B., Gutknecht, D., 2008. Three-dimensional CFD modeling of morphological bed changes in the Danube River. Water Resour. Res. 44, W09422. https://doi.org/10.1029/2007WR006402

Fröhlich, J., von Terzi, D., 2008. Hybrid LES/RANS methods for the simulation of turbulent flows. Prog. Aerosp. Sci. 44, 349–377. https://doi.org/10.1016/j.paerosci.2008.05.001

Johannesson, H., Parker, G., 1989a. Velocity Redistribution in Meandering Rivers. J. Hydraul. Eng. 115, 1019–1039. https://doi.org/10.1061/(ASCE)0733-9429(1989)115:8(1019)

Johannesson, H., Parker, G., 1989b. Secondary Flow in Mildly Sinuous Channel. J. Hydraul. Eng. 115, 289–308. https://doi.org/10.1061/(ASCE)0733-9429(1989)115:3(289)

Odgaard, A.J., 1986. Meander Flow Model. I: Development. J. Hydraul. Eng. 112, 1117–1135. https://doi.org/10.1061/(ASCE)0733-9429(1986)112:12(1117)

Rodi, W., Constantinescu, G., Stoesser, T., 2013. Large-Eddy Simulation in Hydraulics, CRC Press. ed.

Shaheed, R., Mohammadian, A., Yan, X., 2021. A Review of Numerical Simulations of Secondary Flows in River Bends. Water 13, 884. https://doi.org/10.3390/w13070884

Smagorinsky, J., 1963. General Circulation Experiments with the Primitive Equations: I. The Basic Experiment. Mon. Weather Rev. 91, 99–164. https://doi.org/10.1175/1520-0493(1963)091<0099:GCEWTP>2.3.CO;2

Spalart, P.R., 2009. Detached-Eddy Simulation. Annu. Rev. Fluid Mech. 41, 181–202. https://doi.org/10.1146/annurev.fluid.010908.165130

Uijttewaal, W.S.J., 2014. Hydrodynamics of shallow flows: application to rivers. J. Hydraul. Res. 52, 157–172. https://doi.org/10.1080/00221686.2014.905505

Vacondio, R., Dal Palù, A., Ferrari, A., Mignosa, P., Aureli, F., Dazzi, S., 2017. A non-uniform efficient grid type for GPU-parallel Shallow Water Equations models. Environ. Model. Softw. 88, 119–137. https://doi.org/10.1016/j.envsoft.2016.11.012

Vacondio, R., Dal Palù, A., Mignosa, P., 2014. GPU-enhanced Finite Volume Shallow Water solver for fast flood simulations. Environ. Model. Softw. 57, 60–75. https://doi.org/10.1016/j.envsoft.2014.02.003

Wright, N.G., Hargreaves, D.M., 2013. Environmental Applications of Computational Fluid Dynamics, in: Environmental Modelling. pp. 91–109. https://doi.org/10.1002/9781118351475.ch6

1.4 References

2 Analysis and 2D modelling of curvature-induced secondary currents

This Chapter is essentially constituted by a manuscript published in Advances in Water Resources (Lazzarin and Viero, 2023)[1]. It focuses on curvature-induced secondary flows, which are ubiquitous in nature because of the generally curved course of rivers. Three-dimensional (3D) models explicitly account for their effect at the cost of a large computational effort, so that it is desirable to account for the effects of secondary flows in reduced-order models. The focus here is on an existing, general-purpose, 2D-depth-averaged hydro-morphodynamic model, based on flexible grids on a cartesian frame, which has been enhanced to include the effects of the secondary currents on the flow structure, on the mixing of passive tracers, and on the bedload transport.

The non-uniform vertical distribution of velocity in the streamwise and spanwise directions, as determined by the curvature of streamlines and the onset of a helical (spiral) secondary flow, is considered by introducing proper dispersive terms in the SWEs, an anisotropic diffusivity tensor in the advection-diffusion equation, and a correction to the direction of bed shear stress for the bedload transport. Different approaches and parameterizations available in the technical literature are recast in a unique form and compared to each other in terms of flow field, tracer transport, and bed evolution, using data from laboratory experiments and real-world case studies. The model includes a novel, pure 2D implementation of a non-linear model that accounts for the saturation effect, which limits the growth of the helical flow intensity in relatively sharp bends.

The results obtained from the model applications show the efficacy of the different approaches and allow to highlight when and where it is important to account for the effects of curvature-induced secondary currents. The assessment of different key-factors, implementation techniques, constraints for a proper mesh design, the suitability of local and non-local approaches, and the role of bathymetry, leads to a set of guidelines that provides a complete review of effective and parsimonious (in terms of computational cost) strategies for 2D hydro- and morpho-dynamic modelling in river bends.

[1] Lazzarin, T., Viero, D.P., 2023. Curvature-induced secondary flow in 2D depth-averaged hydro-morphodynamic models: An assessment of different approaches and key factors. Adv. Water Resour. 171, 104355. https://doi.org/10.1016/j.advwatres.2022.104355

2.1 Introduction

In river and channel bends, the interplay between the curvature of streamlines in the horizontal plane and the non-uniformity of streamwise velocity along the vertical produces a streamwise-oriented helical flow, because of an imbalance between the outward centrifugal acceleration and the inward pressure gradient (Blanckaert and de Vriend, 2010; Falcon, 1984; van Balen et al., 2010) This curvature-induced secondary current, which acts to deviate the high-velocity thread from the inner to the outer bank (Ahmadi et al., 2009; Bolla Pittaluga et al., 2009; Johannesson and Parker, 1989a; Lien et al., 1999; Seminara et al., 2002; Shimizu et al., 1990; Wu et al., 2004, 2005), has long attracted scientist attention (e.g., Boussinesq, 1868; Thomson, 1877; the tea leaves of Einstein, 1926; see also Bowker, 1988) because of interesting fundamental implications in shaping the riverbed bathymetry, in contributing to bank erosion and meander migration, in enhancing mixing and dispersions of heat and solutes, in increasing flow resistance, etc.(Constantinescu et al., 2013; Demuren and Rodi, 1986; Duan, 2004; Gu et al., 2016; Iwasaki et al., 2016; Jang and Shimizu, 2005; Koken et al., 2013; Lai et al., 2012; Papanicolaou et al., 2007; Termini, 2014).

The most natural way of modelling secondary currents is employing full three-dimensional (3D) models, which naturally resolve curvature-induced helical flows (Keylock et al., 2012). Starting from pioneering applications in the ’70 (Leschziner and Rodi, 1979; Pratap and Spalding, 1975), the increased computational power has now allowed modelling long stretches of natural rivers with full 3D (CFD, Computational Fluid Dynamics), but the need of suitable computing facilities and of large computational time still hinder their widespread application (Fischer-Antze et al., 2008; Horna-Munoz and Constantinescu, 2018).

The search for efficient strategies to account for curvature-induced secondary flow in reduced-order hydraulic models, started by Van Bendegom in 1947 by looking at the flow field in a single bend, has so far produced many different approaches and modelling strategies (Blanckaert and de Vriend, 2010; Camporeale et al., 2007; Lane, 1998). Most of these are linear (or weakly non-linear) models, valid for low curvatures of the river axis and slowly varying bed topography, hence suitable to model long-term migration of large-scale meandering rivers.

To meet the specific needs of practical engineering problems involving fluvial hydro- and morpho-dynamics, two-dimensional (2D) free-surface shallow water models still represent a valid compromise between efficiency and effectiveness (Shaheed et al., 2021; Uijttewaal, 2014). In 2D depth-averaged models, the vertical profile of the velocity is assumed implicitly, and is commonly taken constant (Bates, 2022; Ghamry and Steffler, 2002). To account for the effects of secondary flows in channel bends, the shallow water equations (SWEs) are enriched with dispersive stresses (Bora and Khalita, 2020; Camporeale et al., 2021; Song et al., 2012), which parameterize the momentum transfer produced by the streamwise-oriented helical flow.

The simplest approach to account for curvature-induced secondary flows in 2D models assumes instantaneous adaptation of secondary flow intensity to the driving

curvature. The dispersive stresses are directly linked to the local streamline curvature (Begnudelli et al., 2010; Duan, 2004; Guan et al., 2016; Lien et al., 1999; Song et al., 2012). Actually, the problem is further complicated because the streamline curvature progressively generates secondary flow, i.e., with a phase-lag due to inertia, and the helical flow is subject to different dissipative mechanisms as well (Blanckaert and de Vriend, 2004, 2003). The lagged formation of helical flow in steady state applications was simulated by introducing an adaptation length (Blanckaert and de Vriend, 2003; De Vriend, 1981; Johannesson and Parker, 1989b; Kikkawa et al., 1976; Rozovskii, 1957; Wu et al., 2005, 2004). A more rigorous and general approach requires solving a transport-diffusion equation for vorticity (or angular momentum), with centrifugal force and resistance mechanisms acting as source and sink terms, respectively (Bernard and Schneider, 1992; Einstein and Li, 1958; Ikeda and Nishimura, 1986; Kalkwijk and Booij, 1986; Odgaard, 1986). At the cost of additional computational demand, this approach doesn't suffer from local singularities in the curvature field and reproduces the slow decay of the helical flow, which vanishes at a long distance downstream of a bend (Bai et al., 2019).

Concerning the implementation of the above methods, modelling approaches proliferated with regard to: *i)* the basic conservation principle, such as extra equations from the Navier Stokes equations (Ghamry and Steffler, 2002; Jin and Steffler, 1993; Yeh and Kennedy, 1993), reduced versions of the momentum equation in the transversal direction (e.g., Kalkwijk and Booij, 1986; Odgaard, 1986), or the conservation of streamwise angular momentum (e.g., Bernard and Schneider, 1992; Finnie et al., 1999); *ii)* the vertical profile for the streamwise velocity component, either logarithmic (Bernard and Schneider, 1992; De Vriend, 1977, 1981; Kitanidis and Kennedy, 1984; Shimizu et al., 1990) or power-law (Odgaard, 1986; Wu et al., 2004; Yeh and Kennedy, 1993); *iii)* the vertical profile for the spanwise velocity component, typically linear with zero mean (Odgaard, 1986) albeit notable variations such as polynomial expressions (e.g., De Vriend, 1977, 1981; Kikkawa et al., 1976; Shin and Seo, 2021); *iv)* the way in which local curvature is estimated and possibly filtered to avoid numerical instabilities (Abad et al., 2008; Begnudelli et al., 2010); *v)* the use of boundary-fitted orthogonal curvilinear grids, which naturally allow evaluating longitudinal and transversal terms (e.g., Blanckaert and de Vriend, 2003; Demuren, 1993), as opposed to general-purpose unstructured meshes in a Cartesian reference frame that are more flexible in case of unevenly curved bends and wandering riverbeds (Jin and Steffler, 1993; Nikora and Roy, 2011); *vi*) the treatment of impervious banks using either the free- or no-slip condition, each one entailing specific pros and cons (Blanckaert, 2001).

In general, the basic model assumptions limit the scope of such 2D models to the case of mild curvatures. Indeed, in the case of sharp bends, curvature-induced secondary flows are characterized by relevant non-linear feedbacks. The helical flow, with its outward transport of streamwise momentum, modifies both the horizontal pattern and the vertical profiles of flow velocity: the high-velocity thread is moved outward, and the vertical profile is flattened, which means weakening the helical flow production mechanism (Blanckaert, 2009; Blanckaert and de Vriend, 2003; Blanckaert and Graf, 2004;

Wei et al., 2016). This feedback-based non-linear process, referred to as saturation of secondary flow, has been assessed quite recently, and its implementation in 2D depth-averaged models is still in its infancy (Guan et al., 2016; Ottevanger et al., 2012; Qin et al., 2019; Shin and Seo, 2021; Xiao et al., 2022).

Finally, the implementation of 2D model accounting for curvature-induced secondary flows, as well as their application to laboratory and real-world case studies, lead to face many other subtle factors: examples are the proper inclusion of high spatial gradients of water depth associated to compound cross-sections and irregular bathymetries, the computation of dispersive stresses at the wet/dry interface or at the mesh (lateral) boundaries, the need of accounting for lateral wall friction (particularly for laboratory applications with rectangular cross-sections), effective strategies to employ coarser computational meshes, etc.

The present study aims at providing a comprehensive assessment of curvature-induced secondary flows in the frame of general-purpose, depth-averaged 2D models for river hydro- and morpho-dynamics on flexible grids based on a cartesian frame (i.e., not on a curvilinear coordinate system). Different parameterizations available in the technical literature are recast in similar form and implemented in a 2D finite-element hydrodynamic model, for both the cases of instantaneous adaptation of helical flow intensity and of transport of streamline vorticity. The saturation of secondary flow in the case of strong curvatures is modelled introducing a pure 2D extension of the model by Blanckaert and de Vriend (2003); saturation effects can be accounted for with any of the approaches for secondary flow implemented in the model. The hydrodynamic module for curvature-induced secondary flows is then integrated with a module for transport of passive tracers, and with a morphodynamic module solving for the bedload sediment transport.

The Chapter is organized as follows. The theoretical models for curvature-induced flows are presented in Sect. 2, along with an in-depth description of implementation techniques. The model is verified against several laboratory experiments, both with fixed and movable bed (Sect. 3). A model application to a real case-study (Po River) is used to assess some key factors in 2D depth-averaged hydro- and morphodynamic modelling of real rivers. The relevant aspects emerged in this study are then discussed in light of the recent advances on the subject and of open issues (Sect. 4). A set of conclusions closes the Chapter.

2.2 Accounting for curvature-induced secondary flows in 2D models

2.2.1 Shallow water equations with dispersive stresses

On a horizontal Cartesian frame with axes (x, y), the 2-D depth-averaged Navier-Stokes equations with the hypothesis of hydrostatic pressure distribution, commonly known as De Saint Venant or shallow water equations (SWEs), read:

$$\begin{aligned}
&\frac{\mathrm{D}}{\mathrm{D}t}\left(\frac{q_x}{Y}\right) - \frac{1}{Y}\left(\frac{\partial Re_{xx}}{\partial x} + \frac{\partial Re_{xy}}{\partial y}\right) + \frac{1}{Y}\left(\frac{\partial D_{xx}}{\partial x} + \frac{\partial D_{xy}}{\partial y}\right) + \frac{\tau_{bx}}{\rho Y} + g\ \frac{\partial h}{\partial x} = 0 \\
&\frac{\mathrm{D}}{\mathrm{D}t}\left(\frac{q_y}{Y}\right) - \frac{1}{Y}\left(\frac{\partial Re_{xy}}{\partial x} + \frac{\partial Re_{yy}}{\partial y}\right) + \frac{1}{Y}\left(\frac{\partial D_{yx}}{\partial x} + \frac{\partial D_{yy}}{\partial y}\right) + \frac{\tau_{by}}{\rho Y} + g\ \frac{\partial h}{\partial y} = 0 \\
&\eta(h)\frac{\partial h}{\partial t} + \frac{\partial q_x}{\partial x} + \frac{\partial q_y}{\partial y} = 0
\end{aligned} \tag{2-1}$$

where t is time, D/Dt is the material (Lagrangian) time derivative, $\mathbf{q} = (q_x, q_y)$ are the depth-integrated velocity components, Y is the equivalent water depth (i.e., water volume per unit area, Defina, 2000), Re are the Reynolds turbulent stresses in the horizontal plane, (τ_{bx}, τ_{by}) are the bed shear stress components, ρ is the water density, g is gravity, and h is the water surface elevation over a datum. In the continuity equation, $\eta(h) \in]0,1]$ is a depth-dependent storage coefficient defined as the wet area fraction (Defina, 2000). The dispersive stresses D_{xx}, D_{xy}, and D_{yy} emerge from the integration of non-uniform vertical distribution of velocity over the water depth, and are defined as

$$\begin{aligned}
D_{xx} &= \int_0^Y [u'(z)]^2\, dz \\
D_{xy} = D_{yx} &= \int_0^Y u'(z)v'(z)dz \\
D_{yy} &= \int_0^Y [v'(z)]^2\, dz
\end{aligned} \tag{2-2}$$

where the apostrophe denotes the difference between the real and the depth-averaged velocity component (note that the velocity vector is here defined as $\mathbf{w} = (u, v) = \mathbf{q}/Y$):

$$\begin{aligned}
u'(z) &= u(z) - u \\
v'(z) &= v(z) - v
\end{aligned} \tag{2-3}$$

Dispersive stress terms thus account for the subscale spatial variations of the unresolved velocity field. To obtain close-form expressions of the dispersive terms, it is convenient to use a local (s, n) reference frame, with s the longitudinal (streamwise) and n the transversal (spanwise) directions (see Figure 2-1a), and to assume simple vertical distributions of the flow velocity components along s and n. Among the different expressions used in previous studies, a power law distribution can be assumed for the streamwise component, w_s, which allows for a simpler derivation of dispersive stresses. According to Odgaard (1986):

$$\frac{w_s(z)}{w} = \frac{m+1}{m}\left(\frac{z}{Y}\right)^{\frac{1}{m}} \tag{2-4}$$

being $w = \sqrt{u^2 + v^2}$ the magnitude of the depth-averaged velocity and m a friction parameter ($m = \chi\kappa / g^{1/2}$ with χ the Chezy coefficient and $\kappa = 0.4$ the von Karman

constant). For the spanwise velocity component, w_n, a linear profile with zero mean is commonly used (Jin and Steffler, 1993; Kalkwijk and Booij, 1986; Odgaard, 1986):

$$\frac{w_n(z)}{w} = v_{ns}^* \left(\frac{2z}{Y} - 1\right) \tag{2-5}$$

where $v_{ns}^* = v_{ns}/w$ is the non-dimensional transversal velocity component at the free-surface. Integration on the water depth provides (Begnudelli et al., 2010; Lien et al., 1999; Wu et al., 2004)

$$\begin{aligned} D_{ss} &= Y \frac{w^2}{m(2+m)} \\ D_{sn} = D_{ns} &= Y \frac{w^2}{1+2m} v_{ns}^* \ \ \text{sign}(R) \\ D_{nn} &= Y \frac{(v_{ns}^* w)^2}{3} \end{aligned} \tag{2-6}$$

being R the radius of curvature of depth-averaged streamlines (R is positive for clockwise bends in the flow direction, and negative vice-versa). Finally, these terms are rotated into the (x, y) coordinate frame by expressing the rotation matrix in terms of velocity components, to read

$$\begin{aligned} D_{xx} &= D_{ss} \frac{u^2}{w^2} - 2D_{sn} \frac{uv}{w^2} + D_{nn} \frac{v^2}{w^2} \\ D_{xy} = D_{yx} &= D_{ss} \frac{uv}{w^2} + D_{sn} \left(\frac{u^2 - v^2}{w^2}\right) - D_{nn} \frac{uv}{w^2} \\ D_{yy} &= D_{ss} \frac{v^2}{w^2} + 2D_{sn} \frac{uv}{w^2} + D_{nn} \frac{u^2}{w^2} \end{aligned} \tag{2-7}$$

Lien et al. (1999) reported an equivalent derivation of these terms for the case of a logarithmic vertical profile of streamwise velocity.

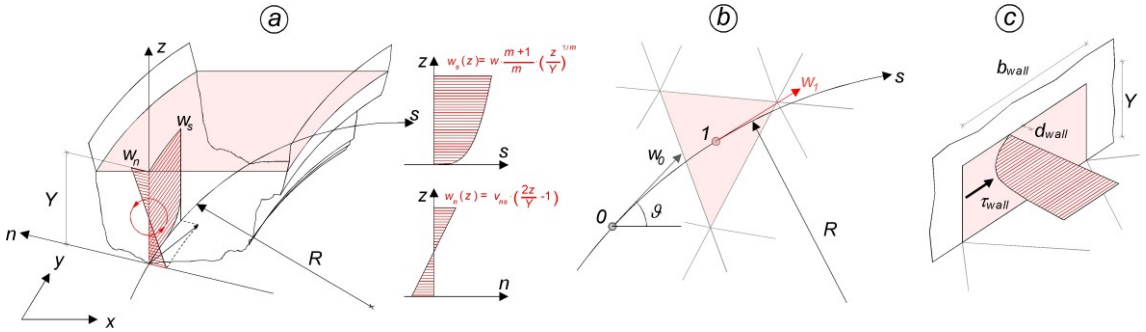

Figure 2-1. a) schematics of main and secondary flows in a channel bend, with notation; b) estimation of the local streamline curvature; c) model for wall friction.

It's worth noting that the net contribution to momentum (Eq. (2-1)) of dispersive stresses D_{ij}, with i and j denoting either x or y, depends on their spatial derivatives rather than on their magnitude. Concerning the role of the single dispersive terms, D_{ss} does not depend on the secondary flow; it acts in the streamwise direction by hindering both spatial acceleration and deceleration. The mixed D_{sn} term is the most important term for simulating secondary flows; its spatial gradient may lead to additional resistance at the inner side of bends and to acceleration at the outer side of bends (Dietrich and Smith, 1983), thus accounting for the effect of outward momentum transfer ascribed to the helical flow. D_{nn} may produce a spanwise net stress that, depending on the spanwise gradient of flow velocity (w) and secondary flow intensity (v_{ns}^*), may lead to a larger free-surface transversal slope.

2.2.2 Instantaneous-adaptation and vorticity-transport approaches

The dispersive stresses for curvature-induced secondary flows, which depend on the helical flow intensity, can be expressed in terms of non-dimensional spanwise velocity component at the free-surface, v_{ns}^*. Basically, v_{ns}^* can be evaluated using two different approaches: *i)* a local approach, which implies instantaneous adaptation of the helical flow intensity to the local flow features, and *ii)* a vorticity-transport approach, which accounts for generation, transport, and dissipation of the helical flow.

In the local approach, which is simpler and less computationally demanding, v_{ns}^* is a direct function of local water depth, velocity, and streamline curvature. As a major drawback, the local approach does not consider the inertia of secondary flow, and the spatially distributed field of v_{ns}^* becomes particularly sensible to local variations of the flow field and streamline curvature, particularly in the vicinity of sharp boundaries (e.g., bridge piers, abutments).

The vorticity-transport approach models the helical flow in terms of streamwise vorticity component, which emerges from the non-uniformity of the spanwise velocity (Einstein and Li, 1958). Usually, rather than solving the complete equation for three-dimensional vorticity vector (Blanckaert and de Vriend, 2004), depth-average simplified versions of the vorticity equations are solved for the streamwise component of vorticity, ω, (Finnie et al., 1999; Uchida and Fukuoka, 2014). The general form of the transport equation for streamwise vorticity in the (x, y) horizontal plane is:

$$\frac{\mathrm{D}\omega}{\mathrm{D}t} = \Omega_{PROD} - \Omega_{DISS} \tag{2-8}$$

in which Ω_{PROD} is a production term depending on the imbalance between the centrifugal acceleration and the transversal pressure gradient, and Ω_{DISS} is a dissipation term that derives from the bottom stresses (Farhadi et al., 2018; Nezu, 2005). Several formulations have been proposed in the technical literature to estimate the production and dissipation terms of Eq. (2-8). Although formally different, being obtained from different basis assumptions, they all share a similar structure, as shown in the following.

Noting that the streamwise vorticity component, ω, is twice the angular velocity, Ω, and assuming the linear profile for spanwise velocity of Eq. (2-5), it results:

$$\omega = 2\Omega = 2\frac{v_{ns}}{Y/2} = 4\frac{v_{ns}}{Y} \tag{2-9}$$

Under the hypothesis of slowly-varying water depth, Eq. (2-8) can be written directly in terms of v_{ns} in the general form

$$\frac{\mathrm{D}v_{ns}}{\mathrm{D}t} = f_D k_P \frac{w^2}{R} - k_D \frac{v_{ns} w}{Y} \tag{2-10}$$

being k_P and k_D production and dissipation coefficients, whose formulation depends on the basic conservation principle; f_D is a coefficient introduced to account for non-linearity in the production of helical flow (see Sect. 2.2.3).

Kalkwijk and Booij (1986) derived a transport-diffusion equation starting from the momentum equation in the transversal direction and using a logarithmic vertical profile for streamwise velocity. This approach is also implemented in Delft3D, with a slightly different formulation for the production term (see Chavarrías et al., 2019). A similar approach has been proposed by Odgaard (1986), which used a power law (Eq. (2-4)) for the vertical profile of streamwise velocity. Actually, both these studies worked with the assumption of steady state, yet the generalization to unsteady flow is straightforward.

Bernard and Schneider (1992) obtained the transport-diffusion equation by imposing angular momentum conservation on a cross-section and assuming a logarithmic vertical profile for the longitudinal velocity component; in the present work, for the sake of simplicity, the same approach has been reformulated using the power law in Eq. (2-4).

Eq. (2-10) can be used to estimate the transversal surface velocity v_{ns}^* for both the vorticity-transport approach and the instantaneous-adaptation approach. Indeed, the instantaneous-adaptation approach implicitly assumes that an equilibrium condition is locally attained elsewhere, which is equivalent to assume that the material derivative of streamwise vorticity (i.e., the left-hand side term in Eq. (2-10)) vanishes. In this case, v_{ns}^* can be evaluated directly (and locally) as

$$v_{ns}^* = \frac{v_{ns}}{w} = f_D \frac{k_P}{k_D}\frac{Y}{R} \tag{2-11}$$

Compared to the local approach, which allows estimating the transversal velocity calculating production dissipation terms solely, the vorticity-transport method has a higher computational cost since the transport equation (2-10) must also be solved.

Table 2-1. Collection of the main formulations for secondary flow proposed in the literature. Ω, I, and v_{ns} measure the secondary flow intensity. In the Bernard and Schneider (1992) formulation, ω is the streamwise vorticity, C_F is a friction parameter, C_A, C_B, C_C, C_2 are model parameters that are combined in the production, A_S, and decay, D_S, coefficients. In the Kalkwijk and Booji (1986) formulation, $k_b = k_b(s)$ is a calibration parameter that accounts for the phase lag.

	Bernard and Schneider (1992)	**Kalkwijk and Booji (1986)**	**Odgaard (1986)**
Derived from	Angular Momentum Conservation on Transversal Section	Steady state momentum equation in the transversal direction	Steady state momentum equation in the transversal direction
Transported quantity	$\Omega = \frac{C_A C_B C_2 \omega}{12}$	$I = k_b \frac{wY}{R}$	$v_{ns} = \frac{2m+1}{2\kappa^2 m}\frac{wY}{R}$
Exp. for transv. velocity at the f. s.	$v_{ns} = \frac{Y\omega}{4} = \frac{Y}{4}\frac{12\Omega}{C_A C_B C_2}$	$v_{ns} = 3\frac{I}{\kappa^2}\left(\frac{1}{2} - \frac{1}{m}\right)$	as above
Original transport-eq.	$\frac{D\Omega}{Dt} = \frac{1}{6}\frac{(wC_AC_2)^2}{RY}\sqrt{C_F} - 3C_C\sqrt{C_F}\frac{\Omega w}{Y}$	$\frac{d\left(k_b\frac{wY}{R}\right)}{ds} = \frac{2\kappa^2}{m-2}\frac{w}{R}(1-k_b)$	$\frac{dv_{ns}}{ds} = \frac{2m+1}{m(m+1)}\frac{w}{R} - \frac{2\kappa^2}{m+1}\frac{v_{ns}}{Y}$
Normalized transport-eq.	$\frac{Dv_{ns}}{Dt} = \frac{\sqrt{6A_S}}{2}\frac{\kappa}{m}\frac{w^2}{R} - D_S\frac{\kappa}{m}\frac{wv_{ns}}{Y}$	$w\frac{dv_{ns}}{ds} = \frac{3}{m}\frac{w^2}{R} - \frac{2\kappa^2}{m-2}\frac{wv_{ns}}{Y}$	$w\frac{dv_{ns}}{ds} = \frac{2m+1}{m(m+1)}\frac{w^2}{R} - \frac{2\kappa^2}{m+1}\frac{wv_{ns}}{Y}$
Transv.velocity at equilibrium	$v_{ns}^* = \frac{\sqrt{6A_S}}{2D_S}\frac{Y}{R}$	$v_{ns}^* = \frac{3}{2}\frac{(m-2)}{m\kappa^2}\frac{Y}{R}$	$v_{ns}^* = \frac{2m+1}{2\kappa^2 m}\frac{Y}{R}$

Table 2-1 reports the different expressions for production and dissipation terms available in the literature, also expressed according to the form of Eqs. (2-10) and (2-11). In Figure 2-2a, the magnitude of the transversal velocity component at the free-surface is plotted for different value of the Strickler roughness coefficient, K_s. The Bernard and Schneider model, reformulated assuming a power law vertical profile (red dashed line) is very similar to their original, lag-law based model (red continuous line). The models by Odgaard (1986) show an opposite trend with respect to that of Kalkwijk and Booij (1986). By increasing values of K_s (i.e., moving toward smoother beds), the vertical profile of streamwise velocity component is progressively flatter, which entails a reduced production of helical flow; yet, a smoother bed also entails reduced resistances to spiral motion. The two above models give different weight to these two opposing factors.

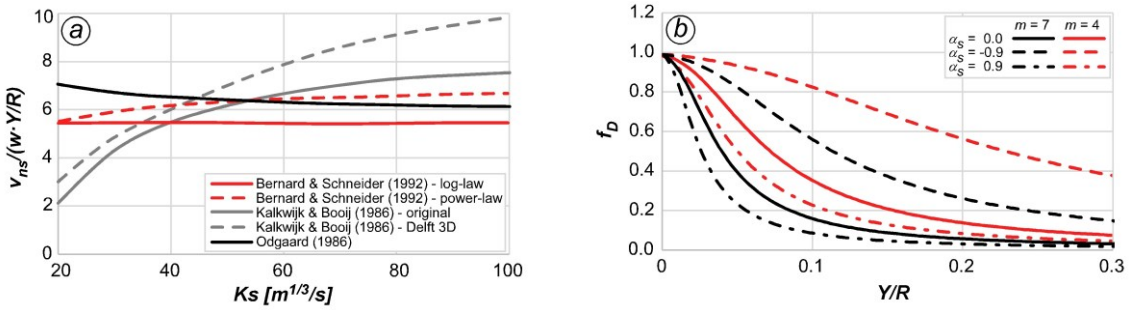

Figure 2-2. a) magnitude of the transversal velocity at the free-surface, v_{ns}, scaled by $w(Y/R)$, evaluated with different approaches using eq. (2-11) with $f_D = 1$. b) dampening factor for vorticity production, f_D, for different values of the friction parameter m and the normalized spanwise gradient of streamwise velocity α_s.

2.2.3 Saturation of secondary flows

In Eq. (2-10), as well as in Eq. (2-11), assuming $f_D = 1$ leads to linear models in which the intensity of secondary flow increases indefinitely with the streamline curvature (Camporeale et al., 2007; Song et al., 2012). This is not the real case, particularly for higher curvature ratios Y/R, because of the so-called saturation effect (Bai et al., 2019; Blanckaert, 2009; Blanckaert and de Vriend, 2003). The dampening factor $f_D \in [0,1]$ is introduced in Eq. (2-10) to reduce the production term in all the formulation here implemented when the saturation mechanism plays a role.

Blanckaert and de Vriend (2003) proposed a parameterization in which f_D is a function of the bend parameter β, which in turn depends on the normalized transversal gradient of the depth averaged velocity, α_s:

$$
\begin{aligned}
f_D &= 1 - \exp\left(-\frac{0.4}{1.05\beta^3 - 0.89\beta^2 + 0.5\beta}\right) \\
\beta &= \sqrt{\frac{Y}{|R|}}\left(\frac{0.41}{m}\right)^{-0.55}(\alpha_s + 1)^{0.25} \\
\alpha_s &= \frac{R}{w}\frac{\partial w}{\partial n}
\end{aligned}
\tag{2-12}
$$

The key parameter is here α_s, which varies from $\alpha_s = -1$, i.e., potential flow (or free-vortex) velocity distribution with maximum velocity at the inner side, to $\alpha_s = 1$, i.e., forced-vortex with maximum velocity at the outer side (Blanckaert and de Vriend, 2003; Ottevanger et al., 2012). The rationale is that $\alpha_s = -1$ generally at the bend entrance, where the helical-flow production is stronger and the outward momentum transfer has still to affect the flow; as opposite, α_s tends to 1 as the high-velocity thread shifts to the outer side of the bend, i.e., where the vertical profile of velocity is likely to be flattened and the production of helical-flow weakened. Accordingly, the dampening factor f_D decreases for increasing α_s (Figure 2-2b). Through the bend parameter β, f_D also depends on hydrodynamic variables (Y and R) and on bottom friction (m). For increasingly sharp bends, f_D decreases, indicating that non-linear effects become increasingly important in limiting the growth of helical flow.

The non-linear model by Blanckaert and de Vriend (2003) has been conceived for reduced order models developed on curvilinear reference frames, typically used as meander-migration models, in which the secondary currents are parameterized based on momentum balance at the channel centreline. Ottevanger (2013) proposed to extend the model to the whole channel width by extending the secondary flow intensity estimated at the centreline modulated with empirical power-law weighting functions. Such an extension is limited to regular-shaped cross-sections and presumes the knowledge of the channel centreline and walls. Iterative procedures are required to deal with more complex geometries (Qin et al., 2019). The generalization of this nonlinear model to a form that is suitable to general-purpose 2D schemes is still to be sought.

2.2.4 A pure 2D approach and the treatment of banks

Within the scope of general-purpose 2D depth-averaged models, which include the salient features of curvature-induced secondary flows, the approach used to account for impervious banks and the transversal distribution of the D_{sn} dispersive stress deserves some discussions.

As well explained by Blanckaert (2001), it is known since Johannesson and Parker (1989a) that, in a channel bend, the D_{xy} dispersive stress must satisfy two conditions: *i*) it should be positive in the central region of the cross section, where the helical flow produces the highest transversal momentum flux, and *ii*) it should decay to zero toward the impervious banks, where the direction of secondary flow is mostly vertical and the velocity progressively reduces due to sidewall friction. When applying linear models for secondary currents to strongly curved flows, the helical flow intensity is generally overestimated when the (physically sound) hypotheses of no-slip condition is assumed (e.g., Blanckaert, 2001; Lien et al., 1999). Indeed, in the external part of the bend, the no-slip condition amplifies the (negative outward) spanwise gradient of velocity, entailing a larger, streamwise-oriented, net stress at the outer side of the bend.

A simple solution that has been often adopted in previous studies (Lien et al., 1999; Song et al., 2012) is adopting the free-slip condition at impervious banks. The spanwise gradient of velocity is reduced, and so it is the dispersive stress D_{xy}; unfortunately, this causes an unphysical momentum flux at the banks (Johannesson and Parker, 1989a). Moreover, while assuming a free-slip condition at the banks entails minor drawbacks in case of relatively large cross-sections, the sidewall friction plays a significant role in case of cross-sections with large aspect ratios, typical of artificial channels and laboratory flumes, and should be accounted for.

Physics-based analytical solutions proposed in previous studies (e.g., Ikeda et al., 1990) are unsuitable to general-purpose 2D depth-averaged models, for which the channel centreline and width, as well as the distance from the banks, cannot even be identified. Actually, the bank location can change substantially depending on the water level in typical compound cross-sections (e.g., passing from full-bank to flood discharge), as well as due to movable-bed dynamics in case of active (i.e., migrating, braided, anabranching) riverbeds.

In general-purpose 2D models based on a Cartesian (i.e., not curvilinear) reference frame, only local variables (i.e., the flow depth and velocity, the radius of curvature R, etc.) can be used to estimate the helical flow strength (Jin and Steffler, 1993; Koch and Flokstra, 1980). Hence, here we explore the practical solution of implementing a model for secondary flow, including the associated non-linear saturation effects, based on local variables only. The effectiveness of such a pure 2D approach has to be verified by means of model applications (the reader is referred to Sect. 2.3 and 2.4). The basic idea is that considering the physics-based saturation effects, rather than the unphysical free-slip condition at sidewalls or other case-specific tuning parameters, could alleviate the overestimation of secondary flow that is produced in strongly curved bends when the no-slip condition acts at impervious banks.

Of course, providing a physically sound representation of the complex 3D phenomena occurring in strongly curved channel bends is beyond the scope of the present work. The goal is achieving a cost-effective, versatile, and useful tools for engineering applications.

2.2.5 Advection-diffusion equation in the presence of secondary currents

The advection-diffusion equation allows to determine the evolution in time and space of the vertically-averaged concentration, C, of tracers and substances transported by the flow. It is used to model suspended sediment, pollutant transport, and other transported quantities such as the vorticity ω (Sect. 2.2.2). The advection-diffusion equation can be written as:

$$\frac{\partial YC}{\partial t} + \nabla \cdot C\mathbf{q} - \nabla \cdot (Y\varepsilon_T \nabla C) - \nabla \cdot (Y\mathbf{D_D}\nabla C) = S \tag{2-13}$$

where $\nabla \cdot$ the 2D divergence operator, $\varepsilon_T = \nu_T / \sigma_T$ is the turbulent diffusivity, commonly expressed as a function of the eddy viscosity, ν_T, and of the Schmidt number, σ_T (Duan, 2004), $\mathbf{D}_D$ is an anisotropic diffusivity tensor that accounts for dispersion, and S is a source term.

The dispersive-diffusion term is often neglected in the practice (i.e., $\mathbf{D}_D = 0$), and the turbulent diffusivity is tuned using the Schmidt-number as a calibration parameter for representing experimental data in general conditions (smaller values for the Schmidt number increase the mixing and vice-versa) (Duan, 2004; Hu et al., 2017). However, the curvature-induced helical flow enhances the lateral mixing (Engmann, 1986; Fischer, 1969; Lee and Kim, 2012; Moncho-Esteve et al., 2017; Rishnappan and Lau, 1977). Particularly, large curvature and strong secondary currents entail a marked anisotropic diffusivity that needs to be modelled with a suitable parameterization (Demuren and Rodi, 1986; Duan, 2004). This generally suffices to make the calibration of the Schmidt number unnecessary (i.e., $\sigma_T = 1$ can be assumed) in the case of channel bends.

The principal components of the $\mathbf{D}_D$ tensor, in the local (s, n) reference frame, can be expressed in the following general form:

$$D_{Dss} = \alpha_{Ds} u_* Y \qquad D_{Dnn} = \alpha_{Dn} u_* Y \qquad D_{Dsn} = D_{Dns} = 0 \tag{2-14}$$

where u_* is the friction velocity and α_{Ds}, α_{Dn} are proper parameters (Elder, 1959; Holly and Usseglio-Polatera, 1984; Shin et al., 2020). Different formulations for α_{Ds} and α_{Dn} are available in the literature, depending on flow and environmental conditions, e.g., the shape of the velocity profile (Seo and Baek, 2004) or the presence of vegetation (Lou et al., 2020). Following Elder (1959), a common choice is $\alpha_{Ds} = 5.93$. To account for the presence of helical flows, α_{Dn} can be estimated as a function of the transversal velocity at the free-surface, v_{ns}, as a result of depth-averaging (Fischer et al., 1979; Lee and Seo, 2013). Considering the vertical distributions of velocity expressed by Eqs. (2-4) and (2-5), results in

$$\alpha_{Dn} = \frac{1}{6\kappa}\left(\frac{v_{ns}}{u_*}\right)^2 \tag{2-15}$$

Finally, by rotating the principal-component tensor onto the *(x, y)* reference frame, the diffusivity components D_{Dij} become (Alavian, 1986):

$$\begin{aligned} D_{Dxx} &= D_{Dss}\frac{u^2}{w^2} + D_{Dnn}\frac{v^2}{w^2} \\ D_{Dxy} &= D_{Dyx} = (D_{Dss} - D_{Dnn})\frac{uv}{w^2} \\ D_{Dyy} &= D_{Dss}\frac{v^2}{w^2} + D_{Dnn}\frac{u^2}{w^2} \end{aligned} \tag{2-16}$$

The advection-diffusion equation, enriched by the anisotropic diffusivity tensor $\mathbf{D_D}$, accounts for the additional mixing induced by the secondary circulations, yet a constant distribution of the concentration is assumed along the vertical direction. This is not always true when considering the transport of suspended sediments, which is also modelled by the same advection-diffusion equation. Generally, the concentration of suspended sediments is much higher in the lower part of the water column, so that the helical flow produces a net flux of sediment concentration in the transversal direction, towards the inner side of bends. Additional dispersive terms should be introduced in Eq. (2-13) to account for the vertical distributions of both the flow velocity and the concentration of suspended sediments (e.g., Rouse profile). The introduction of these additional terms is discussed in detail in Appendix D.

2.2.6 The 2DEF finite element numerical model

The different parameterizations of curvature-induced secondary currents are implemented in the framework of the 2DEF Finite Element hydrodynamic model (D'Alpaos and Defina, 2007; Defina, 2003; Viero et al., 2014, 2013). The model solves Eqs. (2-1), which constitute a modified version of the full shallow water equations, to deal with wetting and drying processes over irregular topography (Defina, 2000). The bottom friction is expressed using the Strickler-Manning formulation; it is treated semi-implicitly to enhance model stability (Cea and Bladé, 2015; Valiani et al., 2002; Viero and Valipour, 2017).

The computational domain is discretized with 2D triangular elements. A staggered scheme is used in which water levels are defined at the grid nodes and assumed to vary piecewise linearly through the domain; flat triangular elements, characterized by a constant elevation, convey the discharge among adjacent nodes. In the framework of semi-implicit, mixed Eulerian-Lagrangian scheme, in the momentum equation the material (Lagrangian) derivative of the depth-averaged velocity is replaced by the finite difference formulation:

$$\frac{\mathrm{D}\mathbf{w}}{\mathrm{D}t} = \frac{\mathbf{w} - \mathbf{w}_0}{\Delta t} \tag{2-17}$$

where the subscript "0" indicates the terms at the previous time step and position (backward along the Lagrangian trajectory). Under the hypothesis of slowly varying flows, momentum equations are linearized and then solved for $\mathbf{q} = \mathbf{w}Y$, which in turn are substituted into the continuity equation, and solved with a Finite Element Galerkin's method (Defina, 2003). The semi-implicit nature of the scheme limits its applicability to subcritical flows, yet relaxes the Courant-Friedrichs-Lewy (CFL) number restriction on the computational time step. A single system of N algebraic equations, being N the number of nodes, is solved at each time step by a modified conjugate gradient method. Considering that the accuracy of the scheme allows for using relatively coarse meshes, the model turns out to be particularly efficient.

2.2.6.1 Computation of the local streamline curvature

The Lagrangian approach for convective terms is used also to estimate the local radius of curvature of the streamlines, basing on the spatial variation of the direction of the velocity (Bonetto and Defina, 1998). Denoting with ϑ the angle of the velocity vector to the x axis (positive counter clockwise) and with R the local radius of curvature of the streamline (Figure 2-1b), the distance ds can be written as:

$$ds = -R\ [\vartheta(s + ds) - \vartheta(s)] = -R\ d\vartheta \tag{2-18}$$

Observing that $tan\,\vartheta = v/u$ and $cos\,\vartheta = u/w$, the derivative of ϑ can be expressed in terms of velocity components as:

$$\frac{d}{ds}\left(\frac{v}{u}\right) = \frac{d}{ds} tan\,\theta = \frac{1}{cos^2\,\vartheta}\frac{d\vartheta}{ds} = \left(\frac{w}{u}\right)^2 \frac{d\vartheta}{ds} \tag{2-19}$$

The local streamline curvature, $1/R$, is then obtained by combining Eqs. (2-18) and (2-19):

$$\frac{1}{R} = -\ \frac{d\vartheta}{ds} = -\left(\frac{u}{w}\right)^2 \frac{d}{ds}\left(\frac{v}{u}\right) = -\frac{u^2}{w^2}\left(\frac{1}{u}\frac{dv}{ds} - \frac{v}{u^2}\frac{du}{ds}\right) = \frac{1}{w^2}\left(v\frac{du}{ds} - u\frac{dv}{ds}\right) \tag{2-20}$$

For slowly varying flows, $\Delta s \cong w_1 \Delta t$, and the spatial derivative of the velocity components can be approximated as:

$$\left.\frac{du}{ds}\right|_1 \cong \frac{u_1 - u_0}{w_1 \Delta t}; \qquad \left.\frac{dv}{ds}\right|_1 \cong \frac{v_1 - v_0}{w_1 \Delta t} \tag{2-21}$$

where the label "1" denotes the centre of a generic cell. Hence, making use of Eqs. (2-20) and (2-21), the local curvature is finally given by:

$$\frac{1}{R_1} \cong \frac{1}{w_1^3 \Delta t}[v_1(u_1 - u_0) - u_1(v_1 - v_0)] = \frac{1}{w_1^3 \Delta t}[u_1\ v_0 - v_1 u_0] \tag{2-22}$$

2.2.6.2 Computation of the Reynolds turbulent stresses

The horizontal components of Reynolds turbulent stresses are modelled with the Boussinesq approximation and the depth integrated eddy viscosity by Stansby (2003) and Uittenbogaard and van Vossen (2004) (see also Viero, 2019). The Reynolds terms in Eqs. (2-1) are

$$Re_{ij} \cong \nu_T Y \left(\frac{\partial u_i}{\partial j} + \frac{\partial u_j}{\partial i} \right) \tag{2-23}$$

with indexes i and j denoting either x or y, ν_T the eddy viscosity, and $u_i = q_i/Y$ the generic depth-averaged velocity component. Looking at the first equation in (2-1), under the hypothesis of smooth spatial variations of the eddy viscosity, the first Reynolds stress component becomes

$$\begin{aligned} \frac{\partial Re_{xx}}{\partial x} + \frac{\partial Re_{xy}}{\partial y} &\cong \nu_T Y \left[\frac{\partial}{\partial x}\left(2\frac{\partial u_x}{\partial x} \right) + \frac{\partial}{\partial y}\left(\frac{\partial u_x}{\partial y} + \frac{\partial u_y}{\partial x} \right) \right] = \\ &= \nu_T Y \left(\frac{\partial^2 u_x}{\partial x^2} + \frac{\partial^2 u_x}{\partial y^2} \right) + \nu_T Y \frac{\partial}{\partial x}\left(\frac{\partial u_x}{\partial x} + \frac{\partial u_y}{\partial y} \right) \end{aligned} \tag{2-24}$$

According to the continuity equation in (2-1), the last right-hand side term is proportional to the temporal variation of the water level, and is negligible in case of slowly varying flows. Hence, the Reynolds stress can be estimated as

$$\begin{bmatrix} \frac{\partial Re_{xx}}{\partial x} + \frac{\partial Re_{xy}}{\partial y} \\ \frac{\partial Re_{yx}}{\partial x} + \frac{\partial Re_{yy}}{\partial y} \end{bmatrix} \cong \nu_T Y \begin{bmatrix} \frac{\partial^2 u_x}{\partial x^2} + \frac{\partial^2 u_x}{\partial y^2} \\ \frac{\partial^2 u_y}{\partial x^2} + \frac{\partial^2 u_y}{\partial y^2} \end{bmatrix} = \nu_T Y \nabla^2 \mathbf{u} \tag{2-25}$$

Considering that these terms have to be computed for each element of an unstructured triangular mesh, the divergence theorem is used to obtain the average cell value of the Reynolds stresses:

$$\frac{\nu_T Y}{A_e} \int_{A_e} \nabla^2 \mathbf{u}\, dA = \frac{\nu_T Y}{A_e} \int_{\Gamma_e} \nabla \mathbf{u} \cdot \mathbf{n}_\Gamma\ d\Gamma \approx \frac{\nu_T Y}{A_e} \sum_k \nabla \mathbf{u}_k \cdot \mathbf{n}_k\ L_k \tag{2-26}$$

in which A_e is the area and Γ_e the boundary of the computational element, $\mathbf{n}_\Gamma$ is the unit-vector normal to the cell boundary (positive outward), k identifies each of the three cell sides, whose length is L_k.

Denoting with O the centroid of the cell and with O_k the centroid of the cell adjacent to the k-th side of the cell, and with d_k the projection of the segment $\overline{OO_k}$ onto $\mathbf{n}_k$, the last term of Eq. (2-26) becomes

$$\frac{2\nu_T}{A_e}\sum_k(\mathbf{u}_{Ok}-\mathbf{u}_O)\frac{p_k L_k}{d_k} \tag{2-27}$$

in which the weight $p_k = \min(Y_k/Y;\ 1)$ accounts for the fact that Reynolds stresses take only place at the wet interface shared by adjacent cells (e.g., if the adjacent cell is dry, no Reynolds stress occurs). For cell sides belonging to the mesh boundary, assuming $\mathbf{u}_{Ok} = \mathbf{u}_O$ (or, equivalently, $p_k = 0$) allows simulating the slip-condition.

2.2.6.3 Computation of the dispersive stress terms

Similar to the Reynolds stresses, the computation of dispersive stresses in Eqs. (2-1) requires a suitable evaluation of the spatial derivatives of the D_{ij} terms defined at Eq. (2-7). Denoted the dispersive terms with

$$\mathbf{D} = \begin{bmatrix} D_{xx} & D_{xy} \\ D_{yx} & D_{yy} \end{bmatrix} \tag{2-28}$$

the dispersive stresses are given by $\nabla \cdot \mathbf{D}$. The average of the dispersive stresses for each computational cell can be evaluated making use of the divergence of $\mathbf{D}$:

$$\frac{1}{A_e}\int_{A_e}\nabla\cdot\mathbf{D}\,dA = \frac{1}{A_e}\int_{\Gamma_e}\mathbf{D}\cdot\mathbf{n}_\Gamma\,d\Gamma \approx \frac{1}{A_e}\sum_k \mathbf{D}_k\cdot\mathbf{n}_k\,L_k \tag{2-29}$$

in which $\mathbf{D}_k$ is the tensor of dispersive terms evaluated at the center of the k-th cell side. This can be obtained as the average of the $\mathbf{D}$ terms, previously computed for adjacent cells and weighted with the distance of centroids to the center of the k-th cell side.

Concerning the dampening factor, which accounts for the saturation of secondary flow in case of sharp bends, the key point is the computation of the transversal gradient of the velocity, which appears in Eq. (2-12) within α_s, and is equal to $\partial w/\partial n = \nabla w \cdot \mathbf{n}$, with $\mathbf{n}$ the unit vector normal to the local flow direction. Making use of the divergence theorem, for each computational cell the average value of the velocity gradient is evaluated as

$$\frac{1}{A_e}\int_{A_e}\nabla w\,dA = \frac{1}{A_e}\int_{\Gamma_e} w\mathbf{n}_\Gamma\,d\Gamma \approx \frac{1}{A_e}\sum_k w_k\,\mathbf{n}_{\Gamma k}\,L_k \tag{2-30}$$

where the velocity at the side centre, w_k, is computed as the average of the w at adjacent cells weighted with the distance of centroids to the center of the k-th cell side, L_k is the length of the k-th cell side, and $\mathbf{n}_{\Gamma k}$ is the outward unit vector normal to the cell side.

2.2.6.4 *Wall function to account for no-slip condition at sidewalls*

At the mesh boundaries, the model allows imposing a classical slip conditions, or to use a wall function to account for additional friction exerted by sidewalls. In the latter case, an additional stress component, parallel to the wall direction, is added to the momentum balance of wall-adjacent elements. It is computed as (Wu et al., 2000):

$$\tau_{wall} = \rho w^2 \left[\frac{\kappa}{\ln\left(\frac{30 \cdot d_{wall}}{e_s}\right)} \right]^2 \tag{2-31}$$

where e_s is the equivalent sand grain roughness of lateral walls and d_{wall} is a wall-distance within the logarithmic layer (see Figure 2-1c), assumed equal to

$$d_{wall} = \frac{50\,\nu}{u^*} \tag{2-32}$$

where ν is the kinematic viscosity of water, and u^* the shear velocity. For each grid cell, the wall shear stress is applied on the surface $Y \cdot b_{wall}$, being b_{wall} the length of the vertical wall.

2.2.6.5 *Numerical scheme for the transport-diffusion equation*

The transport-diffusion equation (Sect. 2.2.5) is solved using a conservative, second-order in-space numerical scheme. The scheme is equivalent to that described by Casulli and Zanolli (2005), with the substantial difference that variables are located oppositely in the two staggered meshes. In Casulli and Zanolli (2005), the model cells are control volumes that exchange fluxes through the cell-sides; in the present model, the triangular elements convey fluxes from a node to the others, or from two nodes to the remaining one. The second order accuracy in space, for the advective terms, is achieved using an upwind, total variation diminishing (TVD) scheme; to avoid spurious oscillations, the SUPERBEE limiter is applied based on two consecutive gradients of nodal tracer concentration. For each node of the grid, the preliminary step is computing the upstream concentration as the average concentration of all the upstream nodes, weighted with the value of incoming water discharge (Casulli and Zanolli, 2005). Then, for each element, the direction of the velocity vector determines each couple of nodes that exchange flow and tracer with each other, and the concentration value at these two connected nodes is completed with the upstream concentration. The two consecutive gradients allow applying the TVD limiter, and the limited gradient of concentration is finally used to compute the tracer flux between nodes.

2.2.6.6 Bedload Transport

The bed evolution module of the 2DEF model, described in Defina (2003), is based on the Exner sediment balance equation:

$$(1-n)\frac{\partial z_b}{\partial t} + \nabla \cdot \mathbf{q_b} = 0 \tag{2-33}$$

where n is the bed sediment porosity, z_b the bottom elevation (see also Appendix B for a detailed description of the techniques adopted to evaluate the bottom elevation in case of staggered grids), and $\mathbf{q_b}$ the volumetric sediment transport rate per unit width, expressed as (Struiksma, 1985):

$$|\mathbf{q_b}| = q_{b0}\left(1 - \chi c_f \frac{\partial z_b}{\partial s}\right) \tag{2-34}$$

being c_f the friction coefficient ($c_f = K_s^2 Y^{4/3}/g$) and χ an empirical factor to account for the effect of longitudinal slope on transport rate ($\chi = 0.03$ according to Crosato and Struiksma, 1989). The effect of the longitudinal slope on the sediment transport rate, and the possible corrections to account for it, are discussed also in Appendix C. As evaluating the bed slope is not straightforward in case of staggered grids, different techniques to improve its estimation has been investigated and implemented in the model (see Appendix B). The sediment transport rate, q_{b0}, is evaluated with a continuous variant (Carniello et al., 2012) of the threshold-based Meyer-Peter and Müller (MPM) formula:

$$q_{b0} = 8\sqrt{g d_s^3 (s-1)}\, T^{1.5} \quad \text{with} \quad T = -\theta_C + \sqrt[4]{\theta_C^4 + \mu\theta^4} \tag{2-35}$$

where d_s is the characteristic (median) sediment diameter, $s = \rho_s/\rho$ the relative density of sediments, μ the ripple factor (Vermeer, 1986), θ the Shields parameter, and θ_C the threshold value for incipient bedload transport. Compared to the original MPM formulation, the continuous variant provides smoother (hence more stable), practically equivalent solutions.

The components of the sediment rate, q_{bx} and q_{by}, are obtained from $|\mathbf{q_b}|$ as a function the direction of sediment transport, which in turn depends on the near-bed flow velocity. In channel bends and meandering rivers, using the mean velocity of the primary flow to estimate the bedload transport is often incorrect since the curvature-induced secondary flow can significantly affect the flow (and sediment) direction at the bottom (Abad et al., 2008; Kitanidis and Kennedy, 1984). The inward-oriented velocity at the bottom is the main cause of bend scour and of point-bar accretion, respectively at the outer at the inner sides of bends (Bathurst et al., 1977; Engel and Rhoads, 2012; Rozovskii, 1957).

Empirical corrections have been proposed in literature for representing the deviation of bedload transport to the mean flow velocity. Olesen (1987) suggested the following angular correction:

$$\Delta\beta = A_c \frac{Y}{R} \tag{2-36}$$

where A_c is a parameter typically assumed in the range $7 \div 12$. Accordingly, the bottom velocity can be estimated as:

$$\mathbf{w}_\mathrm{b} = (u + \Delta\beta \cdot v; v - \Delta\beta \cdot u) \tag{2-37}$$

Such an approach still finds widespread applications in hydro-morphological models (Vanzo et al., 2021). Yet, a major limitation comes from the direct dependence on the local streamline curvature, as in the instantaneous-adaptation approach for secondary flows (Sect. 2.2.2), which may produce unphysical results in case of large curvatures (inertia and saturation are not considered). Moreover, the bottom characteristics, such as the bed roughness that shape the vertical profile of flow velocity, is not accounted for explicitly. As a consequence, such a correction model needs, at least, robust and site-specific calibration.

Alternatively, when curvature-induced helical flow is modelled effectively, the bottom deviation angle $\Delta\beta$ can be evaluated depending on the near-bed transversal velocity component. This is expected to provide a more accurate estimation of bedload than using empirical, local corrections (Wang and Tassi, 2014), as inertia, saturation, and vertical velocity profiles can be all accounted for. According to the linear velocity profile of Eq. (2-5), the transversal velocity component at the bottom is opposite to that at the free-surface, i.e., $-v_{ns}$. The near-bed velocity becomes equal to

$$\mathbf{w}_\mathrm{b} = (u_b; v_b) = (u + v_{ns}^* \cdot v; v - v_{ns}^* \cdot u) \tag{2-38}$$

and it forms an angle $\delta = \arctan(v_b/u_b)$ to the x axis. The direction of sediment transport, α, is also influenced by the bed slope (Baar et al., 2018; Chavarrías et al., 2019), which is accounted for according to Struiksma (1985):

$$\alpha = \arctan\left[\frac{\mathrm{sen}(\delta) - \frac{1}{f(\theta)}\frac{\partial z_b}{\partial y}}{\cos(\delta) - \frac{1}{f(\theta)}\frac{\partial z_b}{\partial x}}\right] \tag{2-39}$$

The function $f(\theta)$ weights the influence of the transverse bed slope and is estimated as (Talmon et al., 1995):

$$f(\theta) = \zeta \cdot \sqrt{\theta} \qquad \text{with} \quad \zeta = 9(d_s/Y)^{0.3} \tag{2-40}$$

Besides accounting for the effect of longitudinal and transversal slopes, the model also includes a sub-model for sediment redistribution in case of bed slope exceeding the repose slope (see Appendix C), which allows simulating a specific mechanism of bank erosion and retreat (Abderrezzak et al., 2016).

2.3 Results

2.3.1 Test with fixed-bed, mild-curvature, laboratory experiments

The effectiveness of secondary flow parameterizations described in the previous section is first verified by comparing the hydrodynamic field, modelled with different approaches, to the laboratory data from the RIPRAP test facility experiment (Bernard and Schneider, 1992; Finnie et al., 1999).The RIPRAP channel is $L = 274$ m long and $B = 5.27$ m wide, with 2:1 bank slope in the lower part of lateral walls (Figure 2-3). The four bends (90° and 135° right wise, 90° left wise and 135° right wise) have a constant centreline radius of curvature $R = 15.2$ m. The longitudinal slope is 0.216 % and the Strickler roughness coefficient is K_S =38.5 m$^{1/3}$/s.

The numerical mesh is made of 6,293 nodes and 11,528 triangles, with mean linear size of 45 cm (i.e., channel width to cell-side-length ratio, $B/\Delta x$, of about 12). The model of Odgaard (1986) is used for the source terms in Eq. (2-10) and (2-11) (see also Table 2-1), and the wall function of Eq. (2-31) is used to enforce the no-slip condition at the lateral boundaries, thus accounting for the presence of side walls. As boundary conditions, constant flowrate ($Q = 4.25$ m^3/s) and water depth ($Y_D = 0.8$ m) are imposed at the inlet and outlet sections, respectively.

Figure 2-4 shows the spanwise profiles of depth-averaged velocity, in steady state conditions, for the 11 cross-sections of Figure 2-3; the experimental data (red dots, from Finnie et al., 1999) are compared with model results obtained without considering dispersive stresses (dotted lines), with the instantaneous-adaptation (solid lines), and with the vorticity transport (dash-dotted lines) approaches. For the same cases, the plan view of Figure 2-5 shows the location of the main stream (high-velocity thread). In Appendix A (Supplementary Material), Figure 2-25 highlights the importance of using a wall function to account for the resistance induced by sidewalls, and Figure 2-26 and Figure 2-27 the performance of the different formulations, collected in Table 2-1, for the source terms of Eq. (2-10) and (2-11).

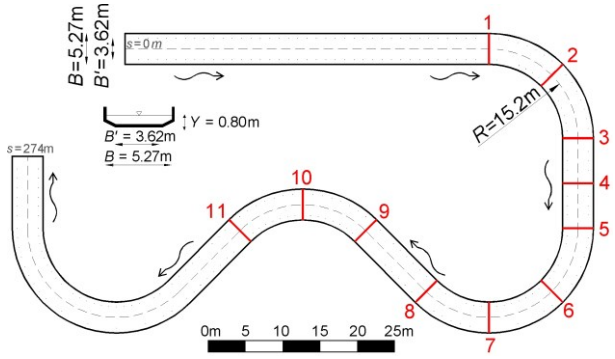

Figure 2-3. The RIPRAP facility channel (Finnie et al., 1999) with numbered cross-sections.

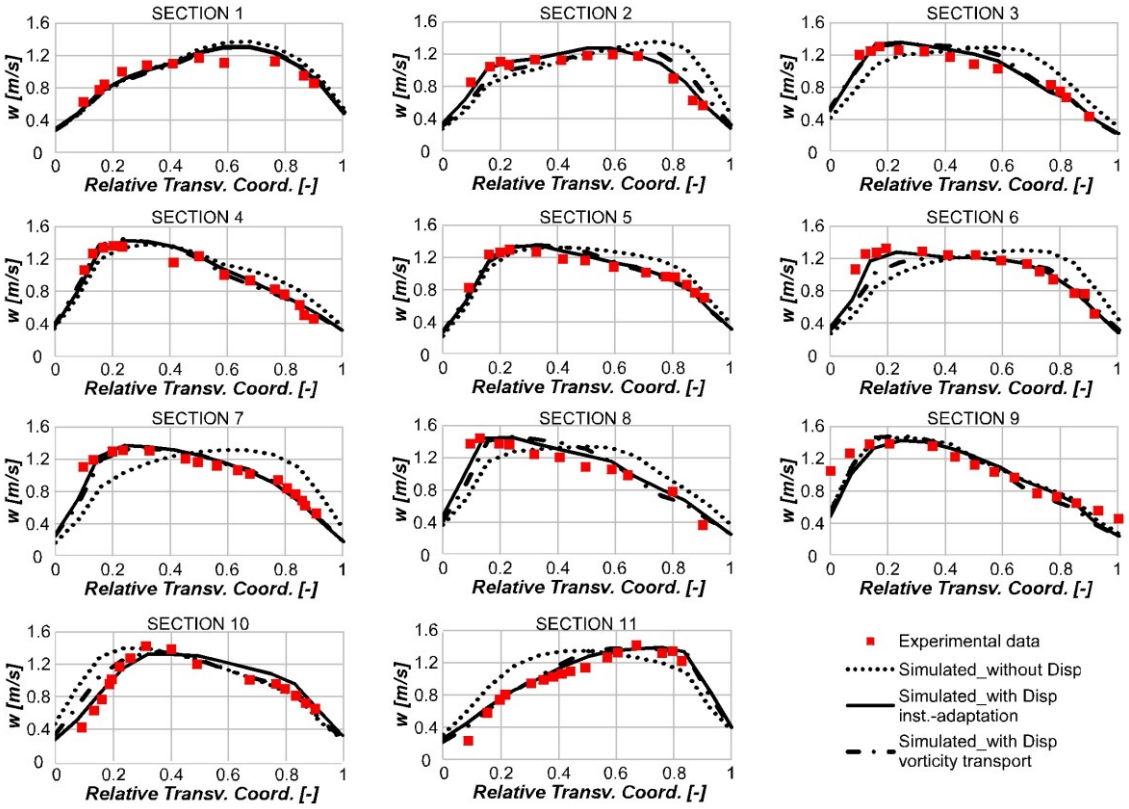

Figure 2-4. Transversal profiles of depth-averaged velocity in the RIPRAP test (Finnie et al., 1999): measured data (red dots) and modelled profiles without dispersive terms (dotted lines), with the instantaneous-adaptation approach (solid lines) and with the vorticity-transport approach (dash-dotted lines). The relative transversal coordinate spans the channel width from the left bank.

Figure 2-4 confirms that accounting for curvature-induced secondary flow is necessary to obtain reasonable transversal velocity profiles in the presence of bends. While the difference with a classical 2D formulation without dispersive terms is striking, the local instantaneous-adaptation and the vorticity-transport approaches perform similarly to each other; they both reproduce the experimental data very well, with the vorticity-transport approach slightly retarding the development of the secondary flow, and in turn the outer shift of higher velocities, at the beginning of bends (see Sect. 2, 6, and 10). The mean RMSE for the 11 sections is 0.224 m/s without dispersive terms 0.109 m/s using the local approach and 0.123 m/s using the vorticity-transport approach.

The dispersive stresses in the SWEs produce deceleration of the flow in the inner part and acceleration at the outer part of the bend (Dietrich and Smith, 1983), thus shifting the high-velocity thread toward the outer side of bends compared to the simulation without dispersive terms (Figure 2-5). Figure 2-5 also shows one of the main differences between the instantaneous-adaptation and the vorticity-transport approaches; by looking at the undisturbed flow approaching the first bend, the outward shift of the high-velocity thread is faster with the local approach (Figure 2-5a), as it doesn't account

for rotational inertia. On the contrary, the vorticity-transport approach can account for the phase lag, which becomes more important in the last part (and downstream) of bends. Indeed, the vorticity-transport approach (Figure 2-5b) shows a persistent deviation of the high-velocity thread well after the bend (i.e., when there is no more curvature of the streamlines). In the case of multiple subsequent bends, the residual helical flow interacts with the secondary current that grows in the following bend (Abad and Garcia, 2009), thus increasing or decreasing the intensity of the helical flow depending on the curvature sign of successive bends. Passing from the first to the second bend, the high-velocity thread returns to the channel centre with the local approach, whereas it remains at the outer (left) side of the channel by transporting the vorticity. On the contrary, the change in curvature sign in the two last bends produces a retarded outward shift of the high-velocity thread in Figure 2-5b.

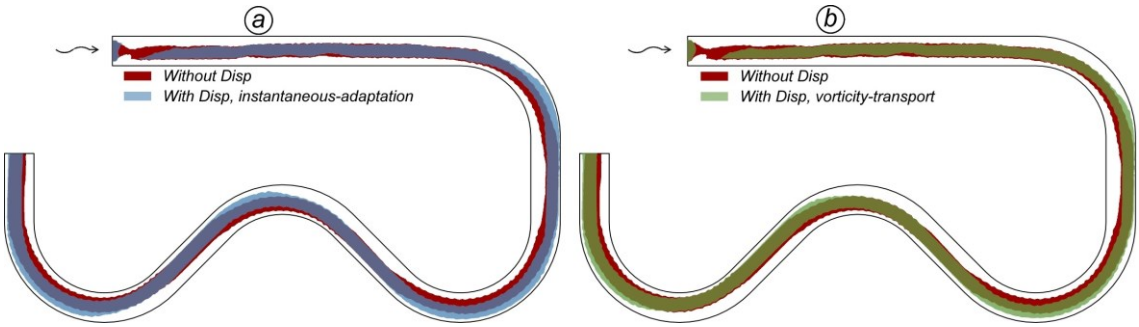

Figure 2-5. Main stream flow (velocity higher than 1.15 m/s) for the model without the dispersive terms (red) and a) with the instantaneous-adaptation approach (blue), b) with the vorticity-transport approach (green) for curvature-induced secondary flow.

In the RIPRAP experiment, the width ratio $Y/B \approx 0.2$ is quite low; notwithstanding, the sidewalls of the channel affect significantly the transversal velocity profile. As shown in Figure 2-25 (Appendix A. Supplementary Material), without including a wall function for the boundary elements, the model overpredicts the flow velocity close to the walls, and at some sections this overprediction becomes larger when including the dispersive stresses for curvature-induced helical flow.

The different formulations implemented for the source terms k_P and k_D in Eq. (2-10) and (2-11), reported in Table 2-1, produce very similar results. The different solutions become nearly indistinguishable both using the instantaneous-adaptation and the vorticity-transport approach (Figure 2-26 and Figure 2-27 in Appendix A: Supplementary Material).

2.3.2 Test with fixed-bed, strong-curvature, laboratory experiments

In strongly curved bends, the strong secondary circulations produced by the large streamline curvature flatten the vertical profile of velocity, thus weakening the mechanism of helical-flow production in what is called the saturation of secondary flows (Blanckaert and de Vriend, 2003).

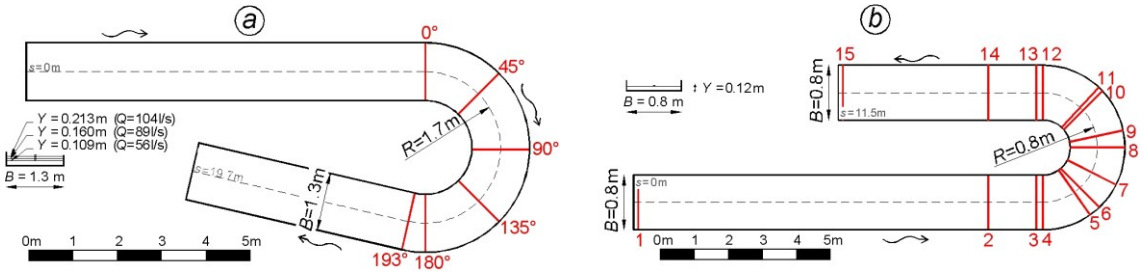

Figure 2-6. a) The EPFL channel (Blanckaert and de Vriend, 2003), and b) the Rozovskii (1957) channel, with numbered cross-sections.

We use the experiments of Blanckaert and de Vriend (2003) and Rozovskii (1957), in which the curvature is strong and the saturation effect plays a key role, to check the model accuracy in terms of secondary circulation strength and spatial pattern.

The Ecole Polytechnique Fédérale Lausanne (EPFL) channel (Blanckaert and de Vriend, 2003) has a length L = 19.7 m and a width B = 1.3 m, with vertical side walls. The bend develops for 193° with a constant curvature (radius R = 1.7 m at the centreline, Figure 2-6a). For the experiment here considered, the bottom is flat and fixed, and the Strickler coefficient is K_S = 60 m$^{1/3}$/s. Three different steady-flow experiments have been conducted with inflow of 56, 89, and 104 l/s and a downstream water depth of 10.9, 16.0, and 21.3 cm, respectively. With fixed upstream discharge and downstream water level, numerical simulations have been run until steady state conditions are attained. For the three scenarios, the bend sharpness is Y/R = 0.065, 0.095, and 0.125.

The dampening factor, f_D, introduced in Sects. 2.2.2 and 2.2.3 is computed for each computational cell based on the local flow variables, in particular on the transversal gradient of longitudinal velocity, α_s. Figure 2-7 shows that, in the first part of the bend, the high-velocity thread is located at the inner side of the bend ($\alpha_s < 0$ as in a potential flow), vorticity is still developing and the interaction with the primary flow is negligible: the production of streamwise vorticity is maximum ($f_D \approx 1$). In the second part of the bend, as the high-velocity thread is moved outward by the momentum transfer associated to the helical flow (α_s progressively increases), the non-linear saturation feedback mechanism becomes important and the production of vorticity is reduced ($f_D \ll 1$). At the downstream end of the bend, the high-velocity thread is close to the outer bank and $\alpha_s \approx 1$. Expectedly, by increasing the bend sharpness Y/R, the saturation effect develops faster and becomes stronger (second and third column in Figure 2-7), with the consequence that the helical flow intensity does not grow much with Y/R.

In Figure 2-8, the model results are compared with experimental data in terms of the non-dimensional quantity $\langle f_n^2 \rangle$ (angle brackets highlight depth-averaging), which measures the strength of the secondary circulation and is defined as (Blanckaert and de Vriend, 2003):

$$\langle f_n^{\,2} \rangle = \frac{\langle v_{ns}^2 \rangle}{\left(\frac{wY}{R}\right)^2} \tag{2-41}$$

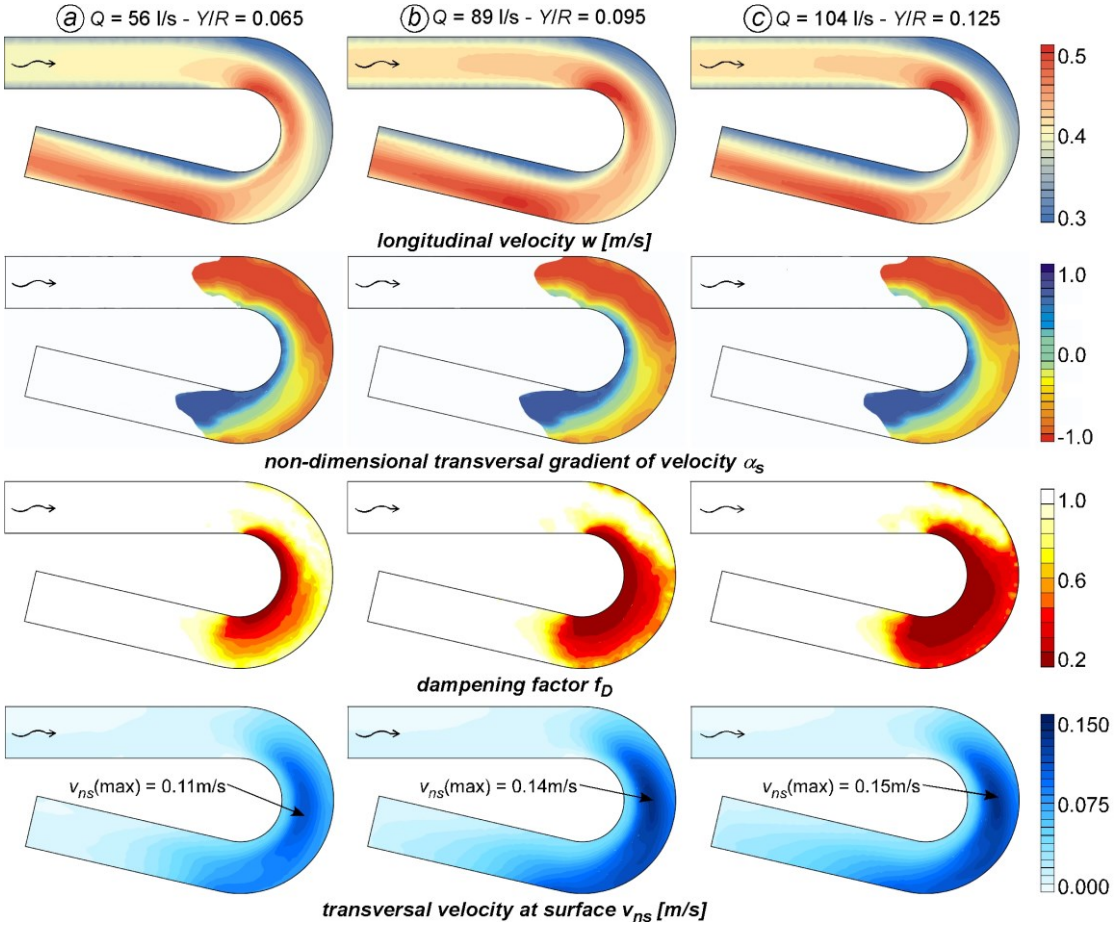

Figure 2-7. Spatial distribution of the depth-averaged flow velocity, w, of the normalized transversal gradient of velocity, α_s, of the dampening factor, f_D, and of the transversal velocity at the free surface, v_{ns}, for a) Q = 56 l/s, b) Q = 89 l/s, and c) Q = 104 l/s. Note that the α_s field has been masked where the local curvature radius, R, is larger than 20 m (both R and α_s tend to infinity in straight reaches).

Comparing the results with experimental data, the non-linear model allows to predict the magnitude of the secondary flow far more precisely than the linear model, confirming the effectiveness of the present approach. It has to be said that, while $\langle f_n^2 \rangle$ magnifies the secondary flow strength (thus the difference between linear and non-linear models), the change in the flow field obtained by accounting for non-linear saturation model is quite small in the first case (Q = 56 l/s), and more important for the largest discharge values. This suggests that accounting for non-linear effects improves the model predictions, and becomes fundamental for larger values of the bends sharpness.

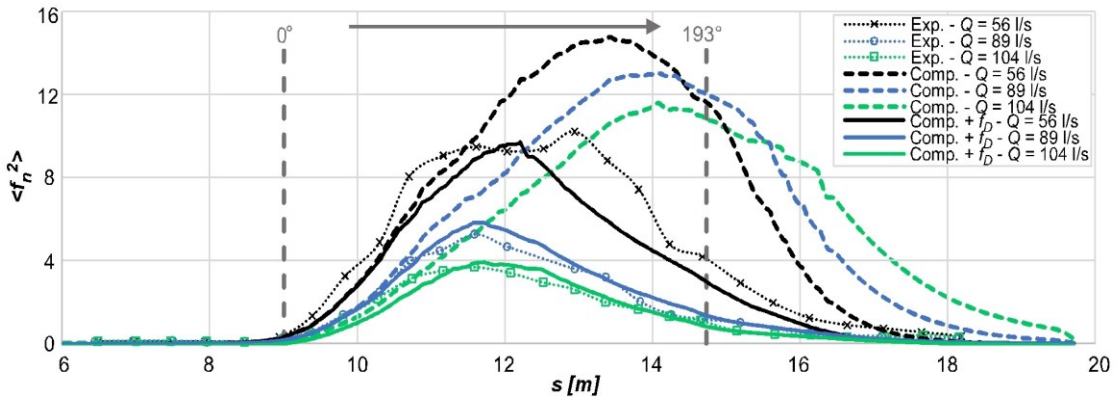

Figure 2-8. Magnitude of the secondary current, $\langle f_n^2 \rangle$. Comparison of experimental data (symbols, adapted from Blanckaert and de Vriend, 2003) with the results of the linear (dashed lines) and non-linear (solid lines) models, for the three discharge values considered in the experiments.

The channel used by Rozovskii (1957) has a length L = 11.5 m and a width B = 0.8 m, with vertical side walls. The bend develops for 180° with a constant curvature (radius R = 0.8 m at the centreline, Figure 2-6b). For the experiment here considered, the bottom is flat and fixed, and the Strickler roughness coefficient is K_S = 70 m$^{1/3}$/s. The inlet velocity is w = 0.26 m/s, and the downstream water depth is Y = 5.1 cm. The bend sharpness is $Y/R \approx 0.07$.

The model results, obtained with the no-slip condition at the sidewalls, are compared with the measured data in terms of depth-averaged velocity at different cross-sections (Figure 2-9), and in terms of water surface elevation along the channel at the inner and outer sidewalls (Figure 2-10). The model without dispersive terms overpredicts the velocity peak at the inner part of the bend, as can be noted especially between Section 5 and 11 in Figure 2-9. Introducing the dispersive terms with a linear formulation (i.e., f_D = 1 in Eq. (2-10) or (2-11)), the high-velocity thread is shifted to the outer side of the bend (dash-dotted lines), overestimating the observed redistribution of velocity, especially in the final part of the bend. Including the representation of the saturation mechanisms leads to a general improvement of model predictions. The free-surface profiles in Figure 2-10 show that a classical 2D model without dispersive terms tends to underpredict the head losses. The linear model for secondary currents leads to a significant overestimation of head losses, probably because the flow is much confinated toward the outer side of the bend. Again, including the non-linear effects improves the model prediction.

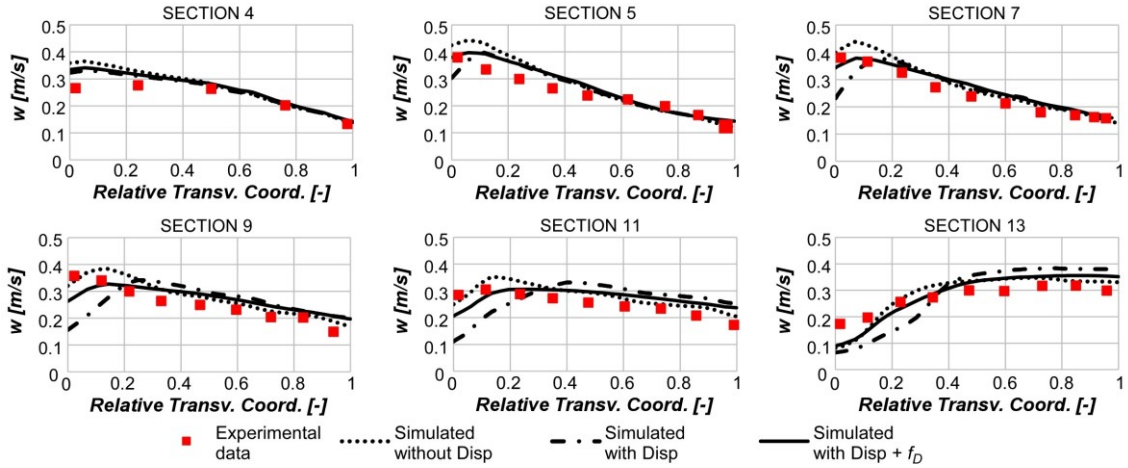

Figure 2-9. Transversal profiles of depth-averaged velocity for the Rozovskii (1957) experiment (red squares), compared with model results without dispersive stresses (dotted lines), with the linear, instantaneous-adaptation approach (dash-dot lines), and with the non-linear model (solid line). The transversal coordinate spans the channel width from the left to the right bank.

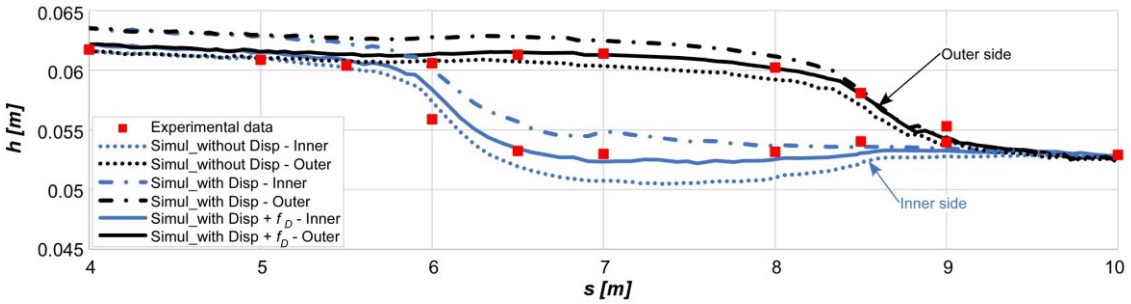

Figure 2-10. Longitudinal profiles of water surface elevation at the outer (black lines) and inner (blue lines) sides of the bend. Red squares are the data measured by Rozovskii (1957); model results are shown without considering dispersive terms (dotted lines), with the linear model for secondary currents (dash-dot lines), and including the non-linear saturation effect (solid lines).

The interest here is checking the effectiveness of the pure 2D non-linear model for secondary flow in terms of transversal distribution of dispersive stresses, as discussed in Sect. 2.2.4. For the experiment by Blanckaert and de Vriend (2003) with a discharge of 89 l/s, Figure 2-11a shows the spanwise distribution of the D_{sn} dispersive term at 90° from the beginning of the bend; the red line shows the measured data as reported by Ottevanger (2013). Linear models, either analytical (Ottevanger, 2013) or the present numerical scheme (green and black dash-dotted lines, respectively) overrate the dispersive stress, especially close to the sidewalls where it has to decay to zero (Blanckaert, 2001; Johannesson and Parker, 1989a) Prediction from the non-linear model with the no-slip condition at sidewalls (black solid line) is in good agreement with the

empirical formulation by Ottevanger (2013), and not too far from the measured data. A comparison among the same models and formulations, for the experiment by Rozovskii (1957), is reported in Figure 2-11b in terms of transversal velocity at the free-surface, $-v_{ns}$, which stands for the helical flow intensity. Although measured data are not available, it emerges that *i*) linear formulations (dash-dotted lines) lead to excessively strong circulation, *ii*) the no-slip condition at the sidewalls reduces the momentum redistribution close to the banks (black lines), and *iii*) accounting for both the sidewall friction and the non-linear saturation effects (black solid line) improves the physical soundness of the solution.

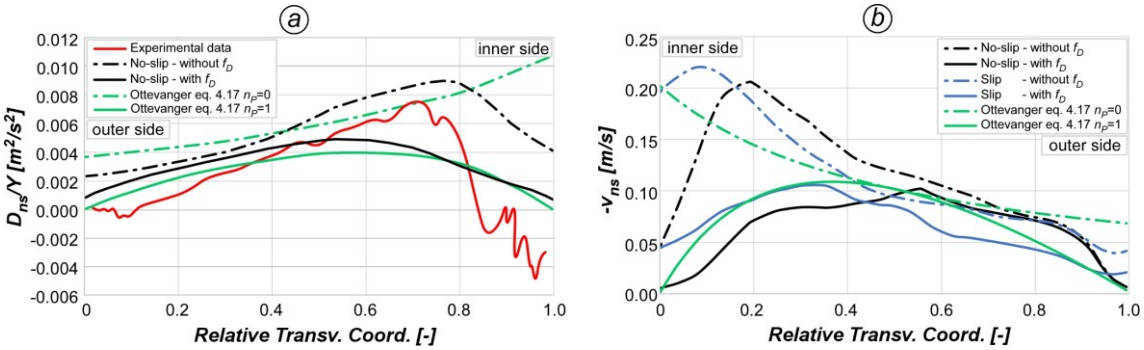

Figure 2-11. a) Transversal profiles of the D_{ns}/Y dispersive term for the 89 l/s experiment by Blanckaert and de Vriend (2003) at 90° from the beginning of the bend. The red line resembles the experimental data reported by Ottevanger (2013). b) Transversal profiles of the helical flow intensity (in terms of $-v_{ns}$) for the Rozovskii (1957) experiment at cross-section 6. In both panels, dash-dotted lines denote linear formulations; for the present model, black and blue lines correspond to no-slip and free-slip condition at the sidewall, respectively; the green lines are the theoretical profiles from Ottevanger (2013), referring to a linear model and its power-law extension (dash-dotted and solid lines, respectively).

2.3.3 Transport of passive tracers in curved channel

To test the model effectiveness in reproducing the transport of a generic passive tracer in presence of curvature-induced secondary currents, we use the experiments of Chang (1971), which have been subject to many model applications (see e.g., Begnudelli et al., 2010; Duan, 2004; Duan and Nanda, 2006; Ye and McCorquodale, 1997). The flume is 35.4 m long and it has two opposite 90° bends with a radius of curvature R = 8.53 m; the cross-section is rectangular and the width is B = 2.34 m. The mean velocity on the channel is U = 0.367 m/s and the water depth is Y = 0.115 m, which are obtained imposing an upstream inflow of 0.0988 m³/s, a downstream water level of 0.115 m, and running the model until steady state conditions are attained. A conservative tracer is then introduced with point injections located at 3 different transversal coordinates (the injection points are named IP_1, IP_2, and IP_3 in Figure 2-12), prescribing a constant value for the flowrate of the passive tracer (Q_C = 0.01 m³/s).

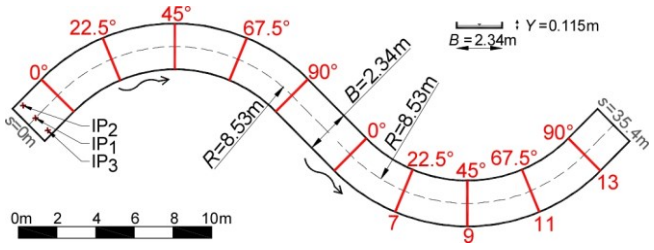

Figure 2-12. Layout of the flume used in the experiments by Chang (1971), with the location of the three point injections (IP_1, IP_2, IP_3) considered in the experiments.

The mesh resolution is a key factor for controlling the numerical diffusion in transport problems (Begnudelli et al., 2010; Casulli and Zanolli, 2005). To test the mesh-dependency of the model solution, three different mesh grids have been used, with 3,396 (mesh 1x), 13,349 (mesh 4x), 49,587 (mesh 16x) elements, respectively. These are obtained through halving the sides of each elements (i.e., the number of elements is about 4 times greater at each refinement). For the three meshes, the channel width to cell-side-length ratio, $B/\Delta x$, is about 10, 20, and 40. Figure 2-28 and Figure 2-29 in Appendix A (Supplementary Material) show that only the finest mesh (16x, channel width to cell-side-length ratio of about 40) leads to reliable results; with the coarser meshes (1x and 4x), numerical diffusion becomes unacceptably high.

Using the finest mesh, the concentration profiles (Figure 2-13) are in good agreement with the experimental data of Chang (1971). The comparison of solutions obtained with and without considering the curvature-induced dispersion (grey and black lines in Figure 2-13) highlights the enhanced diffusion generated by the helical flow, well described introducing the dispersive terms in the transport-diffusion equation.

When a proper mesh resolution is used, the dispersive terms in the advection-diffusion equation allow reproducing the correct tracer distribution in the curved channel with the Schmidt number $\sigma_T = 1$. Contrarily, to match the experimental data without using these dispersive terms, the Schmidt number has to be tuned to lower values (Figure 2-30 in Appendix A: Supplementary Material), so as to increase the spanwise diffusion artificially (Rodi, 2017; Ye and McCorquodale, 1998).

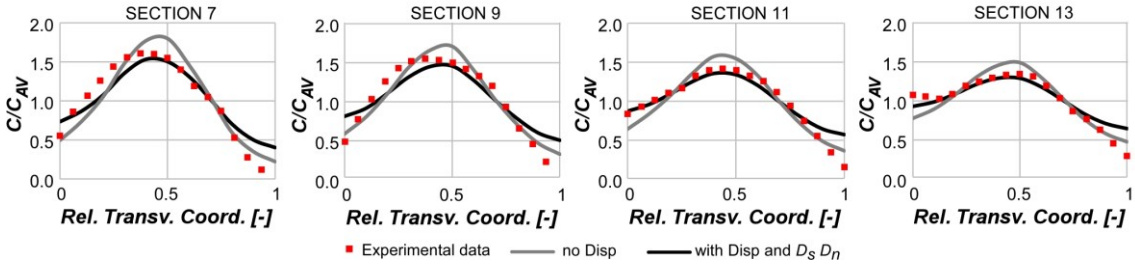

Figure 2-13. For the Chang (1971) experiment with point injection IP_1 and for the finest mesh (16x), transversal profiles of relative concentrations for Sections 7, 9, 11, and 13: experimental data (red dots) and model results without (grey lines) and with (black lines) dispersive terms in the momentum advection-diffusion equations.

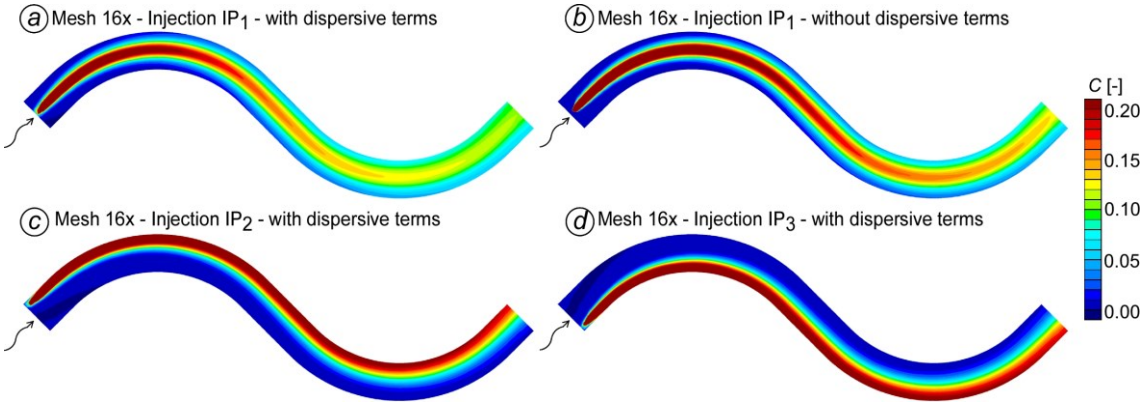

Figure 2-14. For the Chang (1971) experiment, depth-averaged normalized concentration obtained with the finer mesh 16x. For IP_1, with (a) and without (b) dispersive terms in the momentum and transport-diffusion equations; for IP_2 (c) and IP_3 (d) with dispersive terms.

The top views of Figure 2-14a,b, referring to the same scenarios of Figure 2-13, suggest that the strength of the secondary flow is modest in the experiments of Chang (1971). This is confirmed by looking at Figure 2-14c,d (lateral injection points IP_2 and IP_3): the tracer remains almost confined closed to the lateral walls, according to the experimental data and numerical results shown by Duan (2004) and Moncho-Esteve et al. (2017).

Finally, the role of the longitudinal dispersion terms (D_s in Eq. (2-14)) is highlighted in Figure 2-31 in Appendix A (Supplementary Material) by releasing the tracer at point IP_1 starting at $t = 0$, on a steady baseflow. With $D_s = 0$, the leading front of the "coloured" water reveals that the high-velocity thread is located at the inner side (free-vortex flow, weak velocity redistribution performed by the secondary current); the additional anisotropic, streamwise diffusion provided by the D_s terms makes the leading front faster and closer to the channel centreline.

2.3.4 Bedload transport – Laboratory experiments

The parametrization of curvature-induced helical flows allows to estimate the near-bed transversal component of the flow velocity, thus predicting more precisely the direction of the bedload transport. To analyse this influence on the bed evolution, we considered the experiment performed by Koch and Flokstra (1980) at the Laboratory of Fluid Mechanics (LFM) channel. The channel has a rectangular cross-section (width $B = 1.7$ m) and a U-shape bend with curvature radius $R = 4.25$ m measured at the centreline. The longitudinal bed slope is 0.18% and the Strickler roughness coefficient is $K_S = 36$ m$^{1/3}$/s. The discharge is $Q = 0.17$ m^3/s and the downstream water depth is $Y = 0.2$ m. The bed sediment has a median diameter $d_s = 0.78$ mm and a relative density $s = 2.65$.

The mesh has 1,719 nodes and 3,040 elements, corresponding to about 8 elements per channel width. The simulations started from a previously-computed steady flow over a bed with only streamwise slope; then, keeping fixed the inflow discharge and the

downstream water level, the bed is left free to evolve until an equilibrium state is reached.

Without any corrections to account for helical flow, the bottom shear stresses are aligned to the primary flow (Figure 2-15a). Introducing the secondary current correction, bottom stresses change the direction inward (Figure 2-15b). This produces an imbalance in the bedload transport, with leads to scouring at the outer side and bed accretion at the inner part of the bend.

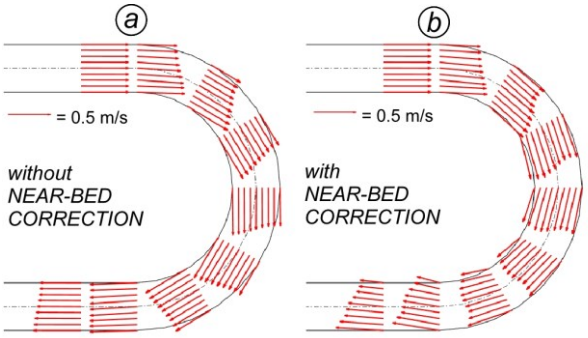

Figure 2-15. Water velocity vectors at the bottom without (a) and with (b) correction for the secondary flow.

The bed topography at equilibrium is shown in the colour maps of Figure 2-16 in terms of erosion/deposition with respect to the initially flat bed, Δz, and in the transversal profiles of bed elevations reported in Figure 2-17 (see also Figure 2-32 in Appendix A: Supplementary Material, which plots the difference among computed and measured values of Δz). With respect to the experimental data (Figure 2-16a), a 2D model with no corrections for the bedload direction leads to completely unreliable results: only the accelerations and decelerations associated to the free-vortex flow field at the beginning and at the end of the bend produce some modification of the bed (Figure 2-16b). The empirical correction of bedload direction proposed by Olesen (1987), with $A_c = 10$ in Eq. (2-36), tends to overestimates both erosion and depositions (Figure 2-16c); especially, as this correction is based on the local radius of curvature, scour and deposition start at the very beginning of the bend (no phase lag) and proceed uniformly along the bend (in the experiment scour and erosion slightly decrease). At 135° the computed Δz is over 3 times larger than the measured one (Figure 2-17).

The explicit parametrization of the secondary current and the correction of bedload direction proposed by Bernard and Schneider (1992), leads to better estimations; compared to the instantaneous-adaptation approach (Figure 2-16d), the vorticity-transport approach in Figure 2-16e correctly reproduces the initial phase lag and the increased scour at the end of the bend, close to the outer wall. The cross-sections in Figure 2-17 show that the inclusion of secondary flow, according to Bernard and Schneider (1992), well reproduces the inner aggradation, whereas the outer scour is underestimated.

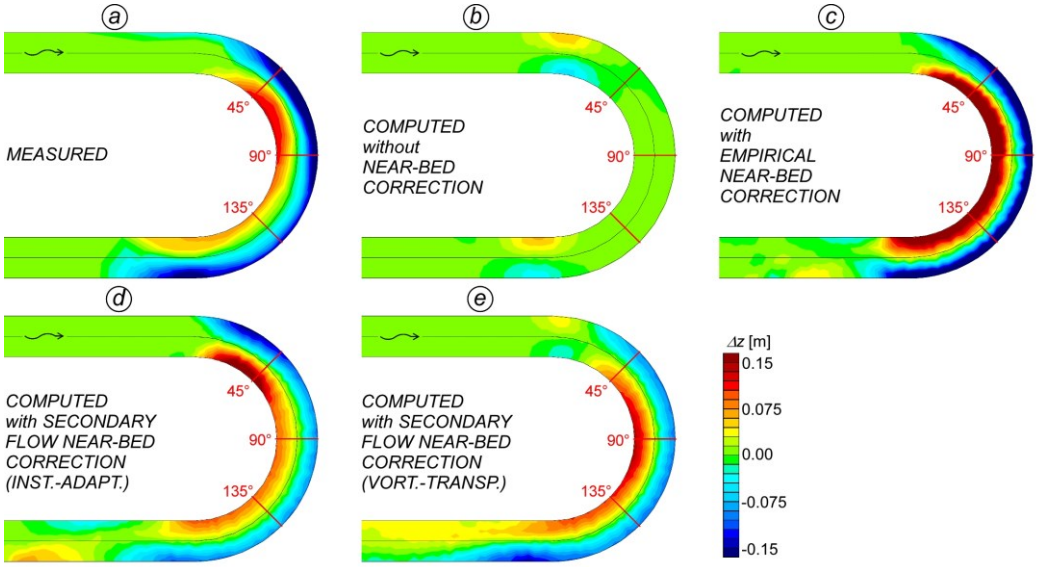

Figure 2-16. Bed elevation with respect to the undisturbed flat bed ($\Delta z > 0$ denotes deposition, $\Delta z < 0$ erosion). a) Experimental data reproduced from Koch and Flokstra (1980); b) model results without any correction for bed-load direction; c) model results with empirical bed-load direction correction ($A = 10$ in Eq. (2-36)); d) model results with dispersive terms correction (instantaneous-adaptation approach), e) model results with dispersive terms correction (vorticity-transport approach).

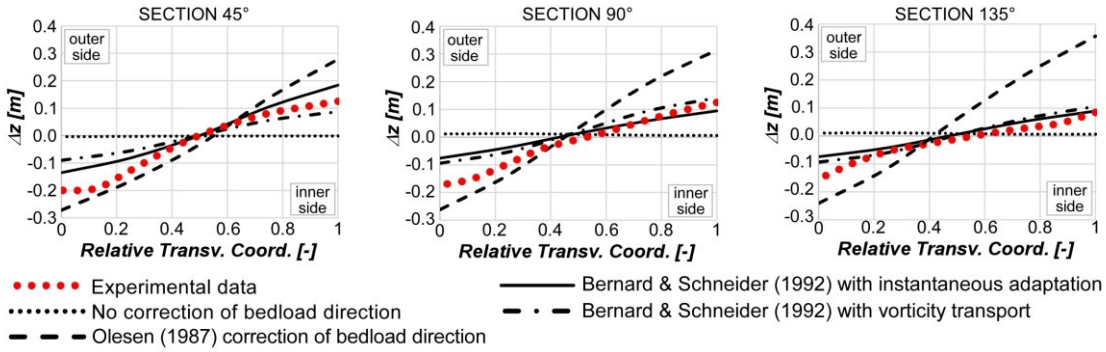

Figure 2-17. Transversal profiles of bed elevation at 45°, 90°, and 135°with the results provided by different modelling approaches compared to the Koch and Flokstra (1980) experimental data.

Finally, Figure 2-18 shows a comparison of the scour/deposition produced by the three different models for secondary flow here implemented. The bed evolution is estimated using different parametrization for secondary currents intensity. Compared to Bernard and Schneider (1992), which is in good agreement with experimental data, the models of Kalkwijk and Booji (1986) and Odgaard (1986) slightly underestimate the magnitude of Δz, yet with a very similar spatial pattern (see also Figure 2-33 in Appendix A: Supplementary Material, which plots the difference among computed and measured values of Δz).

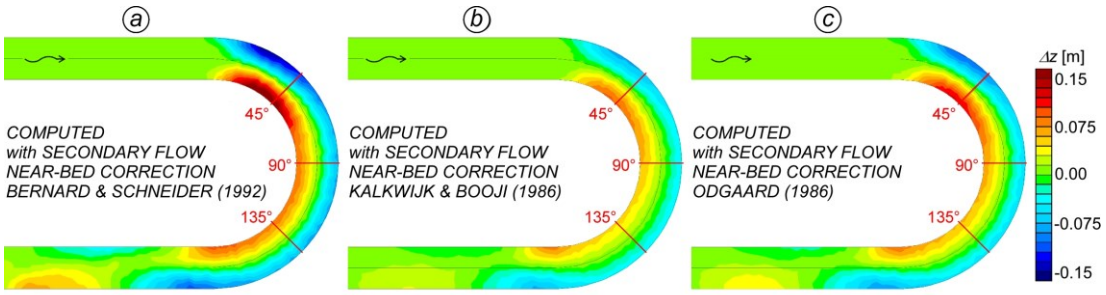

Figure 2-18. Bed topography in terms of erosion/deposition with respect to a flat bed, computed with the dispersive terms corrections computed using the instantaneous-adaptation approach and the formulations of (a) Bernard and Schneider (1992), (b) Kalkwijk and Booji (1986), and (c) Odgaard (1986).

2.3.5 Real-world case study: fixed and mobile bed

The model is finally applied to a real-world case study, the ~50 km long reach of Po River (Northern Italy) between the Mincio and the Panaro confluences, i.e., from 12 km upstream of Ostiglia to 8 km downstream of Ficarolo (Figure 2-19). The meandering reach has been modelled using a 2D triangular grid with 58,570 nodes and 114,452 elements. We focus on three meandering bends, denoted as M1, M2, and M3 in Figure 2-19. Table 2-2 reports additional details. The bathymetry, derived from a 2004 multibeam survey merged with a 2008 LiDAR survey, is shown in Figure 2-34 in Appendix A (Supplementary Material).

A fixed water level, derived from an available rating curve, is used as downstream boundary condition. We then considered three different discharge scenarios, named Q_3990, Q_7400, Q_11500 (where Q denotes the discharge expressed in m^3/s and imposed the inlet section).

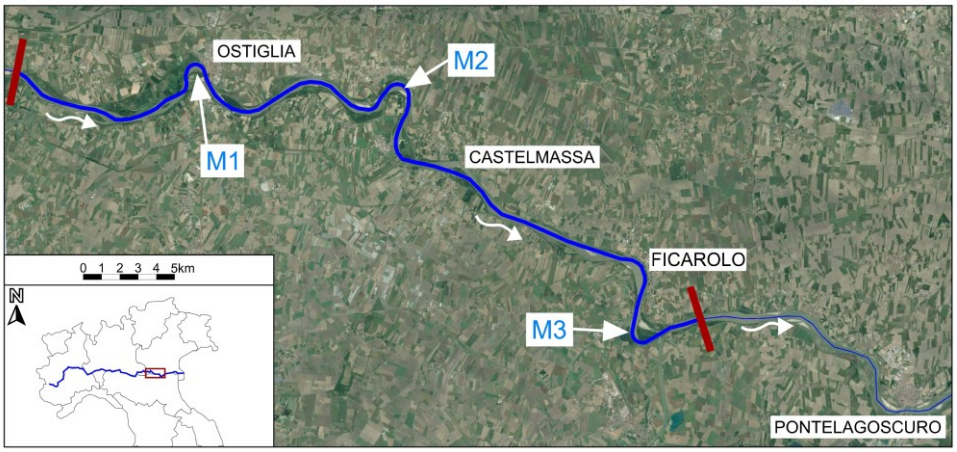

Figure 2-19. The meandering reach of the Po River (Italy) between the Mincio and Panaro confluences.

For each discharge scenario, a first set of simulations has been performed with the fixed, real bathymetry, with and without including the dispersive terms in the momentum equations. The inclusion of secondary flow correction entails minor changes to the flow field. An example is shown in Figure 2-20; at the AA cross-section (meander M1), the increase and the outer shift of the peak velocity, obtained by including the correction for the secondary flow, is absolutely modest, and it further decreases for lower flowrate values (e.g., Q = 3,990 m³/s, Figure 2-20b). Using the instantaneous adaptation or the vorticity-transport approach entails negligible differences as well (dashed and solid lines in Figure 2-20b). Similar results are obtained for meanders M2 and M3 (some relevant parameters are reported in Table 2-2). The depth-averaged velocity field at meander M1, for the discharge Q = 11,500 m³/s and including the dispersive stresses in the momentum equations, is shown in Figure 2-21. The w = 2 m/s isoline is plotted for both the cases with (magenta) and without (orange) the dispersive stresses, again without any substantial difference. These results suggest that including the dispersive terms for curvature-induced secondary flow is inessential to model the depth-averaged 2D flow field in natural rivers with fixed deformed bed. This is discussed in detail Section 2.4.5. Nonetheless, it has been already pointed out that that secondary flow plays a major role with respect to the development of the bed topography (Blanckaert, 2010; Shimizu et al., 1990).

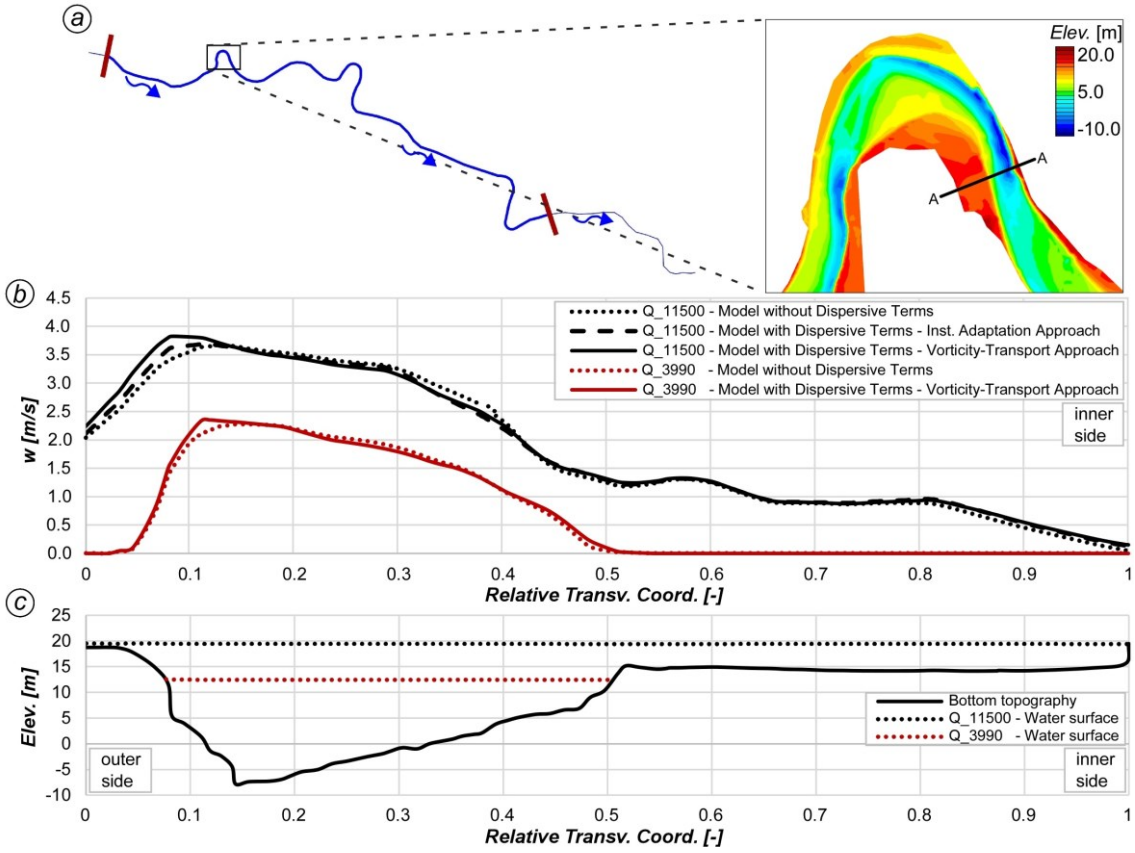

Figure 2-20. Po River case study. Transversal profiles at the AA cross-section (at meander M1, panel a) of the depth-average velocity (b) and water and bed levels (c).

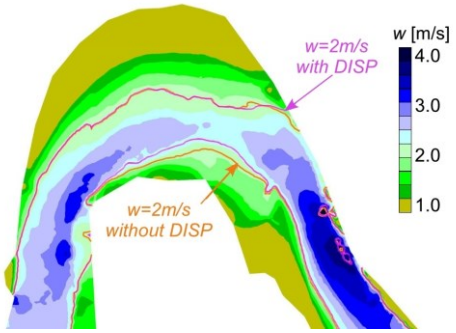

Figure 2-21. Spatial distribution of the depth-average velocity at meander M1 for Q_11500 and isoline for w = 2 m/s without (orange) and with (magenta) dispersive terms in the momentum equations.

Table 2-2. Po River case study. Characteristics of the simulations and relevant flow variables for scenarios Q_3990, Q_7400, and Q_11500; the depth-average velocity is computed either neglecting (w) or considering (w^*) the dispersive terms.

		Q_3990			**Q_7400**			**Q_11500**		
Discharge	[m³/s]	3,990			7,400			11,500		
D.s. water lev	[m]	8			12			16		
		M1	**M2**	**M3**	**M1**	**M2**	**M3**	**M1**	**M2**	**M3**
Y_{MAX}	[m]	21.5	20.6	20.8	25.1	24.5	25.0	28.7	28.0	28.8
R	[m]	480	630	570	480	630	570	480	630	570
w_{MAX}	[m/s]	2.71	2.59	2.32	3.95	3.27	2.59	4.37	3.39	2.58
D_{s_MAX}	[Pa]	29	23	22	50	28	26	53	49	29
v_{s_MAX}	[m/s]	0.27	0.30	0.35	0.41	0.32	0.41	0.51	0.36	0.23
w^*_{MAX}	[m/s]	2.91	2.68	2.45	4.24	3.30	2.65	4.66	3.98	2.59
w^*_{MAX}/w_{MAX}	[-]	1.07	1.03	1.06	1.07	1.01	1.02	1.07	1.17	1.01

The Po River case study is then used to check the ability of the different approaches for curvature-induced secondary flow in modelling the relevant hydro-morphodynamic processes and to produce real-like bathymetric configurations. Hence, a set of mobile-bed simulations has been run starting from a flat bed, i.e., an unbalanced bathymetric configuration obtained by linearly interpolating the bed elevation from the mesh inlet to the outlet (Figure 2-22b, the surveyed bed is shown in Figure 2-22a). The movable-bed simulations, either with or without dispersive terms and correction for bedload direction, are run with a constant discharge Q = 11,500 m³/s until an equilibrium bed condition is reached. The inclusion of dispersive stresses and the correction for bedload direction are actually necessary to obtain reliable bed configurations, as demonstrated by comparing the equilibrium configuration obtained in the two different modelling approaches (Figure 2-22c). Interestingly, reliable equilibrium bathymetries are obtained also using the empirical correction for the bedload direction proposed by Olesen (1987), with A_c = 10, or considering a lower discharge of Q = 7,400 m³/s (see Figure 2-35 in Appendix A: Supplementary Material).

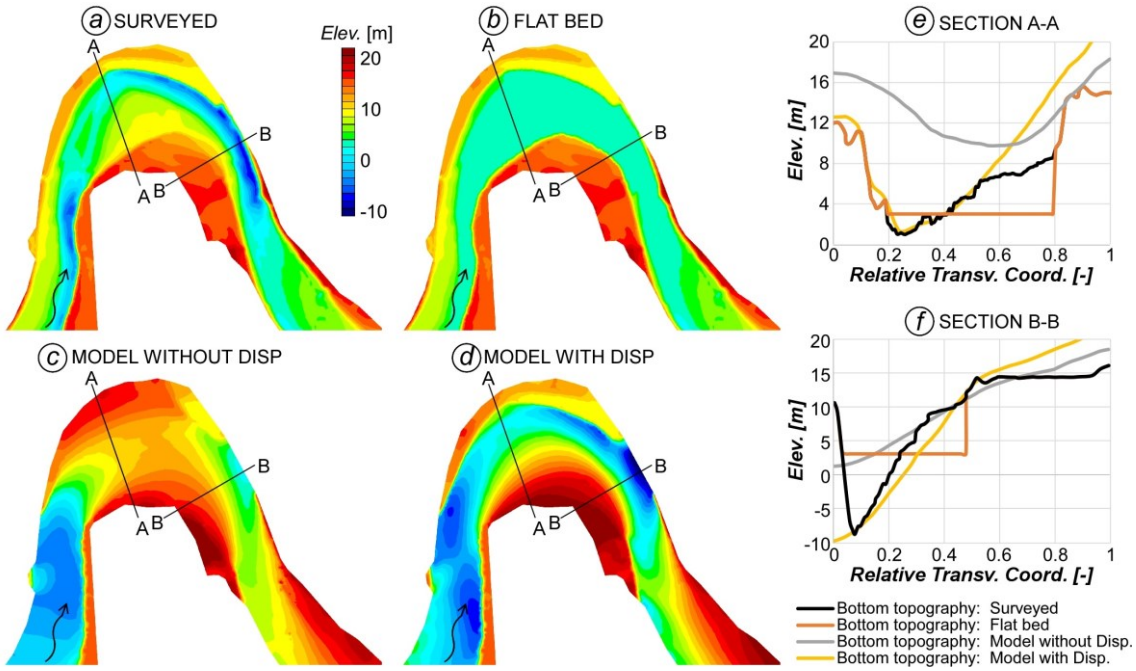

Figure 2-22. Po River case study, meander bend M1. Surveyed bathymetry (a), flat bed used as initial condition for mobile-bed simulations (b), bed equilibrium condition modelled without (c) and with (d) dispersive terms and correction of bedload direction (vorticity-transport approach). The different bed configurations are also shown at cross-sections AA and BB (e,f).

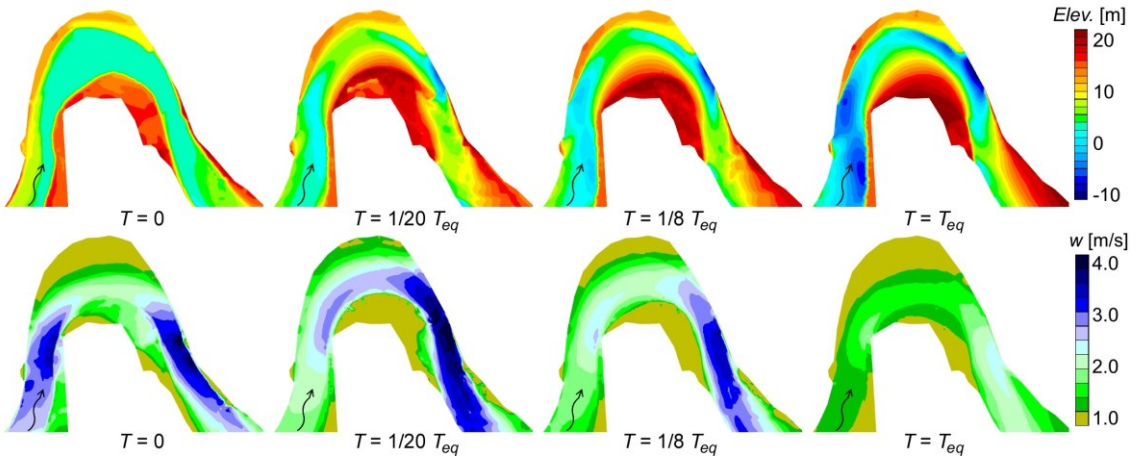

Figure 2-23. Po River case study, meander bend M1. Bed evolution from an initial flat bed up to the equilibrium condition: modelled bathymetry (upper row) and flow velocity (lower row) at different time instants (0, 1/20 T_{eq}, 1/8 T_{eq}, and T_{eq}), with the time needed to reach the equilibrium condition being $T_{eq} \approx 2$ years.

Figure 2-23 shows the bed evolution and the depth-averaged velocity field, from the initially flat bed to the equilibrium condition (reached at time $T_{eq} \approx 2$ years), modelled considering the dispersive terms. With the flat bed, the high-velocity thread is located at the inner part of the bend, and the flow then collides at an oblique angle with the outer bank; in this situation, the secondary flow is relatively strong, and so is the velocity redistribution entailed by the dispersive terms. As time advances, sediments are carried toward the accreting point bar, in the inner part of the bend, due to the inward direction imposed by the helical flow. The main part of the discharge then flows over the deepest part of the bend, driven by topographic steering (Blanckaert, 2010) more than by momentum redistribution induced by the secondary flow. Approaching the equilibrium condition, the importance of topographic steering increases, and the already weak effect of dispersive terms further reduces.

2.4 Discussion

This study deals with the inclusion of helical flow secondary currents in two-dimensional, general-purpose, river- and flood-models. The implementation of different modelling approaches and the application to several case studies, both in the laboratory and in the field, shed light on a set of interesting issues, which are here discussed.

2.4.1 The role of dispersive terms in momentum and transport-diffusion equations

The model applications described in the previous section highlighted the importance of including the dispersive terms; yet, not all these terms play an important role, nor are always necessary.

In the momentum equations, the most important contribution is given by the diagonal term D_{sn}; its spatial gradient entails additional resistance at the inner side of bends and acceleration at the outer side of bends (Dietrich and Smith, 1983), which are the outcome of the outward momentum transfer generated by the helical flow. The D_{ss} and D_{nn} terms are often neglected in the technical literature (e.g., Finnie et al., 1999). Indeed, the streamwise variation of D_{ss} is generally smooth, and the D_{nn} term is typically much smaller than D_{sn} when the curvature ratio, Y/R, is much lower than 1 (Lien et al., 1999). In the model applications described above, the inclusion of the D_{ss} and D_{nn} terms (not shown) produced negligible modifications in the model outcomes.

In the equation for transport and diffusion of conservative tracers and suspended matters, the inclusion of dispersive terms suffices to avoid the calibration of the Schmidt number to match experimental data. However, in transport/diffusion problems, the mesh resolution is the key factor to control the numerical diffusion and to obtain reliable results.

2.4.2 Model sensitivity to the mesh resolution

The dispersive terms for curvature-induced secondary flows rely on the proper evaluation of the transversal gradient of the D_{sn} dispersive stress. The effectiveness of

the helical-flow parameterization then depends on the mesh resolution. We performed an ad-hoc sensitivity analysis of the model results to the mesh resolution for the above case studies.

As a representative example, for the RIPRAP experiment, we compared the model results obtained with four different mesh (Figure 2-24):

- *mesh_1x*: cell-side-length ≈ 2.00 m, $B/\Delta x$ = 4, tot. 1,112 cells;
- *mesh_10x*: cell-side-length ≈ 0.45 m, $B/\Delta x$ = 10, tot. 11,528 cells;
- *mesh_40x*: cell-side-length ≈ 0.22 m, $B/\Delta x$ = 24, tot. 43,395 cells;
- *mesh_160x*: cell-side-length ≈ 0.11 m, $B/\Delta x$ = 48, tot. 166,965 cells;

with $B/\Delta x$ the channel width to cell-side-length ratio.

Figure 2-24 shows that the dispersive terms, which comes from the transversal derivatives of the D_{sn} stresses, are smoothed out excessively using the coarsest *mesh_1x*. The *mesh_10x* well adheres to the experimental velocity data (Figure 2-24f). The *mesh_40x* improves the representation of dispersive terms, particularly close to the channel walls where the highest gradients of dispersive terms are located (Figure 2-24b), leading to an improved spanwise distribution of flow velocity (Figure 2-24f). Finally, as shown in Figure 2-24g, the far increased computational need required by *mesh_160x* (vertical bars) is not counterbalanced by a further improvement of the solution (the velocity RMSE does not reduce for $B/\Delta x$ > 10).

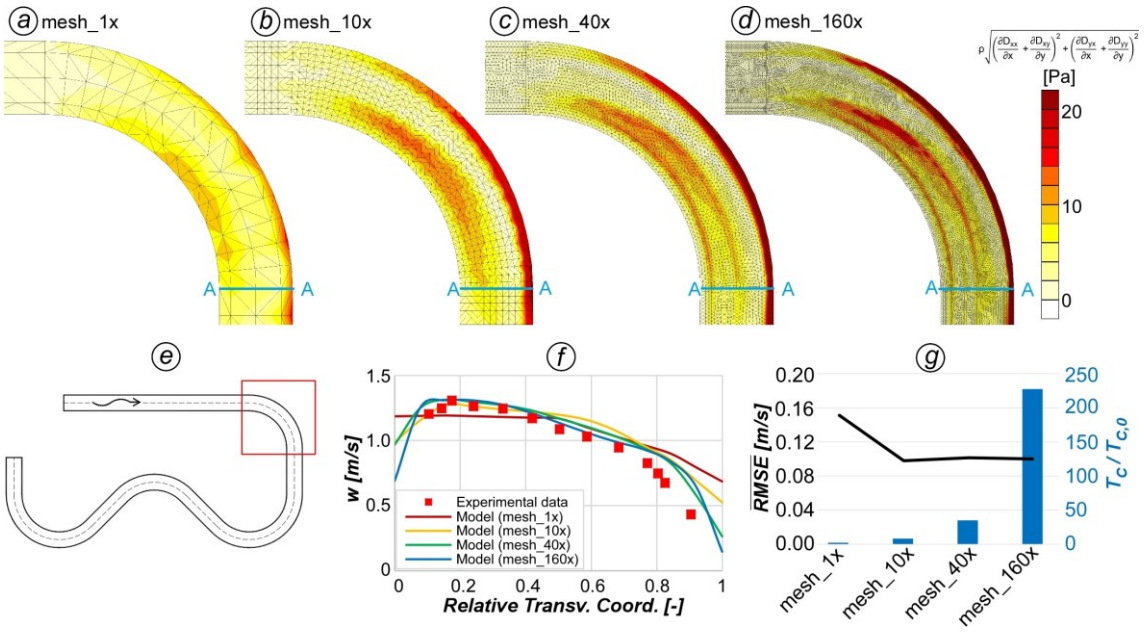

Figure 2-24. (a-d) Magnitude of dispersive terms in the first bend of the RIPRAP facility channel for different mesh resolutions; (e) location of the first bend, and (f) transversal distribution of depth-averaged flow velocity at cross-section AA for the different mesh resolutions; (g) Computational time (vertical bars) with respect to the 1x mesh and velocity RMSE (black line) for the different mesh resolutions.

The mesh resolution was shown to have a far more important role in controlling the numerical diffusion of passive tracers and suspended matters (Sect. 2.3.3), which requires finer meshes ($B/\Delta x \approx 40$) than for including the parameterization of secondary-flow on momentum equations only ($B/\Delta x \approx 10 \div 20$). Using a coarser mesh with the Schmidt number tuned to larger values is a computationally efficient alternative; however, it entails extra diffusion in straight river segments and a loss of predictive ability (ah-hoc calibration becomes mandatory).

The choice of the grid structure (e.g., structure or unstructured, regular or irregular) is another issue that can affect the numerical diffusion of transported tracers (Casulli and Zanolli, 2005). While unstructured meshes allow for a greater flexibility and easier adaptation to irregular boundaries, the computation of the spatial gradients of dispersive stresses may become challenging close to geometrical singularities and at interfaces where elements size changes abruptly (Nabi et al., 2016). An ad-hoc sensitivity analysis (not shown here) demonstrated that, when a proper mesh resolution is chosen, the schemes described at Sects. 0 led to an accurate estimation of the spatial gradients irrespective of the kind of structured mesh employed (e.g., regular, aligned with flow, or irregular cell patterns).

2.4.3 Modelling approaches to dispersive stress estimation

Different options have been implemented to estimate the helical flow intensity, which regard the local or transported approach (i.e., with instantaneous adaptation or by transporting the streamwise vorticity component), the theoretical formulation for the secondary flow parameterization (i.e., the expression for k_P and k_D in Eqs. (2-10) or (2-11)), the inclusion of wall functions and of a non-linear model for secondary flow saturation. The choice of the most suitable approach mainly depends on the geometrical configuration of the channel. Here we collect some general criteria.

The local approach is the easiest to implement, the cheapest from a computational standpoint, and particularly suitable for long, regular bends. As it neglects the secondary-flow inertia, the helical flow intensity can be overpredicted in high-curvature bends, especially at the entrance of the bend, or mispredicted in tight succession of counterrotating bends. Moreover, the local approach is very sensitive to geometrical singularities that entail abrupt variations of streamline curvature (also in straight river segments, where spurious local variations of dispersive stresses can appear). Thus, to avoid the onset of unphysical dispersive stresses, it is a good practice to apply a spatial smoothing (e.g., a Shapiro filter, Shapiro, 1970) to the streamline curvature field. The vorticity-transport approach, which intrinsically smooths out possible unevenness in the streamline curvature field as a result of the secondary flow inertia, is surely more robust and physically sound, yet more demanding from a computational standpoint. It is advisable for river channels in which the bathymetry presents some unevenness, in the case of sharp bends, and in tight sequences of bends.

The different parameterizations of secondary flow here implemented (see Table 2-1) lead to dispersive stresses, D_{ij}, whose magnitude are quite different; however, the dispersive terms in the momentum equations, which depend on the spatial gradients of

D_{ij}, are coherently predicted by the different parameterizations herein tested. The model applications of Sect. 2.3 suggested that the different theoretical formulations are practically equivalent to each other.

The magnitude of dispersive terms in momentum equations, which depends on the gradients of dispersive stresses D_{ij}, is generally negligible at the channel centreline and maximum towards the banks, where both flow velocity and the dispersive stress tend to zero and their derivatives reach the maximum values (Blanckaert, 2001; Johannesson and Parker, 1989a). In case of compact, low aspect-ratio cross-sections, the velocity gradient at the banks is greatly affected by the no-slip condition at the channel walls. In these cases, which are generally found in laboratory flumes, the use of wall functions to account for side-wall friction is mandatory. Instead, in natural bends, the effect of lateral wall is less significant as banks are tilted and the aspect ratio is far larger; in this kind of cross-sections, velocity reduces progressively in the transversal direction, dictated by the progressive reduction of water depth. Consequently, the free-slip condition at sidewalls is generally an acceptable hypothesis in natural rivers.

Finally, the model applications showed that the saturation of secondary flow has to be accounted for, to limit the intensity of helical flow, when strong secondary currents act to flatten the vertical profile of the streamwise velocity component (Blanckaert, 2009; Blanckaert et al., 2013). When (and where) the saturation effect becomes important is not only a function of the bend curvature, but also of the local flow field. Indeed, the key parameter governing the occurring of saturation is the spanwise gradient of the longitudinal velocity component, which describes if the high-velocity thread locates at the inner (free-vortex type flow) or at the outer (forced-vortex type flow) of the bend. Importantly, the local flow field and the transversal gradient of velocity, α_s, also depend on the bed bathymetry, i.e., flat or deformed (outward tilted).

This can be seen also by looking at the spatial distribution of the parameter α_s (the normalized transversal gradient of the depth-averaged velocity). For a flat-bed rectangular cross-section, α_s is expected to approach −1 at the beginning of the bend (free-vortex flow type) and to progressively increase along the bend to denote forced-vortex flow type (Blanckaert, 2010). This is roughly depicted in the upper panels of Figure 2-7. Instead, in a real bend with deformed bed, the high-velocity thread locates at the outer side of the bend due to topographic steering, keeping $\alpha_s \approx 1$ at the inner side, and $\alpha_s \approx -1$ at the outer side all along the bend (Figure 2-36 in Appendix A: Supplementary Material). As a result, the helical flow intensity is dampened by the saturation model ($f_D \ll 1$) at the main core of the flow (outer side of the bend) where the velocity and the centrifugal force are highest, and limited by the low streamwise velocity at the inner side of the bend (where the dampening factor $f_D \approx 1$ would let the helical flow to develop free). Interestingly, when the depth-averaged flow field is mainly driven by the bathymetry, the spatial distribution of α_s remain broadly the same either considering or ignoring the dispersive terms (Figure 2-36 in Appendix A: Supplementary Material). The role of bend bathymetry is further discussed in the Sect. 2.4.5.

A relevant aspect concerning the model implementation is that the saturation effect can be effectively assessed with a pure 2D approach thus avoiding any reference to the

channel centreline or width (Gu et al., 2016; Ottevanger et al., 2012), nor requiring time-consuming iterative procedures to estimate the non-linear parameters (Qin et al., 2019). In this way, the validity of traditional 2D models is extended to relatively sharp bends in a straightforward manner and without dramatic increase of the computational burden. The modeller should be aware that 2D models, equipped with this kind of description of secondary flows, cannot represent the formation of counterrotating secondary cells in very sharp bend (Blanckaert and de Vriend, 2010; Stoesser et al., 2010).

2.4.4 Ill-posedness and instability in 2D secondary flow models

The recent study by Chavarrías et al. (2019) highlighted an important issue concerning the possible ill-posedness of 2D depth-averaged models with linear formulation for the secondary flow. They considered the case in which the helical flow intensity is computed using a transport equation. Ill-posedness was shown to appear in the form of non-physical oscillations of the flow field, which increase with increased grid refinement. They demonstrated that adding a certain amount of diffusion, particularly in the spanwise direction, may lead to a well-posed problem and provide stable solutions. Besides that, they observed that accounting for the saturation effect may have a similar stabilizing effect, as saturation models act to dampen any kind of unbounded production of helical flow intensity, as in the case of unstable short waves.

On the one hand, we stress that, while 2D models compute the intensity of the helical flow locally, the secondary flow typically emerges as a unique rotating cell in the physical domain. Hence, to be physically consistent, the helical flow intensity computed by 2D models should vary smoothly in the spanwise direction. Of course, enhanced transversal diffusion, as that provided by the use of coarse grids, is beneficial in this regard. On the other hand, it is interesting to note that, in the numerical experiments by Chavarrías et al. (2019), model instabilities as a result of ill-posedness were significant for a grid with $B/\Delta x = 100$ and disappeared when they used a coarser grid with $B/\Delta x = 10$, comparable with the grid resolution used (and suggested as reasonable) in the present study.

2.4.5 The interplay of secondary flow and bed bathymetry

The importance of secondary flow in shaping hydro- and morphodynamics in curved channels, as well as the ability of 2D models to effectively capture the effects of helical flow, have been long debated in the literature (Alho and Mäkinen, 2010; Guan et al., 2016; Kasvi et al., 2015, 2013; Lane, 1998). A tangled picture also emerges from the case studies assessed in Sect. 2.3; including the dispersive terms in the momentum equations was crucial in the case of laboratory experiments, yet it entailed minor changes to the flow field in the real-world case of the Po River considering the surveyed bed bathymetry. The different behaviour might be attributed to different curvature ratios among these tests. We then computed, for the model applications presented in Sect. 2.3, different scaling parameters that have been proposed to measure the strength of curvature-induced secondary flow and its effects on hydrodynamic (Kashyap et al.,

2012). According to the values collected in Table 2-3, the secondary flow correction is most important in the EPFL channel of Blanckaert and de Vriend (2003) followed by that of Rozovskii (1957), and less important for the Chang (1971) case. This ranking agrees with the outcomes of the model applications shown in Sect. 2.3.1 and 2.3.3, respectively. In fact, we used the experimental data by Chang (1971) only to check the transport and diffusion module, because the effect of dispersive terms on the depth-averaged 2D hydrodynamics was negligible. Looking at the Po River case study, the parameters of Table 2-3 are actually lower (but not substantially lower) than those computed in the laboratory experiments described above. The small differences do not justify the weak to negligible effect of secondary flows on the depth-averaged hydrodynamics of the Po River test case. Similarly, the velocity redistribution by secondary flow is known to be much important for narrow cross-sections (e.g., $B/Y \approx 10$) and negligible in shallow ones with $B/Y > 50$ (Blanckaert, 2011; Blanckaert and de Vriend, 2010; Constantinescu et al., 2013) but, again, the aspect ratio of the Po River case study is not so different to justify the basically different behaviour.

The above considerations and the results shown in Sect. 2.3.5 suggest that the main reason for the controversial results obtained in the previous and present applications stems from the fact that the development of (and the role played by) secondary flows essentially depends on the bed bathymetry. In the Po River test, the surveyed bottom is deformed (see the cross-section in Figure 2-20 and the colour map in Figure 2-22a), whereas the laboratory tests dealt with compact cross-sections with flat bed and vertical walls. By performing additional numerical experiments in which the bed was artificially flattened, it was shown that the flow field in the Po River bends with deformed bathymetry is mainly driven by the bed topography (i.e., the so-called topographic steering) than by momentum exchanges and velocity redistribution ascribed to curvature-induced secondary flow (Blanckaert, 2010; Chen and Duan, 2006; Deng et al., 2021; He, 2018; van Balen et al., 2010).

Table 2-3. Scaling parameters for the strength of curvature-induced secondary flow computed for the case studies presented in Sect. 2.2.2.

				Scaling parameter for secondary flow strength					
Case study	Trial	Effects on flow field		Odgaard (1989)	Johannesson & Parker (1989b)	Bolla Pittaluga et al. (2009)	Blanckaert and de Vriend (2003)	Blanckaert and de Vriend (2010)	
			$\frac{B}{Y}$	$\frac{Y}{R} \times 100$	$C_f^{-1}\frac{2Y}{B}$	$C_f^{-1/2}\frac{Y}{R}$	$C_f^{-0.275}\left(\frac{Y}{R}\right)^{0.5}$	$C_f^{-1}\frac{Y}{R}$	$\frac{B}{R}$
Chang (1971)	-	no	19.17	1.41	4.11	0.09	0.33	0.56	0.27
RIPRAP fac.	-	yes	6.50	5.33	43.16	0.63	0.90	7.48	0.35
LFM flume	-	yes	8.50	5.00	89.77	0.98	1.15	19.08	0.43
EPFL ch.	Q_104	yes	6.10	12.53	71.82	1.85	1.56	27.46	0.76
EPFL ch.	Q_89	yes	8.13	9.41	49.04	1.33	1.32	18.75	0.76
EPFL ch.	Q_56	yes	11.93	6.41	29.40	0.85	1.05	11.24	0.76
Rozovskii	-	yes	13.33	7.50	29.33	1.05	1.17	14.67	1.00
Po River case study	Q_11500	weak	12.50	3.33	65.76	0.68	0.96	13.70	0.42
	Q_7400	no	16.67	2.50	44.81	0.48	0.81	9.34	0.42
	Q_3990	no	25	1.67	27.42	0.31	0.64	5.71	0.42

Of course, the fact that the depth-averaged 2D flow field is not significantly altered by the secondary circulation and can be roughly predicted by traditional 2D models without including dispersive terms, does not imply that secondary circulations do no play a role at all. Secondary circulations, with presence of inner and outer streamwise-oriented vortical cells, still amplify the boundary shear stresses, altering the transport of sediments and posing a threat to bank stability; this picture further complicates in very sharp bends (Blanckaert, 2011; Constantinescu et al., 2013). Accounting for the effects of curvature-induced secondary flow in 2D hydro-morphological models remains almost necessary, in particular when the bathymetric configuration is far from equilibrium conditions (Shimizu et al., 1990), or when the bathymetry could be subject to strong variations (e.g., long-term simulations). However, the vast majority of natural river bends are mildly curved and/or have a deformed bed; in these conditions, the depth-averaged 2D flow field is nearly independent of dispersive terms, and the major outcome of curvature-induced secondary circulations is by far the change in bedload direction. This explains why many hydro-morphological models only implements empirical formulations to correct the bedload direction to account for the effect of secondary flows (e.g., Defina, 2003; Vanzo et al., 2021).

2.5 Conclusions

A correction for curvature-induced secondary flow in channel and river bends is implemented in the hydro- and morpho-dynamic model 2DEF. The dispersive terms appearing in the momentum equations are expressed according to three different formulations, recast in similar form. The computation can be performed assuming the instantaneous-adaptation of secondary flow to the driving streamline curvature, or accounting for inertia and phase-lag of the helical flow via a vorticity-transport approach. The effect of impervious banks is accounted for using wall functions. The classical linear model for secondary flow is completed with a novel, pure 2D implementation of a robust non-linear model accounting for the saturation of secondary flow occurring in relatively sharp bends. Dispersive terms are added also to the transport and diffusion equation, and accounted for in the morphodynamic module for bedload transport and mobile bed evolution.

Model applications to laboratory tests and to a real river, with both fixed and mobile beds, confirm the importance of accounting for secondary flow and the validity of the approaches. The different formulations for dispersive terms perform similarly. The local, instantaneous-adaptation approach is less demanding and suitable to isolated bends in riverbeds with a regular bathymetry (in addition, the streamline curvature field must be smoothed out to avoid numerical instabilities). All the local approaches (either to compute the dispersive stresses or to correct the direction of bedload transport) produce unphysical results in presence of geometrical singularities such as bridge piers or abutments. The inertia of secondary flow, which is accounted for intrinsically when transporting the streamwise vorticity, filters out the typical unevenness characterizing

the bathymetry and the curvature field of real rivers and possible geometrical singularities.

The non-linear model for secondary flow saturation is a fundamental ingredient to counteract the excessive growth of helical flow intensity in relatively sharp bends and to produce physically sound spatial distributions of dispersive stresses. To this purpose, wall functions are needed to model the effect of vertical, impervious walls; nonetheless, in real rivers with tilted banks, wall functions are unnecessary.

Curvature-induced secondary flows are shown to produce important modifications to the depth-averaged flow field in case of rectangular cross-sections (i.e., flat bed in the spanwise direction). The high-velocity thread is moved from the inner to the outer side of the bend, and saturation of secondary flow soon becomes important, even for not excessively sharp bends. On the contrary, in real rivers with formed bathymetry (outer scour) the moderate streamline curvature and the already-formed bed bathymetry make the effects of the correction less evident in terms of depth-averaged flow field. The estimation of secondary flow intensity remains important for modelling the transport of suspended matter and, above all, for repercussions on bedload transport and morphological setting. However, in real river with formed bathymetry, empirical corrections for the direction of bedload transport, based on the local streamline curvature and without including dispersive terms in the momentum equations, generally perform satisfactorily.

2.6 Appendix A: Supplementary Material

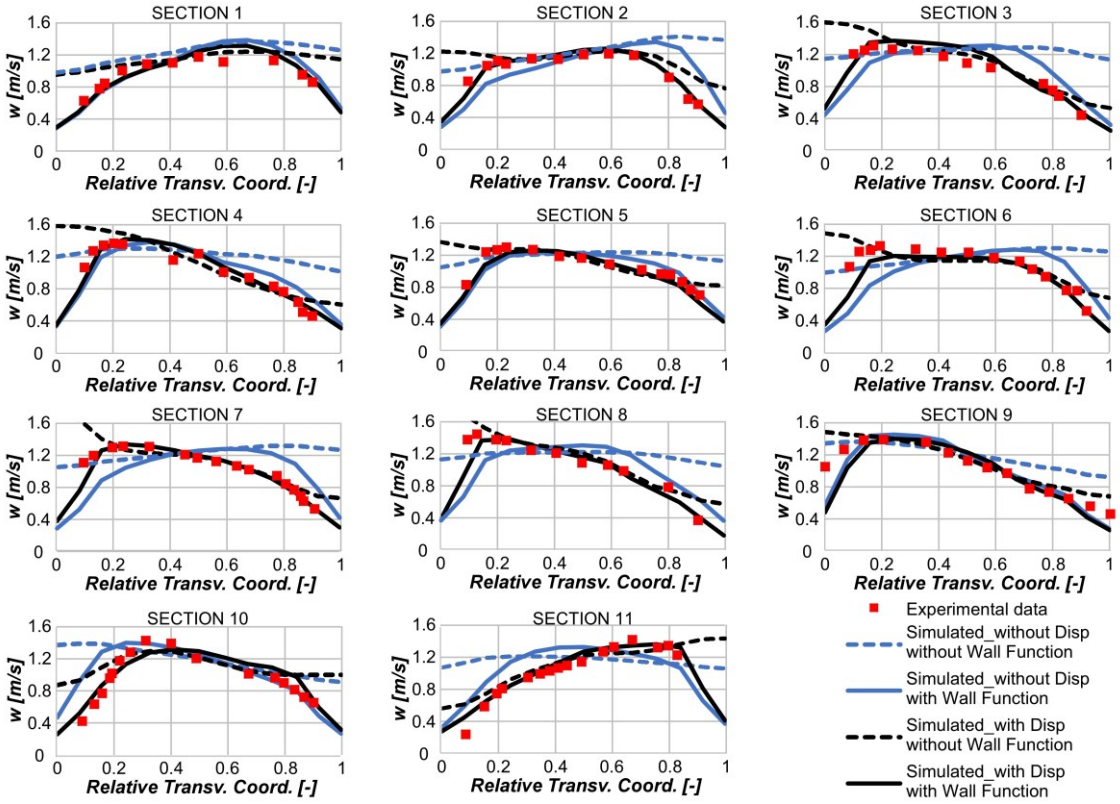

Figure 2-25. Transversal profiles of depth-averaged velocity in the RIPRAP test (Finnie et al., 1999): measured data (red dots) and modelled profiles to show the effect of considering (continuous lines) or neglecting (dashed lines) the sidewall resistance, for the case without (blue) and with (black) dispersive terms. The relative transversal coordinate spans the channel width from the left bank.

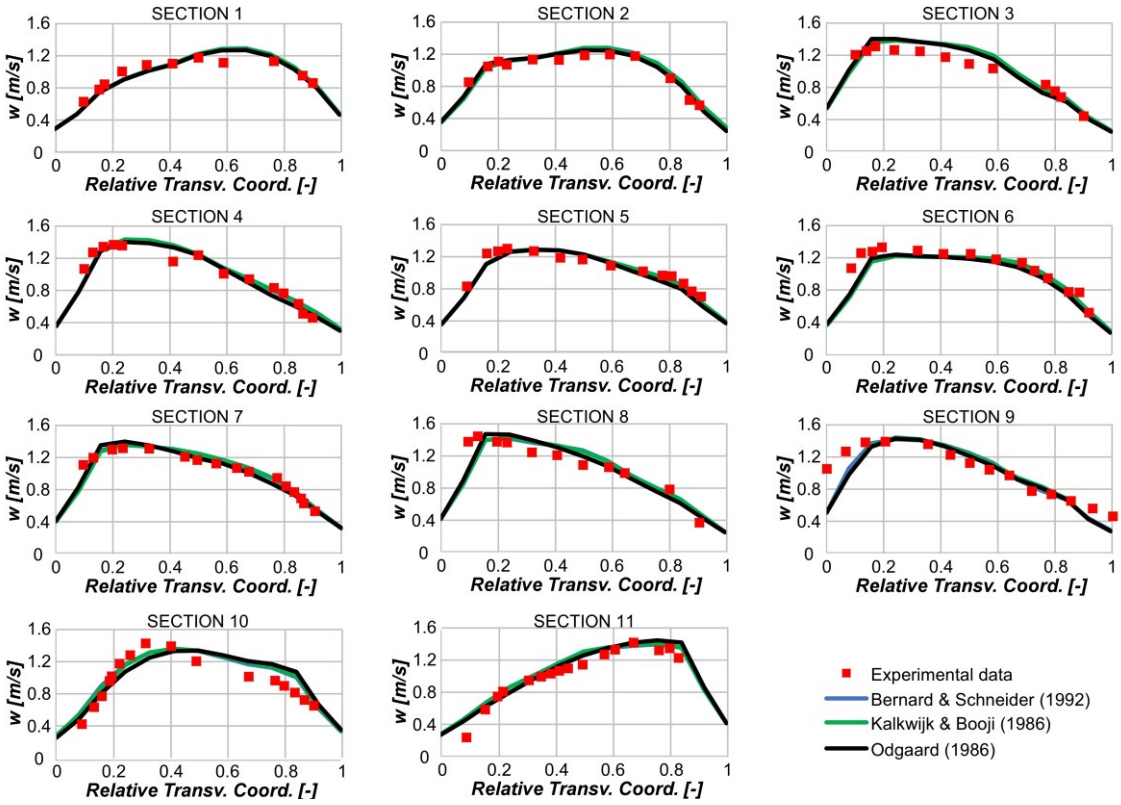

Figure 2-26. Transversal profiles of depth-averaged velocity in the RIPRAP test (Finnie et al., 1999): measured data (red dots) and modelled profiles to show the results obtained with different formulations of the secondary flow parameterization: Bernard and Schneider (1992) in blue, Kalkwijk and Booji (1986) in green, and Odgaard (1986) in black. Results are obtained using the local (instantaneous-adaptation) approach. The relative transversal coordinate spans the channel width from the left bank.

2.6 Appendix A: Supplementary Material

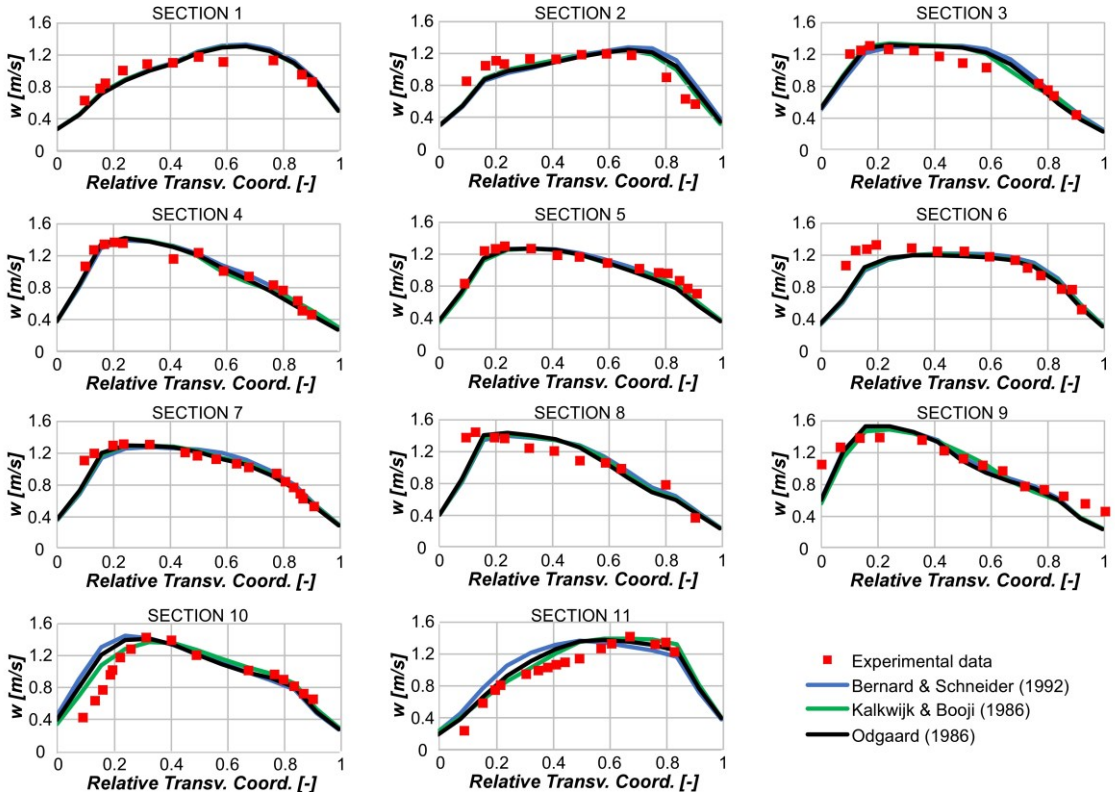

Figure 2-27. Transversal profiles of depth-averaged velocity in the RIPRAP test (Finnie et al., 1999): measured data (red dots) and modelled profiles to show the results obtained with different formulations of the secondary flow parameterization: Bernard and Schneider (1992) in blue, Kalkwijk and Booji (1986) in green, and Odgaard (1986) in black. Results are obtained using the vorticity-transport approach. The relative transversal coordinate spans the channel width from the left bank.

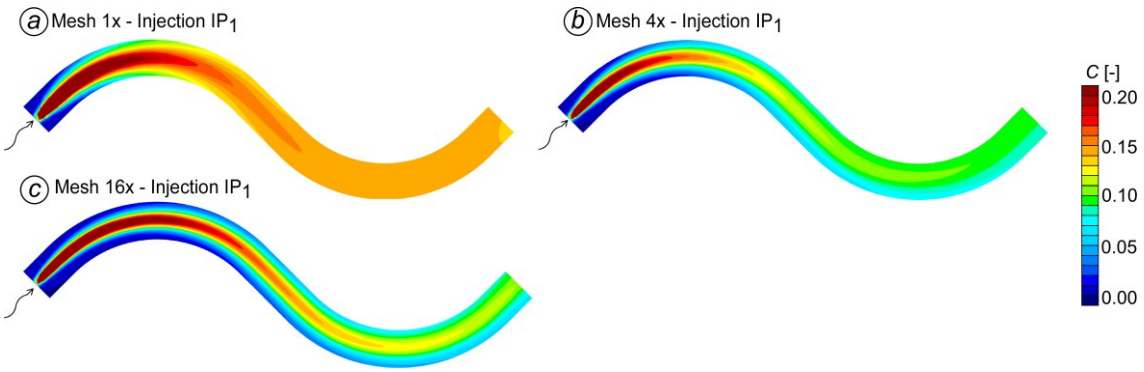

Figure 2-28. Transport of a passive tracer in the presence of helical flow: depth-averaged concentration field for the experiment of Chang (1971) for different mesh refinements. The injection point is in the centre of the channel (IP_1). Mesh 1x has about 10, Mesh4x has 20, and Mesh 16x has 40 cells per channel width.

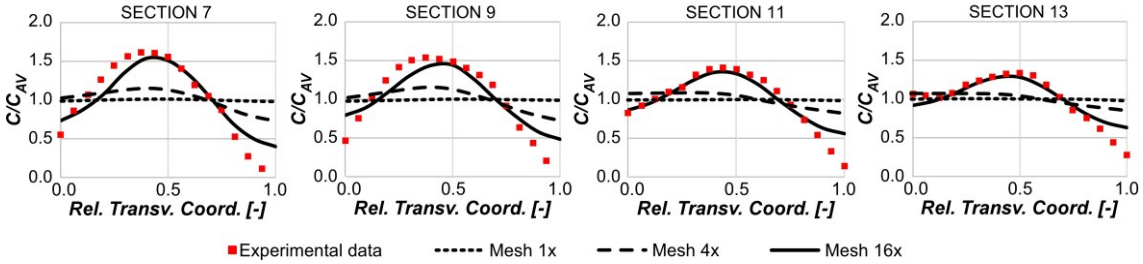

Figure 2-29. Transport of a passive tracer in the presence of helical flow: transversal profiles of the depth-averaged normalized concentration for the experiment of Chang (1971) at Sections 7, 9, 11, and 13. The injection point is in the centre of the channel (IP_1). Experimental data (red dots) and numerical profiles obtained with the three different mesh refinements. Mesh 1x has about 10, Mesh4x has 20, and Mesh 16x has 40 cells per channel width.

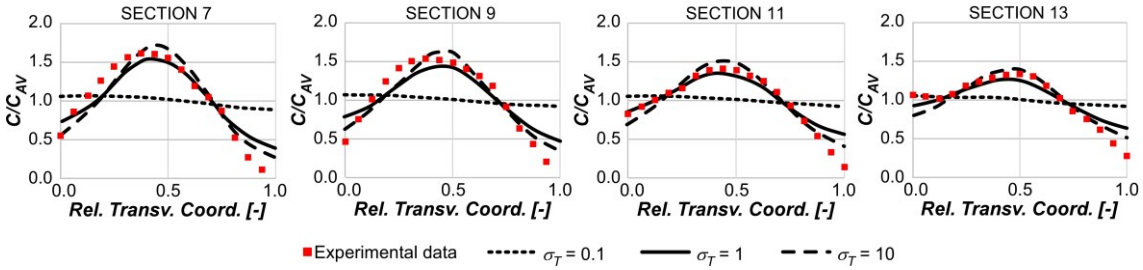

Figure 2-30. As in Figure 2-29, with no dispersive terms in momentum and transport-diffusion equations, for Mesh 16x and different values of the Schmidt number: $\sigma_T = 1$ (solid lines), $\sigma_T = 0.1$ (dotted lines), $\sigma_T = 10$ (dashed lines).

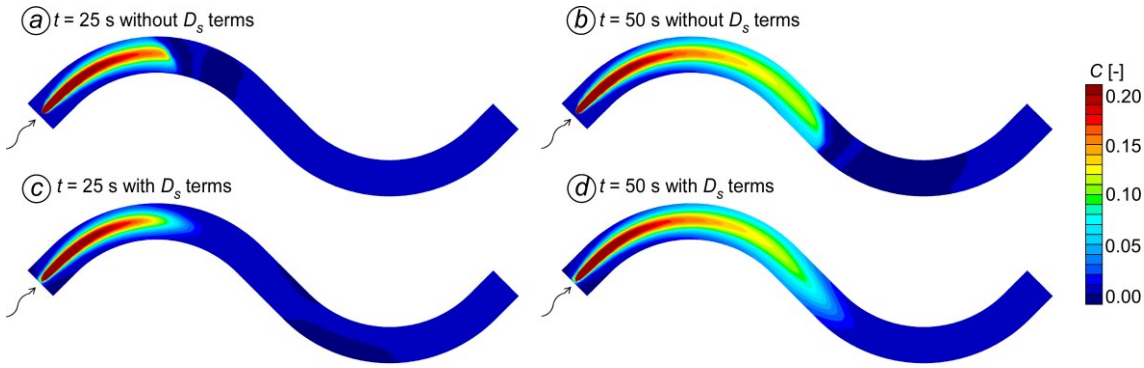

Figure 2-31. Transport of a passive tracer in the presence of helical flow: depth-averaged concentration fields for the experiment of Chang (1971). Concentration fields at different time instants (the tracer is injected starting from $t = 0$ s) either ignoring (upper panels) or considering (lower panels) the longitudinal dispersion.

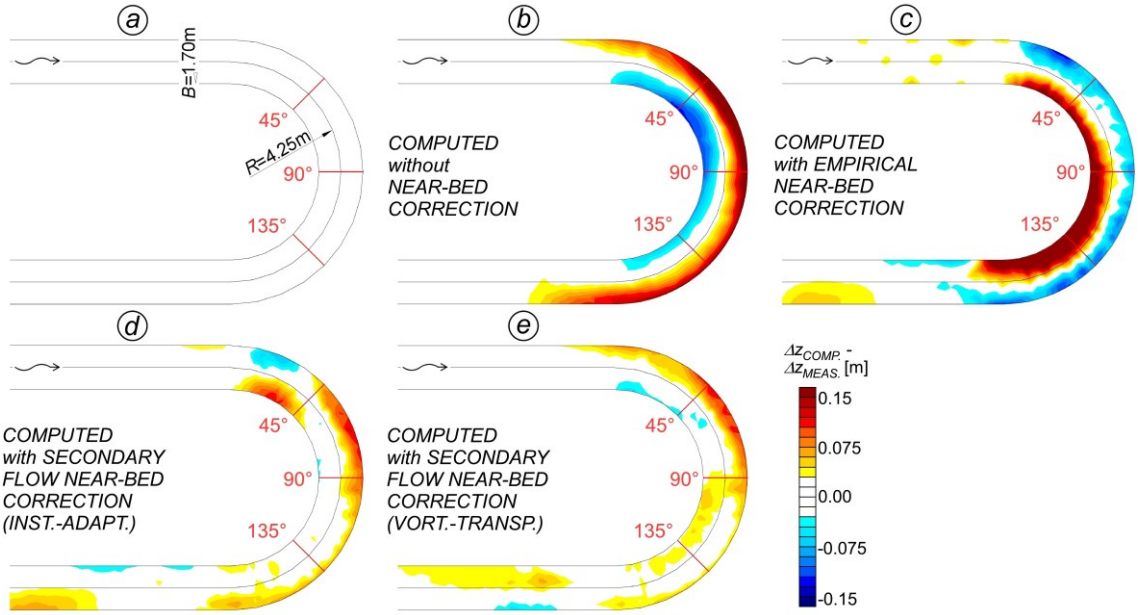

Figure 2-32. In panel a, channel configuration of the laboratory experiment of Koch and Flokstra (1980). Difference among the Δz computed with the present model and the Δz measured in the laboratory experiment of Koch and Flokstra (1980), using b) model results without any correction for bed-load direction; c) model results with empirical bed-load direction correction (A = 10 in Eq. (2-36)); d) model results with dispersive terms correction (instantaneous-adaptation approach), e) model results with dispersive terms correction (vorticity-transport approach).

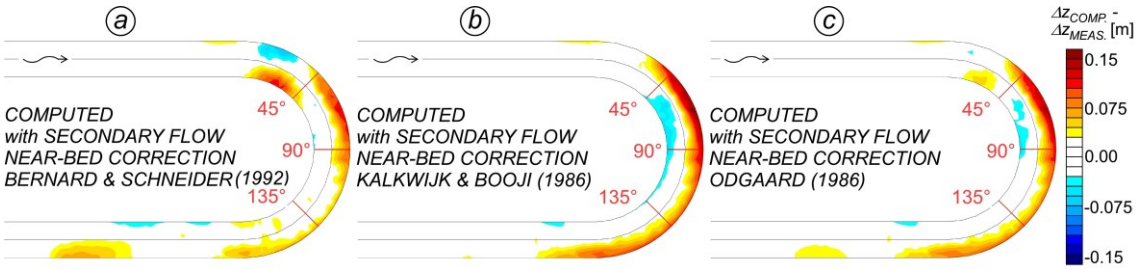

Figure 2-33. Difference among the Δz computed with the present model and the Δz measured in the laboratory experiment of Koch and Flokstra (1980), using the dispersive terms corrections computed using the instantaneous-adaptation approach and the formulations of (a) Bernard and Schneider (1992), (b) Kalkwijk and Booji (1986), and (c) Odgaard (1986).

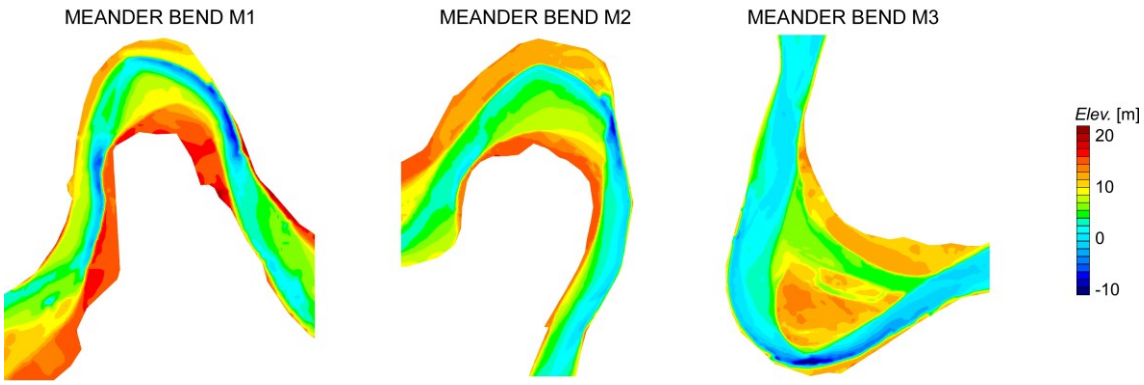

Figure 2-34. Po River case study: surveyed bathymetry for meander bends M1, M2, and M3.

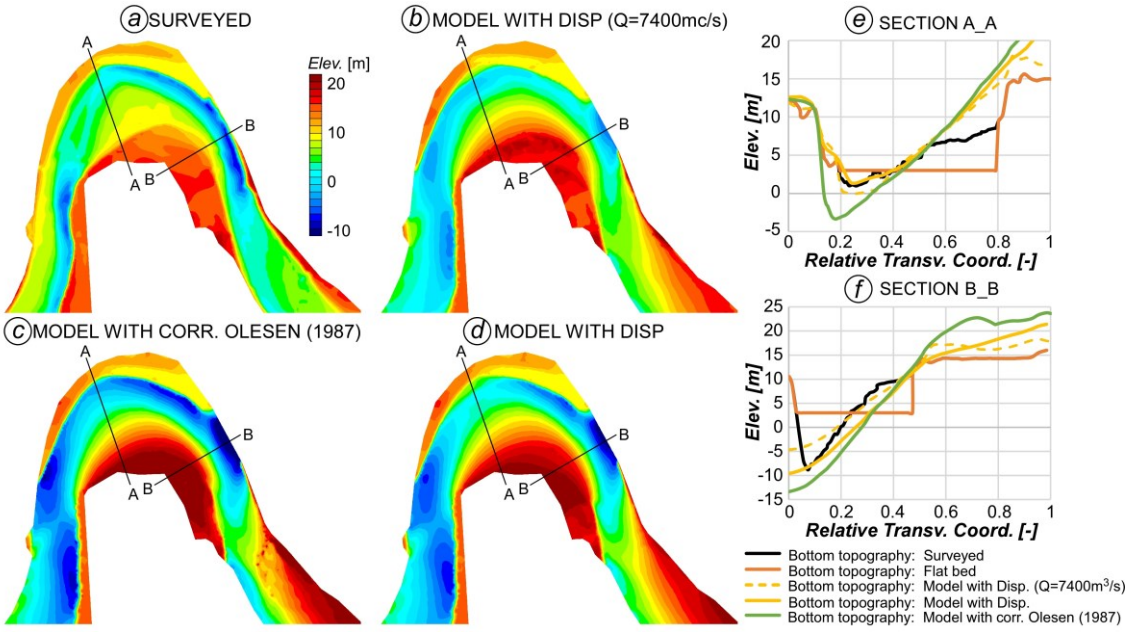

Figure 2-35. Po River case study. Surveyed bathymetry (a), bed equilibrium condition modelled with dispersive terms and correction of bedload direction for Q = 7,400 m³/s (b), bed equilibrium condition modelled without dispersive terms but with the empirical correction of bedload direction (Olesen, 1987) for Q = 11,500 m³/s (c), bed equilibrium condition modelled with dispersive terms and correction of bedload direction for Q = 11,500 m³/s (d). The different bed configurations are also shown at cross-sections AA and BB (e,f).

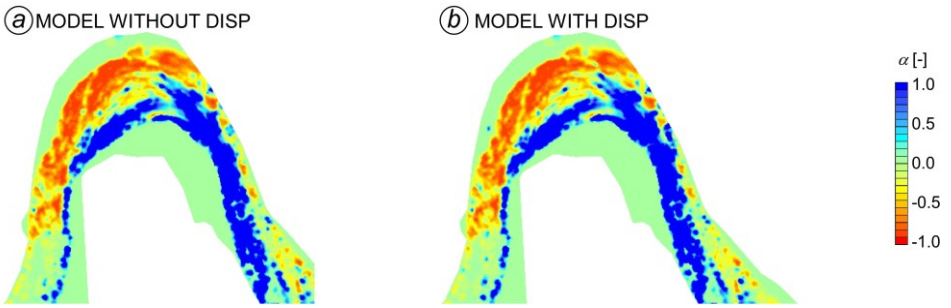

Figure 2-36. Po River case study for the Q = 11,500 m³/s discharge scenario. Spatial distribution of the normalized transversal gradient of velocity, αs, in meander M1 without (a) and with (b) dispersive terms in the momentum equations. The negligible difference means that the real bathymetry shifts the flow at the outer part of the bend, and secondary flow does not entail additional changes to the depth-averaged flow field.

2.7 Appendix B: Estimation of bed elevation and slopes in case of staggered grids

2.7.1 An efficient method for reconstructing nodal elevations from element barycentric values

The hydrodynamic model in the 2DEF framework is based on a staggered triangular mesh, in which the water levels are defined at the nodes of the computational grid and the flow rates at the center of the triangular cells/elements (see 2.2.6). The representation of the bed elevation is also provided by values defined at the center of the elements. The bed load transport model is based on sediment mass fluxes exchanged through the edges of the elements, which accounts for the elevation of the elements as well (Bonetto and Viero, 2016). However, the suspended load transport model included in the 2DEF solves mass balances on the nodes. Hence, values of the bed elevations are updated at nodes at each time step, even if the bed elevation in the model is represented through values at the center of the elements. This requires a precise conversion of element elevations into nodal elevations. In other word, a reliable method should be found to obtain elevations at the nodes of the grids ($z_{b,i}$) which satisfy the elevations at the center of the cells ($z_{b,j}$). In this way, in case of mobile bed simulations with suspended sediment transport, the representation of the bed elevation through nodal values would be exact with respect to the element values.

Imposing nodal elevations to satisfy the elevation at the barycenter of each j-th element leads to:

$$z_{b,j} = \sum_{i=1}^{3} \frac{z_{b,i}}{3} \tag{2-42}$$

In general, the number of the elements composing the computational grid is larger than the number of the nodes. The solution of the associated exact linear system is then overdetermined, and it is needed to be solved through *QR* decompositions. However, this is expensive from a computational point of view, and inefficient for the purpose of a conversion that is needed to be executed at each time step.

A second method, although less precise, consists in assigning the elevation of the *i*-th node through averaging the elevations of the elements which share the *i*-th node, as:

$$z_{b,i} = \frac{1}{A_i} \sum_{j=1}^{n_j} \frac{z_{b,j}\, A_{e,j}}{3} \tag{2-43}$$

where n_j is the number of elements connected to the *i*-th node, A_i is the area pertaining to the *i*-th node and $A_{e,j}$ the area of the *j*-th element. This is the method currently implemented in the 2DEF model given its good balance among precision and efficiency.

The method here proposed is based on a Galerkin approximation. In detail, the method uses the same decomposition introduced for the solution of the continuity equation to solve the equation:

$$z_b = z_{b,j} \tag{2-44}$$

which can be written as:

$$\sum_{i=1}^{n} z_{b,i} \xi_i\,(x_G, y_G) = z_{b,j}(x_G, y_G) \tag{2-45}$$

being (x_G, y_G) the coordinate of the barycenter of the *j*-th element, and ξ_i the shape functions.

Imposing the residual *r* to be orthogonal to the nodal function, the previous equation becomes:

$$\int_{A_e} \xi_j r\, dA_e = 0 \rightarrow \int_{A_e} \xi_j \left[\sum_{i=1}^{n} z_{b,i} \xi_i\,(x_G, y_G) - z_{b,j}(x_G, y_G) \right] dA_e = 0 \tag{2-46}$$

which can be solved using the conjugate gradient method (GCM., the same used to solve the continuity equation of the hydrodynamic model).

The availability of the Galerkin decomposition makes the model computationally cheap. The obtained nodal elevations still do not satisfy exactly the barycentric elements elevation. However, results based on different case studies showed that the proposed method allows for a representation through nodal elevations that is more adherent to the elements representation if compared to the method implemented in the current version of the 2DEF model. In particular, the method here proposed has been shown to

provide more precise nodal values in case of discontinuities in the bottom elevations, such as in the channel banks (see e.g., Figure 2-37).

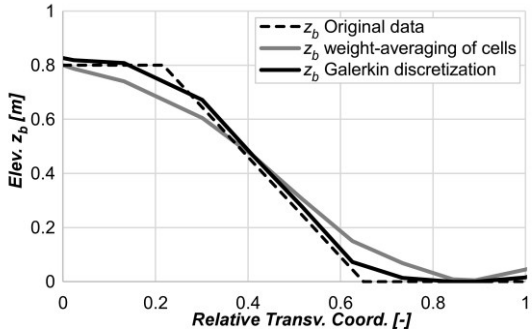

Figure 2-37. Bottom elevation z_b defined at the grid nodes, based on values at the centre of the cells. The dashed line represents elevations through interpolation of element elevations, the grey line of nodal elevation (through weight-averaging of cell), and the black line of nodal elevation (solving the Galerkin discretization through CGM).

2.7.2 Techniques to improve the estimation of longitudinal and transversal slopes in riverbeds

The estimation of bed slope is fundamental to obtain reliable predictions of the river morphology, especially at the banks and in the channel bends. Both the longitudinal and the transversal slope may generate contributions of the weight that enhance or impede the entrainment of bed particles.

In the case of an unstructured computational grid, the reconstruction of the spatial gradients of the river bed is straightforward if the elevation is defined for each element basing on nodal values. In this case, it is:

$$\frac{\partial z_b}{\partial x} = \frac{1}{2A_e}\sum_{i=1}^{3} z_{b,i}\, n_{i,x}\, L_i$$
$$\frac{\partial z_b}{\partial y} = \frac{1}{2A_e}\sum_{i=1}^{3} z_{b,i}\, n_{i,y}\, L_i \qquad (2\text{-}47)$$

where $\boldsymbol{n} = (n_x, n_y)$ is the unit vector normal to the edge, and L is the edge length (subscript i refers to the edge opposite to the i-th node).

The method based on Eq. (2-47) is computationally cheap but it can not be applied strictly in the 2DEF framework, since the bed load transport model is based on the elevations defined at the center of the elements. Two alternative methods to calculate the element slopes basing on the elevations of neighboring elements are here proposed.

A first method considers a sub-triangulation (subscript k', see Figure 2-38a), which is based on the three elements neighboring the j-th cell, labelled with the subscript k. In detail, the edge shared between the j-th and the k-th cells is labelled k', and the sub-

triangulation is based on the central point of this edge. Called $z_{b,k'}$ the elevation at the center of the k'-th edge, the three values $z_{b,k'}$ constitute nodal elevations in the sub-element. Thus, derivatives of z_b are computed as:

$$\frac{\partial z_b}{\partial x} = \frac{1}{2A_e}\sum_{k'=1}^{3} z_{b,k'}\, n_{k',x}\, L_{k'} = \frac{1}{A_e}\sum_{k=1}^{3} z_{b,k}\left(-n_{k,x}\, L_k\right)$$
$$\frac{\partial z_b}{\partial y} = \frac{1}{2A_e}\sum_{k'=1}^{3} z_{b,k'}\, n_{k',y}\, L_{k'} = \frac{1}{A_e}\sum_{k=1}^{3} z_{b,k}\left(-n_{k,y}\, L_k\right) \tag{2-48}$$

This method is formally analogous to the previous. However, the sub-triangulation on the center of the edges allows to use directly the elements elevations. As a drawback, it is necessary to use the elevation of the neighboring elements to obtain the edge elevation $z_{b,k'}$.

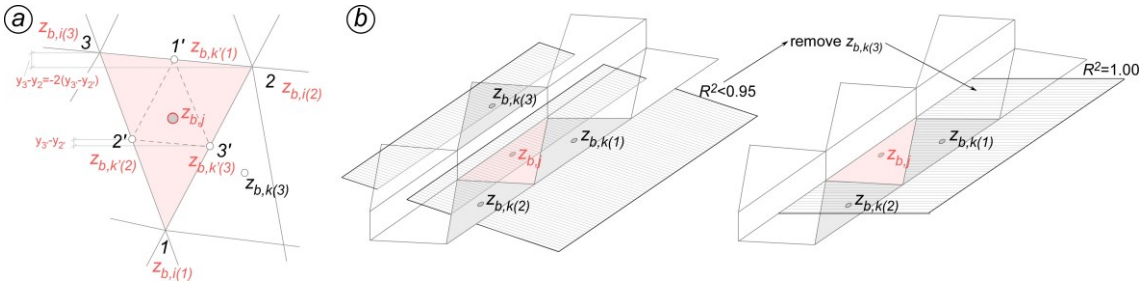

Figure 2-38. Sketches for the calculation of the bed slope a) basing on the sub-triangulation, and b) near a discontinuity (bank).

A second method to reconstruct the bed elevation gradients is based on the least-squares (LS) reconstruction, which is a higher order reconstruction method. The least-squares reconstruction is obtained by solving an objective function for the values of the gradients which minimize the sum of the squares of the differences between elevations in the actual and neighboring cells. The objective function to be minimized is given by:

$$\sum_{k=1}^{N} w_{j,k}^2 E_{j,k}^2 \tag{2-49}$$

being w a weight function, and E the error which is evaluated considering a linear approximation for the bed level. In this case the bed level computed in the neighboring element is:

$$z_{b,k} = z_{b,j} + \left.\frac{\partial z_b}{\partial x}\right|_j \left(x_k - x_j\right) + \left.\frac{\partial z_b}{\partial y}\right|_j \left(y_k - y_j\right) + E(\Delta x^2, \Delta y^2) \tag{2-50}$$

Imposing the minimization along the x and y directions yields:

$$\begin{cases} a_j \dfrac{\partial z_b}{\partial x} + b_j \dfrac{\partial z_b}{\partial y} = d_i \\ b_j \dfrac{\partial z_b}{\partial x} + c_j \dfrac{\partial z_b}{\partial y} = e_i \end{cases} \tag{2-51}$$

where:

$$a_j = \sum_{k=1}^{N} w_{j,k}^2 \left(x_k - x_j\right)^2 \quad b_j = \sum_{k=1}^{N} w_{j,k}^2 \left(x_k - x_j\right)\left(y_k - y_j\right) \quad c_j = \sum_{k=1}^{N} w_{j,k}^2 \left(y_k - y_j\right)^2 \quad d_j = \sum_{k=1}^{N} w_{j,k}^2 \left(x_k - x_j\right)\left(z_{b,k} - z_{b,j}\right) \quad e_j = \sum_{k=1}^{N} w_{j,k}^2 \left(y_k - y_j\right)\left(z_{b,k} - z_{b,j}\right) \tag{2-52}$$

which can be solved using e.g., the Cramer's rule.

The method based on the LS reconstruction allows to consider either the three elements directly neighboring the *j*-th cell (i.e., all elements sharing an edge with the *j*-th element) or all the neighboring elements (i.e., all elements sharing a node with the *j*-th element). In the latter case, the result becomes smoothed.

The precision of the reconstruction can be tested through the coefficient of determination R^2. Results on selected case studies showed that near discontinuity (e.g., channel banks), the LS reconstruction may still predict inaccurate results (i.e., $R^2 < 0.95$). The reason is the approximation with a linear function passing through the center of the elements. This assumption does not hold where there is a spatial discontinuity (e.g., a channel bank, as in the schematic example of Figure 2-38b). In other words, the LS reconstruction considers the elevation of an adjacent element which is not coplanar with the *j*-th element.

To avoid possible errors, a useful technique is to apply an inverse distance weighting (*IDW*) on the direction orthogonal to the water flow, assuming that large discontinuities such as channel banks are generally parallel to the water flow. Then, the element providing the largest deviation between measured and predicted elevations is excluded from the LS reconstruction. In this case the computation of the derivatives becomes exact being based on the plane for the three points (i.e., the center of the actual and of the two adjacent elements).

This correction enhances the precision especially for coarser meshes and in channel with constant slope (Figure 2-39 and Figure 2-40). In real bathymetries, especially when using sufficiently refined grids, the precision by the different methods is similar (not shown).

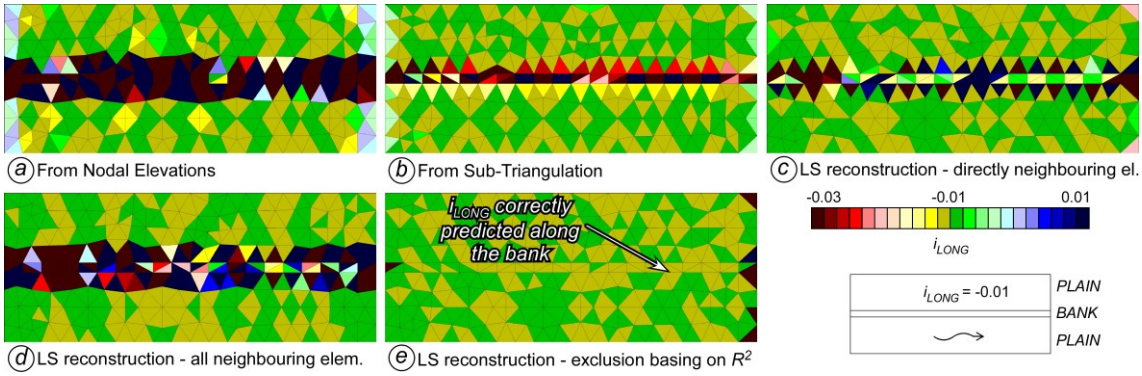

Figure 2-39. Estimation of the longitudinal slope (i_{LONG} = -0.01) using different methods (a-e).

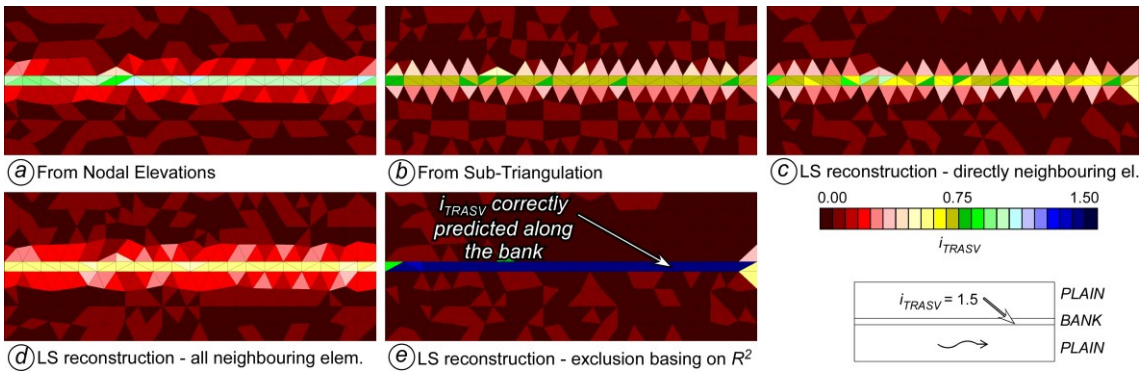

Figure 2-40. Estimation of the transversal slope (i_{TRASV} = 1.5 on the bank, i_{TRASV} = 0 elsewhere) using different methods (a-e).

2.8 Appendix C: Sediment Transport in Inclined Beds

2.8.1 Effect of longitudinal slope on the bedload discharge

In the bedload transport model, a classical (1D) Meyer-Peter and Müller relation is coupled with the Exner equation to guarantee the continuity of sediments (see 2.2.6.6). The Meyer-Peter and Müller relation has been found for a nearly plane bed, but, as already mentioned, longitudinal bed slopes may vary the flux of transported sediments. Two are the main approaches traditionally proposed for correcting the bedload transport in longitudinally inclined beds:

- corrections on the bedload transport rate;
- corrections on the critical shear stress.

Besides the longitudinal slope (available from nodal/element elevations), the additional parameters needed for evaluating bedload transport on inclined beds include the angle of repose of particles (depending on soil).

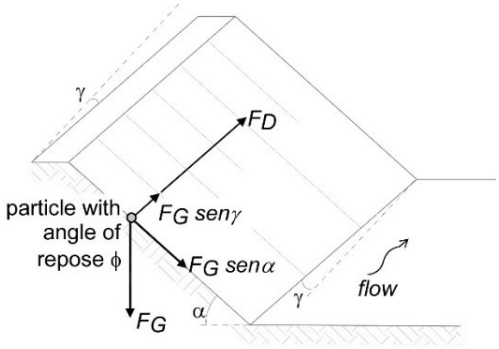

Figure 2-41. Sketch of the forces acting on a solid particle in case of longitudinal and transversal slopes

2.8.1.1 Corrections on the bedload transport rate

These methods consist in augmenting the bedload transport rate for a nearly horizontal bed, $q_{b,0}$, by a factor that depends primarily on the slope along the flow direction, γ.

In the current version of the model 2DEF, the intensity of sediment transport accounts for the effect of the longitudinal slope as (Struiksma, 1985):

$$q_b = q_{b,0}[1 - \chi\, c_F\, tg\,(\gamma)] \tag{2-53}$$

where $c_F = k_S^2 Y^{1/3}/g$ is the friction factor and χ is a coefficient accounting for the effect of stream-wise bed slope (χ = 0.03 after Olesen, 1987, as reported by Crosato and Struiksma, 1989).

Koch and Flokstra (1980), as extended by Talmon et al. (1995), proposed the following expression:

$$q_b = q_{b,0}[1 - tg\,(\gamma)] \tag{2-54}$$

Bagnold (1966), instead, proposed to calculate the bedload transport rate as:

$$q_b = q_{b,0}\left(\frac{tg(\phi)}{cos(\gamma)[tg\,(\gamma) + tg\,(\phi)]}\right) \tag{2-55}$$

2.8.1.2 Corrections on the critical shear stress

These methods consist in adapting the critical shear stress found for a nearly horizontal bed (i.e., from Shields diagram), $\tau_{C,0}$, to account for the effect of the local slope by proper multiplying factor(s). Considering the inclination and the planar component of weight, and imposing equilibrium among the forces acting on a particle located in the bank (see Figure 2-41), one can find:

$$\tau_C = k_\alpha k_\gamma\, \tau_{C,0} \tag{2-56}$$

where τ_C and $\tau_{C,0}$ represent the critical shear stress for inclined and for flat bed respectively, and k_α and k_γ are coefficients for considering the transversal and longitudinal slope, respectively. Lane (1955) proposed the following formula for the two coefficients:

$$k_\alpha = \cos(\alpha)\sqrt{1-\frac{tg^2(\alpha)}{tg^2(\phi)}} \qquad k_\gamma = cos(\gamma)\left(1-\frac{tg\,(\gamma)}{tg\,(\phi)}\right) \tag{2-57}$$

where α and γ are the transversal and longitudinal slope angle, respectively, and ϕ the angle of repose of particles. Similar expressions to the Lane's formula have been widely used for the critical bed shear stress correction (e.g., Dey, 2004; Ikeda, 1982).

Other formulations have been proposed in the technical literature. Dey (2003) from laboratory experiment found the following relation:

$$k_\gamma k_\alpha = 0.954\left(1-\frac{\gamma}{\phi}\right)^{0.745}\left(1-\frac{\alpha}{\phi}\right)^{0.372} \tag{2-58}$$

Seminara et al. (2002), which complemented the analysis of Kovacs and Parker (1994) by adding the effect of the lift forces, proposed to evaluate the correction on the critical shear stress for an arbitrarily slopping bed solving the equation:

$$(1-\Delta)\left(k_\gamma k_\alpha\right)^2 + 2\left(\frac{\Delta}{\sqrt{1+tg^2(\gamma)+tg^2(\alpha)}}+\frac{sin(\gamma)}{tg(\phi)}\right)k_\gamma k_\alpha + \frac{1+\Delta}{1+tg^2(\phi)+tg^2(\alpha)}\left(\frac{tg^2(\alpha)+tg^2\,(\gamma)}{tg^2(\phi)}-1\right)=0 \tag{2-59}$$

2.8.1.3 Comparison

The above options have been implemented in the 2DEF module for bedload transport, allowing the user to select the most suitable approach for each application.

The different formulations presented above can provide different importance to the slope correction. To exemplify, in Figure 2-42 the effects of the aforementioned corrections are compared in terms of $q_b/q_{b,0}$, for a sloped channel with $\tan(\gamma)$ = 1 ‰ and different values of the bed shear stress τ.

As a general indication, $q_b/q_{b,0}$ values remain the same for the three corrections based on augmenting the bedload transport rate. Among the three, in the present example the correction of Struiksma (1985) provides higher values of $q_b/q_{b,0}$, which means a larger contribution of the longitudinal slope. In case of the corrections of the critical shear stress, the bedload transport process begins at low shear stress conditions and the correction is significant when τ is slightly higher than τ_C. When $\tau \gg \tau_C$ the correction becomes negligible. The correction of Dey (2001) provides higher values of $q_b/q_{b,0}$, especially slightly above the incipient motion condition.

Some of the corrections listed above consider also other parameters in their formulation (these parameters were assumed fixed in the comparison of Figure 2-42). Most of them include the angle of repose of the particles. The correction of Struiksma (1985) depends also on the friction factor c_F, which in turn depend on the water depth and on the Strickler coefficient. While the Strickler coefficient is generally uniform in the riverbed (at least at a large spatial scale), the water depth may show strong variations, especially because of deformed riverbed, such as in banks. This induce additional variability on the magnitude of the correction.

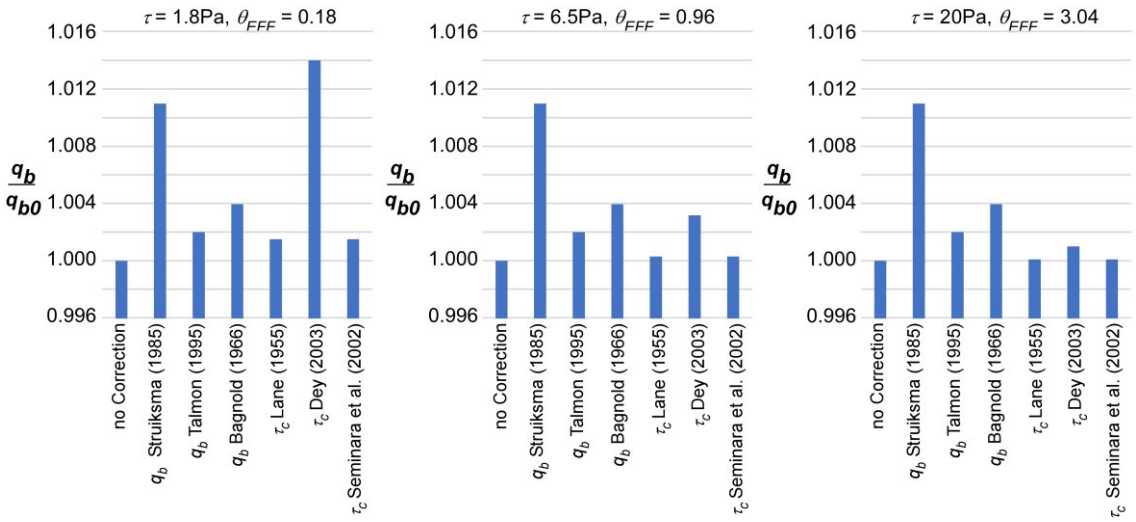

Figure 2-42. Effect of the slope correction for the bedload transport rate in terms of q_b/q_{b0} for different values of the bed shear stress τ. Other parameters are mean diameter d_{50} = 5mm, Strickler coefficient K_S = 50m$^{1/3}$/s, water depth Y = 0.76 m, angle of repose of the particles $\phi = 0.6 \approx 31°$. $\theta_{EFF} = \theta - \theta_C$ measure the excess of shear stress in terms of Shields parameter, θ (θ_C is the threshold value for incipient bedload transport).

2.8.2 Sub-model for sediment redistribution in case of bed slope exceeding the repose slope

Longitudinal and transversal slopes can intensify the bed load transport induced by hydrodynamic actions through adding additional contributions of force because of the weight. If the slope is larger than a certain threshold (i.e., angle of repose) the particles can be entrained also in case of no hydrodynamic actions. The bathymetry is then naturally modified such that every computational cell has a slope less steep than the angle of repose. The sediment redistribution in case of excess of bed slope has been implemented as a sub-model in the existing bed load transport model of the 2DEF framework. The approach followed in the proposed method is based on the estimation of the mass fluxes passing through cell edges to modify bathymetry until stable conditions are established.

Pairs of elements whose inclination δ exceeds a prescribed value of critical slope ϕ (conveniently assumed to be equal to the angle of repose of particles) are first

individuated. In this case, each edge of the cell is analyzed evaluating the elevation difference $d_{h,k} = z_{b,j} - z_{b,k}$ and the planar distance l_k among centroids of the actual cell j and the adjacent cell k, projected along the direction of the maximum slope (see Figure 2-43 for the meaning of symbols).

The particles redistribution occurs from the actual cell to the adjacent(s) only if $\delta_k = d_{h,k} / l_k$ exceeds the critical slope. The mass flux is directed as the maximum slope of the actual cell and it is estimated in order to recover the critical slope among the two cells.

To ensure the conservation of the mass of sediments, supposing sediment density as constant, the volume exchanged among the cells must be the same, namely:

$$V_{j,k} = -\Delta_j \, Ae_j = \Delta_k \, Ae_k \tag{2-60}$$

where $V_{j,k}$ is the volume exchanged among elements j and k, $\Delta = z'_b - z_b$ is the variation of elevation and A_e the area of the cell. Moreover, the total variation must recover the critical slope, namely:

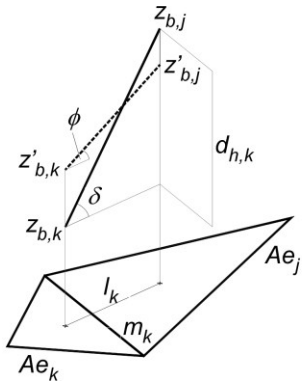

Figure 2-43. Schematization of mass failure process among two cells in which the critical repose slope is exceeded

$$-\Delta_j + \Delta_k = l_k \, \delta - l_k \, \phi \tag{2-61}$$

Solving these equations for Δ_j, one finds:

$$\Delta_j = l_k \, \frac{(\delta - \phi)}{1 + {Ae_j}/{Ae_k}} \tag{2-62}$$

Thus, the mass flux per unit width passing into the k-element, $q_{s,k}$, is estimated as:

$$q_{s,k} = \frac{\Delta_j \; Ae_k}{m_k \; dt} \tag{2-63}$$

where dt is the computational time step and m_k the length of the adjacent edge.

Computing all the mass fluxes from higher cells to lower cells ensures the redistribution of the bottom elevations recovering the critical slope. It should be noted that the rearrangement takes a certain time T (i.e., a number of time steps) since the variation in adjacent cells elevation may produce excesses of slope for different couples of elements; and the process ends when an equilibrium condition is reached in the entire domain. The time T is usually much shorter than the morphological time scale. Moreover, the process can be further smoothed with proper coefficients that reduce q_s to avoid sudden changes in the bathymetry that may induce numerical issues.

To show the effectiveness of this approach, the evolution of an inclined bank ($\delta = 1.6 \approx 59°$) is represented in transversal sections of Figure 2-44a and Figure 2-44b ,

which consider medium and low values for the critical repose slope respectively ($\phi = 0.6 \approx 31°$ and $\phi = 0.4 \approx 22°$). The evolution of a vertical wall is represented in the transversal section of Figure 2-44c when prescribing a low value for the critical repose slope ($\phi = 0.4 \approx 22°$). In all the cases, the bed elevation rearranges to satisfy the prescribed angle of repose; the number of time steps required for equilibrium ranges from about 25 (for the case in Figure 2-44a) to 150 (for the case in Figure 2-44c).

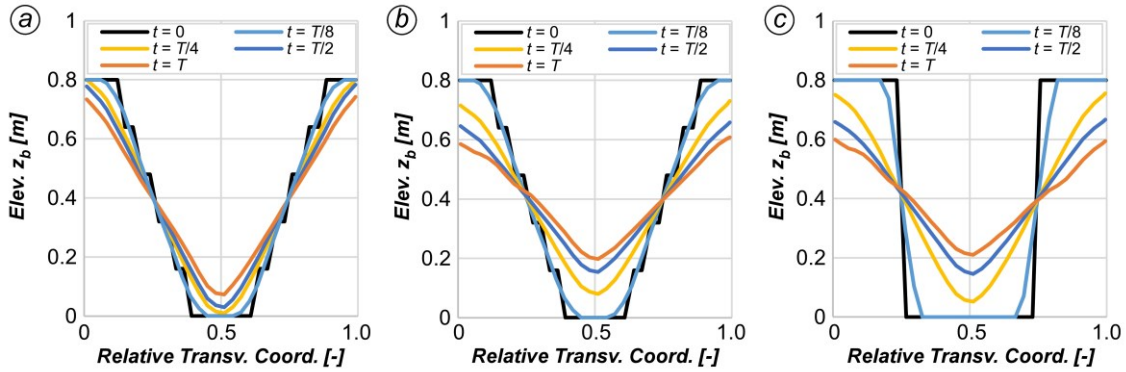

Figure 2-44. In panel a and b, inclined bank evolution prescribing medium and low values for the critical repose slope ($\phi = 0.6 \approx 31°$ and $\phi = 0.4 \approx 22°$, respectively); in panel c vertical bank evolution prescribing a low value for the critical repose slope ($\phi = 0.4 \approx 22°$)

2.9 Appendix D: Influence of secondary flow on the suspended load transport

The influence of the secondary flow on the transport of a passive tracer is considered through the anisotropic diffusive tensor $\mathbf{D}_D$, with the (possible) introduction of a mixing coefficient/Schmidt number (e.g., Chang, 1971; Duan, 2004), as detailed in 2.2.5. This approach considers the additional mixing induced by the transversal circulation, but still assumes a constant concentration of the passive scalar along the vertical direction.

The advection-diffusion equation is used also for the suspended sediment transport. However, previous numerical experiments showed that in real rivers strong differences are observed against the comparison with measured data. Especially in bends, the calibration of the mixing coefficient has been shown to require unphysical values (Arailopoulos, 2014).

One reason that can explain these discrepancies is the skewed vertical profile of the suspended sediment (see e.g., typical Rouse vertical distributions), in which highest values are usually located in the lower part of the water column. A net sediment flux is then induced in the transversal direction because of the spanwise velocity components generated by the secondary currents. In particular, as typically high concentrations of sediments are at the bottom of the water column, a net sediment flux directed to the inner part of the bend is generated by the transversal velocity component near the bed, which is directed to the inner part of the bend as well.

In channel bends the influence of secondary flow on suspended sediment should be modelled explicitly, considering proper vertical distributions of the velocity and of the concentration. Thus, dispersive terms for the concentration flux should be added in the transport-diffusion equation (Arailopoulos, 2014; Huang et al., 2006; Jia et al., 2019). Given vertical distributions for the velocity (longitudinal and transversal components) and for the concentration (simplified version of Rouse equation), the analytic integration of the difference with the depth-averaged values provides supplementary terms to be added to the advective and the diffusive terms. The advection-diffusion equation (Eq. (2-13)) for suspended sediment is then re-written as:

$$\frac{\partial YC}{\partial t} + \nabla \cdot C\boldsymbol{q} - \nabla \cdot (Y\varepsilon_T \nabla C) - \nabla \cdot (Y\boldsymbol{D_D}\nabla C) + \frac{\partial DC_x}{\partial x} + \frac{\partial DC_y}{\partial x} = S \tag{2-64}$$

where DC_x and DC_y are the dispersive terms, written as:

$$\begin{aligned} DC_x &= \int_0^Y u'(z)C'(z)dz = \frac{DC_s u - DC_n v}{w} \\ DC_y &= \int_0^Y v'(z)C'(z)dz = \frac{DC_s v + DC_n u}{w} \end{aligned} \tag{2-65}$$

being $C'(z)$ the difference among the vertical profile of the suspended sediment concentration and its depth-averaged value. As seen in section 2.2, it is convenient to use a local reference frame in which DC_s and DC_n are the dispersive stress in the streamwise and in the spanwise directions.

In the present application the vertical distributions of the velocity are assumed as in Eqs. (2-4) and (2-5). A simplified Rouse profile (Swart, 1976; see also the recent Boudreau and Hill, 2020) is assumed for the vertical distribution of suspended sediments concentration:

$$C(z) = Ck_C \left(\frac{z}{a}\right)^{-Ro} \tag{2-66}$$

where C is the depth-averaged concentration, R_0 is the rouse number, a is the height of the bed load layer and k_C is defined as:

$$k_C = \frac{(Y-a)(1-R_0)}{(Y^{1-R_0} - a^{1-R_0})a^{R_0}} \tag{2-67}$$

Dispersive stresses DC_s and DC_n are then written as:

$$\begin{aligned} DC_s &= \int_0^Y [w_s(z) - w][C(z) - C]dz \\ &= \int_0^Y \left[\frac{m+1}{m}\left(\frac{z}{Y}\right)^{1/m} w - w\right]\left[k_C\left(\frac{z}{a}\right)^{-R_0} - C\right]dz = wC\,k_s \end{aligned} \tag{2-68}$$

$$DC_n = \int_0^Y w_n(z)[C(z) - C]dz = \int_0^Y \left[\left(\frac{2z}{Y} - 1\right) v_{ns}^* w\right]\left[k_C \left(\frac{z}{a}\right)^{-R_0} - C\right] dz$$
$$= wC\, k_n$$

with the coefficients:

$$k_s = \frac{1}{mY^{1/m}a^{-R_0}}\left[k_C(m+1)\frac{Y^{1/m-R_0+1}}{1/m - R_0 + 1} - \frac{(m+1)a^{-R_0}Y^{1/m+1}}{1/m+1} - \frac{k_C m Y^{1/m-R_0+1}}{-R_0+1} + ma^{-R_0}Y^{1/m+1}\right] \quad (2\text{-}69)$$

$$k_c = \frac{v_{ns}^* k_C Y^{-R_0+1}}{a^{-R_0}}\left[\frac{-R_0}{(-R_0+2)(-R_0+1)}\right]$$

These terms have been implemented in the 2DEF model similarly to the dispersive terms in the SWEs (see 2.2.1), and their effectiveness have been tested using the Rozovskii channel experiment (see Figure 2-6 and details of the experiment in section 2.3.2), in which larger transversal components of velocity are observed especially at the middle of the (sharp) bend (Figure 2-45a). Being higher concentration of sediments in the lower part of the water column, and being the transversal velocity directed to the inner part of the bend, these terms induce a supplementary concentration flux directed toward the inner part (Figure 2-45b and Figure 2-46a). As a consequence, the sediments are deposed in the inner part of the bend, which further enhances bar accretion (Figure 2-45c and Figure 2-46b). Though the introduction of the terms confirms a larger sediment flux is directed to the inner part of the band, no experimental data for validation are nowadays available. Future research will be needed to compare results with laboratory data.

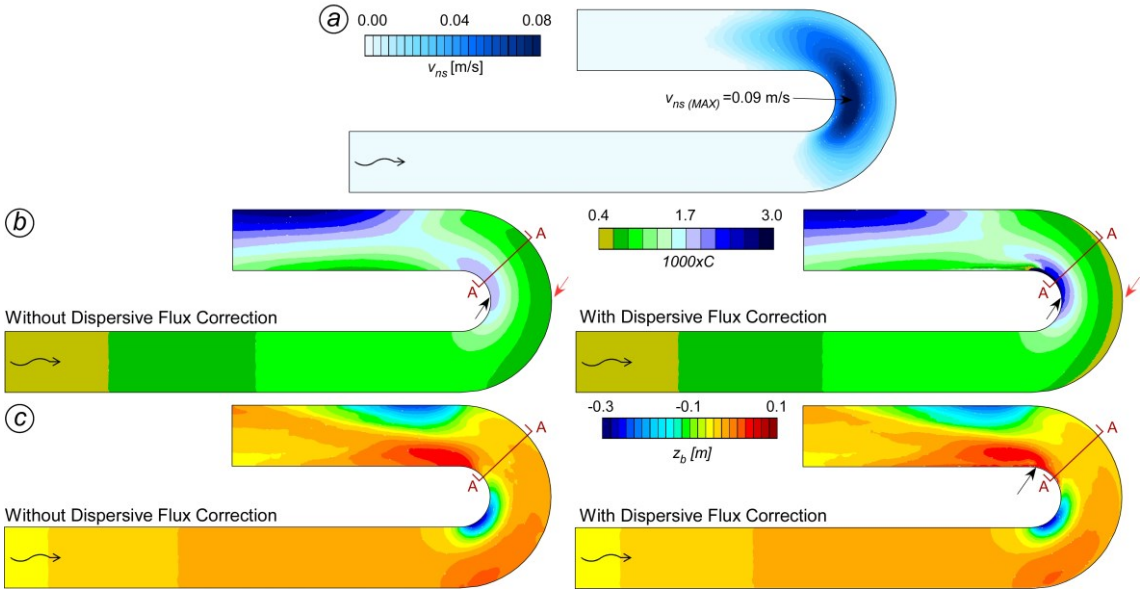

Figure 2-45. Magnitude of secondary currents measured by the transversal velocity at the free surface v_{ns} (a), depth-averaged concentration of suspended sediment C (b), bed elevation at equilibrium z_b (c), either without (left) and with (right) the dispersive flux correction for suspended sediment. Red and black arrows indicate the points with larger difference among the model without and with dispersive flux correction for the transport of suspended sediment concentration.

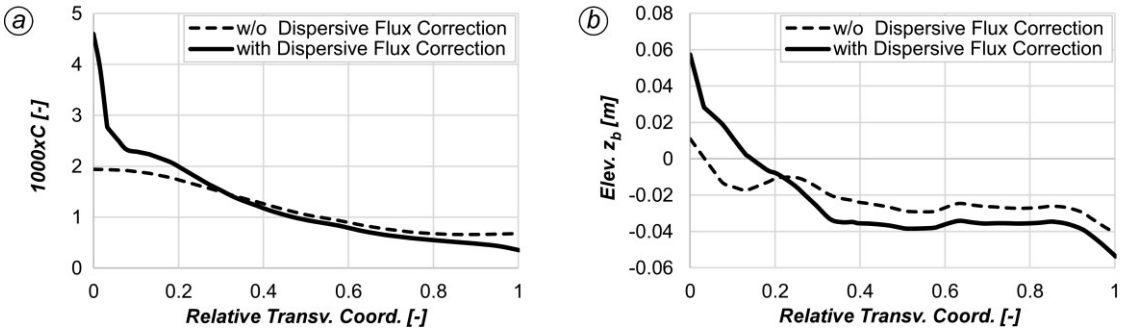

Figure 2-46. Depth-averaged concentration of suspended sediment C (a) and bed elevation z_b at equilibrium (b) in transversal section AA, either without (left) and with (right) the dispersive flux correction for suspended sediment.

2.10 References

Abad, J.D., Buscaglia, G.C., Garcia, M.H., 2008. 2D stream hydrodynamic, sediment transport and bed morphology model for engineering applications. Hydrol. Process. 22, 1443–1459. https://doi.org/10.1002/hyp.6697

Abad, J.D., Garcia, M.H., 2009. Experiments in a high-amplitude Kinoshita meandering channel: 1. Implications of bend orientation on mean and turbulent flow structure. Water Resour. Res. 45, W02401. https://doi.org/10.1029/2008WR007016

Abderrezzak, K.E.K., Moran, A.D., Tassi, P., Ata, R., Hervouet, J.-M., 2016. Modelling river bank erosion using a 2D depth-averaged numerical model of flow and non-cohesive, non-uniform sediment transport. Adv. Water Resour. 93, 75–88. https://doi.org/10.1016/j.advwatres.2015.11.004

Ahmadi, M., Ayyoubzadeh, S., Montazeri Namin, M., Samani, J., 2009. A 2D Numerical Depth-averaged Model for Unsteady Flow in Open Channel Bends. J. Agric. Sci. Technol. 11, 457–468.

Alavian, V., 1986. Dispersion Tensor in Rotating Flows. J. Hydraul. Eng. 112, 771–777. https://doi.org/10.1061/(ASCE)0733-9429(1986)112:8(771)

Alho, P., Mäkinen, J., 2010. Hydraulic parameter estimations of a 2D model validated with sedimentological findings in the point bar environment. Hydrol. Process. 24, 2578–2593. https://doi.org/10.1002/hyp.7671

Arailopoulos, I., 2014. Morphological modelling with suspended sediment transport in river bends. TU Delft.

Baar, A.W., de Smit, J., Uijttewaal, W.S.J., Kleinhans, M.G., 2018. Sediment Transport of Fine Sand to Fine Gravel on Transverse Bed Slopes in Rotating Annular Flume Experiments. Water Resour. Res. 54, 19–45. https://doi.org/10.1002/2017WR020604

Bagnold, R.A., 1966. An approach to the sediment transport problem from general physics. US Gov. Print Off.

Bai, R., Zhu, D., Chen, H., Li, D., 2019. Laboratory Study of Secondary Flow in an Open Channel Bend by Using PIV. Water 11, 659. https://doi.org/10.3390/w11040659

Bates, P.D., 2022. Flood Inundation Prediction. Annu. Rev. Fluid Mech. 54, 287–315. https://doi.org/10.1146/annurev-fluid-030121-113138

Bathurst, J.C., Thorne, C.R., Hey, R.D., 1977. Direct measurements of secondary currents in river bends. Nature 269, 504–506. https://doi.org/10.1038/269504a0

Begnudelli, L., Valiani, A., Sanders, B.F., 2010. A balanced treatment of secondary currents, turbulence and dispersion in a depth-integrated hydrodynamic and bed deformation model for channel bends. Adv. Water Resour. 33, 17–33. https://doi.org/10.1016/j.advwatres.2009.10.004

Bernard, R.S., Schneider, M., 1992. Depth-Averaged Numerical Modeling for Curved Channels. Tech Rep HL-92-9 U.S. Army Engineer Waterways Experiment Station, Vicksburg, Miss.

Blanckaert, K., 2011. Hydrodynamic processes in sharp meander bends and their morphological implications. J. Geophys. Res. Earth Surf. 116, F01003. https://doi.org/10.1029/2010JF001806

Blanckaert, K., 2010. Topographic steering, flow recirculation, velocity redistribution, and bed topography in sharp meander bends. Water Resour. Res. 46, W09506. https://doi.org/10.1029/2009WR008303

Blanckaert, K., 2009. Saturation of curvature-induced secondary flow, energy losses, and turbulence in sharp open-channel bends: Laboratory experiments, analysis, and modeling. J. Geophys. Res. Earth Surf. 114, F03015. https://doi.org/10.1029/2008JF001137

Blanckaert, K., 2001. Discussion of "Bend-Flow Simulation Using 2D Depth-Averaged Model." J. Hydraul. Eng. 127, 167–170. https://doi.org/10.1061/(ASCE)0733-9429(2001)127:2(167)

Blanckaert, K., Constantinescu, G., Uijttewaal, W., Chen, Q., 2013. Hydro- and morphodynamics in curved river reaches; recent results and directions for future research. Adv. Geosci. 37, 19–25. https://doi.org/10.5194/adgeo-37-19-2013

Blanckaert, K., de Vriend, H., 2004. Secondary flow in sharp open-channel bends. J. Fluid Mech. 498, 353–380. https://doi.org/10.1017/S0022112003006979

Blanckaert, K., de Vriend, H.J., 2010. Meander dynamics: A nonlinear model without curvature restrictions for flow in open-channel bends. J. Geophys. Res. Earth Surf. 115, F0401. https://doi.org/10.1029/2009JF001301

Blanckaert, K., de Vriend, H.J., 2003. Nonlinear modeling of mean flow redistribution in curved open channels. Water Resour. Res. 39, 1375. https://doi.org/10.1029/2003WR002068

Blanckaert, K., Graf, W.H., 2004. Momentum Transport in Sharp Open-Channel Bends. J. Hydraul. Eng. 130, 186–198. https://doi.org/10.1061/(ASCE)0733-9429(2004)130:3(186)

Bolla Pittaluga, M., Nobile, G., Seminara, G., 2009. A nonlinear model for river meandering. Water Resour. Res. 45, W04432. https://doi.org/10.1029/2008WR007298

Bonetto, I., Defina, A., 1998. Rappresentazione dei termini di accelerazione convettiva in un modello bidimensionale della propagazione di onde lunghe in acque basse (Numerical discretization of the advective terms in a Finite Element shallow water equations model). Proc XVI Convegno Idraul. E Costr. Idraul. 53–64.

Bonetto, I., Viero, D.P., 2016. Esperimenti numerici sul trasporto solido di fondo (Numerical Experiments on Bedload Transport). Proc XXV Convegno Idraul. E Costr. Idraul. 128, 91–94.

Bora, K., Khalita, H.M., 2020. A Semi-Coupled Model for Morphological Flow Simulation in River Bend. J. Appl. Fluid Mech. 13, 1611–1622. https://doi.org/10.36884/jafm.13.05.30842

Boudreau, B.P., Hill, P.S., 2020. Rouse revisited: The bottom boundary condition for suspended sediment profiles. Mar. Geol. 419, 106066. https://doi.org/10.1016/j.margeo.2019.106066

Boussinesq, J., 1868. Mémoire sur l'influence des frottements dans les mouvements réguliers des fluides; XII- Essai sur Ie movement permanent d'un liquide dans un canal horizontal axe circulaire. J. Mathématiques Pures Appliquées, 2eme Serie, Tome XIII, 413.

Bowker, K., 1988. Albert Einstein and Meandering Rivers. Earth Sci. Hist. 7, 45. https://doi.org/10.17704/eshi.7.1.yk72n55q84qxu5n6

Camporeale, C., Cannamela, F., Canuto, C., Manes, C., 2021. Stability analysis of open-channel flows with secondary currents. J. Fluid Mech. 927, A32. https://doi.org/10.1017/jfm.2021.769

Camporeale, C., Perona, P., Porporato, A., Ridolfi, L., 2007. Hierarchy of models for meandering rivers and related morphodynamic processes. Rev. Geophys. 45, RG1001. https://doi.org/10.1029/2005RG000185

Carniello, L., Defina, A., D'Alpaos, L., 2012. Modeling sand-mud transport induced by tidal currents and wind waves in shallow microtidal basins: Application to the Venice Lagoon (Italy). Estuar. Coast. Shelf Sci. 102–103, 105–115. https://doi.org/10.1016/j.ecss.2012.03.016

Casulli, V., Zanolli, P., 2005. High resolution methods for multidimensional advection–diffusion problems in free-surface hydrodynamics. Second Int. Workshop Unstructured Mesh Numer. Model. Coast. Shelf Ocean Flows 10, 137–151. https://doi.org/10.1016/j.ocemod.2004.06.007

Cea, L., Bladé, E., 2015. A simple and efficient unstructured finite volume scheme for solving the shallow water equations in overland flow applications. Water Resour. Res. 51, 5464–5486. https://doi.org/10.1002/2014WR016547

Chang, Y.C., 1971. Lateral mixing in meandering channels. University of Iowa.

Chavarrías, V., Schielen, R., Ottevanger, W., Blom, A., 2019. Ill posedness in modelling two-dimensional morphodynamic problems: effects of bed slope and secondary flow. J. Fluid Mech. 868, 461–500. https://doi.org/10.1017/jfm.2019.166

Chen, D., Duan, J.D., 2006. Simulating sine-generated meandering channel evolution with an analytical model. J. Hydraul. Res. 44, 363–373. https://doi.org/10.1080/00221686.2006.9521688

Constantinescu, G., Kashyap, S., Tokyay, T., Rennie, C.D., Townsend, R.D., 2013. Hydrodynamic processes and sediment erosion mechanisms in an open channel bend of strong curvature with deformed bathymetry. J. Geophys. Res. Earth Surf. 118, 480–496. https://doi.org/10.1002/jgrf.20042

Crosato, A., Struiksma, N., 1989. Analysis of a 2 D bed topography model for Rivers, in: River Meandering (Eds S. Ikeda and G. Parker). pp. 153–180. https://doi.org/10.1029/WM012p0153

D'Alpaos, L., Defina, A., 2007. Mathematical modeling of tidal hydrodynamics in shallow lagoons: A review of open issues and applications to the Venice lagoon. Comput. Geosci. 33, 476–496. https://doi.org/10.1016/j.cageo.2006.07.009

De Vriend, H.J., 1981. Steady flow in shallow channel bends. Tech Rep 81-3 Fluid Mech. Lab., Dep. of Civ. Eng., Delft Univ. of Technol., Delft,Netherlands.

De Vriend, H.J., 1977. A Mathematical Model Of Steady Flow In Curved Shallow Channels. J. Hydraul. Res. 15, 37–54. https://doi.org/10.1080/00221687709499748

Defina, A., 2003. Numerical experiments on bar growth. Water Resour. Res. 39, 1092. https://doi.org/10.1029/2002WR001455

Defina, A., 2000. Two-dimensional shallow flow equations for partially dry areas. Water Resour. Res. 36, 3251–3264. https://doi.org/10.1029/2000WR900167

Demuren, A.O., 1993. A numerical model for flow in meandering channels with natural bed topography. Water Resour. Res. 29, 1269–1277. https://doi.org/10.1029/92WR02907

Demuren, A.O., Rodi, W., 1986. Calculation of flow and pollutant dispersion in meandering channels. J. Fluid Mech. 172, 63–92. https://doi.org/10.1017/S0022112086001659

Deng, S., Xia, J., Zhou, M., Li, Z., Duan, G., Shen, J., Blanckaert, K., 2021. Secondary Flow and Flow Redistribution in Two Sharp Bends on the Middle Yangtze River. Water Resour. Res. 57, e2020WR028534. https://doi.org/10.1029/2020WR028534

Dey, S., 2004. Critical bed shear for initial movement of sediments on a combined lateral and longitudinal slope. Hydrol. Res. 35, 153–164. https://doi.org/10.2166/nh.2004.0011

Dey, S., 2003. Threshold of sediment motion on combined transverse and longitudinal sloping beds. J. Hydraul. Res. July 2003, 405–415. https://doi.org/10.1080/00221680309499985

Dietrich, W.E., Smith, J.D., 1983. Influence of the point bar on flow through curved channels. Water Resour. Res. 19, 1173–1192. https://doi.org/10.1029/WR019i005p01173

Duan, J.G., 2004. Simulation of Flow and Mass Dispersion in Meandering Channels. J. Hydraul. Eng. 130, 964–976. https://doi.org/10.1061/(ASCE)0733-9429(2004)130:10(964)

Duan, J.G., Nanda, S.K., 2006. Two-dimensional depth-averaged model simulation of suspended sediment concentration distribution in a groyne field. J. Hydrol. 327, 426–437. https://doi.org/10.1016/j.jhydrol.2005.11.055

Einstein, A., 1926. Die Ursache der Mäanderbildung der Flußläufe und des sogenannten Baerschen Gesetzes. Naturwissenschaften 14, 223–224. https://doi.org/10.1007/BF01510300

Einstein, H.A., Li, H., 1958. Secondary currents in straight channels. Eos Trans. Am. Geophys. Union 39, 1085–1088. https://doi.org/10.1029/TR039i006p01085

Elder, J.W., 1959. The dispersion of marked fluid in turbulent shear flow. J. Fluid Mech. 5, 544–560. https://doi.org/10.1017/S0022112059000374

Engel, F.L., Rhoads, B.L., 2012. Interaction among mean flow, turbulence, bed morphology, bank failures and channel planform in an evolving compound meander loop. Geomorphology 163–164, 70–83. https://doi.org/10.1016/j.geomorph.2011.05.026

Engmann, E., 1986. Effect of Channel Bends on Transverse Mixing. Niger. J. Technol. 10, 57–72.

Falcon, M., 1984. Secondary Flow in Curved Open Channels. Annu. Rev. Fluid Mech. 16, 179–193. https://doi.org/10.1146/annurev.fl.16.010184.001143

Farhadi, A., Sindelar, C., Tritthart, M., Glas, M., Blanckaert, K., Habersack, H., 2018. An investigation on the outer bank cell of secondary flow in channel bends. J. Hydro-Environ. Res. 18, 1–11. https://doi.org/10.1016/j.jher.2017.10.004

Finnie, J., Donnell, B., Letter, J., Bernard, R.S., 1999. Secondary Flow Correction for Depth-Averaged Flow Calculations. J. Eng. Mech. 125, 848–863. https://doi.org/10.1061/(ASCE)0733-9399(1999)125:7(848)

Fischer, H.B., 1969. The effect of bends on dispersion in streams. Water Resour. Res. 5, 496–506. https://doi.org/10.1029/WR005i002p00496

Fischer, H.B., List, J.E., Koh, C.R., Imberger, J., Brooks, N.H., 1979. Mixing in inland and coastal waters. Academic press.

Fischer-Antze, T., Olsen, N.R.B., Gutknecht, D., 2008. Three-dimensional CFD modeling of morphological bed changes in the Danube River. Water Resour. Res. 44, W09422. https://doi.org/10.1029/2007WR006402

Ghamry, H.K., Steffler, P.M., 2002. Effect of Applying Different Distribution Shapes for Velocities and Pressure on Simulation of Curved Open Channels. J. Hydraul. Eng. 128, 969–982. https://doi.org/10.1061/(ASCE)0733-9429(2002)128:11(969)

Gu, L., Zhang, S., He, L., Chen, D., Blanckaert, K., Ottevanger, W., Zhang, Y., 2016. Modeling Flow Pattern and Evolution of Meandering Channels with a Nonlinear Model. Water 8, 418. https://doi.org/10.3390/w8100418

Guan, M., Wright, N.G., Sleigh, P.A., Ahilan, S., Lamb, R., 2016. Physical complexity to model morphological changes at a natural channel bend. Water Resour. Res. 52, 6348–6364. https://doi.org/10.1002/2015WR017917

He, L., 2018. Distribution of primary and secondary currents in sine-generated bends. Water SA 44, 118. https://doi.org/10.4314/wsa.v44i1.14

Holly, F.M., Usseglio-Polatera, J., 1984. Dispersion Simulation in Two-dimensional Tidal Flow. J. Hydraul. Eng. 110, 905–926. https://doi.org/10.1061/(ASCE)0733-9429(1984)110:7(905)

Horna-Munoz, D., Constantinescu, G., 2018. A fully 3-D numerical model to predict flood wave propagation and assess efficiency of flood protection measures. Adv. Water Resour. 122, 148–165. https://doi.org/10.1016/j.advwatres.2018.10.014

Hu, D., Zhu, Y., Zhong, D., Qin, H., 2017. Two-Dimensional Finite-Volume Eulerian-Lagrangian Method on Unstructured Grid for Solving Advective Transport of Passive Scalars in Free-Surface Flows. J. Hydraul. Eng. 143, 04017051. https://doi.org/10.1061/(ASCE)HY.1943-7900.0001371

Huang, S., Jia, Y.F., Wang, S.S.Y., 2006. Numerical Modeling of Suspended Sediment Transport in Channel Bends. J. Hydrodyn. 18, 411–417. https://doi.org/10.1016/S1001-6058(06)60113-3

Ikeda, S., 1982. Incipient Motion of Sand Particles on Side Slopes. J. Hydraul. Div. 108, 95–114. https://doi.org/10.1061/JYCEAJ.0005812

Ikeda, S., Nishimura, T., 1986. Flow and Bed Profile in Meandering Sand-Silt Rivers. J. Hydraul. Eng. 112, 562–579. https://doi.org/10.1061/(ASCE)0733-9429(1986)112:7(562)

Iwasaki, T., Shimizu, Y., Kimura, I., 2016. Sensitivity of free bar morphology in rivers to secondary flow modeling: Linear stability analysis and numerical simulation. Adv. Water Resour. 92, 57–72. https://doi.org/10.1016/j.advwatres.2016.03.011

Jang, C.-L., Shimizu, Y., 2005. Numerical Simulation of Relatively Wide, Shallow Channels with Erodible Banks. J. Hydraul. Eng. 131, 565–575. https://doi.org/10.1061/(ASCE)0733-9429(2005)131:7(565)

Jia, Y., Zhang, Y., Yeh, K.-C., Liao, C.-T., 2019. Modeling River Morphodynamic Process Using a Depth-Averaged Computational Model and an Application to a Mountain River, in: Current Practice in Fluvial Geomorphology. IntechOpen, Rijeka, p. Ch. 3. https://doi.org/10.5772/intechopen.86692

Jin, Y., Steffler, P.M., 1993. Predicting Flow in Curved Open Channels by Depth-Averaged Method. J. Hydraul. Eng. 119, 109–124. https://doi.org/10.1061/(ASCE)0733-9429(1993)119:1(109)

Johannesson, H., Parker, G., 1989a. Velocity Redistribution in Meandering Rivers. J. Hydraul. Eng. 115, 1019–1039. https://doi.org/10.1061/(ASCE)0733-9429(1989)115:8(1019)

Johannesson, H., Parker, G., 1989b. Secondary Flow in Mildly Sinuous Channel. J. Hydraul. Eng. 115, 289–308. https://doi.org/10.1061/(ASCE)0733-9429(1989)115:3(289)

Kalkwijk, J.P.Th., Booij, R., 1986. Adaptation of secondary flow in nearly-horizontal flow. J. Hydraul. Res. 24, 19–37. https://doi.org/10.1080/00221688609499330

Kasvi, E., Alho, P., Lotsari, E., Wang, Y., Kukko, A., Hyyppä, H., Hyyppä, J., 2015. Two-dimensional and three-dimensional computational models in hydrodynamic and morphodynamic reconstructions of a river bend: sensitivity and functionality. Hydrol. Process. 29, 1604–1629. https://doi.org/10.1002/hyp.10277

Kasvi, E., Petteri, A., Vaaja, M., Hyyppä, H., Hyyppä, J., 2013. Spatial and temporal distribution of fluvio-morphological processes on a meander point bar during a flood event. Hydrol. Res. 44, 1022–1039. https://doi.org/10.2166/nh.2013.091

Keylock, C.J., Constantinescu, G., Hardy, R.J., 2012. The application of computational fluid dynamics to natural river channels: Eddy resolving versus mean flow approaches. Geomorphology 179, 1–20. https://doi.org/10.1016/j.geomorph.2012.09.006

Kikkawa, H., Kitagawa, A., Ikeda, S., 1976. Flow and Bed Topography in Curved Open Channels. J. Hydraul. Div. 102, 1327–1342. https://doi.org/10.1061/JYCEAJ.0004615

Kitanidis, P.K., Kennedy, J.F., 1984. Secondary current and river-meander formation. J. Fluid Mech. 144, 217–229. https://doi.org/10.1017/S0022112084001580

Koch, F.G., Flokstra, C., 1980. Bed level computations for curved alluvial channels. Proc XIX Congr. IAHR New Delhi India 2, 357–364.

Koken, M., Constantinescu, G., Blanckaert, K., 2013. Hydrodynamic processes, sediment erosion mechanisms, and Reynolds-number-induced scale effects in an open channel bend of strong

curvature with flat bathymetry. J. Geophys. Res. Earth Surf. 118, 2308–2324. https://doi.org/10.1002/2013JF002760

Kovacs, A., Parker, G., 1994. A new vectorial bedload formulation and its application to the time evolution of straight river channels. J. Fluid Mech. 267, 153–183. https://doi.org/10.1017/S002211209400114X

Lai, Y., Thomas, R., Ozeren, Y., Simon, A., Greimann, B., Wu, K., 2012. Coupling a Two-Dimensional Model with a Deterministic Bank Stability Model, in: World Environmental and Water Resources Congress 2012: Crossing Boundaries, Proceedings of the 2012 Congress. pp. 1290–1300. https://doi.org/10.1061/9780784412312.130

Lane, E.W., 1955. Design of Stable Channels. Trans. Am. Soc. Civ. Eng. 120, 1234–1260. https://doi.org/10.1061/TACEAT.0007188

Lane, S.N., 1998. Hydraulic modelling in hydrology and geomorphology: a review of high resolution approaches. Hydrol. Process. 12, 1131–1150. https://doi.org/10.1002/(SICI)1099-1085(19980630)12:8<1131::AID-HYP611>3.0.CO;2-K

Lazzarin, T., Viero, D.P., 2023. Curvature-induced secondary flow in 2D depth-averaged hydro-morphodynamic models: An assessment of different approaches and key factors. Adv. Water Resour. 171, 104355. https://doi.org/10.1016/j.advwatres.2022.104355

Lee, M.E., Kim, G., 2012. Influence of Secondary Currents on Solute Dispersion in Curved Open Channels. J. Appl. Math. 2012, 781695. https://doi.org/10.1155/2012/781695

Lee, M.E., Seo, I.W., 2013. Spatially Variable Dispersion Coefficients in Meandering Channels. J. Hydraul. Eng. 139, 141–153. https://doi.org/10.1061/(ASCE)HY.1943-7900.0000669

Leschziner, M.A., Rodi, W., 1979. Calculation of Strongly Curved Open Channel Flow. J. Hydraul. Div. 105, 1297–1314. https://doi.org/10.1061/JYCEAJ.0005286

Lien, H.C., Hsieh, T.Y., Yang, J.C., Yeh, K.C., 1999. Bend-Flow Simulation Using 2D Depth-Averaged Model. J. Hydraul. Eng. 125, 1097–1108. https://doi.org/10.1061/(ASCE)0733-9429(1999)125:10(1097)

Lou, S., Liu, H., Liu, S., Chen, M., Zhong, G., 2020. Longitudinal and lateral diffusion of solute transport in flow with rigid vegetation. Environ. Sci. Eur. 32, 40. https://doi.org/10.1186/s12302-020-00315-8

Moncho-Esteve, I.J., Folke, F., García-Villalba, M., Palau-Salvador, G., 2017. Influence of the secondary motions on pollutant mixing in a meandering open channel flow. Environ. Fluid Mech. 17, 695–714. https://doi.org/10.1007/s10652-017-9513-4

Nabi, M., Ottevanger, W., Giri, S., 2016. Computational modelling of secondary flow on unstructured grids, in: River Sedimentation - Proceedings of the 13th International Symposium on River Sedimentation, ISRS 2016, Stuttgart, Germany. London, pp. 719–726.

Nezu, I., 2005. Open-Channel Flow Turbulence and Its Research Prospect in the 21st Century. J. Hydraul. Eng. 131, 229–246. https://doi.org/10.1061/(ASCE)0733-9429(2005)131:4(229)

Nikora, V., Roy, A.G., 2011. Secondary Flows in Rivers: Theoretical Framework, Recent Advances, and Current Challenges, in: Gravel-Bed Rivers. John Wiley & Sons, Ltd, pp. 1–22. https://doi.org/10.1002/9781119952497.ch1

Odgaard, A.J., 1989. River Meander Model-I: Development. J. Hydraul. Eng. 115, 1433–1450. https://doi.org/10.1061/(ASCE)0733-9429(1989)115:11(1433)

Odgaard, A.J., 1986. Meander Flow Model. I: Development. J. Hydraul. Eng. 112, 1117–1135. https://doi.org/10.1061/(ASCE)0733-9429(1986)112:12(1117)

Olesen, K.W., 1987. Bed topography in shallow river bends. Delft University of Technology.

Ottevanger, W., 2013. Modelling and parametrizing the hydro- and morphodynamics of curved open channels. Delft University of Technology.

Ottevanger, W., Blanckaert, K., Uijttewaal, W.S.J., 2012. Processes governing the flow redistribution in sharp river bends. Meand. Channels 163–164, 45–55. https://doi.org/10.1016/j.geomorph.2011.04.049

Papanicolaou, A.N., Elhakeem, M., Hilldale, R., 2007. Secondary current effects on cohesive river bank erosion. Water Resour. Res. 43, W12418. https://doi.org/10.1029/2006WR005763

Pratap, V.S., Spalding, D.B., 1975. Numerical Computations of the Flow in Curved Ducts. Aeronaut. Q. 26, 219–228. https://doi.org/10.1017/S0001925900007368

Qin, C., Shao, X., Xiao, Y., 2019. Secondary Flow Effects on Deposition of Cohesive Sediment in a Meandering Reach of Yangtze River. Water 11, 1444. https://doi.org/10.3390/w11071444

Rishnappan, B.G.K., Lau, Y.L., 1977. Transverse Mixing in Meandering Channels with varying Bottom Topography. J. Hydraul. Res. 15, 351–370. https://doi.org/10.1080/00221687709499640

Rodi, W., 2017. Turbulence models and their application in hydraulics: A state-of-the-art review. Routledge. https://doi.org/10.1201/9780203734896

Rozovskii, I.L., 1957. Flow of water in bends of open channels. Academy of Sciences of the Ukrainian SSR: Israel Program for Scientific Translations, Kiev (Washington, D.C., available from the Office of Technical Services, U.S. Dept. of Commerce).

Seminara, G., Solari, L., Parker, G., 2002. Bed load at low Shields stress on arbitrarily sloping beds: Failure of the Bagnold hypothesis. Water Resour. Res. 38, 31–1. https://doi.org/10.1029/2001WR000681

Seo, I.W., Baek, K.O., 2004. Estimation of the Longitudinal Dispersion Coefficient Using the Velocity Profile in Natural Streams. J. Hydraul. Eng. 130, 227–236. https://doi.org/10.1061/(ASCE)0733-9429(2004)130:3(227)

Shaheed, R., Mohammadian, A., Yan, X., 2021. A Review of Numerical Simulations of Secondary Flows in River Bends. Water 13, 884. https://doi.org/10.3390/w13070884

Shapiro, R., 1970. Smoothing, filtering, and boundary effects. Rev. Geophys. 8, 359–387. https://doi.org/10.1029/RG008i002p00359

Shimizu, Y., Yamaguchi, H., Itakura, T., 1990. Three-Dimensional Computation of Flow and Bed Deformation. J. Hydraul. Eng. 116, 1090–1108. https://doi.org/10.1061/(ASCE)0733-9429(1990)116:9(1090)

Shin, J., Seo, I.W., 2021. Nonlinear Shear Effects of the Secondary Current in the 2D Flow Analysis in Meandering Channels with Sharp Curvature. Water 13, 1486. https://doi.org/10.3390/w13111486

Shin, J., Seo, I.W., Baek, D., 2020. Longitudinal and transverse dispersion coefficients of 2D contaminant transport model for mixing analysis in open channels. J. Hydrol. 583, 124302. https://doi.org/10.1016/j.jhydrol.2019.124302

Song, C.G., Seo, I.W., Kim, Y.D., 2012. Analysis of secondary current effect in the modeling of shallow flow in open channels. Adv. Water Resour. 41, 29–48. https://doi.org/10.1016/j.advwatres.2012.02.003

Stansby, P.K., 2003. A mixing-length model for shallow turbulent wakes. J. Fluid Mech. 495, 369–384. https://doi.org/10.1017/S0022112003006384

Stoesser, T., Ruether, N., Olsen, N.R.B., 2010. Calculation of primary and secondary flow and boundary shear stresses in a meandering channel. Adv. Water Resour. 33, 158–170. https://doi.org/10.1016/j.advwatres.2009.11.001

Struiksma, N., 1985. Prediction of 2-D Bed Topography in Rivers. J. Hydraul. Eng. 111, 1169–1182. https://doi.org/10.1061/(ASCE)0733-9429(1985)111:8(1169)

Swart, D.H., 1976. Predictive Equations Regarding Coastal Transports, in: Coastal Engineering. pp. 1113–1132. https://doi.org/10.1061/9780872620834.066

Talmon, A.M., Struiksma, N., Van Mierlo, M.C.L.M., 1995. Laboratory measurements of the direction of sediment transport on transverse alluvial-bed slopes. J. Hydraul. Res. 33, 495–517. https://doi.org/10.1080/00221689509498657

Termini, D., 2014. Bank Erosion and Secondary Circulation in a Meandering Laboratory Flume. 3rd Int. Geogr. Symp. GEOMED2013 10-13 June 2013 Antalya Turk. 120, 496–505. https://doi.org/10.1016/j.sbspro.2014.02.129

Thomson, J., 1877. V. On the origin of windings of rivers in alluvial plains, with remarks on the flow of water round bends in pipes. Proc R. Soc. Lond. 25, 5–8. https://doi.org/10.1098/rspl.1876.0004

Uchida, T., Fukuoka, S., 2014. Numerical calculation for bed variation in compound-meandering channel using depth integrated model without assumption of shallow water flow. Adv. Water Resour. 72, 45–56. https://doi.org/10.1016/j.advwatres.2014.05.002

Uijttewaal, W.S.J., 2014. Hydrodynamics of shallow flows: application to rivers. J. Hydraul. Res. 52, 157–172. https://doi.org/10.1080/00221686.2014.905505

Uittenbogaard, R.E., van Vossen, B., 2004. Subgrid-scale model for quasi-2D turbulence in shallow water. Taylor & Francis Group, London, pp. 575–582. https://doi.org/10.1201/9780203027325. ch72

Valiani, A., Caleffi, V., Zanni, A., 2002. Case Study: Malpasset Dam-Break Simulation using a Two-Dimensional Finite Volume Method. J. Hydraul. Eng. 128, 460–472. https://doi.org/10.1061/(ASCE)0733-9429(2002)128:5(460)

van Balen, W., Uijttewaal, W.S.J., Blanckaert, K., 2010. Large-eddy simulation of a curved open-channel flow over topography. Phys. Fluids 22, 075108. https://doi.org/10.1063/1.3459152

Van Bendegom, L., 1947. Enige beschouwingen over riviermorfologie en rivierverbeteringen (in Dutch). Ing. 59, B1–B12.

Vanzo, D., Peter, S., Vonwiller, L., Bürgler, M., Weberndorfer, M., Siviglia, A., Conde, D., Vetsch, D.F., 2021. BASEMENT v3: A modular freeware for river process modelling over multiple computational backends. Environ. Model. Softw. 143, 105102. https://doi.org/10.1016/j.envsoft.2021.105102

Vermeer, K., 1986. The ripple factor in sediment transport equation. Tech. Rep. R657/ M1314-V, Toegenpast Onderz, Waterstaat Rivers, Delft Hydraul., Delft, Netherlands.

Viero, D.P., 2019. Modelling urban floods using a finite element staggered scheme with an anisotropic dual porosity model. J. Hydrol. 568, 247–259. https://doi.org/10.1016/j.jhydrol.2018.10.055

Viero, D.P., D'Alpaos, A., Carniello, L., Defina, A., 2013. Mathematical modeling of flooding due to river bank failure. Adv. Water Resour. 59, 82–94. https://doi.org/10.1016/j.advwatres.2013.05.011

Viero, D.P., Peruzzo, P., Carniello, L., Defina, A., 2014. Integrated mathematical modeling of hydrological and hydrodynamic response to rainfall events in rural lowland catchments. Water Resour. Res. 50, 5941–5957. https://doi.org/10.1002/2013WR014293

Viero, D.P., Valipour, M., 2017. Modeling anisotropy in free-surface overland and shallow inundation flows. Adv. Water Resour. 104, 1–14. https://doi.org/10.1016/j.advwatres.2017.03.007

Wang, D., Tassi, P., 2014. Secondary Flow Corrections into The Telemac-Mascaret Modelling System. Proc 21st TELEMAC-MASCARET User Conf. 2014 Eds O Bertrand C Coulet Grenoble Fr. 239–247.

Wei, M., Blanckaert, K., Heyman, J., Li, D., Schleiss, A.J., 2016. A parametrical study on secondary flow in sharp open-channel bends: experiments and theoretical modelling. J. Hydro-Environ. Res. 13, 1–13. https://doi.org/10.1016/j.jher.2016.04.001

Wu, W., Jiang, E., China, P.R., Wang, S.S.Y., 2004. Depth-averaged 2-D calculation of flow and sediment transport in the lower Yellow River. Int. J. River Basin Manag. 2, 51–59. https://doi.org/10.1080/15715124.2004.9635221

Wu, W., Rodi, W., Wenka, T., 2000. 3D Numerical Modeling of Flow and Sediment Transport in Open Channels. J. Hydraul. Eng. 126, 4–15. https://doi.org/10.1061/(ASCE)0733-9429(2000)126:1(4)

Wu, W., Shields Jr., F.D., Bennett, S.J., Wang, S.S.Y., 2005. A depth-averaged two-dimensional model for flow, sediment transport, and bed topography in curved channels with riparian vegetation. Water Resour. Res. 41, W03015. https://doi.org/10.1029/2004WR003730

Xiao, Y., Liu, J., Qin, C., Xu, F., 2022. Two-Dimensional Numerical Modeling of Flow Pattern and Bed Topography in Channel Bend. Environ. Model. Assess. https://doi.org/10.1007/s10666-022-09818-5

Ye, J., McCorquodale, J.A., 1998. Simulation of Curved Open Channel Flows by 3D Hydrodynamic Model. J. Hydraul. Eng. 124, 687–698. https://doi.org/10.1061/(ASCE)0733-9429(1998)124:7(687)

Ye, J., McCorquodale, J.A., 1997. Depth-Averaged Hydrodynamic Model in Curvilinear Collocated Grid. J. Hydraul. Eng. 123, 380–388. https://doi.org/10.1061/(ASCE)0733-9429(1997)123:5(380)

Yeh, K., Kennedy, J.F., 1993. Moment Model of Nonuniform Channel-Bend Flow. I: Fixed Beds. J. Hydraul. Eng. 119, 776–795. https://doi.org/10.1061/(ASCE)0733-9429(1993)119:7(776)

3 CFD numerical analysis of turbulent flow over mussels on a gravel bed

The results presented in this Chapter are reported in a manuscript published in Water Resources Research (Lazzarin et al., 2023a)[1], and in a further manuscript submitted for possible publication in Water Resources Research[2].

The Chapter presents the results of the parametrical analysis of the flow around a partially-buried, isolated freshwater mussel, and over clusters of partially-buried mussels, all placed on a gravel bed.

After illustrating the numerical model used in the study, the Chapter describes the turbulent flow around an isolated specimen of the freshwater *Unio Elongatulus* mussel. Though the isolated shell can be considered as a particular case of surface-mounted obstacle, studying the flow over a live mussel is complicated by the coarse substrate, the complex shape of the shell and the filtering activity of the mollusk. Thus, the relevant parameters investigated in the study are the bed roughness, the burrowing ratio of the shell and the filtering discharge through the mussel incurrent and excurrent siphons. The analysis focuses on the mean flow and the turbulent kinetic energy (*TKE*), as well as on the vortical structures generated around the mussel, the flow in the wake and the vortex shedding.

As mussels tend to aggregate to form clusters of elements with different spatial densities, evaluating how the flow structure changes in case of a musselbed provides further insights on the mean flow and on the turbulent structures at the organism scale. In clusters of elements mussel-to-mussel interactions affect the flow approaching each shell, and must be accounted for to provide a more realistic view of the environmental conditions in which mussels live, compared to the canonical case of an isolated mussel. The main parameter analyzed in the second part of this Chapter is the mussel density (i.e., the number of mussels per unit area). The effects of the bed roughness and the filtering activity of the mussels are also investigated at different mussel densities.

The present analysis of the flow around mussels has also important ecological and biological implications. Freshwater mussels are among the most imperilled fauna, hence investigating the flow at the organism scale can be of importance to sustain their

[1] Lazzarin, T., Constantinescu, G., Di Micco, L., Wu, H., Lavignani, F., Lo Brutto, M., Termini, D., Viero, D.P., 2023. Influence of bed roughness on flow and turbulence structure around a partially-buried, isolated freshwater mussel. Water Resour. Res. 59, e2022WR034151. https://doi.org/10.1029/2022WR034151

[2] Lazzarin, T., Constantinescu, G., Wu, H., Viero, D.P. Fully Developed Open Channel Flow over Clusters of Freshwater Mussels Partially Buried in a Gravel Bed. Submitted for publication in Water Resour. Res.

conservation. Factors that influence the life of the mussel are also investigated in the study, in case of both isolated specimens and clusters of elements. Precisely, the mean drag forces and the bed shear stresses (that influence mussel stability) and the jet of filtered water exhaled from the excurrent siphon (that influence the availability of nutrients and foods) are analyzed depending on the aforementioned controlling parameters.

3.1 Introduction

Freshwater mussels are mollusks living at the sediment–water interface, and they are common in sand and gravel bed rivers. Given their non-negligible importance in fluvial environments, they are identified as ecosystem engineers to highlight their role in increasing the sustainability of river ecosystems (Marion et al., 2014; Polvi and Sarneel, 2018; Vaughn, 2018). Among the various roles, freshwater mussels constitute a fundamental link in many food chains (Atkinson and Vaughn, 2015; Howard and Cufey, 2006; Vaughn et al., 2008), contribute to the filtration of suspended material (Hajisafarali et al., 2022; Kreeger et al., 2018), provide suitable habitat for fish, insects and benthic organisms (Gutiérrez et al., 2003), increase bed stability especially in gravel-bed rivers (Lohrer et al., 2004), and can be used as bioindicators for water quality (Doucet et al., 2021; Haag, 2012).

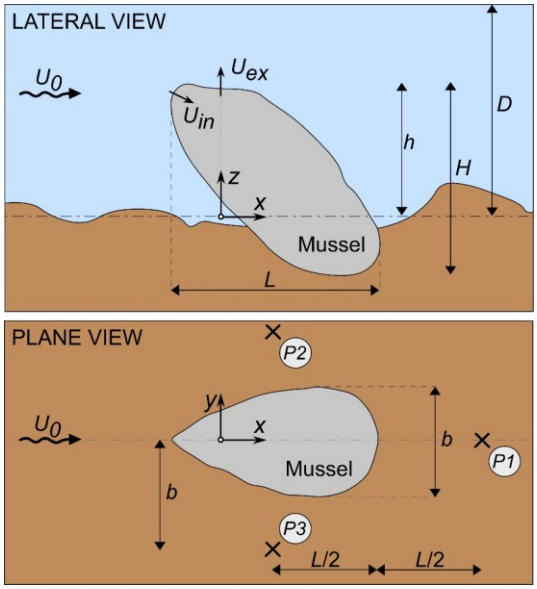

Figure 3-1. Sketch of the mussel shell. U_0 is the section-averaged velocity in the channel, L, H and b are the mussel's length, height and width in the x, y, z reference frame, respectively (the position $z = 0$ identifies the mean bed elevation), h is the height of the exposed part, U_{in} and U_{ex} are the mean velocities through the incurrent and the excurrent siphons, respectively, and D is the height of the water column above the bed. P1, P2, P3 are the horizontal locations where vertical profiles of the streamwise velocity were measured experimentally (see Sect. 3.2.5).

Freshwater mussels have a shell composed by two valves, symmetric respect to a central axis (Figure 3-1). In the lower part of the shell, a muscular foot guarantees the anchoring to the bed. The foot also allows small movement of the mussel, in both the horizontal and the vertical direction.

Generally, live mussels have been observed to move reacting to the surrounding environment such that they assume an orientation parallel to the incoming flow. Though many factors influence the mussel orientation, the alignment with the incoming flow allows to minimize the total drag force and the probability of being dislocated from the substrate (Di Maio and Corkum, 1997; Wu and Constantinescu, 2022). Mussels are generally partially burrowed in the bed, and anchored in the substrate with the foot, which is not visible and located below the mean bed level (Vaughn et al., 2008). The level of burial can change to adapt to flow conditions.

The mussels have siphons to communicate with the surrounding environment and to acquire nutrients. An incurrent (or inhaling) siphon is generally oriented upstream and it is used to acquire organic particles and nutrients from the surrounding flow. The excurrent (or exhaling) siphon is oriented upwards, still in the frontal part of the mussel. Mussels use the exhaling siphon to reintroduce in the channel a jet of filtered water, which has low concentrations of nutrients and organic particles (Kumar et al., 2019; O'Riordan et al., 1995; Perles et al., 2003). For this reason, freshwater mussels are important for filtering water flows. The role of water purifier is among the key functions of freshwater mussels in river ecosystem, and their filtering rate has been measured experimentally (see e.g., Kryger & Riisgård, 1988; Monismith et al., 1990; Nishizaki & Ackerman, 2017). Though the filtering rate depends on the specie and the dimension (Bunt et al., 1993), mussels can also change their filtering rate in response of variable flow conditions.

In many part of the world, freshwater mussels are among the most common benthic invertebrates (Allen & Vaughn, 2009; Strayer, 2008). However, they are also among the world's most imperilled fauna (Ferreira-Rodríguez et al., 2019; Froufe et al., 2017; Lopes-Lima et al., 2017; Lopez et al., 2022; Lydeard et al., 2004; Simeone et al., 2021; Strayer et al., 2004). Mussels life is strongly connected with the aquatic environment in which they are found (Lopez et al., 2022). In particular, the chemical and biological characteristics of the water, in terms of availability of nutrients, water pH and temperature, can all affect mussel life. The survival of the mussels also depends on the flow hydrodynamics, which can modify environmental conditions and play a key role for the conservation of these mollusks. The mutual influences between mussels and flow are then of great importance for their conservation. Understanding the hydrodynamic responses of freshwater mussels and individuating regions with a favorable habitat for mussels, can be useful to sustain their population over long times (Blettler et al., 2010; Engelhardt et al., 2004; Nakato et al., 2007; Sullivan and Woolnough, 2021; Zigler et al., 2008). Hence, studying mechanisms and factors that can threaten mussel life (e.g., critical stability, nutrients availability) can shed a new light on techniques to guarantee mussel survival in natural streams. At the moment, important gaps on the mussel-flow interactions at the organism

scale still hinder the actions to be pursued (Lopez and Vaughn, 2021), even if a full understanding of factors influencing mussel life, as well as the ecological role played by the mussels, require an interdisciplinary approach involving ecological, biomechanical and environmental fluid mechanics research tools (Nikora, 2010).

As most of the invertebrates living at the sediment-water interface, freshwater mussels are sensitive to shear stresses in the river reach (Modesto et al., 2023; Morales et al., 2006; Strayer, 1999). Regions of high bed shear stress are associated to a lower probability of mussel survival (Newton et al., 2008). High bed shear stresses generally correlate with mussel dislocation, because of drag forces acting on the emerged part of the shell, and of sediment entrainment at the bed that induces local scour near the shells. These mechanisms are enhanced during floods because both the mean drag forces and the mean bed shear stresses increase, thus increasing the probability of mussel dislocation. During floods instantaneous values also show larger variations with respect to the mean values, which further increases the probability of the mussel to lose anchor from the substrate. For this reason, floods and extreme events are among the main causes that threaten mussel conservation (Sansom et al., 2018).

Large-scale turbulent structures and high values of the turbulence kinetic energy (*TKE*) at the shells may also affect the quality of the habitat and, possibly, the survival of the mussel (Rehmann et al., 2003). The mussel shell constitutes a submerged, surface-mounted obstacle, which increases velocity and shear stresses on its sides, and produces a recirculation region in the wake downstream. Various other vortical structures form, and interact with those generated at the individual particles of the rough bed and at the neighboring mussels, if present (Chang and Constantinescu, 2013). Most of them (e.g., horseshoe vortices, wake vortices, base and tip vortices in the wake) are observed above the surface of the bed, and generally they extend until an elevation comparable with the emerged part of the shells. As a consequence, their presence and/or their passage induce instantaneous fluctuations on the flow field, and they can amplify the instantaneous values of bed shear stresses and drag forces on the mussel, thus affecting the ability of the mussel to remain anchored to the bed. Together with macro-scale characteristics of the flow (e.g., flow velocity), these local turbulent structures are also expected to be of influence for the mussel life, thus requiring analysis of the flow at the organism scale.

Most of the previous studies on the interactions among flow and mussels at the organism scale include laboratory experiments (Wu et al., 2020). Earlier studies focused on characterizing the phytoplankton distribution within the boundary layer (e.g., Butman et al., 1994; O'Riordan et al., 1995). Nikora et al. (2002) analyzed the internal boundary layer (e.g., velocity and turbulence profiles) over a patch of horse mussels through *in situ* measurements in a tidal environment. Crimaldi et al. (2002) measured turbulent structures over a laboratory bed with 0.027 m long model clams. Considering different densities and emerging heights, they concluded that spacing strongly affects the probability of the mussel to remain anchored to the bed. van Duren et al. (2006) used living, 0.039 m long mussels to assess the effects of mussel filtering activity on mussel-bed boundary layer structure. The filtering effect has been demonstrated to be crucial

especially if the excurrent velocity was relatively high compared to the mean incoming flow. Crimaldi et al. (2007) also evaluated the effect of the filtering activity on velocity and concentration profiles making use of models of 0.009 m long clams. The siphonal activity was accounted for also in the experimental studies of Kumar et al. (2019), considering an isolated mussel with siphons facing both upstream and downstream, and of Sansom et al. (2018), considering a bed with mussels at a low spatial density (i.e., 10 mus/m^2). Sansom et al. (2020), instead, used Particle Image Velocimetry (PIV) to characterize flow over a rough bed with models of shells ~0.030 to 0.040 m long at relatively high spatial densities. Mussels was partially-burrowed in the substrate and placed at spatial densities spanning from 0 mus/m^2 to 100 mus/m^2. The model mussels, however, did not account for the filtering activity of the mollusks. They observed a change in flow regime for higher mussel densities (above 25 mus/m^2), with reduced flow velocity and bed shear stresses in the mussel region. Largest turbulent shear stresses, instead, were located at the top of the protruding shells, away from the bed. As a consequence, the dislodgement potential exerted on the mussels was observed to be reduced for clusters with high mussel densities.

Besides laboratory experiments, the mussel-flow interactions at the organism scale have been investigated also through numerical approaches that resolve the energetically important turbulent eddies in the flow. Previous studies focused on vortical structures generated by mussels, their dynamics and their effects on the drag forces, on the capacity of the flow to induce local scour, and on the mixing between the excurrent siphon jet of filtered water and the overflow rich in phytoplankton. Among the studies, Wu et al. (2020) considered a single partially-burrowed mussel placed on a flat bed, while Constantinescu et al. (2013) a small cluster of three mussels, still mounted on a flat bed. The effect of the angle of attack was discussed later by Wu & Constantinescu (2022).

As a first drawback of previous numerical studies, they refer to the case of a smooth horizontal bed. However, mussels are generally found in sand or gravel rivers. Coarse substrates enhance both bed stability and water mixing. As these are key aspects for their survival, mussels live on bed whose roughness is relatively high. The mean sediment size (e.g., as quantified by the d_{50} and d_{90} diameters) of the bed particles can be as high as 10% of the height of the emerged part of the mussel, h. Particles composing gravel beds induce energetic eddies to form in case of turbulent flows. As a consequence, TKE values above the bed surface are higher if compared to the case of a smooth, horizontal channel with the same Reynolds number. This effect is observed in case of graded sediments, and it is enhanced when particles with heterogeneous dimensions are present. Though depending also on the relative size of the sediment diameter and the water depth, large size particles constitute larger-scale roughness elements and act as surface-mounted obstacles, with a role similar to that of a mussel shell. In any case, in rough, gravel beds eddies generated by the bed sediments may alter the flow field approaching the mussel shell. The interactions of these eddies with the turbulent structures generated by the shell should be considered, as they influence the flow approaching the mussel. These interactions can affect both the instantaneous and the mean flow field in the shell region,

and ultimately the drag forces on the shell and the bed shear stress near the mussels, which are important for the mussel stability. For this reason, considering a gravel bed is expected to provide more realistic predictions of the actions of flow on mussels. To this end, differently from the aforementioned studies based on eddy resolving techniques, that simulate the case of smooth beds, the present work refers to the case of a rough bed to approximate a natural benthic environment, and to evaluate to what extent the bed roughness controls the dynamics of the larger-scale coherent structures, the forces on the shell, and the mixing between the filtered water entering the channel through the excurrent siphon and the surrounding flow. As mussels are common in rough bed rivers, understating the flow structure in case of mussels placed over gravel beds is of particular interest to understand actions to be pursed to preserve their life in natural streams.

As a second drawback, previous studies refer to isolated specimens, or to small groups of mussels with low spatial densities. In natural rivers, instead, mussels form large clusters (or arrays), known as mussel beds (Morales et al., 2006; van de Koppel et al., 2008). Though the positions of the mussels are strongly irregular in the clusters, the value of the mussel array density (i.e., the number of mussels per unit area) is generally used to characterize clusters of mussels. Values are highly variable, and they depend on several factors (e.g., mussel species, environmental conditions, etc.). On some river beds they also exceed 200 mus/m^2 (Strayer et al., 1994). In case of mussel beds, the flow and the vortical structures are expected to differ from those observed in the canonical case of an isolated mussel (Sansom et al., 2022). Mussel-to-mussel interactions increase with the array density increasing. As a consequence, the effect on the surrounding flow becomes also function of the position inside the array and of the relative position of each mussel with respect to neighboring ones, while for an isolated mussel it is mainly a function of the geometry of the protruding part of the shell and of the filtering discharge. In the case of an array of mussels, the drag forces on the shells are also expected to differ if compared to the case of an isolated mussel. As mussels are partially sheltered by neighboring shells, the destabilizing drag forces are expected to decrease with increasing mussel density. In cluster of mussels, the filtering activity of single mollusks also interfere with that of the surrounding ones; hence, the availability of nutrients can be influenced by the mussel density, besides the mixing capacity of the surrounding flow. All these reasons justify the study of clusters of mussels at different spatial densities to complement the results obtained for the canonical case of an isolated mussel.

The present work is based on numerical simulations with eddy resolving techniques, which constitute a powerful tool to provide information on the dynamics of the large-scale turbulence in case of complex three-dimensional domain, with elements of irregular shapes (Keylock et al., 2012, 2005). The vortical structures of the flow, the interaction of these coherent structures with the bed and the mussel surface and their role in transport and mixing processes, require the use of 3D approaches as information collected in 2D planes does not describe completely the complex interactions occurring in such cases. Also, solving the flow over the individual roughness elements forming the rough bed surface, either in case of the bed particles and in case of mussel shells,

provides more realistic results rather than simply accounting for the bed roughness via empirical roughness models (e.g., Wu et al., 2021). This is the case of the present study which is based on a gravel bed surface obtained from a flume experiment conducted as part of a larger research program, and on a shape of the shells that accurately reproduces that of an *unionid* mussel, and includes the filtering flows through the excurrent and incurrent siphons.

The numerical approach used in the present study resolves the flow past the mussel shells, and allows to investigate the near-bed flow in the roughness layer and to provide complete information of the entire flow field in the region where mussels are placed. The advantage of this numerical approach is particularly clear especially if compared to laboratory experiments. In this latter case, information on the mean flow and turbulence variables (e.g., *TKE*, Reynolds stresses) is constrained by the experimental measurements, and it is generally available in a limited number of sections and/or in a limited number of horizontal locations around the mussel (Crimaldi et al., 2002; Kumar et al., 2019; Sansom et al., 2018). Measurements near the mussels are also difficult to perform experimentally, especially at high mussel densities, due to the very small spacing among the shells.

The present study refers to a *Unio Elongatulus* freshwater mussel, which is a popular mussel in riverine and lake environments in Northern Italy (Froufe et al., 2017; Lopes-Lima et al., 2017; Marrone et al., 2019) The shell of the *Unio Elongatulus* mussel is more streamlined compared to the *Lampsilis Siliquoidea* mussel used by Wu et al. (2020a) and Wu & Constantinescu (2022) in their numeircal analysis for the case of a single specimen on a flat bed. Also, the *Unio Elongatulus* mussel is typically inclined toward the incoming flow, such that the front and the back side present large differences (Figure 3-1). *L. Siliquoidea* mussels, instead, have a more symmetrical shell and they are typically found to be less tilted toward the incoming flow.

The first part of the present research focuses on the interactions between the flow and an isolated mussel placed on a gravel bed. The interest is to understand how an undisturbed flow approaches the shell and which are the turbulent coherent structures forming. Quantifying drag forces and describing the mixing of the excurrent jet induced by the incoming flow are also of interest for the mussel conservation. The present study complements the previous numerical researches, which refer to the case of smooth beds, by analyzing the influence of bed roughness on flow and turbulence structures. The second part of the research, instead, focuses on musselbeds. Compared to previous studies conducted with freshwater mussels, the present work investigates the effect of the density of the mussel array up to large values corresponding to highly dense mussel beds (e.g., 500 mussels/m^2). In this case the interest is the analysis of the fully developed flow, which corresponds to the flow at large distances from the leading edge of the array. This is motivated by the fact that in natural rivers musselbeds can extend over several kilometers. After the development of a rough bed boundary layer at the leading edge of the array, at a distance, this boundary layer is expected to reach the free surface, and the flow reaches a new 'fully-developed' state. This new state still depends to the characteristics of the open channel flow approaching the mussel bed to a large extend

(e.g., flow discharge), but it is strongly influenced by the characteristics of the musselbed, and it is observed until the end of the musselbed.

A first main goal of the study is to understand to what extent bed roughness affects flow, turbulent kinetic energy and the dynamics of vortical structures around an isolated, partially-burrowed mussel shell. A related goal is to quantify the effect of increasing bed roughness on the mean drag forces acting on the exposed part of the shell and the associated drag coefficients, and on mixing between the excurrent siphon jet and the surrounding flow. A second main goal of the study is to understand to what extent the mussel density influences the aforementioned aspects. This requires analyzing the interactions between the eddies generated by the gravel bed particles and the mussel shells, and the mussel-to-mussel interactions in case of arrays of shells. Other research questions the present study tries to answer regard how does bed roughness and mussel densities affect the formation and strength of the base vortices induced by active filtering and of tip vortices induced in the wakes, and how is wake vortex shedding affected by increasing bed roughness. Besides the bed roughness and the mussel density, the study also investigates the role of the mussel shape, by the comparison with previous studies on different species, of the filtering activity of the mussel, by varying the discharge through the siphons, and of the burial level, by changing the height of the exposed part of the shells.

After describing the computational model and its validation by means of experimental measurements (Sect. 3.2), the present study first provides information for the case of an isolated mussel on a rough bed (Sect. 3.3). The main parameter investigated is the bed roughness, quantified as the main grain diameter, d_{50}. The study considers beds of different roughness, from the case of a gravel bed to the canonical case of a smooth bed. The study also considers different heights of the exposed part of the mussel, h, as the interactions between eddies generated by the rough bed and by the exposed part of the shell are controlled to a large degree by the d_{50}/h ratio. Another parameter investigated in the present study is the filtering velocity ratio, *VR*. defined as the ratio between the excurrent jet velocity, U_{ex}, and the bulk velocity in the channel, U_0. This is motivated by the previous study of Wu et al. (2020a), which has shown that increasing *VR* the drag force acting on the shell increases, suggesting that mussel could limit their filtering activity at high flow conditions to better resist dislocation from the substrate. Then, the study is complemented with the case of clusters of mussels placed on a rough bed, which are investigated in a similar way (Sect. 3.4). In this case, a single value of the exposed height of the mussel is considered. The parameters investigated in this Section include the mussel array density, ρ_M, the ratio between the bed roughness height and the protruding height of the mussel, d_{50}/h, and the filtering velocity ratio, *VR*. Some conclusions close the Chapter, where limitations of the present work and future research objectives are also discussed (Sect. 3.5).

3.2 Geometry, Computational Approach and Model Validation

3.2.1 Geometry

The rough bed surface used in the present simulations was the reproduction of a real water-worked gravel bed sample from laboratory, with d_{50} = 3.1 mm and d_{90} = 5.0 mm (Figure 3-2a). In present study the main focus was on the flow around the partially-buried mussels. The critical effect induced by the gravel bed, and desired to be captured by the numerical simulations, was the generation of turbulent eddies induced by bed particles and their interactions with the mussel shells. For this reason, the bed was assumed to be impermeable, and only the surface of the gravel bed (i.e., the part directly exposed to the flow) was modelled. The lower part of the particles and the pores below them were instead ignored. Some simulations included in the present studies considered a flatbed (i.e., d_{50} = 0.00 mm), while others considered a deformed bed surface obtained by multiplying the vertical elevation of the original gravel bed by a factor 0.5. This surface has a of lower roughness, corresponding to d_{50} = 2.46 mm.

The geometry of the mussel shell has been obtained as a 3-D reproduction of the real shell of an *Unio Elongatulus* mussel. The mussel has a total length of 0.080 m and it is placed with the major axis forming a 45° angle with the bed, according to its usual position in the real habitat observed from field observations, as pictured in Figure 3-1. The mussel was aligned with the incoming flow (i.e., angle of attack 0°). The projected dimensions along x,y,z axis was length L = 0.055 m, width b = 0.020 m and height H = 0.050 m. Considering the emerging part of the shell, the length, L, and the width, b, were approximatively constant for the different levels of mussel burial considered in the present work. The height, h, of the emerging part of the shell (i.e., the part above the bed surface) decreased with increasing mussel burrowing. The inhaling siphon was pointing upstream, while the exhaling siphon, which was located downstream of the inhaling siphon, was pointing upwards (Figure 3-2b). In the simulations, the width of the shell was constant, such that the small change in the volume of the shell during the filtering process, which results from the opening of the shell, was neglected.

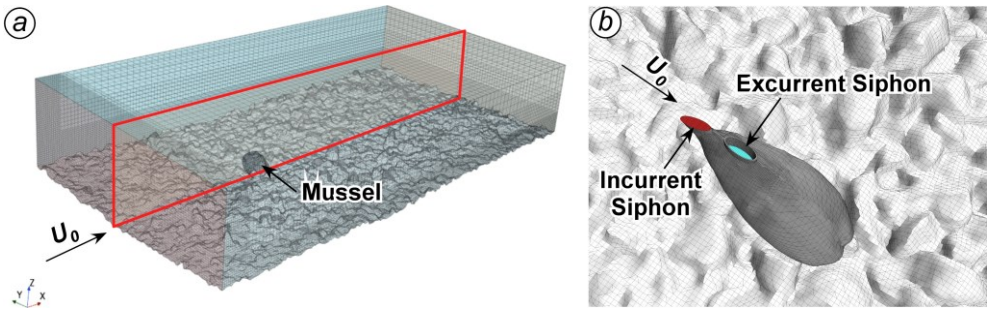

Figure 3-2. Computational domain with a rough bed surface and an isolated mussel. a) three-dimensional (3-D) view of the computational domain (red rectangle shows the y / H = 0 plane); b) 3-D view of the mussel, highlighting the positions of the incurrent and excurrent siphons.

3.2.2 Numerical model

The simulations were performed with the finite-volume, viscous flow solver in STAR-CCM+. The same computational suite has been widely used to simulate and to accurately predict complex flows in natural environments containing highly-unsteady vortices, as well as steady and unsteady flows in channels containing large-scale flow obstructions (e.g., Constantinescu, 2014; Horna-Munoz and Constantinescu, 2018; Keylock et al., 2012; Lazzarin et al., 2023b).

The Detached Eddy Simulation (DES) approach was adopted in the present study to reproduce the energetically important eddies in the flow. DES is a hybrid approach between the Reynolds-Averaged-Navier-Stokes (RANS) and the Large Eddy Simulations (LES). It reduces to RANS equations near the solid boundaries (Constantinescu et al., 2003: Heinz, 2020; Menter et al., 2021). Instead, the LES mode is used over the rest of the computational domain (Chang et al., 2007a).

In RANS, the Reynolds decomposition and the time averaging of equations (continuity and Navier-Stokes) correspond to apply a time filter. The additional Reynolds stresses, that arise in the time-filtered equations, represent the effect of turbulence on the mean flow. In LES, flow quantities are not averaged in time; rather, turbulent motions are split into large- and small-scale eddies, with the former resolved and the latter modelled. The small-scale motions are modelled making use of a spatial filtering that depends on the local mesh size. Equations are equivalent to the RANS equations with the additional turbulent stress term that arises from the filtering operation performed by a subgrid model. The main difference is that in RANS the stress term represents the total effect of turbulence, whereas in LES only the effect of the small-scale motions.

In the present simulations the base RANS model was the Shear Stress Transport (SST) k-ω model (Menter, 1994; Menter et al., 2003). The DES formulation is obtained by modifying the definition of the specific dissipation term, ω, depending on the specific approach.

Grid elements are assigned to either RANS or LES regions depending on the turbulence length scale. In the RANS region, the turbulence length scale is proportional to the distance to the closest solid boundary. By contrast, the turbulence length scale in DES is redefined such that it becomes proportional to the local grid size away from the solid boundaries and the eddy viscosity becomes proportional to the square of the local grid spacing, as in the LES model.

In the present simulations, a passive scalar was used to study the mixing of the jet from the excurrent siphon. A transport equation was solved for the passive scalar, and the Prandtl number was set to 1, which is generally the standard in these applications (Chang et al., 2007b).

The viscous sublayer was fully resolved to avoid the introduction of wall functions (i.e., at least one grid point was situated inside the viscous sublayer in the wall normal direction; this required the thickness of the near-wall cell to be lower than $5\nu/u^*$, being ν the kinematic viscosity and u^* the local shear velocity). DES calculations with this kind

of approach have been demonstrated to accurately predict flow and turbulence statistics for open channel flows and flow in natural river reaches (Constantinescu, 2014; Constantinescu et al., 2003; Constantinescu and Squires, 2003; Keylock et al., 2012; Kirkil and Constantinescu, 2009). Such DES simulations have been also used to study the flow fields in open channel flows with either isolated specimens or arrays of surface-mounted emerged and submerged obstacles (Chang et al., 2007a, 2020; Koken and Constantinescu, 2021), and with large-scale roughness elements, such as arrays of 2-D dunes (Chang and Constantinescu, 2013).

The governing equations were discretized on unstructured, Cartesian-like grids. The Navier-Stokes equations were advanced in time using a Semi-Implicit Method for Pressure Linked Equations (SIMPLE) algorithm. In this algorithm an intermediate velocity is calculated by solving the momentum equations without the pressure term, and then a pressure correction is introduced to calculate the final velocity that ensures the continuity equation is satisfied (Patankar and Spalding, 1972; Qin et al., 2021; Xu et al., 2022) The convection terms in the momentum equations were discretized making use of a Hybrid-Bounded central difference scheme. It couples a bounded central difference scheme in LES regions, and a higher-order upwind scheme in RANS regions. Advection-diffusion equations were used for the eddy viscosity and for the passive scalar introduced through the excurrent siphons of mussels. Convective terms in the transport equations were discretised with a second-order upwind scheme, while diffusive and pressure gradient terms were discretised with a second-order central scheme. The temporal discretization was implicit, and the solver was parallelized using message passing interface for application in computing clusters.

3.2.3 Computational Model and Boundary conditions

The gravel bed surface and the geometry of the mussel shell were obtained from the digitalization of the real samples. They were reconstructed as separate geometries making use of an accurate close-range photogrammetric survey (ground sample distance of ~0.06 mm). This technique has been shown to well capture the geometry of gravel beds (Chen et al., 2019). A Nikon D5200 digital camera have been used, and classical Structure from Motion (SfM) and Multi-View Stereo (MVS) allowed to match the images to obtain dense point clouds. The point clouds for the 0.40 m wide and 1.0 m long bed surface consisted of 1.9 million points. That of the mussel shell consisted of 172,000 points. The point clouds have been exported as a triangulated meshes in stereolithography files (*.stl*), with a spatial resolution of 0.4 mm for the bed and 0.1 mm for the mussel shell. The three-dimensional models of the gravel-bed and of the mussel have been imported into the STAR-CCM+ software to build the computational mesh.

For simulations considering an isolated mussel, the original scanned bed was used in the simulations. Instead, in the case of musselbeds, the original graved bed surface was used to obtain a larger bed surface. Using symmetry projections, the new surface has been generated such that the bed elevation was identical at the upstream and at the downstream edges of the computational domain, and also at its right and left sides (this was needed to impose periodic boundary conditions, as described later in the text).

The isolated mussel has been positioned equidistant from the later sides, at a longitudinal distance of 0.2 m (i.e., 4 H) from the upstream part of the gravel bed surface. When considering musselbeds, the positions of the mussels in the array have been determined using a randomization procedure. Additional constraints allowed to maintain a nearly uniform mussel density in the different parts of the domain, and to guarantee a minimum distance between neighboring mussels. The surface of the mussel shell was copied and placed over the bed surfaces, and centered at the spatial coordinates provided by the aforementioned procedure.

Once the mussels were placed on a smooth or a rough bed corresponding to the desired level of burial, the mussel parts beneath the bottom were removed to obtain the final mesh (Figure 3-2a). No-slip boundary conditions were then applied on the bed surface and on the mussel shells. The turbulent kinetic energy was imposed to be zero on all solid surfaces, and the standard relationships were used to specify the turbulence vorticity on these surfaces (Menter, 1994).

To mimic the two mussel siphons (Figure 3-2b), additional parts have been added to the surface of the mussel shell. To provide a realistic representation of the interactions between the excurrent jet and the overflow, the exhaling siphon has been modelled with a vertical pipe inside the upper part of the mussel, as in Wu et al. (2020a). A fixed mass flow was specified on the incurrent siphon surface (mass outlet), and at the entrance section of the excurrent siphon pipe (mass inlet). The values of discharge corresponded to the desired filtering flow, and it was constant in time for each simulation. A constant concentration of passive scalar ($C_0 = 1$) has also been assigned at the inlet section of the exhaling siphon to study the excurrent jet. At the solid surfaces and at the free surface, the gradients of C in the normal direction were set equal to zero (Chang et al., 2007). The excurrent pipe was removed in the simulations conducted with no active filtering, and a cap was placed on the top of the excurrent siphon.

In the simulations the ceiling was fixed. This corresponds to the rigid-lid approximation (i.e., non-deformable free surface). Accordingly, proper boundary conditions have been assigned at this boundary (e.g., zero shear stress for velocity, zero vertical gradient for other variables). In the present case, the rigid-lid approximation can be considered acceptable. Indeed, deformations of the free-surface are expected to induce negligible effects on the flow field close to the mussels, given the low value of the Froude number and the high submergence of the emerged part of the shell (Hajimirzaie et al., 2012; Koken and Constantinescu, 2009; Shamloo et al., 2001; Wu et al., 2020).

Simulations considering an isolated mussel made use of an assigned velocity distribution as inlet boundary condition. The distribution was obtained from a precursor simulation performed in a channel with the same cross section at the inlet section and with a length of 0.36 m. In this precursor simulation, periodic boundary conditions were imposed in the streamwise direction to obtain the fully-developed velocity distribution, as well as the inlet distributions of the turbulent kinetic energy, k, and the turbulence vorticity, ω, for which transport equations are solved in the RANS regions of the present DES model. Once the precursor simulation reached a steady state, data was imposed at the inlet section of the main model. Symmetry boundary conditions have also been

imposed at the two later boundaries of the main model. At the exit section, a pressure outlet boundary condition was used. The passive scalar concentration, *C*, was set to 0 at the inlet boundary, and it was set equal to the value at the immediate interior cell at the outlet boundary. The gradients of *C* in the direction normal to surfaces were set to zero.

Boundary conditions were different in the simulations conducted with arrays of mussels. As the goal was to study the fully developed flow over musselbeds, periodic boundary conditions have been imposed in both the streamwise and spanwise directions for flow velocity and turbulence model variables. In the longitudinal direction, the value of mass flow rate was imposed to be fixed. Periodic conditions on these boundaries was assigned also to the scalar concentration, though prescribing zero-gradients in the normal direction at the impermeable surfaces.

3.2.4 Computational mesh

The computational grids were created using the mesh generator in STAR-CCM+. They were made of hexahedral cells, which provided a higher degree of flexibility. Near the irregular surfaces (e.g., at the bed and at the shells), mesh refinements and trimmed cells provided a conformal mapping of these surfaces. This procedure also ensured smooth transitions between regions of different mesh refinements.

Regions close to the mussel and to the gravel bed required higher levels of discretization to represent the irregular surfaces with sufficient degree of precision. For this reason, the mesh was nested-like to allow a local refinement where higher resolutions were needed; in particular, the computational domain has been decomposed into three regions with a progressive decrease in the dimension of the computational cells approaching the lower part of the water column. In the upper region, the computational cells had a dimension of 0.0048 m; going toward the bed, where higher resolutions were required, the mesh has been refined using cells with dimensions of 0.0024 m and 0.0012 m (Figure 3-3). The last value corresponds to about 20-25 wall units for cells near the bed and the protruding shells in the direction tangent to the surfaces. In the wall normal direction at least one grid point was ensured to be in the viscous sublayer. The regions near the siphons have been refined with elements of size 0.0005 m.

The mesh generation consisted in the remeshing of the geometrical surfaces with the desired precision, and in the subsequent generation of the 3D volume mesh. In the present simulations, the computational domain was made by approximatively 6’000’000 elements for cases with a single mussel. The total number of cells used for investigating cases with musselbeds was close to 13’000’000, as the geometrical domain was larger and the regions with high resolution at the siphons were more.

Results of numerical simulations have been first checked to be grid independent in the initial phase of the study. One of the rough-bed case simulations has been performed with different levels of grid refinement. Considering the region directly above the gravel bed, the investigated range of the grid sizes spanned from 0.0008 m to 0.0030 m. The grid independency of the solution has been observed below the value of 0.0012 m (referred to the part of the domain in the vicinity of the gravel bed). Simulations with finer grids

in this part of the domain showed negligible variations of velocity, vorticity and *TKE* if compared to the results obtained with a resolution of 0.0012 m near the bed. For this reason, simulations included in this study have been performed with a resolution of 0.0012 m in the lower region, as in the computational grid pictured in Figure 3-3.

The same code was used in the investigations of Wu et al. (2020a), who already conducted grid sensitivity analysis to determine the grid resolution needed to obtain accurate and grid-independent results near the mussels. The grid refinement in the mussels region was similar to those of the present study, which confirms the validity of the approach, given the similar values of the Reynolds numbers in the two studies.

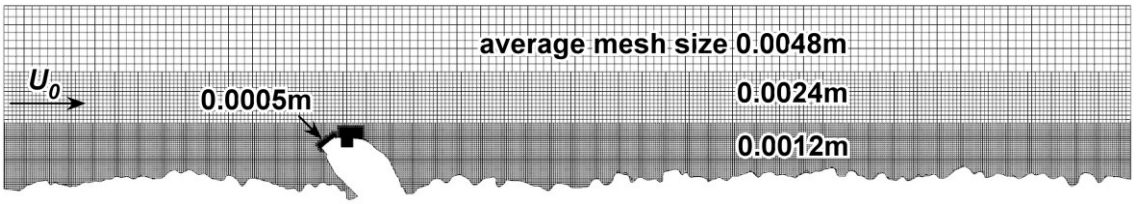

Figure 3-3. Computational mesh in a longitudinal section cutting an isolated mussel.

The irregular gravel bed considered in the present study demanded for solving the turbulence above bed particles. This in turn required a higher number of computational cells near the bed. For unit area of the computational domain, the number of cells used in the present study is roughly three times higher than the number of cells used by Wu et al. (2020a) and Wu & Constantinescu (2022) in the case of a flat bed.

3.2.5 Model validation

The numerical model used in the present study was already validated for flow past isolated, partially-burrowed mussels by Wu et al. (2020a). An additional validation of the model has been performed by reproducing a laboratory experiment of flow over a mussel on a gravel bed with d_{50} = 3.10 mm. Both the gravel bed and the mussel shell used in the experiments were the same reproduced in the numerical model.

The experiment has been performed in a recirculating flume 11 m long and 0.40 m wide at the Hydraulic Laboratory of the Department of Engineering – University of Palermo (Lazzarin et al., 2023a; Termini et al., 2022). The laboratory conditions corresponded to that of the numerical simulation with an isolated mussel with no active filtering, bed roughness d_{50} = 3.10 mm, water depth D = 0.103 m, and height of the exposed part of the mussel h = 0.024 m (i.e., submergence ratio D/h = 4.3). The streamwise velocity has been measured with a vertical resolution of 0.003 m in 3 verticals around the mussel and at the inlet. A non-intrusive ultrasonic velocity profiler DOP2000 by Signal Processing S.A. have been used.

The experimental test has been reproduced with the numerical model described in the previous Sections. In particular, the structure of the computational grid was the same as for the other simulations included in this study. However, in this simulation the lateral boundaries have been set as smooth walls to mimic the experimental conditions.

Moreover, at the inlet, the vertical velocity profile obtained from experimental measurement has been assumed as constant along the width. For a better representation of experimental conditions, a temporal fluctuation has been added randomly to the velocity imposed at the inlet section. The maximum magnitude of the fluctuation has been set to be 10% of the values of the local velocity based on fluctuations observed in the laboratory setup. The other boundary conditions were identical to the ones discussed in Sect. 3.2.3.

The vertical velocity profiles extracted from the numerical model are compared to measured data in Figure 3-4, which refer to horizontal locations P1, P2 and P3 shown in Figure 3-1. The level of agreement is overall good. Some local small differences are still present, but they do not affect the predictive ability of the model, considered that the effects of secondary flow and the variability of the streamwise velocity in the spanwise direction were ignored (a single vertical profile was measured at the inlet section). The magnitude of these differences is lower than 0.1 U_0. This is similar to what observed by Wu et al., 2020 for the case of a mussel partially burrowed on a smooth bed, when considering the discrepancies among the simulated velocity and the experimental values of Sansom et al., 2020.

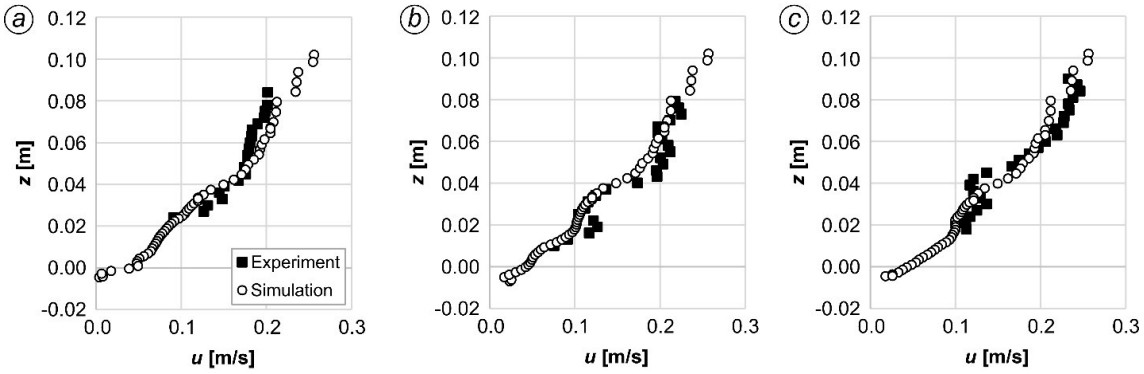

Figure 3-4. Vertical profiles of mean streamwise velocity at points P1 (a), P2 (b), and P3 (c) (see Figure 3-1) predicted by the validation simulation and measured experimentally over a rough bed (d_{50}/H = 0.062).

3.3 Flow over an Isolated Mussel

3.3.1 Test cases

The simulations discussed in the present Section consider an isolated specimen of the mussel, and were performed in a nearly rectangular channel, 0.360 m (7.2 H). wide and 0.690 m (13.8 H) long (Figure 3-2a). The flow depth in the smooth-bed simulations was D = 0.103 m (~2 H). This value corresponds to the average flow depth in the rough-bed simulations. Though this means changing the energy slope within the rigid-lid approximation (see Sect. 3.2.3), this approach has the advantage that it allows a direct comparison among different cases (same channel Reynolds number, same flow depth, etc.). The flow rate through the channel was the same for all the simulations and equal to Q = 0.0061 m³/s, corresponding to a section-averaged, or bulk, velocity U_0 = 0.164 m/s. The Froude number was F = 0.16, the bulk Reynolds number Re = 16'900.

Simulations were performed for a total time of 17 s (~27.1 D/U_0), of which 7 s (~11.2 D/U_0) to reach statistically steady condition and 10 s (~15.9 D/U_0) for averaging.

The mass flow rates through the incurrent and excurrent siphons were equal ($Q_{in} = Q_{ex}$), and maintained constant in time. As the cross section of the exhaling siphon was 1.1 time larger than that of the inhaling siphon, lower values of velocity were prescribed at its boundary to maintain the same discharge through the two siphons. In the simulations presented in this Section, the values of discharge through the siphons are 0.0, $1.55 \cdot 10^{-6}$ and $3.10 \cdot 10^{-6}$ m³/s. The corresponding excurrent siphon velocities, U_{ex}, are 0.0, 0.1 and 0.2 m/s, respectively, while the values of the velocity ratio, $VR = U_{ex}/U_0$, are 0, 0.61 and 1.22. All values are in the expected range for the species and the dimensions of mussels similar to the *Unio Elongatulus* specimen considered in this study. While the intermediate value (VR = 0.61) can be considered representative of the average filtering discharge (Monismith et al., 1990; Sansom et al., 2018), the highest value (VR = 1.22) is close to the upper threshold observed for mussels of similar size (Bunt et al., 1993).

The simulations discussed in the present Section include 15 cases, described in Table 3-1, which contains their main geometrical parameters. Table 3-2, instead, contains some of the results discussed in the following parts of the Chapter. Simulations with VR = 0 and the gravel bed with d_{50} = 3.10 mm were performed considering three different levels of mussel burial (h = 0.024, 0.019 and 0.014 m corresponding to h/H = 0.48, 0.38 and 0.28, respectively). Maintaining VR = 0 and h/H = 0.48, further simulations were performed with a bed of reduced roughness (d_{50}/H = 0.049) and with a smooth bed (d_{50}/H = 0). These five simulations were repeated using VR = 0.61 and VR = 1.22 to investigate the effect of the active filtering.

Table 3-1. Matrix of test cases with flow and geometrical properties. Variables h, H, L, b, U_{ex}, U_0 are defined in Figure 3-1; d_{50} is the mean grain size of the rough bed.

h/H	d_{50}/H	$VR = U_{ex}/U_0$	L/H	b/H	b/L	h/b	d_{50}/h
(-)	(-)	(-)	(-)	(-)	(-)	(-)	(-)
0.48	0.062	0	1.02	0.40	0.39	1.20	0.13
0.38	0.062	0	0.98	0.40	0.41	0.95	0.16
0.28	0.062	0	0.94	0.40	0.43	0.70	0.22
0.48	0.049	0	1.00	0.40	0.40	1.20	0.10
0.48	0.000	0	0.96	0.40	0.42	1.20	0.00
0.48	0.062	0.61	1.02	0.40	0.39	1.20	0.13
0.38	0.062	0.61	0.98	0.40	0.41	0.95	0.16
0.28	0.062	0.61	0.94	0.40	0.43	0.70	0.22
0.48	0.049	0.61	1.00	0.40	0.40	1.20	0.10
0.48	0.000	0.61	0.96	0.40	0.42	1.20	0.00
0.48	0.062	1.22	1.02	0.40	0.39	1.20	0.13
0.38	0.062	1.22	0.98	0.40	0.41	0.95	0.16
0.28	0.062	1.22	0.94	0.40	0.43	0.70	0.22
0.48	0.049	1.22	1.00	0.40	0.40	1.20	0.10
0.48	0.000	1.22	0.96	0.40	0.42	1.20	0.00

Table 3-2. Matrix of test cases with main results. Variables h, H, U_{ex}, U_0 are defined in Figure 3-1; d_{50} is the mean grain size of the rough bed; L_R is the length of the recirculation region at the back of the mussel; $A_x(h)$ is the projected frontal area in the x-direction; F_{dx}, F_{dy} and F_{dxy} are the streamwise, spanwise and total horizontal drag forces acting on the exposed part of the shell; C_{dx}^{MEAN} and C_{dx}^{RMS} are the mean streamwise drag coefficient and the root mean square of the streamwise drag coefficient, respectively.

h/H	d_{50}/H	$VR = U_{ex}/U_0$	L_R/h	A_x/H^2	$F_{dx}/\rho U_0^2 H^2$	$F_{dy}/\rho U_0^2 H^2$	$F_{dxy}/\rho U_0^2 H^2$	C_{dx}^{MEAN}	C_{dx}^{RMS}
(-)	(-)	(-)	(-)	(-)	(-)	(-)	(-)	(-)	(-)
0.48	0.062	0	2.3	0.131	0.0105	0.0016	0.0106	0.160	0.013
0.38	0.062	0	2.6	0.096	0.0057	0.0004	0.0057	0.119	0.019
0.28	0.062	0	3.2	0.050	0.0024	0.0003	0.0025	0.097	0.019
0.48	0.049	0	2.3	0.131	0.0102	0.0012	0.0103	0.155	0.007
0.48	0.000	0	2.7	0.131	0.0099	0.0007	0.0100	0.152	0.007
0.48	0.062	0.61	2.4	0.131	0.0113	0.0026	0.0116	0.172	0.015
0.38	0.062	0.61	2.6	0.096	0.0064	0.0024	0.0069	0.135	0.026
0.28	0.062	0.61	3.2	0.050	0.0028	0.0012	0.0031	0.113	0.023
0.48	0.049	0.61	2.4	0.131	0.0111	0.0015	0.0112	0.169	0.007
0.48	0.000	0.61	2.9	0.131	0.0107	0.0008	0.0107	0.163	0.009
0.48	0.062	1.22	2.5	0.131	0.0094	0.0027	0.0098	0.143	0.016
0.38	0.062	1.22	2.9	0.096	0.0043	0.0017	0.0047	0.091	0.010
0.28	0.062	1.22	3.6	0.050	0.0015	0.0008	0.0017	0.060	0.022
0.48	0.049	1.22	2.7	0.131	0.0092	0.0021	0.0095	0.141	0.007
0.48	0.000	1.22	3.1	0.131	0.0086	0.0012	0.0087	0.132	0.007

Freshwater mussels generally live in water bodies with flow depths ranging from some tens of centimetres to couple of meters. Based on this information, and considering the typical size and burial ratio of mussel, mussels do not place themselves in very shallow water, which motivates the fact that the test cases discussed in the present Section, and included in Table 3-1, consider a relatively high submergence (i.e., $D/h > 4$).

Though the submergence ratio D/h is among the key parameters when studying flow around submerged obstacles (Hajimirzaie et al., 2012; Papanicolaou et al., 2018; Singh et al., 2019), Shamloo et al. (2001) observed that in case of submergence ratios $D/h > 4$ the interactions between the water surface and the wake are negligible. According to this, the rigid lid approximation has been assumed for the set-up of the numerical model (Sect. 3.2.3). Cases with low submergence ratios (e.g., $D/h < 1.5$), instead, are characterized by a more complex flow physics, with strong obstacle-free surface interactions (Lacey and Rennie, 2012; Sadeque et al., 2009, 2008), which requires a numerical model with a deformable free surface (e.g., the Volume of Fluid two-phase scheme). Given the fact that these cases are less relevant for mussels in natural streams, the present study refers to cases with relatively large submergence.

In any case, to evaluate the effect of varying the submergence, additional simulations were performed with a lower flow depth ($D = 0.069$ m, $D/h = 2.9$) for three different values of VR (i.e., 0.00, 0.61 and 1.22), maintaining constant the burial level ($h/H = 0.48$) and the bed roughness ($d_{50}/H = 0.062$). Results of simulations performed with $D = 0.069$ m and $D = 0.103$ m showed negligible differences, thus simulations conducted with $D = 0.069$ m are not included in Table 3-1 and Table 3-2 for brevity.

3.3.2 Mean Flow and Turbulent Kinetic Energy

Flow over an isolated mussel represents a particular case of flow past submerged, surface-mounted obstacle. Accordingly, a recirculation region forms at the back of the mussel, and the flow passing above the top of the mussel descents to the bed downstream of its shell. To measure the length of the recirculation region, the point in which the flow reattaches to the bed is determined by considering the adjacent cells with opposite velocity. The streamwise distance measured from the centre of the exhaling siphon to this point is labelled L_R. A visual representation of the recirculation length L_R is provided in Figure 3-5a for the $h/H = 0.48$, $d_{50}/H = 0$, $VR = 0$ case, where the recirculation bubble is highlighted by means of the 2-D streamlines in the $y/H = 0$ vertical plane.

The distributions in Figure 3-5 also allow to evaluate the differences in the streamwise velocity whether the bed is smooth (Figure 3-5a,b) or rough (Figure 3-5c,d). Particularly, in the near bed region gravel particles reduce the streamwise velocity, which is expected to influence the flow approaching the mussel and to affect the adverse pressure gradients in the frontal part of the shell. Adverse pressure gradients are in turn connected with the possible formation of a horseshoe vortex at the junction line between the shell and the bed surface. The thickness of this reduced-velocity region is larger upstream the mussel, but becomes almost negligible in the wake, where low values of velocity are observed only in between bed particles. The distributions in Figure 3-5 also

allow to evaluate the influence of the active filtering (Figure 3-5b,d, for $VR = 0.61$). The main effect is the presence of a jet of water injected vertically in the surrounding flow from the upper part of the mussel. The jet realigns with the incoming flow downstream the shell, at a distance from the excurrent siphon. The dynamics of the excurrent jet are important as they affect the transport of nutrients and organic matter in the surrounding environment. For $VR < 1$ water in the jet has a lower velocity compared to the surrounding flow, such that the region of reduced streamwise velocities becomes thicker with increasing VR (e.g., compare cases with $VR = 0$ in Figure 3-5a,c and $VR = 0.61$ in Figure 3-5b,d). The excurrent jets develop above the top of the mussels and they are marginally affected by the bed roughness. The comparison between Figure 3-5b and Figure 3-5d shows that the jets develop almost independently of d_{50}/H.

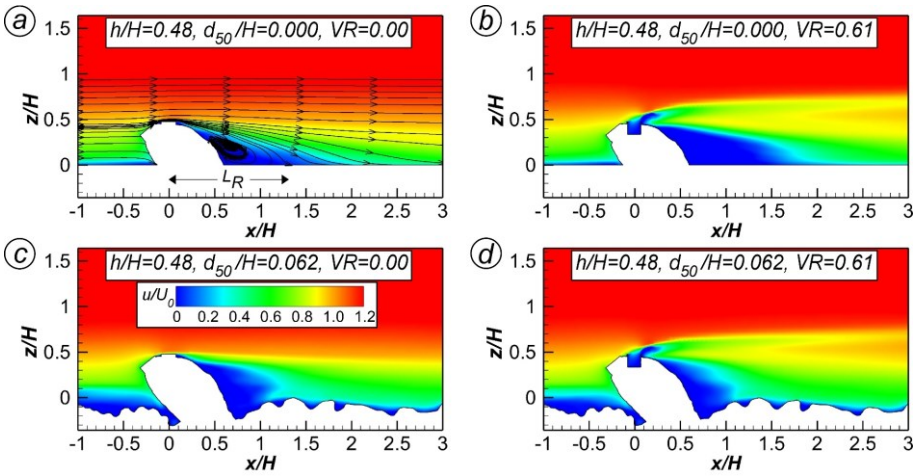

Figure 3-5. Mean streamwise velocity, u/U_0, in the $y/H = 0$ plane for different simulations (a-d). L_R denotes the maximum streamwise length of the mean-flow recirculation region based on 2-D streamline patterns.

Recirculation regions in the wake are observed in all the simulations, though the size of these regions, as measured by the streamwise length L_R (Figure 3-5), is different depending on the controlling parameters here analysed. Figure 3-6 visualizes the length of the recirculation region as a function of the main parameters investigated in the study (i.e., bed roughness, velocity ratio, and exposed height of the shell). As the size of the recirculation region depends on the height of the emerged part of the shell, as observed in previous studies with canonical submerged obstacles, L_R is non dimensionalized through the emerged height, h. The length of the recirculation region decreases with the bed roughness (Figure 3-6a), as L_R is strongly reduced in the simulations with $d_{50}/H = 0.062$ and $d_{50}/H = 0.042$. Compared to the case of a smooth bed, L_R decreases of about 25% in case of a rough bed. This can be explained by the enhanced turbulent dissipation in the wake induced by the interactions among the flow and the irregular bed surface. This effect has been observed independently of the filtering activity of the mussel. Figure 3-6b shows the effect of the filtering activity on the length of the

recirculation region. As expected, L_R increases when increasing VR, because the jet increases the thickness of the region with reduced velocity. Though the rate of increasing decrease with increasing bed roughness, differences in the value of L_R are generally modest (e.g., L_R increase of 10-15% when passing from $VR = 0.61$ to $VR = 1.22$). As mentioned, the most important parameter controlling the length of the recirculation region is the height of the exposed part of the shell, h. As expected, when increasing h/H, L_R increases. However, L_R/h decreases with a rate that is fairly independent of the value of VR, as shown in Figure 3-6c for the cases with $d_{50}/H = 0.062$. This trend is in agreement with the findings of Wu et al. (2020) for an isolated mussel (*L. Siliquoidea*) placed on a smooth bed.

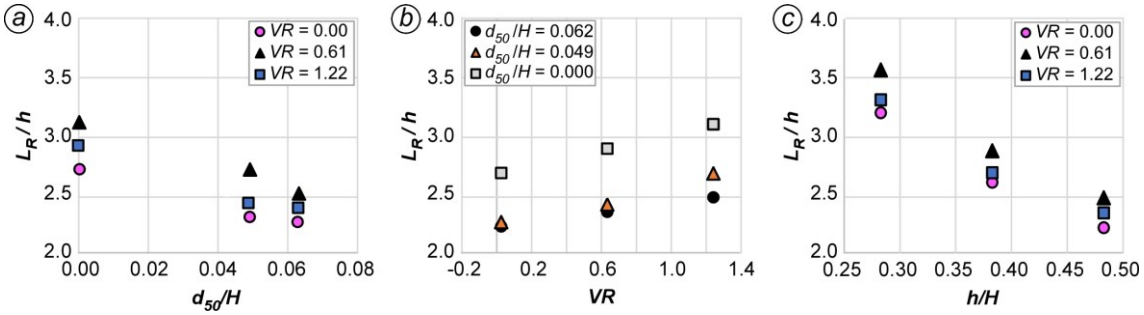

Figure 3-6. Nondimensional length of the recirculation region, L_R/h, (see Figure 3-5a) as a function of a) the bed roughness, d_{50}/H (for different values of VR, and $h/H = 0.48$), b) the exhaling velocity ratio, VR (for different values of d_{50}/H, and $h/H = 0.48$), c) the mussel burrowing level, h/H (for different values of VR, and $d_{50}/H = 0.062$).

The adverse pressure gradient at the front of the mussel induces a strong downflow which in turn may generate a horseshoe vortex to form at the junction line between the mussel and the bed. The formation of an horseshoe vortex was observed for the case of the *L. Siliquoidea* considered in the study of Wu et al. (2020). In the present case, which refers to the shape of a *Unio Elongatulus* mussel, no horseshoe vortices are observed to form at the upstream face of the mussel in the smooth-bed simulations (Figure 3-7a,b). The difference can be explained by the different shape of the two mussels (the *Unio Elongatulus* has a more streamlined shape), and by the inclination of the mayor axis of the *Unio Elongatulus*. The geometry and the anchoring of the shell are then of great importance for the formation of vortical structures near the mussels. Compared to the case of the *L. Siliquoidea* considered by Wu et al. (2020), the shape and the inclination of the *Unio Elongatulus* suppress the formation of horseshoe vortices, and, in turn, one of the main mechanism for local bed erosion around the shell is dampened.

Horseshoe vortices are suppressed also in the case of a gravel bed. Though in this case the sheet of main vorticity is observed above the bed because of the presence of large bed particles upstream the mussel (Figure 3-7c,d), closer inspections of the flow field show no horseshoe vortices form (see also Sect. 3.3.3).

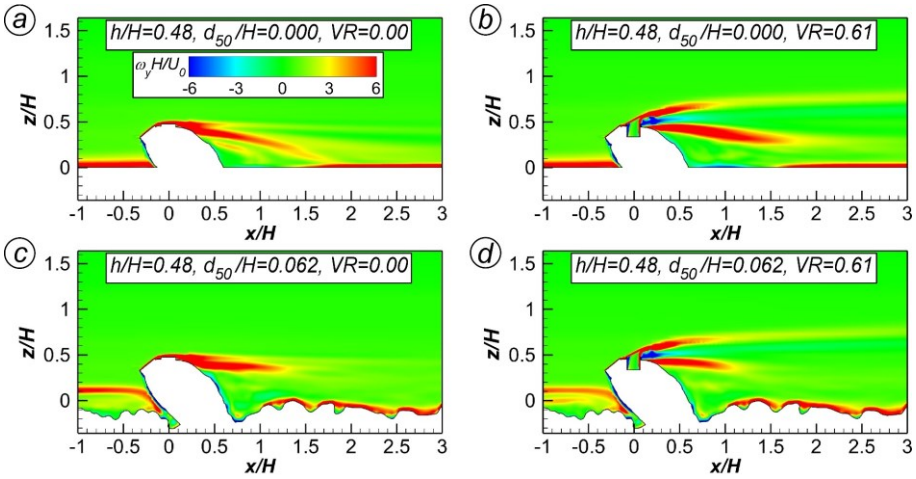

Figure 3-7. Mean flow spanwise vorticity, $\omega_y H/U_0$, in the $y/H = 0$ plane for different simulations (a-d).

Another important effect of the bed roughness is that the length of the separated shear layer forming at the top of the mussel is reduced. This is a clear effect of the bed roughness, as eddies induced by bed particles interfere with the wake downstream the mussel. This result agrees with the decrease of the recirculation length L_R when increasing d_{50}/H (Figure 3-5). The inclination of the sheet of high vorticity at the top of the shear layer also differs depending on the bed roughness, as the tilt is reduced in simulations with $d_{50}/H = 0.062$. This is another consequence of bed roughness.

In the simulations with the active filtering on, besides the shear layer forming at the top of the mussel, a second shear layer is observed above the excurrent siphon. It forms because of the interaction between the exhaled jet and the outer flow moving over the mussel.

The suppression of the horseshoe vortices in the case of the *Unio Elongatulus* shell is confirmed by the *TKE* distributions in Figure 3-8. In the smooth bed simulations (Figure 3-8a-c) no amplifications of *TKE* are observed at the upstream face of the mussel. Some turbulent amplifications in this region are observed in case of a rough bed (Figure 3-8d-i), which is consistent with the presence of the vorticity sheet forming above the bed because of large bed particles. These amplifications are independent of the mussel burial level and on the exhaling velocity ratio. This suggests that the amplifications of *TKE* in the frontal part of the shell may be the consequence of large-scale turbulence originated because of the presence of a gravel bed, rather than being related to the generation of horseshoe vortices because of the mussel shell.

Amplifications of *TKE* are observed in the wake downstream the mussel for all the cases. *TKE* values observed in the smooth bed cases are relatively low, especially with no active filtering (Figure 3-8a).Comparing results of simulations with a flat bed with the results obtained by Wu et al. (2020) in their corresponding simulations, amplifications of *TKE* in case of a *Unio Elongatulus* are about one order of magnitude lower. This is a result of the different shape and orientation of the mussels used in the

two studies. The *Unio Elongatulus* mussel has a more streamlined shape and, in this case, the anti-symmetric vortex shedding mode is suppressed (see Sect 3.3.5), as opposed to the case of the *L. Siliquoidea* where this was identified as one of the main responsible of the amplification of *TKE* in the wake. In the simulations with active filtering, the excurrent jet induces wake vortices to form, and anti-symmetric shedding is observed at times. This increases the levels of *TKE* in the wake (Figure 3-8b-c), though values are observed to be roughly 50% of those observed by Wu et al. (2020) for similar values of h/H and *VR*, as a consequence of the shape of the mussel. When the active filtering is on, further regions of high *TKE* form above the excurrent-siphons, due to the instabilities generated from the interaction of the jet with the surrounding flow.

In case of a gravel bed, and for the same burial level (Figure 3-8d-f), amplifications of *TKE* are larger compared to the case of a smooth bed. For $h/H = 0.48$, the *TKE* values in the wake downstream the mussel for cases with $d_{50}/H = 0.062$ are roughly two times those observed in the cases with $d_{50}/H = 0.000$ (e.g., compare cases in Figure 3-8a-c and Figure 3-8d-f). This is consistent with the antisymmetric vortex shedding mode becoming dominant when increasing the bed roughness (see Sect. 3.3.5). As observed for the smooth bed simulations, even in the case of a gravel bed, for $VR \geq 0.00$ amplifications of *TKE* are generally larger and a second region of high *TKE* forms at the excurrent jet (Figure 3-8e,f).

When increasing the burial level (i.e., for decreasing h/H) in the simulations performed on a gravel bed, the *TKE* amplifications in the wake decrease (compare Figure 3-8d-f and Figure 3-8g-i). This is consistent with the reduced emerged part of the shell. When h decreases, and approaches d_{50}, the exposed part of the shell also decreases and the effect of the mussel becomes similar to that of the other bed particles.

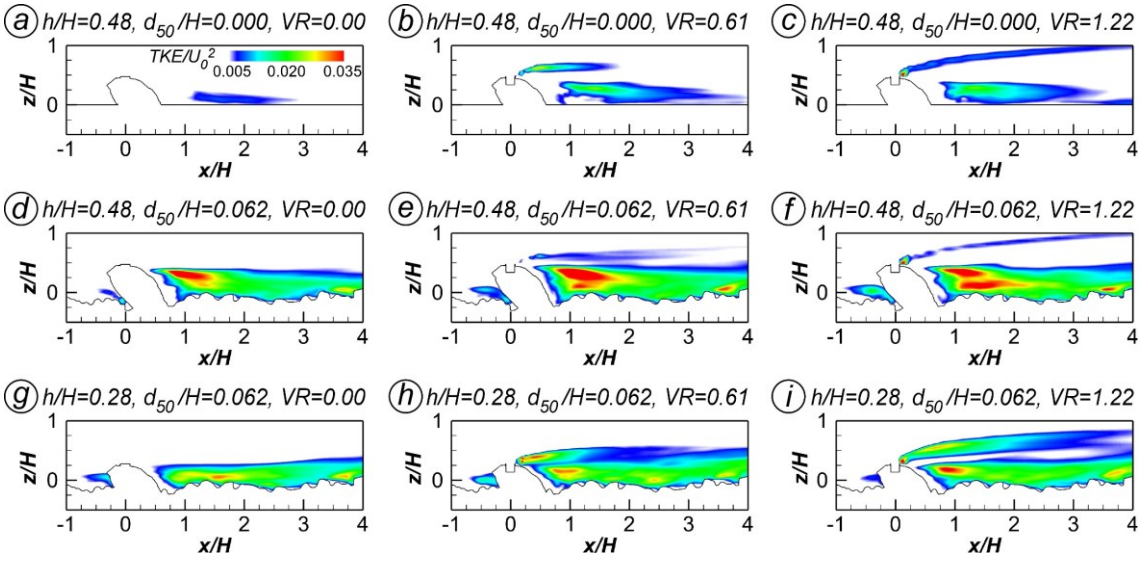

Figure 3-8. Turbulent kinetic energy, TKE/U_0^2, in the $y/H = 0$ plane for different simulations (a-i). Values lower than 0.007 were blanked.

3.3.3 Main Vortical Structures Generated Around the Mussel

Large-scale coherent structures are visualized by means of the Q criterion in Figure 3-9 for some of the test cases included in Table 3-1 considering instantaneous and mean flow fields. These visualizations further confirm that no horseshoe vortices form in the frontal part of the mussel, regardless of the filtering activity of the mussel, as observed from the vorticity and *TKE* distributions in the symmetry plane of the shell (Figure 3-7 and Figure 3-8). Any doubt about the formation of horseshoe vortices at the junction line between the shell and the bed is clarified by Figure 3-10, which pictures the 2-D mean streamline patterns in a vertical plane inclined respect to the symmetry plane $y/H = 0$.

As mentioned, this differ from the case of the *L. Siliquoidea* used by Wu et al. (2020), in which the formation of horseshoe vortices was observed in the mean and instantaneous flow fields. This difference can be explained by the lower degree of bluntness of the *Unio Elongatulus* mussel part of the present study, and by its larger inclination respect to the incoming flow. Both these factors contribute in weakening the downflow forming at the frontal face of the mussel, as confirmed by streamlines in Figure 3-10. As the formation and the coherence of the horseshoe vortices have been shown to depend on the strength of the downflow (Kirkil and Constantinescu, 2009; McCoy et al., 2007), the absence of the horseshoe vortices is a direct consequence of the suppression of the downflow.

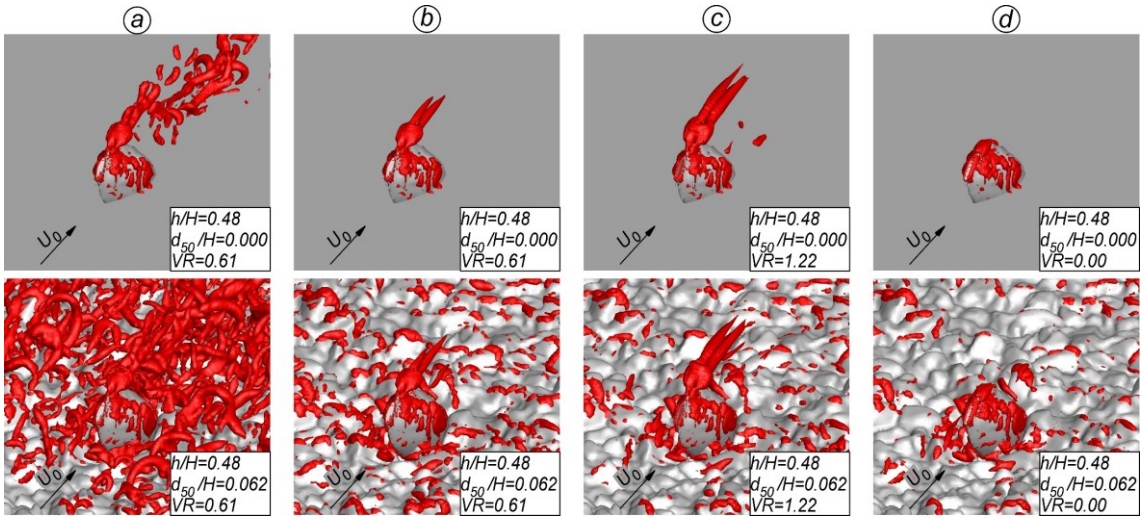

Figure 3-9. Coherent structures visualized using the Q criterion. a) instantaneous flow, $h/H = 0.48$, $VR = 0.61$ simulations with $d_{50}/H = 0$ and 0.062; b) mean flow, $h/H = 0.48$, $VR = 0.61$ simulations with $d_{50}/H = 0$ and 0.062; c) mean flow, $h/H = 0.48$, $VR = 1.22$ simulations with $d_{50}/H = 0$ and 0.062; d) mean flow, $h/H = 0.48$, $VR = 0.00$ simulations with $d_{50}/H = 0$ and 0.062.

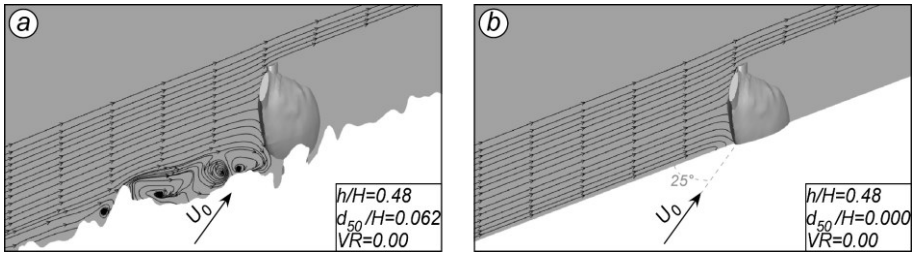

Figure 3-10. Mean flow, 2-D streamline patterns in a vertical plane making a 25° angle with the $y/H = 0$ plane in the $h/H = 0.48$, $VR = 0.00$ simulations with $d_{50}/H = 0.062$ (a) and $d_{50}/H = 0.000$ (b).

Visualizations of mean and instantaneous flow fields in Figure 3-9 confirm that no clear horseshoe vortices form even in the case of a grave bed. In this case, the flow field in front of the mussel is disturbed by the presence of the bed particles. Though 2-D streamline patterns in the vertical section of Figure 3-10a may suggest the presence of a circulation in this plane, the irregular distribution of the streamlines is to be attributed to bed particles and not to the formation of a horseshoe vortex, as confirmed by the Q criterion visualizations in Figure 3-9 and by the vorticity and TKE distributions included in Section 3.3.2. Eddies forming due to bed particles, even close to the junction line between the bed and the mussel shell, are generated by flow separation at the larger particles composing the bed. In particular eddies forming at the frontal part of the shell are enhanced by the adverse pressure gradients and by the (weak) downflow induced by the shell, however they do not extend around the shell and thus they can not be considered as horseshoe vortices.

Figure 3-9 shows also that a pair of close-to-symmetric vortices forms in simulations conducted considering the active filtering of the mussel. These vortices are originated at the excurrent siphon and they are observed to form independently of the bed roughness. These vortices depend on the filtering discharge, as they are not observed to form if $VR = 0.0$, and their coherence increases with increasing VR. For this reason, the generation of these vortices is strongly connected with the dynamics of the excurrent jet. These vortices differ from the pair of counter-rotating vortices forming near the bed surface in the smooth-bed simulations conducted by Wu et al. (2020), which are induced by the presence of the submerged shell. Instead, the vortices noticed in Figure 3-9 for the cases with active filtering should be compared with the second pair of base vortices observed by Wu et al. (2020), forming at an elevation close to the excurrent siphon for the simulations conducted with $VR = 0.7$. One difference between the present case and the results of Wu et al. (2020) is the symmetry of these pairs of vortices. While in the present study the vortices remain symmetrical at high streamwise distance, in the case of Wu et al. (2020), for similar level of burrowing as in the cases pictured in Figure 3-9, only one of these vortices was observed away from the mussel because of the larger asymmetry of the emerged part of the shell. However, for higher levels of mussel burrowing, Wu et al. (2020) observed that the coherence of these vortices becomes similar, as noticed in the case of the in the *Unio Elongatulus* mussel considered in the present study.

The *Q* criterion visualizations in the instantaneous flow provide further insight on the dynamics of these vortices (Figure 3-9a). In the mean flow visualizations the cores of the two vortices are fairly straight and symmetric (Figure 3-9b), suggesting that the vortices may be relatively steady in time. However, this is contradicted by the inspection of the instantaneous flow field (Figure 3-9a), in which a large-scale instability is observed to propagate along the cores of the two vortices. Because of this unsteadiness, the cores of the two vortices move such that they may touch at times. These mutual interactions enhance the dissipation of the vortices such that they break-up and they lose their coherence at a streamwise location. Though the two vortices are clearly visible in the simulations conducted on a gravel bed (Figure 3-9), the streamwise length of the two legs is generally reduced. This happens because the eddies generated by the bed particles may be advected to the upper part of the water column, thus also interacting with the cores of the excurrent jet vortices, further dampening their strength. This effect is expected to be increased for increasing roughness, or, alternatively, for increasing the burial of the mussel, as the excurrent jet gets closer to the bed.

Though Wu et al. (2020) observed the formation of counter-rotating vortices forming near the bed surface in the smooth-bed simulations, *Q* criterion visualizations in Figure 3-9 do not provide any evidence of the eventual formation of such vortices. However, closer inspections of the flow fields highlight that such vortices form in all the simulation with the *Unio Elongatulus* mussel, as demonstrated by the mean streamwise-vorticity distribution in Figure 3-11, which refer to $x/H = 1$ and $x/H = 3$ cross sections and include the 2-D streamline patterns in these planes.

Figure 3-11a represents the case of the simulation with no active filtering and with the flat bed. In this case a pair of vortices is observed in the wake. The slight asymmetry is motivated by the fact that the real shape of the shell is used in the present study, with the two valves being not exactly symmetrical respect to the central axis. The flow is advected in between the vortices cores toward the bed, hence they are tip vortices. Pair of similar tip vortices has been already observed to form at the bed in case of submerged semi-ellipsoids mounted on a smooth bed (Hajimirzaie et al., 2012; Hajimirzaie and Buchholz, 2013). As observed in the present simulations, these vortices are relatively symmetrical, and their coherence remains comparable with the streamwise distance, until they dissipate. The presence of tip vortices at the back of the mussel contrasts with results of Wu et al. (2020), who observed base vortices to form. The difference can be attributed to the shape of the emerged part of the shell, and it is a further confirmation that the shape of the mussel controls the turbulent structures forming in the flow at the organism level.

In case of active filtering (e.g., $VR = 0.61$) and a smooth bed (Figure 3-11b), still the pair of near-bed tip vortices is observed to form. In addition, a pair of vortices situated slightly above the top of the mussel forms because of the excurrent jet, as observed previously by the analysis of *Q* visualizations in Figure 3-9. As flow is advected downward in between their cores, these are base vortices. While the tip vortices in the vicinity of the bed are among the main responsible of a strong downflow at the symmetry plane, which also influence the shedding mode in the wake, as clarified in

Sect. 3.3.4, the base vortices are of influence for the excurrent jet fluid with a role in the mixing between the jet and the surrounding flow.

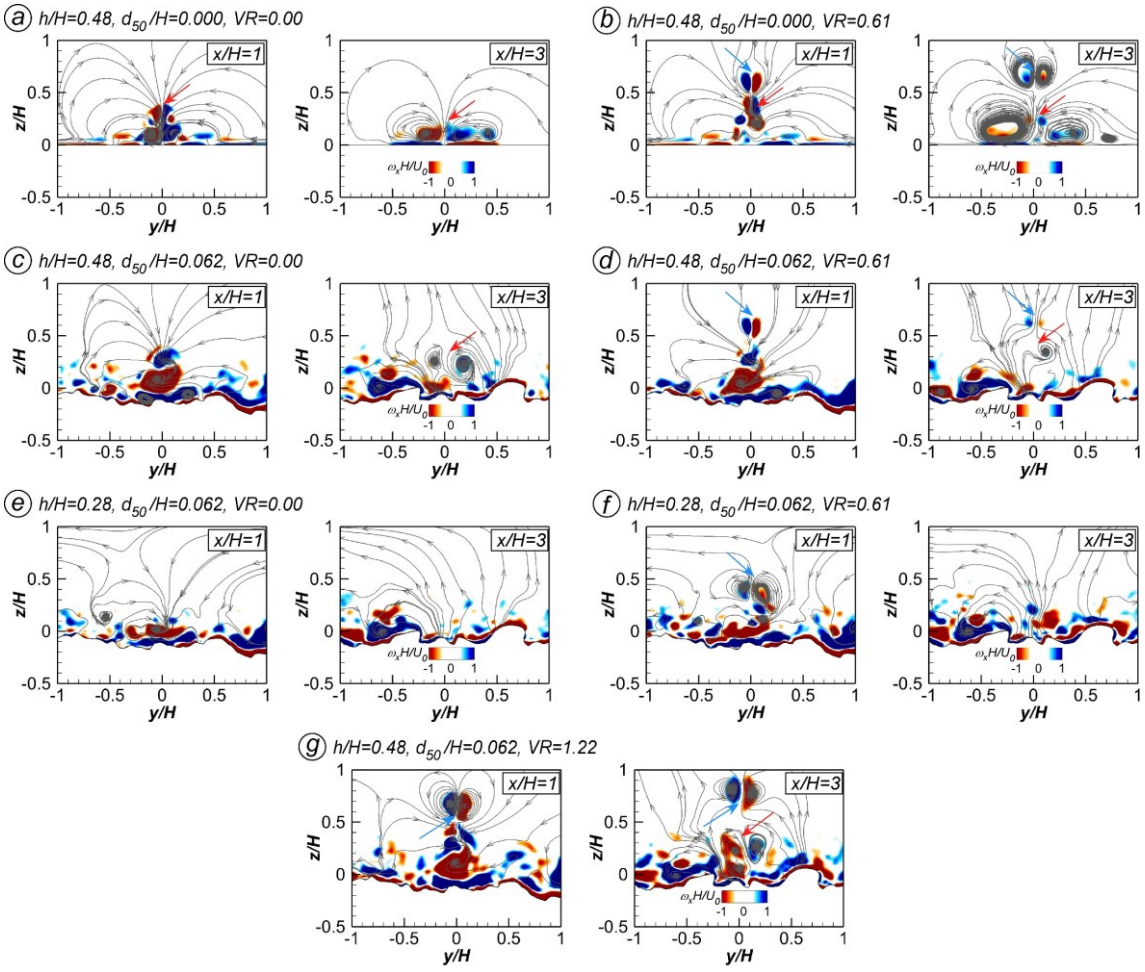

Figure 3-11. Mean flow streamwise vorticity, $\omega_x H/U_0$ (values between −0.5 and 0.5 were blanked), and 2-D mean streamline patterns in the $x/H = 1$ and $x/H = 3$ planes for different simulations (a-g). The red arrows point toward the tip vortices (downwash flow). The blue arrows point toward the base vortices (upwash flow).

The bed roughness in the gravel bed simulations strongly modifies the symmetry of the aforementioned vortices. Though the formation of tip and base vortices is still observed in cases with $d_{50}/h = 0.062$ (e.g., see Figure 3-11c and Figure 3-11d), the degree of symmetry and the coherence of these vortices strongly decrease with respect to the corresponding smooth bed cases. This effect is already visible in the $x/H = 1$ cross-section, but it is furtherly confirmed by results in the $x/H = 3$ planes, in which the pair of vortices becomes hardly visible because of the loss of coherence. This is particularly clear in case of active filtering, as the jet further tends to dampen the coherence of the tip vortices forming at the bed. This is clarified by Figure 3-11d, in which the tip vortices are not observed in the $x/H = 3$ section. The reduction of the symmetry and the loss of

coherence are mainly induced by the interactions of the pair of vortices with the irregular bed surface, and with turbulent eddies generated by the larger bed particles. As a main consequence, the downwelling flows at the symmetry plane are expected to decrease with the roughness.

Though tip vortices near the bed are strongly deformed in simulations with $d_{50}/h = 0.062$, the effect of the roughness is less relevant on the base vortices developing above the excurrent siphon. Being the burrowing ratio relatively low (i.e., $h/D = 0.48$ in Figure 3-11a-d), the excurrent jet and the associated base vortices are situated relatively far from the bed, thus being less affected by the irregular gravel surface. Near the mussel (e.g., $x/H = 1$ section), the base vortices are similar either the bed is smooth or rough. Instead, at larger distances (e.g., $x/H = 3$ section), the cores of the two vortices are not anymore symmetric with respect to the $y/H = 0$ plane in the rough bed cases. A quantitative measure of the effect of the roughness on the base vortices forming at the excurrent siphon jet is provided by the total circulation magnitude Γ_T. Figure 3-12 shows the non-dimensional total circulation $\Gamma_T/(U_0H)$ as a function of x/H. The circulation magnitude, Γ_T, is calculated by integrating the streamwise vorticity, ω_x, in cross-stream (x = constant). The threshold value used to perform the integration over the cores of the vortices is $|\omega_x H/U_0| = 0.3$. The effect of the bed roughness is small for low x/H (i.e., $x/H < 1$) as seen in Figure 3-12a. However, at larger x/H the total circulation decreases faster for higher values of d_{50}/H, because of the interactions among the turbulence induced by the bed and the excurrent siphon jet.

For a constant level of mussel burrowing and a constant bed roughness, the rate of decay of the total circulation decreases when increasing VR. The higher coherence of the vortices for $VR = 1.22$ is motivated by the fact that the jet has a higher initial momentum, such that it penetrates to higher elevations before realigning with the incoming velocity. The base vortices develop at a higher distance from the bed, and they felt less the effect of the turbulence generated at the rough bottom. The increased coherence of the vortices for the higher value of exhaled discharge can be observed also comparing Q visualization in Figure 3-9b,c, and the vorticity distributions in the $x/H = 3$ sections of Figure 3-11. While these base vortices are not visible anymore for the case with $VR = 0.61$ (Figure 3-11d), they are still clearly visible in the case with $VR = 1.22$ (Figure 3-11g).

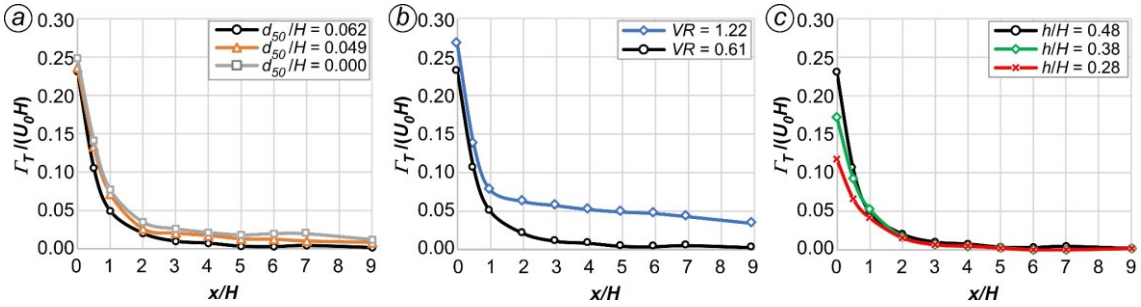

Figure 3-12. Streamwise variation of the total circulation magnitude of the base vortices, $\Gamma_T/(U_0H)$. a) effect of d_{50}/H ($VR = 0.61$, $h/H = 0.48$); effect of VR ($d_{50}/H = 0.062$, $h/H = 0.48$); c) effect of h/H ($d_{50}/H = 0.062$, $VR = 0.61$).

The comparison of Figure 3-11e and Figure 3-11f allows to evaluate how varying the degree of mussel burial affects the dynamics of the base and tip vortices developing at the back of the mussels. When the exposed part of the shell decreases, the tip vortices forming near the bed are expected to be less strong. This is further exacerbated in the case of a rough bed surface because the interactions with the vortices forming at the bed are stronger. Considering the $h/H = 0.28$, $d_{50}/H = 0.062$ simulation (Figure 3-11e), tip vortices are strongly deformed at $x/H = 1$ and are destroyed before reaching the $x/H = 3$ section, where they are not visible. This differs from the correspondent case with $h/H = 0.48$ in which vortices are still visible in the $x/H = 3$ plane (Figure 3-11c, see the red arrow). As observed for the simulations with $h/H = 0.48$, the symmetry and the coherence of tip vortices are generally further dampened in case of active filtering. This is true also in the $h/H = 0.28$ simulation of Figure 3-11f, where tip vortices are destroyed already in the $x/H = 1$ section (compare to the corresponding simulation with $h/H = 0.48$ in Figure 3-11d). The effect of the exposed height h/H in the coherence of the base vortices is evident especially at low values of x/H (Figure 3-12c), where the total magnitude of Γ_T decreases strongly in cases with lower values with h/H because the trajectory of the bed approaches the bottom and the tip vortices induced by the excurrent jet are dampened more strongly by the near-bed turbulence. For higher values of h/H, however, difference becomes negligible, as Γ_T is fairly independent of the values of h/H.

3.3.4 Near-Wake Flow

For the case of a *L. Siliquoidea* over a smooth bed, a pair of base (upwashing) vortices forms at the back of the mussel (Wu et al., 2020). Accordingly, a region of strong upwelling flow is observed downstream the mussel in the symmetry axis ($y/H = 0$ plane) between the cores of the two vortices. At the sides of this region, two larger regions of downwelling flow are induced by the outer part of the vortices. Fluid is here advected to the bed, which explain why larger values of bed shear stresses were observed at the sides of the wake forming at the back of the mussel. Wu et al. (2020) also observed that these regions are close to symmetric for higher levels of mussel burrowing ($h/H \approx 0.25$), when the coherence of the base vortices was comparable. Instead, for relatively low levels of mussel burial ($h/H \approx 0.5$), the coherence of the left-hand-side vortex was larger, as well as the region of downwelling flow in this part of the mussel. This has been attributed to the asymmetry of the shell. For this reason, the shape and the symmetry of the shell are expected to control the near-wake flow. As the *Unio Elongatulus* mussel part of the present study has a different shape and orientation with respect to the *L. Siliquoidea* considered by Wu et al. (2020), differences are expected among the two cases.

In the simulations conducted with a flat bed and with no filtering discharge, a pair of tip (downwashing) vortices has been shown to form at the back of the mussel. The coherence of these vortices is comparable at large distances from the mussel. More importantly, the tip vortices induce a region of strong flow downwelling near the symmetry axis ($y/H = 0$), as pictured in Figure 3-13a for the $h/H = 0.48$, $d_{50}/H = 0$, $VR = 0$ simulation. This is one of the main differences with the case of the *L. Siliquoidea*, in which the base vortices induce an upwelling region to form in the symmetry plane. At the sides

of the shell, two regions of upwelling flow form because the downflow at the front of the mussel reaches the bed surface, and it is diverted laterally and advected upwards by two sides of the mussel. Two other regions of upwelling flow are observed immediately at the back of the mussel, at opposite sides respect to the symmetry axis. The slight asymmetry of the flow regions on opposite sides of the mussels derives from the realistic shape of the mussel, where the two valves are not exactly symmetric respect to the central axis.

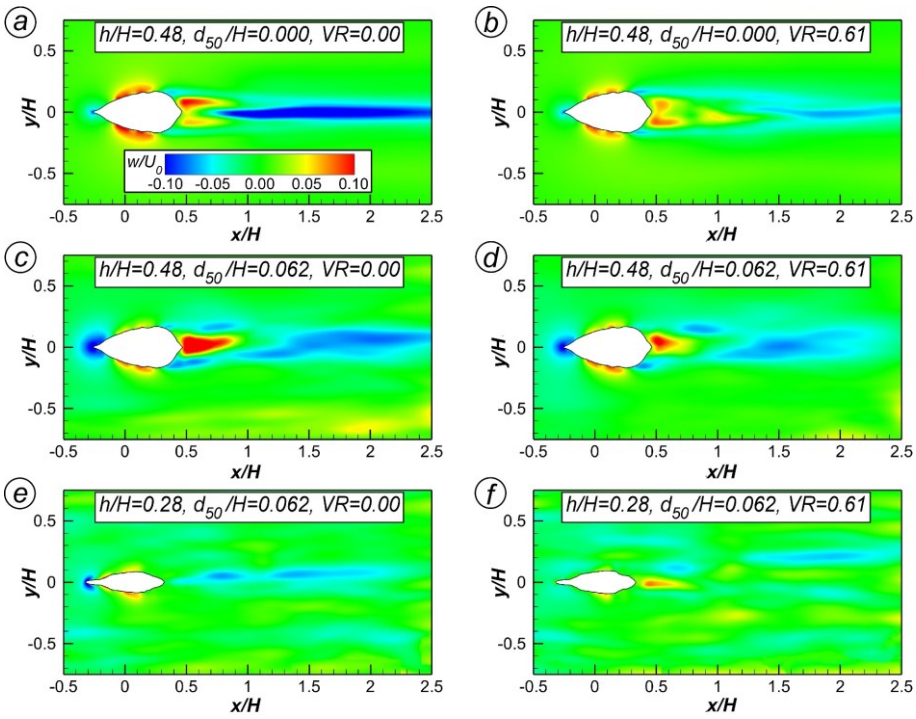

Figure 3-13. Mean vertical velocity, w/U_0, in the horizontal plane $z/H = 0.5$ for different simulations (a-f).

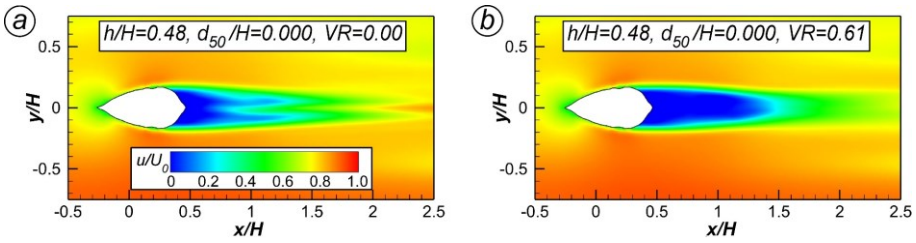

Figure 3-14. Mean streamwise velocity, u/U_0, in the horizontal plane $z/H = 0.5$ for different simulations (a,b).

The strong downflow observed downstream of the shell in the simulation with no filtering activity and with a smooth bed strongly affects the wake forming at the back of the *Unio Elongatulus* mussel. This effect is also highlighted by the distributions of the

streamwise velocity in a horizontal plane ($z/H = 0.5$) pictured in Figure 3-14 with the exhaling velocity ratio VR equal to either 0 and 0.61. In the $VR = 0$ simulation (Figure 3-14a), the recirculation region (i.e., with $u/U_0 \leq 0$) shows a relatively unusual shape, with two elongated regions of low velocity at the back of the mussel. In between them, a region of relatively high velocity flow forms. This happens because of the strong downflow in the symmetry plane, and because, as discussed later in the text, the symmetric shedding mode prevents the flow to recirculate between the two sides at the opposite part with respect to the central axis.

In the $VR = 0.61$ simulation (Figure 3-14b), instead, the shape of the recirculating region is similar to those typically observed past submerged obstacles, in which two vertical vortices are observed at the sides of the recirculation region. These vortices are the legs of the *U*-shaped vortices forming at the back of the submerged body, that border the region of recirculating flow (Chang et al., 2020).

In the rough-bed cases tip vortices are still present near the bed at the back of the shell. However, as highlighted in Section 3.3.2, they are situated further away from the bed and their symmetry is broken because of the irregular bed surface. For this reason, the main region of flow downwelling breaks into multiple asymmetrical subregions. The effect of the tip vortices on the vertical velocity at the back of the mussel is reduced and the strength of the downwelling flow in the symmetry plane is also reduced if compared to the corresponding cases with a flat bed (Figure 3-13c-d). In rough bed simulations, differently from the smooth bed cases, at the frontal side of the mussel a region of downflow is observed, while a small region of strong upwelling flow also forms at the back of the mussel.

As noticed in the smooth bed simulations, the effect of the active filtering is to dampen the downwelling flows and to reduce the symmetry of the regions with relevant vertical velocities forming inside the near wake. This is confirmed also in the simulations conducted with $d_{50}/H = 0.062$ (compare Figure 3-13c and Figure 3-13d).

The level of mussel burial also affects the downflows at the back of the mussel. When the height, h, of the exposed part of the mussel decreases, the upwelling and downwelling flows in the wake are weakened (e.g., compare the cases with $h/H = 0.48$ in Figure 3-13c-d and those with $h/H = 0.28$ in Figure 3-13e-f). This result is expected given that the recirculation region has a reduced length (Figure 3-6c) and the tip vortices in the simulations with $h/H = 0.28$ lose their coherence immediately downstream the shell (Figure 3-11e-f). When decreasing h, the downflow in front of the mussel is also reduced because of the reduced strength of the adverse pressure gradient (e.g. compare Figure 3-13c-d, with $h/H = 0.48$ cases, and Figure 3-13e-f with $h/H = 0.28$ cases).

3.3.5 Vortex Shedding

In the case with smooth, flat bed with $VR = 0$ the symmetric shedding mode dominates and the interactions between the separated shear layers (SSLs) are strongly dampened because of the downwelling flow in between them (Figure 3-15a). The secondary flow generated by the region of flow downwelling maintains the SSLs far

from the symmetry plane, and impedes the natural oscillations of the two legs. As the secondary flow reaches the SSLs, it starts moving away from the bed. This explains the two elongated patches of vorticity forming in between the symmetry plane and the two separated shear layers in Figure 3-15a. Sometimes, the SSLs are disturbed on one side by the detachment and the shedding of patches of vorticity from their legs (e.g., see right frame in Figure 3-15a), but this condition can not be identified as an antisymmetric shedding mode. This differs from the results of Wu et al. (2020), who showed that for a *L. Siliquoidea* mussel with a similar level of burial, and placed on a smooth bed, the antisymmetric mode was the dominant one. For this reason, the shape of the shell can be identified as one of the key parameters in controlling the type and the coherence of the vortices forming in the wake, which in turn determines the dominant shedding mode in the wake.

Increasing the bed roughness up to $d_{50}/H = 0.049$ (not shown here), the wake shedding is similar to the smooth bed case: a symmetric shedding mode is observed with no interactions between SSLs because of flow downwelling, and with some waviness in both SSLs at times. For the rough bed with $d_{50}/H = 0.062$ and $VR = 0$, still the symmetric mode dominates, but for only 70% of the time, while a clear antisymmetric mode can be identified otherwise (Figure 3-15b). Hence, when increasing the bed roughness, the symmetric wake shedding mode weakens, as well as the secondary flow moving toward the two SSLs. As a consequence, the antisymmetric wake shedding mode grows and gradually can become dominant.

Increasing *VR*, for the case of a flat bed, the strength of the downflow is reduced and clear interactions between SSLs can be noticed although for most of times a proper symmetric mode is observed (Figure 3-15c). The elongated patches of vorticity forming in between the symmetry plane and the SSLs are also suppressed because of the weak effect of the downflow (compare Figure 3-15a and Figure 3-15c). This is observed for $VR = 0.61$, and it is even stronger for $VR = 1.22$, where the symmetric mode dominates for about 50% of times.

The effect of the reduced downflow as a consequence of the increased *VR* is more evident increasing the roughness. For $d_{50}/H = 0.062$ the antisymmetric mode for $VR = 0.61$ is stronger if compared to simulations for $VR = 0$, and it clearly becomes the dominant mode (Figure 3-15d). This is amplified when increasing *VR*: if $VR = 0.61$ the antisymmetric mode is observed for ~55% of the time, while if $VR = 1.22$ for ~90% of the time.

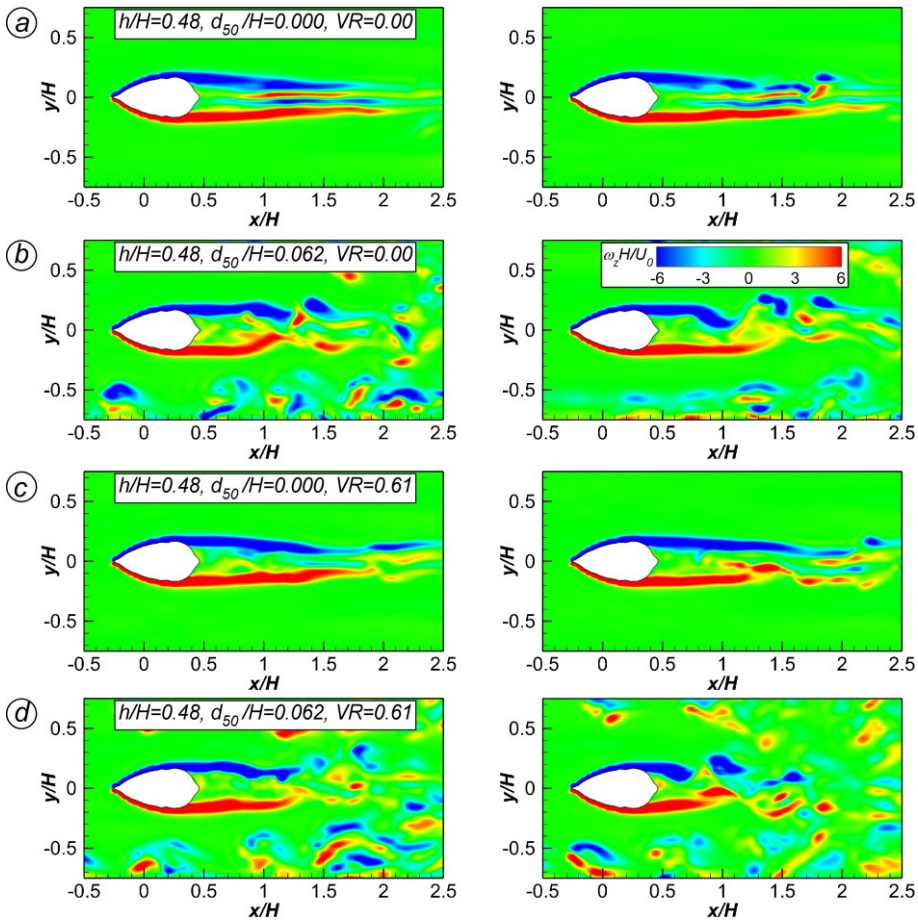

Figure 3-15. Instantaneous-flow, vertical vorticity, $\omega_z H/U_0$, in the horizontal plane $z/H = 0.5$ for different simulations (a-d). Left frames illustrate the symmetric wake shedding mode; right frames illustrate the anti-symmetric wake shedding mode (c-d) or the symmetric mode with a loss of symmetry for the eddies that detach from the downstream part of the separated shear layers (a-b).

3.3.6 Drag Forces

To evaluate the stability of the mussel and its capacity to avoid to be dislocated from the bed, it is important to quantify the drag forces acting on the emerged part of the shell (Dey, 2003; Diedericks et al., 2018; Witman and Suchanek, 1984).

The total force on the mussel, F_{dxy}, is calculated by integrating the mean pressure on the shell, the contribution of the shear component being negligible. The streamwise and the spanwise components are labelled F_{dx} and F_{dy}, respectively. Due to the presence of a gravel bed with irregular particles of different dimensions, values of F_{dx} and F_{dy} have been extracted for the $z > 0$ region to allow a direct comparison of the results provided by the different simulations, and with the smooth bed cases. Streamwise and spanwise components, as well as the magnitude of the total horizontal forces, are also nondimensionalized through the water density ρ, the incoming section-averaged flow

velocity U_0 and the height of the mussel H. All these parameters are constant for all simulations.

Table 3-2 summarizes the values of the main drag force obtained in the simulations. Table 3-2 also reports values for the mean streamwise drag coefficient, C_{dx}^{MEAN}, and its root-mean-square (RMS) fluctuations, C_{dx}^{RMS}. The mean drag coefficient in the x-direction is defined as $C_{dx}^{MEAN} = 2\ F_{dx}/\rho U_0^2 A_x$, where A_x is the projected area of the emerged part of the mussel (in the region $z > 0$). Values of A_x vary with h/H.

The total force on the mussel depends on the mean pressure force on the shell. Generally, highest pressure values are observed in the upstream part of the mussel, where the flow is decelerated and diverted laterally. Lowest values, instead, are observed in the region immediately downstream the excurrent siphon. Since both the shell and the gravel bed are obtained from real specimens, the layout is slightly asymmetric. Hence, the distributions of pressure are slightly different considering the left and the right side, resulting in non-zero values for the mean drag forces F_{dy} in the spanwise direction.

For a fixed value of the burrowing-ratio, h/H, and of the velocity ratio, VR, the drag force in both the streamwise and the spanwise direction increases monotonically with the roughness (Figure 3-16a). However, the rate of increase is higher for the lateral components.

The drag force in the streamwise direction also depend on the value of the exhaling velocity ratio, VR, for a fixed value of bed roughness, and keeping constant the burrowing level, h/H. As highlighted in Figure 3-16b, between $VR = 0$ and $VR = 0.61$ the drag force increases with VR, as observed by Wu et al., 2020 for their simulations with $VR < 0.7$. Between $VR = 0.61$ and $VR = 1.22$, instead, the drag force decreases with VR. It can be supposed that the trend reverses around $VR = 1$, when the velocity injected by the siphon has the same value as the incoming flow. F_{dy}, instead, is increasing monotonically with VR.

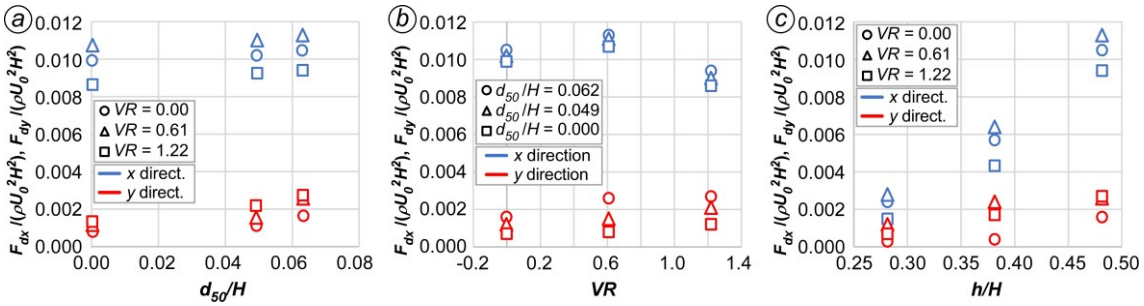

Figure 3-16. Non-dimensional drag forces, $F_{dx}/(\rho U_0^2 H^2)$ and $F_{dy}/(\rho U_0^2 H^2)$, as a function of a) the bed roughness, d_{50}/H (for different values of VR, and $h/H = 0.48$), b) the exhaling velocity ratio, VR (for different values of d_{50}/H, and $h/H = 0.48$), c) the mussel burrowing level, h/H (for different values of VR, and $d_{50}/H = 0.062$). Blue symbols refer to x-direction, red symbols to y-direction.

The value of the drag force is observed to depend also on the burrowing ratio h/H, with the streamwise component increasing with increasing h/H (Figure 3-16c), similarly to what found by Wu et al. (2020) for the case of a flat bed. The spanwise component is also increasing with increasing h/H, although with a lower rate. Interestingly, for the higher value of h/H considered in the present study (i.e., $h/H = 0.48$), the streamwise component is about one-order of magnitude greater than the spanwise component and $F_{dxy} \approx F_{dx}$, especially for the simulations with smooth bed. Considering the simulations with a rough bed and $h/H = 0.48$, values of F_{dy} can be as high as 30% of F_{dx}. However, for higher degree of mussel burial (i.e., lower values of h/H) the spanwise components become not negligible, as they can be as high of 75% the longitudinal components for $h/H = 0.28$ (see Table 3-2 and Figure 3-16c).

Drag coefficients in the streamwise direction are pictured in Figure 3-17. The trends in the variation of their values reflect what observed for the streamwise drag force: values increase increasing the roughness d_{50}/H (Figure 3-17a), or the exposed part of the shell h/H (Figure 3-17c), while for the dependence on VR a non-monotonic trend is observed (Figure 3-17b). The maximum value of C_{dx}^{MEAN} is around 0.17 for $VR = 0.62$ and $h/H = 0.48$. This value is approximatively 50-70% lower than those predicted by Wu et al. (2020), because the *Unio Elongatulus* has a much more streamlined shape of the frontal part compared to the *L. Siliquoidea* considered in the study of Wu et al. (2020). Given that the exposed area A_x varies with the mussel burial, the rate of increase of C_{dx}^{MEAN} with h/H is lower than the rate observed for F_{dx}. In any case, strong differences are still observed varying the exposed height of the mussel. Passing from $h/D = 0.48$ to $h/D = 0.28$, the mean drag coefficient in the streamwise direction is roughly halved, if considering the results of the simulation with $d_{50}/H = 0.062$ and $VR = 1.22$.

Inspections of Table 3-2 also highlight that the values of the drag coefficient fluctuations, C_{dx}^{RMS}, are about one order of magnitude lower than those of C_{dx}^{MEAN} for $h/H = 0.48$. This means that, for higher burrowing ratio, the fluctuations of the drag coefficient are less significant than the mean values in displacing the shell from the bed. Decreasing the exposed height h, while values of C_{dx}^{RMS} are poorly influenced by h, values of C_{dx}^{MEAN} decrease significantly with decreasing h. For $h/H = 0.28$ C_{dx}^{RMS} is found to be only 3 times lower than C_{dx}^{MEAN}, meaning that, at high burial level, fluctuations in the drag force may play a role in the mussel displacement. In this case, C_{dx}^{MEAN} provides a partial information of the capacity of the flow to dislocate the mussel, and the maximum values of the instantaneous drag coefficients would be more suitable for mussel stability calculations than mean values.

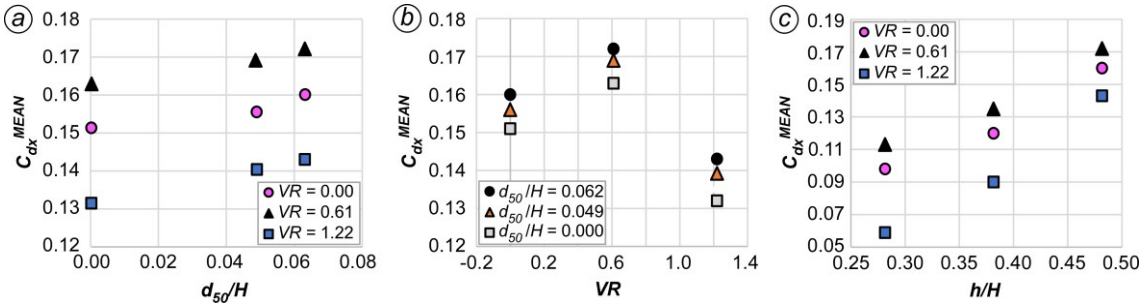

Figure 3-17. Mean drag coefficient, C_{dx}^{MEAN}, as a function of a) the bed roughness, d_{50}/H (for different values of VR, and $h/H = 0.48$), b) the exhaling velocity ratio, VR (for different values of d_{50}/H, and $h/H = 0.48$), c) the mussel burrowing level, h/H (for different values of VR, and $d_{50}/H = 0.062$).

3.3.7 Excurrent Siphon Jet

Mussels are usually identified as ecosystem engineers due to their filtering activity (Vaughn et al., 2004). Water with high concentrations of organic matter and phytoplankton enters in the mussel through the inhaling siphon and a jet with low concentrations is expelled through the exhaling siphon (Haag, 2012; Monismith et al., 1990; Vaughn et al., 2004). The distribution and the availability of nutrients in the flow are then directly connected with the mixing and dilution of the excurrent jet.

To evaluate the dynamics of the jet, a concentration C_0 is prescribed for the passive scalar introduced at the excurrent siphon. Then, an "inverse concentration method" is used (Monismith et al., 1990; Wu et al., 2020). $C = C_0$ represents the clean filtered water, while $C = 0$ represents the water with high concentrations of nutrients and phytoplankton (Figure 3-18). The jet fluid is defined as the fluid with $C > 0.0001C_0$. In the region of excurrent jet, the availability of nutrients is expected to be reduced (i.e., $C > 0$) due to the interaction among the clean water exhaled by the mussel.

The fluid exhaled from the excurrent siphon is injected vertically in the water column as in the case of classical jets in cross flow. However, in the present case the dynamics of the jet are more complex. The jet is introduced in the channel at the exhaling siphon on the top of the mussel, and hence above the bed. The surrounding flow is modified by the emerged body of the mussel shell: for instance, flow is diverted in the frontal part of the shell, a recirculation region forms downstream the shell, with the wake characterized by tip vortices originating because of the shell, etc. All these factors make the present case different form the canonical case of a round vertical jet entering through the bottom of a flat-bed channel (Mahesh, 2013). The picture is even more complicated in case of a rough bed, especially for higher level of the mussel burial, because the dynamics of the jet can be disturbed also by eddies generated by bed particles. The interactions of these eddies with the jet lead to enhancing the local mixing and to diluting more rapidly the jet, compared to a similar case with a flat bed or with larger values of h/H.

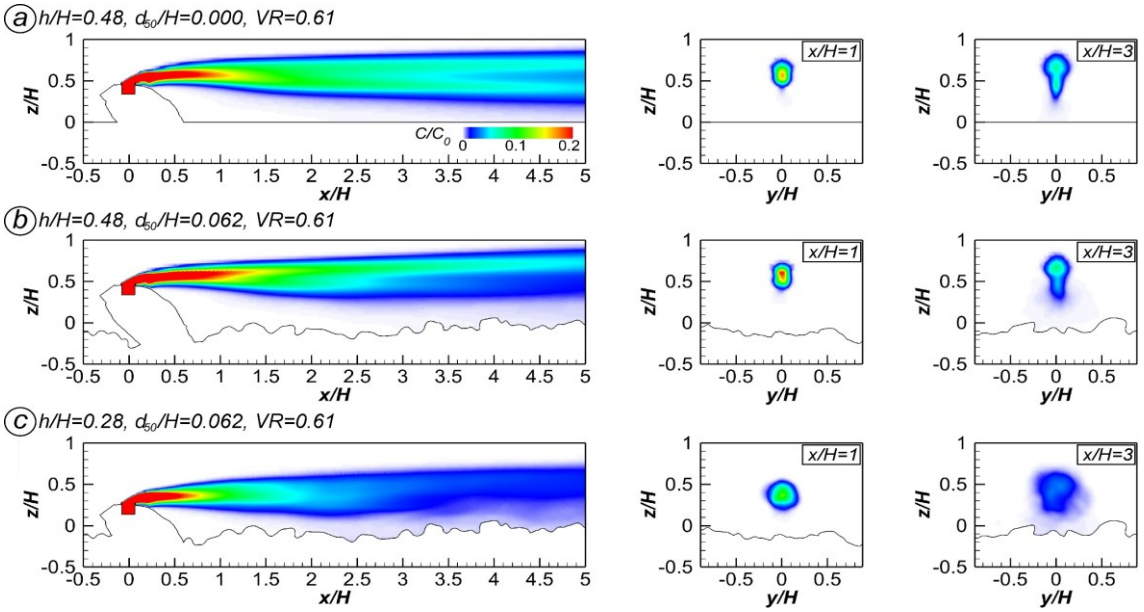

Figure 3-18. Mean concentration of the passive scalar, C/C_0 (values lower than 0.01 were blanked), for different simulations (a-c) in the $y/H = 0$ (left), $x/H = 1$ (center) and $x/H = 3$ (right) section planes.

The mean concentration of the passive scalar, C/C_0, is pictured in Figure 3-18 in the longitudinal plane $y/H = 0$ and in in the transversal planes $x/H = 1$ and $x/H = 3$, for some of the simulations in Table 3-1.

In all the cases with $h/H = 0.48$, the jet is observed to be initially directed upward, but, as soon as it interacts with the incoming flow, it is deflected downstream, parallel to the streamwise direction. The shape of the jet is observed to maintain a roughly ellipsoidal shape along the x-axis. The elliptical cross section is a direct influence of the pair of base vortices that draws jet fluid away from the bed, as shown in the $x/H = 1$ section. Here, the concentration of the passive scalar is also strongly reduced to a value of 0.2 C_0. In the $x/H = 3$ section, still the jet shows a very irregular shape, with an elongated region extending downwards from the lower part of the jet. This elongated region in the symmetry plane ($y/H = 0$) is induced by the counter-rotating tip vortices that draw some of the jet fluid toward the bed (Figure 3-12b and Figure 3-18).

The jet is qualitatively similar when a rough bed is considered instead of a smooth one (see results for the $d_{50}/H = 0.062$, $VR = 0.61$ simulation shown in Figure 3-18b). The effect of the gravel bed is relevant especially in the part close to the bottom, where the turbulent eddies induced by the rough elements generate additional fluctuations and additional mixing of the passive scalar. In the rough bed case, the values of concentration are slightly lower, and the region with high concentration levels is smaller. This is particularly highlighted at the $x/H = 3$ section, where the coherence of the tip vortex is significantly lower in the rough bed simulation. Instead, in the $x/H = 1$ section the coherence of the vortices forming downstream the mussel is comparable for smooth and rough simulations (see also Figure 3-11b and Figure 3-11d). This is confirmed also from

the RMS fluctuation of concentrations (not reported here for brevity): for the gravel bed simulations higher values are located in a layer close to the bed, instead for the smooth bed simulations values are generally lower, except for the region immediately downstream of the exhaling siphon.

The effect of increasing the level of mussel burial can be inferred by the scalar concentration distribution of Figure 3-18c, which refer to the $d_{50}/H = 0.062$, $VR = 0.61$, $h/H = 0.28$ simulation and should be compared with the distribution of Figure 3-18b which pictures the results of the corresponding simulations, but with $h/H = 0.48$. The overall trajectory of the excurrent jet is the same in the two cases, but the cross-sectional shape in the $h/H = 0.28$ simulation is more circular, and no clear elongated regions are visible. This agrees with the suppression of tip vortices in the $h/H = 0.28$ simulation because of eddies generated by the bed particles (Figure 3-11f). Decreasing the exposed height h/H the exhaling siphon, as well as the excurrent jet, approach the gravel bed, and they interact more with the near bed flow turbulent structures induced by bed particles. For this reason, the levels of the mean concentration are strongly dampened along the x-direction. This confirms the role of these eddies at enhancing the mixing between the jet fluid and the surrounding flow. The closer the excurrent jet is to the bed, the stronger these interactions and the concentration dampening are.

To provide a more quantitative measure of the effects of the investigated parameters, the streamwise variation of the maximum passive scalar concentration in cross sections perpendicular to the axis of the jet is pictured in Figure 3-19. This measures the jet dilution. For the same scope, the variation of the volumetric flux of the jet, Q_j, scaled by the volumetric flux out of the excurrent siphon, Q_{j0}, is plotted in Figure 3-20. This variable summarizes the spreading of the jet in the fluid volume.

The decay of the peak concentration C_{MAX}/C_0 is very similar for the values of roughness here analyzed (Figure 3-19a), albeit these simulations are based on a relatively low level of mussel burial ($h/H = 0.48$), with the exhaling jet located relatively far from the bottom. Some slight differences in the values of C_{MAX}/C_0 are observed only at $x/H > 6$ for the simulation with $d_{50}/H = 0.062$. Non-negligible differences, instead, are observed for the volumetric flux of the jet Q_j/Q_0 (Figure 3-20a) depending on the bed roughness. The volumetric flux increases at a higher rate for higher values of the roughness, since the interactions with turbulent eddies induced by the gravel bed increase the mixing and the volume of the jet. At $x/H = 9$ values of Q_j/Q_0 evaluated for the $d_{50}/H = 0.062$ simulation roughly doubles the values obtained for the flat bed simulation.

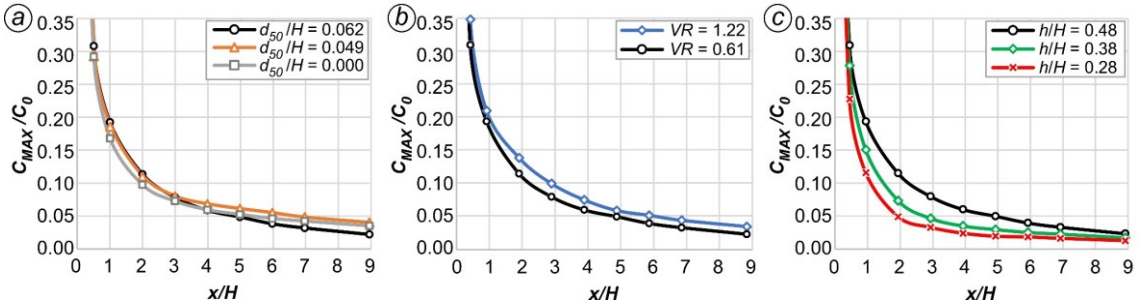

Figure 3-19. Non-dimensional peak scalar concentration, C_{MAX}/C_0, inside the excurrent jet. a) Effect of d_{50}/H (VR = 0.61, h/H = 0.48); b) effect of VR (d_{50}/H = 0.062, h/H = 0.48); c) effect of h/H (d_{50}/H = 0.062, VR = 0.61).

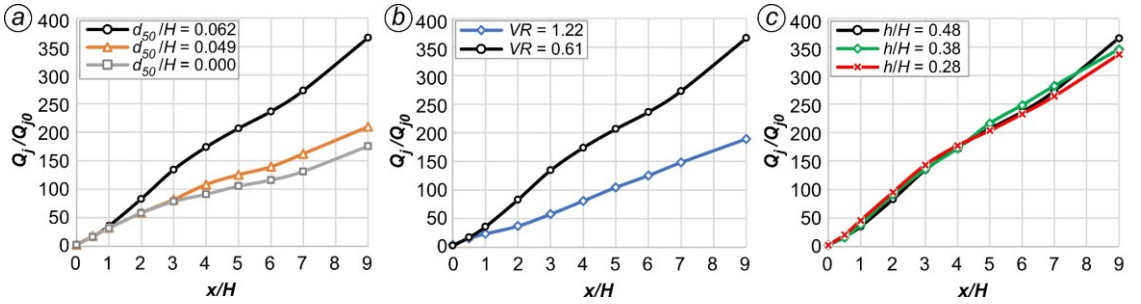

Figure 3-20. Non-dimensional volumetric flux, Q_j/Q_{j0}, of the excurrent siphon jet. a) Effect of d_{50}/H (VR = 0.61, h/H = 0.48); b) effect of VR (d_{50}/H = 0.062, h/H = 0.48); c) effect of h/H (d_{50}/H = 0.062, VR = 0.61).

The constant values of velocity prescribed at the exhaling siphons varies between 0.1m/s (VR = 0.61) and 0.2m/s (VR = 1.22). The different values of VR imply different dynamics of the jet. For higher values of VR the jet has a larger initial momentum and it penetrates up to higher elevations with respect to the location of the excurrent siphon. As a consequence, the streamwise distance needed for the jet to align with the streamwise direction increases when increasing VR. The overall trajectories of the exhaled jet are then different in the simulations with VR = 0.61 and VR = 1.22. Despite that, Figure 3-19b shows that the streamwise variation of C_{MAX}/C_0 is similar in the two cases, considering the simulations with h/H = 0.48 and d_{50}/H = 0.062. In both cases, the exhaling siphon is at an elevation such that the region with higher concentrations (i.e., the upper part of the jet) remains relatively far from the bed. The rate of increase of the volumetric discharge is higher for VR = 0.61 (Figure 3-20b). This again can be explained by the jet trajectory, which is closer to the bottom in the simulations with the lower filtering discharge. Thus, eddies produced by the gravel particles are more likely to interact with the lower part of the jet, which in turn expands. A second reason is related to the growth of flow instabilities near the jet boundaries which are driven by the mean shear between the velocity inside the core of the jet and the velocity in the surrounding flow. This effect is expected to be lower in cases with $VR \simeq 1$, as the excurrent jet velocity is close to the mean velocity of the approaching flow.

Increasing the level of mussel burial (i.e., decreasing h/H) the exhaling siphon gets closer to the bed. As a consequence, the excurrent jet approaches the gravel bed, and the interactions with eddies from the gravel bed are enhanced. These interactions, in turn, enhance the mixing of the passive scalar in the entire volume of the jet. The peak of scalar concentration is therefore strongly dampened along the x-direction, as confirmed by the larger rates of decay for C_{MAX}/C_0 when decreasing h/H (see Figure 3-19c, for the simulations with $d_{50}/H = 0.062$ and $VR = 0.61$). This is particularly clear until $x/H = 2$, while the maximum concentration values become fairly close at $x/H = 8$. This because, once the jet expands enough to touches the bed, the dampening effect of the gravel bed on the scalar concentration reduces. The non-dimensional volume of the jet (Figure 3-20), instead, is not influenced by h/H (Figure 3-20c). This can be the results of two opposite effects. While the cross section of the jet increases with decreasing h/H (Figure 3-18), the streamwise flow velocities decrease with decreasing h/H, because the jet is closer to the bed where the incoming flow has a lower velocity because of the bed roughness.

3.4 Fully-developed flow over Clusters of Mussels

3.4.1 Test cases

The analysis of fully-developed flow over clusters of mussels refers to the same partially-buried *Unio Elongatulus* mussel described in the previous Section for the simulations with an isolated specimen (Figure 3-21a). Main geometrical parameters of the mussel model are described in Section 3.2.1, though in this case a single level of mussel burial has been analyzed, corresponding to $h/H = 0.48$.

The simulations were performed in a rectangular straight open channel. The channel was larger than that used for studying the flow over an isolated mussel. As described in Section 3.2.3, the gravel bed used for analyzing the flow over musselbeds has been generated through symmetry projections in the plane of the original deformed bed. The scope was to ensure that its upstream and downstream boundaries, as well as those on its left and on its rights, were identical. This was needed to impose periodical conditions at these boundaries. The gravel bed used in this Section was 0.5 m (~10 H) wide and 1.0 m (~20 H) long (Figure 3-21b), such that the bed surface was 0.5 m². The flow rate through the channel was $Q = 0.0123$ m³/s, and the section-averaged, or bulk, velocity was $U_0 = 0.164$ m/s, the same as in the simulations presented in Sect. 3.3. The Froude number was $F = 0.14$, the bulk Reynolds number $Re = 24'600$.

By imposing periodic boundary conditions at the upstream and downstream boundaries of the domain, a 1-m long stretch of an infinitely long channel with periodic bathymetry was simulated. Simulations were run until the velocity components became statistically steady in the mean (approximatively at $t = 42$ s = 45.9 D/U_0). Results were analysed over a subsequent 20 s (~21.9 D/U_0) long time interval. The mean flow computed in the periodic domain corresponds to a fully-developed flow solution that will be reached in a very long open channel at very large distances from the leading edge

of the mussel bed. This regime is particularly important, given that mussel beds generally extend over very large distances (e.g., O(km)) in rivers.

The test cases described in the present Section are summarized in Table 3-3, which includes also their main characteristics. Most of the simulations were performed over the rough-bed which reproduces the water-worked gravel bed sample from the laboratory experiment (with d_{50} = 3.10 mm and d_{90} = 5.00 mm). Other simulations were performed over a flat bed (d_{50} = 0.00 mm), and over the gravel bed obtained by multiplying the vertical coordinate of the original rough bed by a factor of 0.5 (d_{50} = 2.46 mm).

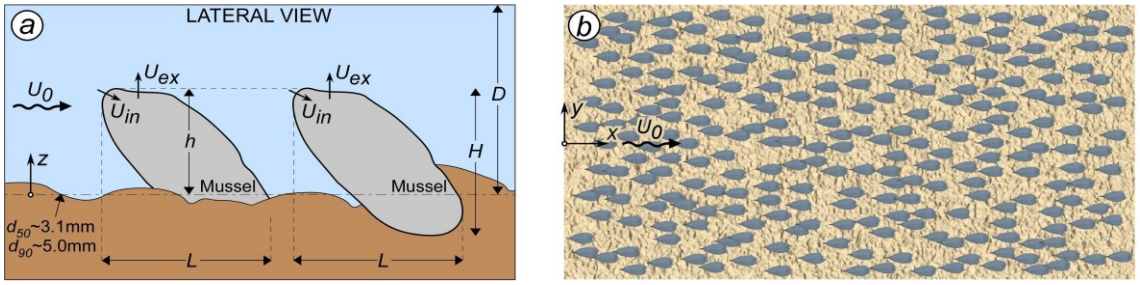

Figure 3-21. (a) sketch showing two of the shells part of the mussel bed (symbols are defined in Figure 3-1), (b) plan view showing the mussel bed with ρ_M = 500 mussels/m².

Table 3-3. Matrix of simulations with relevant parameters. N is the number of mussels in the computational domain, ρ_M is the mussel array density, h is the emerged height of the mussel, d_{50} is the median diameter of the channel bed material, $VR = U_{ex}/U_0$ is the filtering velocity ratio, U_0 is the section-averaged, or bulk, velocity, U_{inner} is the mean streamwise velocity in the region $z < h$, F_{dx}^{MEAN} and C_{dx}^{MEAN} are the array-averaged mean drag force and the mean drag coefficient in the streamwise direction, respectively, as computed by the numerical model (Sect. 3.4.6).

N	ρ_M	d_{50}/h	VR	U_{inner}/U_0	$F_{dx}^{MEAN}/\rho U_0^2 H^2$	C_{dx}^{MEAN}
0	0	0.13	-	-	-	-
13	26	0.13	0.50	0.587	0.0096	0.138
50	100	0.13	0.50	0.557	0.0083	0.120
100	200	0.13	0.50	0.519	0.0074	0.105
150	300	0.13	0.50	0.426	0.0059	0.084
200	400	0.13	0.50	0.387	0.0052	0.074
250	500	0.13	0.50	0.348	0.0044	0.063
50	100	0.00	0.50	0.627	0.0098	0.149
100	200	0.10	0.50	0.530	0.0079	0.116
100	200	0.00	0.50	0.553	0.0082	0.125
250	500	0.10	0.50	0.372	0.0047	0.069
250	500	0.00	0.50	0.390	0.0050	0.076
100	200	0.13	0.00	0.483	0.0077	0.108
100	200	0.13	1.22	0.501	0.0048	0.068
250	500	0.13	0.00	0.353	0.0050	0.072
250	500	0.13	1.22	0.392	0.0032	0.045

The simulations were performed considering clusters of different densities, spanning from 26 mus/m² to 500 mus/m², which correspond to a number of mussels spanning from 13 to 250. An additional simulation with the rough bed and 0 mus/m² allows the comparison with a fully-developed flow over the gravel bed with no-mussels.

The study also considers different level of the mussel filtering activity by varying the filtering discharges through the two siphons of the mussels. In the simulations, the flux rates through the inhaling and the exhaling siphons were equal ($Q_{in} = Q_{ex}$), and the desired values have been maintained constant through all the mussels forming the cluster and in time. The values used were $3.3 \cdot 10^{-8}$, $1.3 \cdot 10^{-6}$ and $3.1 \cdot 10^{-6}$ m³/s, which are among the values expected for this size and species of mussels (Bunt et al., 1993; Kryger and Riisgård, 1988; Monismith et al., 1990). The corresponding values of the velocity ratio, $VR = U_{ex}/U_0$, were 0, 0.5 and 1.22. The intermediate value corresponds to the normal filtering condition, with the excurrent velocity close to that measured by Sansom et al. (2018).

3.4.2 Effects of overflow and bed roughness on the protruding mussels

As described in Section 3.3, flow over an isolated freshwater mussel can be seen as a particular type of flow past a surface-mounted obstacle. As opposed to the canonical obstacles investigated in previous studies, the case of a mussel is further complicated by the irregular shape of the shell and by the filtering activity of the mollusk.

In a cluster of mussels, the presence of neighboring shells induces additional turbulent structures to form and deviates the incoming velocity, making the flow field approaching each shell more complex. Bed roughness also influences the approaching flow, because gravel particles composing the irregular bed surface are additional source of turbulence, in case of both isolated specimens and cluster of mussels.

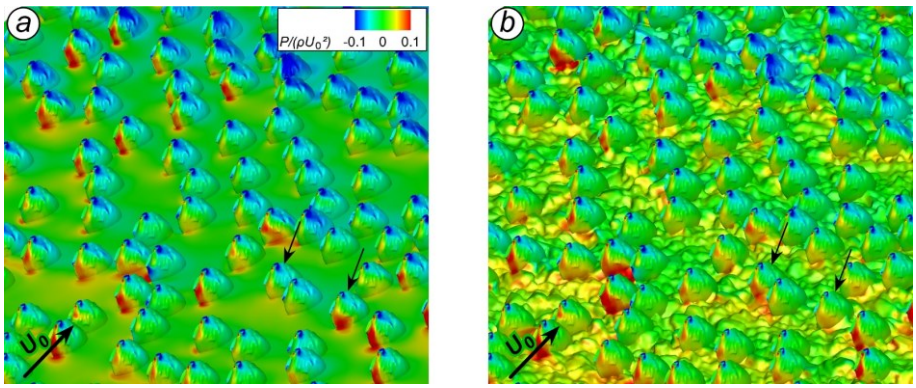

Figure 3-22. Mean pressure, $P/(\rho U_0^2)$, on shells and bed for simulations with $\rho_M = 500$ mussel/m², $VR = 0.50$ for (a) a smooth bed ($d_{50}/h = 0.00$), and (b) a gravel bed ($d_{50}/h = 0.13$).

Figure 3-22 shows the mean pressure on the mussel shells and on the bed for simulations with smooth and rough bed in case of a dense array of mussels (ρ_M = 500 mussel/m²). At a large scale, the mean pressure on the shells decreases along the streamwise direction as a consequence of drag and head losses induced by the musselbed on the flow, which is coherent with the rigid lid assumption (see Sect. 3.2.3). For both smooth and rough bed cases, on each mussel, highest values of the pressure are observed in the frontal part of the shell, immediately below the incurrent siphon. Here, flow is decelerated and it is deviated laterally by the mussel shell. Lowest values of the pressure, instead, are observed just downstream the excurrent siphon, in the upper part of the shell. Although this qualitative trend agrees with what observed for an isolated mussel and it is observed for all the shells regardless the mussel density, notable variations in the values occur depending on the position inside the array, especially for dense clusters (e.g., compare mussels pointed out by the arrows in Figure 3-22a, having similar x coordinates). Different factors concur to modify the pressure distribution on the shells, among which the relative position in the array is one of the most important. Though all the mussels have the same orientation to the incoming flow, neighboring shells can both reduce or increase local values of the pressure, depending on the relative sheltering. The pressure on mussel shells also depends on the bed roughness, because the irregular gravel distribution can substantially contribute in modifying the local flow field (e.g., compare mussels pointed by arrows in Figure 3-22a and Figure 3-22b).

The presence of a high pressure gradient at the front of the mussel induces a downflow, which in some cases may induce an horseshoe vortex to form in the frontal and lateral part of the mussel. The large-scale coherent structures in the instantaneous and mean flow fields (shown in Figure 3-23 for ρ_M = 500 mussel/m² and d_{50}/h = 0.13), reveal no horseshoe vortices form around the upstream base of the mussels, regardless of the array density.

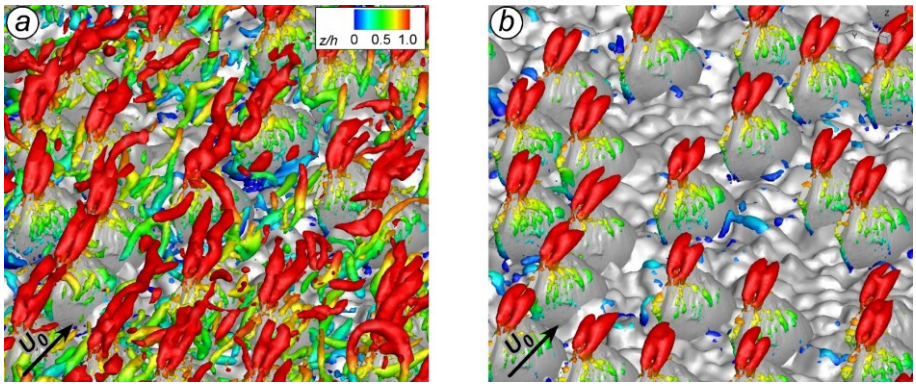

Figure 3-23. Coherent structures visualized using the Q criterion for the instantaneous (a) and the mean (b) flow in the simulation with ρ_M = 500 mussel/m², d_{50}/h = 0.13, VR = 1.22.

Though some small vortex cores are observed in front of the mussels in the rough bed simulations, the comparison with the corresponding flat-bed simulations confirmed that such structures are induced by the gravels. This agrees with the findings exposed in Sect. 3.3 (Lazzarin et al., 2023a) for the case of an isolated *Unio Elongatulus* mussel and

opposed to what Wu et al. (2020) found for an isolated *Lampsilis Siliquoidea* on a smooth bed. The different behavior can be explained considering the vertical inclination of the main axis and by the relatively streamlined shape of the *Unio Elongatulus* shell.

The turbulent structures in Figure 3-23 show that pairs of base (upwashing) vortices originate downstream the excurrent siphons in case of active filtering. As observed for an isolated mussel, they are not present for $VR \simeq 0$ and their strength increases with increasing VR. No clear effects are observed depending on bed roughness, probably due to the relatively low burrowing level considered in the simulations. Despite slight unsteadiness at the legs far downstream the siphons, these vortices represent coherent structures, as clarified by the mean flow field (Figure 3-23). Their structure remains clearly visible also for high mussel densities when jets interfere each other, and it is qualitatively similar for all the mussels in the array (Figure 3-23). However, when increasing the mussel density, these vortices are generally less extended downstream, and their coherence reduces if compared to the case of an isolated mussel because of the interactions with other mussels.

The mussel bed density also influences the distribution of turbulent structures in the roughness layer (i.e., the layer directly influenced by the large-scale roughness, e.g., mussels and gravels, when present). For an isolated mussel a pair of tip (downwashing) vortices forms in the wake (Sect. 1.3.3; Lazzarin et al., 2023a). The coherence of these downwashing vortices is reduced in case of active filtering and especially in case of a rough bed, because the interactions between the vortices and the gravels break their symmetry. This effect is enhanced in the case of mussel arrays, because the mussel-to-mussel interactions contribute in reducing their symmetry. For denser arrays, the formation of these tip vortices downstream the shell is further impeded by the presence of other shells, so that they barely form or they rapidly lose coherence. At very high mussel density, these tip vortices are basically suppressed for all the mussels in the array (i.e., they are not observed for $\rho_M = 500$ mussel/m^2, see Figure 3-23b).

In general, energetic eddies generated by the bed particles and by the protruding shells are located below the top of the mussels and slightly above them. The trajectories of the larger-scale structures are affected by the shells of the downstream mussels. The region situated immediately above the bed generally contains only small coherent structures in cases with a high mussel density even if the bed is rough. This contrasts with the same gravel bed without mussels, in which larger bed particles induce larger coherent structures to form above the bed. The reduction of large-scale coherent structures at the bed when increasing the mussel density is expected to reduce the influence of bed roughness in case of dense clusters, and also to reduce the potential for particle entrainment at the bed.

The interactions of energetic eddies generated by the largest exposed gravels with the mussel shells can be seen in the distributions of the instantaneous out-of-plane vorticity in the $z/D \leq 2/3$ region (Figure 3-24). For a gravel bed without mussels, regions of high vorticity are very close to the bed (Figure 3-24a). At larger bed particles (i.e., emerging from the average bed elevation) flow detachment is observed, with vorticity sheets above the top of these elements and small separated regions downstream. A high-

vorticity region covers the top of the deformed bed, and eddies rarely extend above $z/H > 0.5$. Arrays of mussels, instead, generate more turbulent eddies and modify the flow in the lower part of the water column (Figure 3-24b), such that it is decelerated and the vorticity is reduced, especially where mussels are close to each other. Turbulent eddies generated by the gravels and by the shells interact to each other and they extend up to $z/H \sim 1$.

As observed for an isolated mussel, a separated region forms downstream the shells, and a sheet of high vorticity is observed at the top of the mussels and of their wakes. This is observed also in case of a cluster of mussels (Figure 3-24b), but the main vorticity sheet generally has a reduced length compared to the case of an isolated mussel (Sect. 1.3.2; Lazzarin et al., 2023a). This can be explained both by mussel-to-mussel interactions and by the reduction of the velocity within the roughness layer, which becomes relevant for denser arrays (see Sect. 3.4.4).

For high-density clusters a similar vorticity field is observed for both rough (Figure 3-24b) and smooth beds (Figure 3-24c), confirming that the influence of the gravel roughness is significant only when/where mussels are sparse. The effect of the filtering activity is observed only in restricted areas above the excurrent siphons due to the jet introduced in the water column and interacting with the incoming flow (Figure 3-24d).

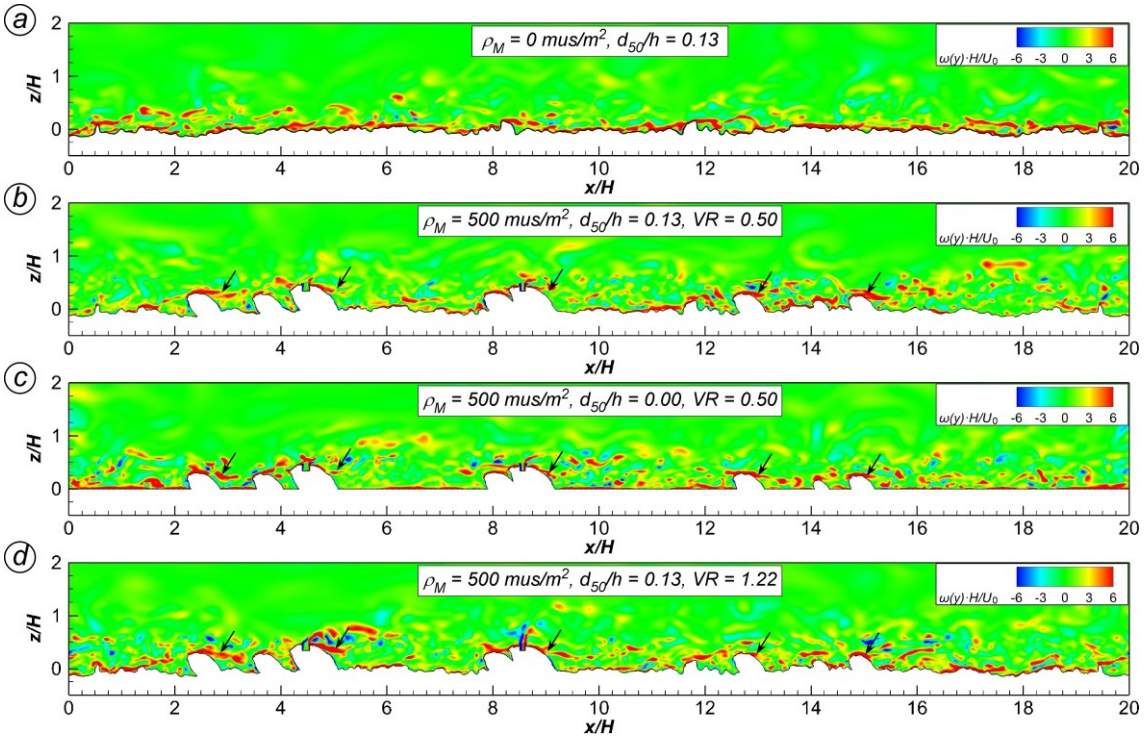

Figure 3-24. Instantaneous spanwise vorticity, $\omega_y H/U_0$, in the $y/H = -0.7$ plane for different simulations (a-d). Black arrows are pointing toward main shear layers on top of the mussels.

3.4.3 3-D Effects on the Mean Flow

The emerging particles of the gravel bed, in simulations without mussels, induce regions with non-negligible mean vertical velocities (Figure 3-25a). By increasing the density of mussels, up- and down-welling flows induced by bed particles are confined to the regions with no mussels. For higher mussel densities, such vertical flows are almost completely suppressed. However, in this case, strong up- and down-welling flows are induced in between the shells (Figure 3-25b) because of mussel-to-mussel interactions, and are observed regardless of the bed roughness. Close-to-symmetric regions of flow upwelling forms at the side of the isolated shells, and in case of neighboring mussels these up-welling regions can merge, enforcing the strength of the vertical motions.

In Section 3.3 (Lazzarin et al., 2023a), a region of strong downwelling flow has been observed to form near the symmetry plane downstream of an isolated mussel over a smooth bed. Although less strong, this downflow was observed also in case of a filtering mussel and in case of a rough bed. For mussels belonging to a cluster, the wake of each mussel interacts with the neighboring shells, such that the down-welling region is practically suppressed for many of them (Figure 3-25b).

To quantify the influence of the mussel density, as well as those of the bed roughness and of the filtering activity, the vertical, time-averaged, downward volumetric flux Q_W has been evaluated numerically at $z/h = 0.5$ as:

$$Q_W = \int_{w<-w_t} |w| \, dA \tag{3-1}$$

where w is the time-averaged vertical component of flow velocity and $w_t = 0.1U_0$ is the threshold value chosen to identify regions of strong downwelling motions.

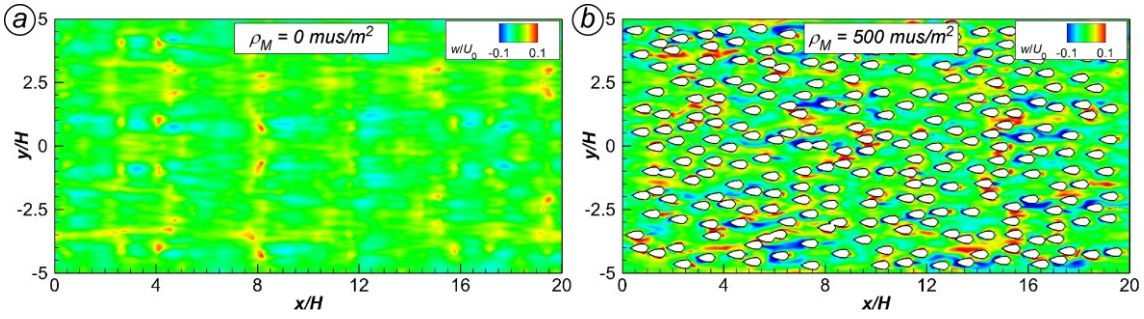

Figure 3-25. Mean vertical velocity, w/U_0, for the simulations with $d_{50}/h = 0.13$, $VR = 0.5$ and with $\rho_M = 0$ mussel/m² (a) and $\rho_M = 500$ mussel/m² (b), in the horizontal plane with $z/h = 0.5$.

The results are shown in Figure 3-26, where Q_W is scaled (left panels) with the average flow rate through a vertical plane of height H and width B, (U_0HB), and also (right panels) with the number of mussels N and the average flow rate through a $H \times H$ vertical plane, (NU_0H^2). $Q_W/(U_0HB)$, and hence the three-dimensionality of the flow, increases

with the mussel density (Figure 3-26). Figure 3-26a also shows that $Q_W/(NU_0H^2)$ decreases with ρ_M for low values of the mussel bed density, and attains an almost constant value for $\rho_M > 100$ mussel/m². This means that, beyond a given mussel density, the intensity of the downwelling flow increases only because of the increasing number of mussels, whereas the vertical flow per mussel remains nearly constant inside the mussel bed.

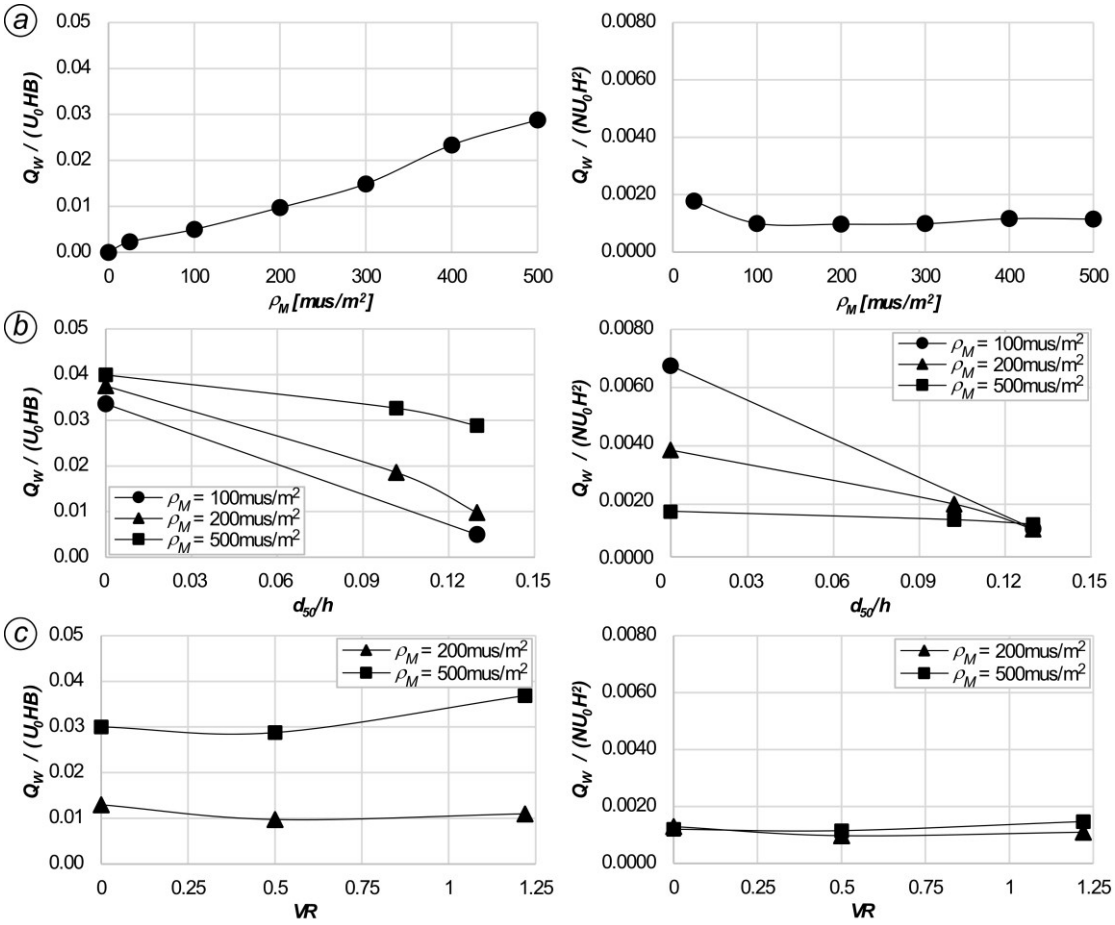

Figure 3-26. Non-dimensional, time-averaged downward discharge through the $z/h = 0.5$ horizontal plane as a function of (a) mussel density ρ_M, (b) bed roughness d_{50}/h (for three values of mussel density), (c) exhaling velocity ratio VR (for two values of mussel density).

Both $Q_W/(U_0HB)$ and $Q_W/(NU_0H^2)$ decrease with the bed roughness increasing (Figure 3-26b), at a rate of decreasing that is higher for low mussel density (e.g., 100 mussel/m²). This is consistent with results obtained for the case of an isolated mussel in Section 3.3 (Lazzarin et al., 2023a). Stronger downflows were observed in simulations with a smooth bed. Instead, when increasing the bed roughness, turbulence produced by gravel particles destroys the symmetry of tip vortices forming downstream the mussel, and the regions of downwelling flow break into multiple asymmetrical subregions of weaker intensity. In case of denser arrays, the bed-induced turbulence comes to play any significant role because the additional turbulence produced by neighboring shells

suppresses the tip vortices and impedes the downflow almost independently of bed roughness.

The filtering activity of the mussel has a fairly negligible effect on Q_W (Figure 3-26c). Both $Q_W/(U_0HB)$ and $Q_W/(NU_0H^2)$ slightly decrease with increasing VR, and then increase for $VR > 0.5$, with a higher rate for $\rho_M = 500$ mussel/m^2. Moderate filtering further weakens the upwelling and downwelling flow motions, whereas the high velocity excurrent jet above the top of the mussels, for higher values of VR, produces stronger coherent structures that enhance the vertical exchanges in the roughness layer.

3.4.4 Streamwise Velocity

The presence of mussels with protruding shells induces additional drag resistance for the flow in the roughness layer, and the total drag increases with the mussel density. The results show that, for increasing mussel density, the streamwise flow velocity decreases in the inner region and increases in the outer region, following the same trend noticed in the flume experiments by Sansom et al. (2020).

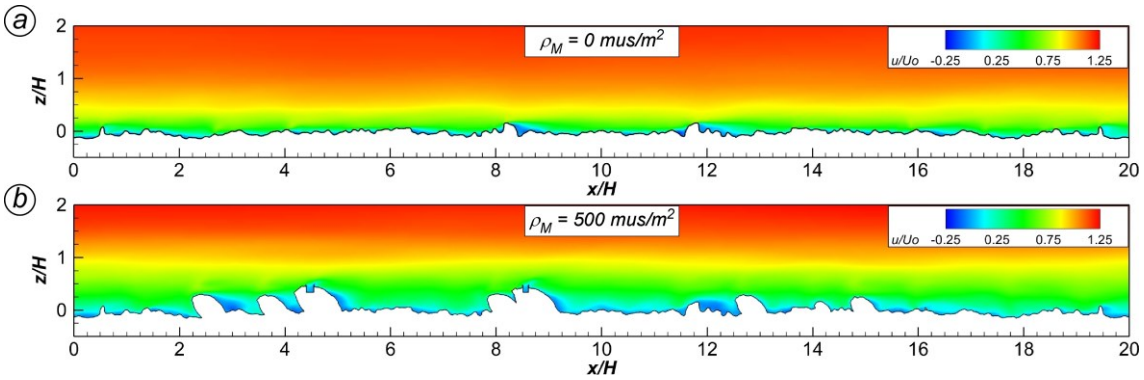

Figure 3-27. Mean streamwise velocity, u/U_0, in the y/H = -0.7 plane for the simulations with d_{50}/h = 0.13, VR = 0.5 and with ρ_M = 0 mussel/m² (a) and ρ_M = 500 mussel/m² (b).

These differences are highlighted in the distributions of the mean streamwise velocity, u/U_0, shown in Figure 3-27 for simulations without mussels and in case of a cluster with $\rho_M = 500$ mussel/m^2.

To obtain a quantitative measure of the effects of the different parameters under investigation on the distribution of the mean streamwise velocity, a double-averaging technique in both the longitudinal and the transversal direction has been used. This is justified by the fact that the flow can be considered quasi-uniform along these two directions because of the periodic boundary conditions imposed. The double-averaged mean velocity $\bar{\bar{u}}$ has been estimated as:

$$\bar{\bar{u}}(z) = \frac{1}{L'B'}\int_0^{L'}\left[\int_0^{B'} u(x,y,z)dy\right]dx \qquad (3\text{-}2)$$

where B' and L' denote the width and the length of the region occupied by the fluid, respectively (i.e., B' and L' do not consider the interior part of the emerging shells). This technique allows to summarize the effect of the three-dimensional flow on a single vertical profile, and to highlight the differences in the vertical distributions for the different simulations.

Figure 3-28a illustrates the effect of the mussel density on the vertical distribution of the double-averaged mean velocity, $\bar{\bar{u}}$. The velocity profile tilts when increasing the mussel density because of the region of reduced velocity forming in between the protruding shells as a consequence of the additional drag. While the effect of the filtering activity has been observed to be modest, and generally restricted to the small region above the excurrent siphons, differences in the vertical profiles of $\bar{\bar{u}}$ are observed depending on bed roughness. These differences are pronounced especially for cases with low mussel density (e.g., see results for ρ_M = 100 mussel/m² in Figure 3-28b), because of the influence of the gravel particles. When increasing the mussel density, instead, the effect of bed roughness wakens progressively (e.g., see results for ρ_M = 500 mussel/m² in Figure 3-28b), because both the net area of the gravel bed is reduced and the effect of the exposed part of the mussel shells prevails on that of the bed particles.

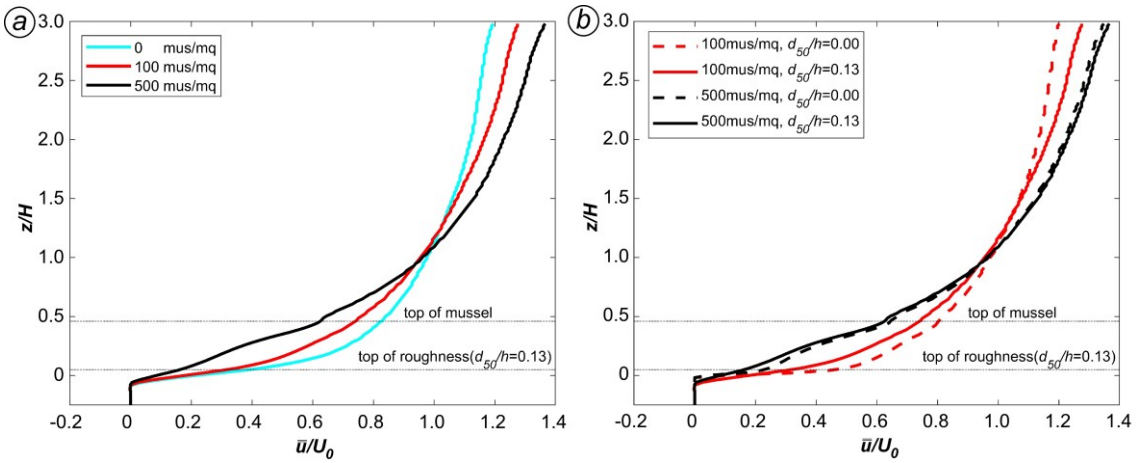

Figure 3-28. Vertical profiles of the double-averaged streamwise velocity, $\bar{\bar{u}}/U_0$, as a function of: a) the mussel density (with d_{50}/h = 0.13, VR = 0.5), and b) the bed roughness (for two values of ρ_M, and with VR = 0.5)

3.4.5 Turbulent Kinetic Energy

The presence of an isolated mussel over a smooth or a gravel bed is known to induce amplifications of the turbulent kinetic energy (TKE) behind the shell and in vicinity of the excurrent jet for cases with active filtering (Lazzarin et al., 2023a; Wu et al., 2020). These amplifications are found also in the present study when considering mussel clusters of low density (e.g., $\rho_M \leq$ 200 mussel/m²).

For higher mussel densities (ρ_M = 500 mussel/m²), Figure 3-29 shows some longitudinal profiles of TKE in the $z/D \leq 2/3$ region. In the case of the gravel bed with no

mussels, amplifications of *TKE* appear downstream of the largest roughness elements (Figure 3-29a), and they are confined in a small region just above the bed surface. This is confirmed also by the peak observed above the bed in Figure 3-30a, that pictures the vertical profile of the double-averaged *TKE*, $\overline{\overline{TKE}}$, computed as:

$$\overline{\overline{TKE}}(z) = \frac{1}{L'B'}\int_0^{L'}\left[\int_0^{B'} TKE(x,y,z)dy\right]dx \tag{3-3}$$

The mussel cluster (Figure 3-29b) reduces both flow velocity and *TKE* close to the bed. Amplifications of *TKE*, generated by the mussel shells, appear at a higher distance from the bed, though generally at $z \leq h$.

The active filtering increases the thickness of the size of the regions of high *TKE* (Figure 3-29c,d). The main regions of high *TKE* are mainly found near the excurrent siphons, downstream of the top of the mussels, and are situated above their top. The few regions of high *TKE* that are observed behind the mussels are generated by the interactions of the siphon-driven coherent structures with the mussel shells. The wakes generated by the shells are very weak, mainly because of the reduction of streamwise velocity inside the roughness layer. Interestingly, the levels of amplification of the *TKE* at the excurrent jets are stronger than that observed for an isolated mussel, and they increase with increasing ρ_M. This can be explained by the turbulent eddies generated by the mussel bed and extending to $z \sim h$, where they interact with the excurrent siphon jets.

$\overline{\overline{TKE}}$ vertical profiles included in Figure 3-30a show peaks of $\overline{\overline{TKE}}$ above the top of the mussels, where the jets are injected in the water column, for cases with $VR = 0.5$. Such amplifications above the top of the mussels are observed also in cases with no active filtering, which agrees with results of previous studies (Sansom et al., 2020). The intensity of these $\overline{\overline{TKE}}$ peaks increases at higher mussel density and/or in case of higher values of *VR*. Another effect is that peaks of $\overline{\overline{TKE}}$ observed at the top of the bed surface for the gravel bed with no mussels weaken when increasing the mussel density. At high values of ρ_M this peak of $\overline{\overline{TKE}}$ is almost suppressed, which is consistent with the reduction of the streamwise velocity in this region (Sect. 3.4.4), and with experimental observations of Sansom et al. (2020). Interestingly, for intermediate values of mussel densities (e.g., $\rho_M = 100$ mussel/m²), the two peaks present similar values of $\overline{\overline{TKE}}$.

For sparse clusters of mussels, the bed roughness amplifies the *TKE* behind the shells and increases its variability also away from the bed surface. This effect is reduced as the mussel bed density increases. If the mussel bed density is high enough (e.g., $\rho_M = 500$ mussel/m²), the *TKE* levels for the rough- and smooth-bed cases are fairly comparable (see Figure 3-29c,e and Figure 3-30b).

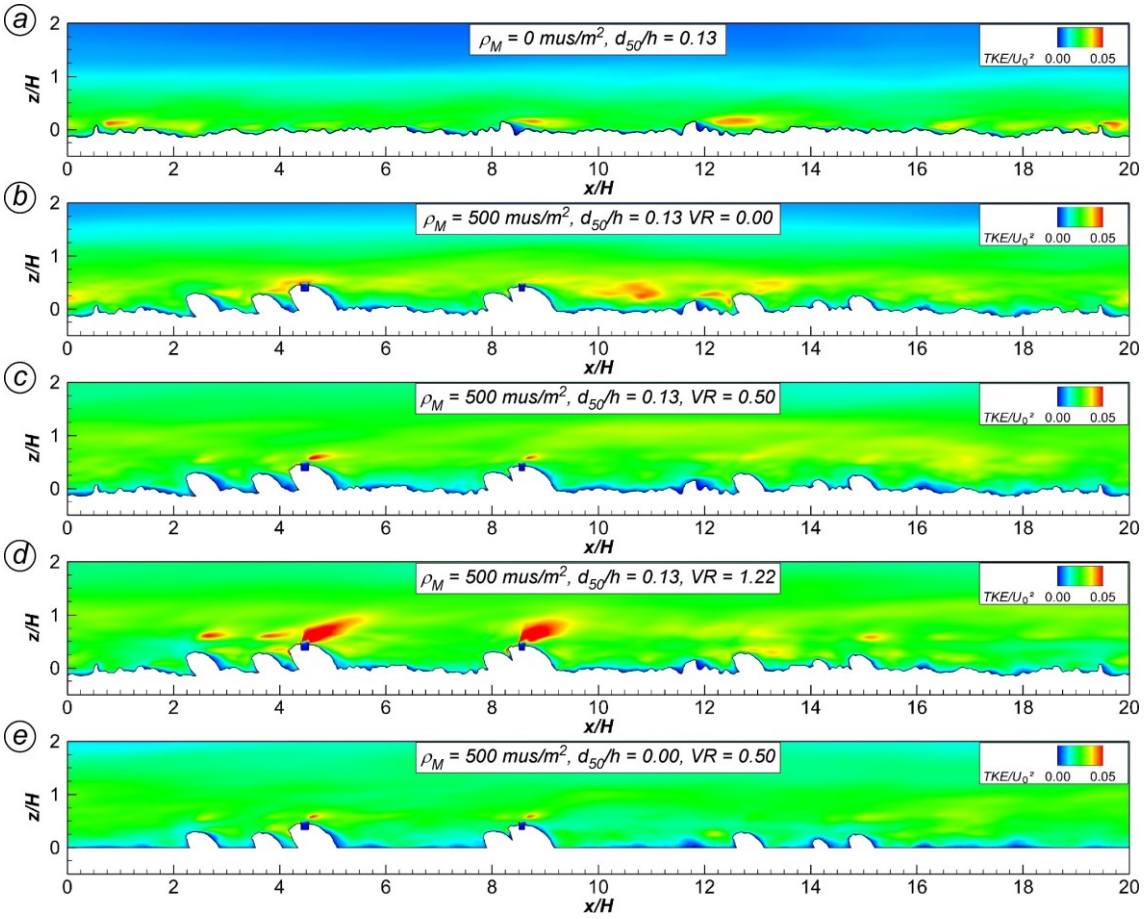

Figure 3-29. Turbulent kinetic energy, TKE/U_0^2, at y/H = -0.7 for different simulations (a-e).

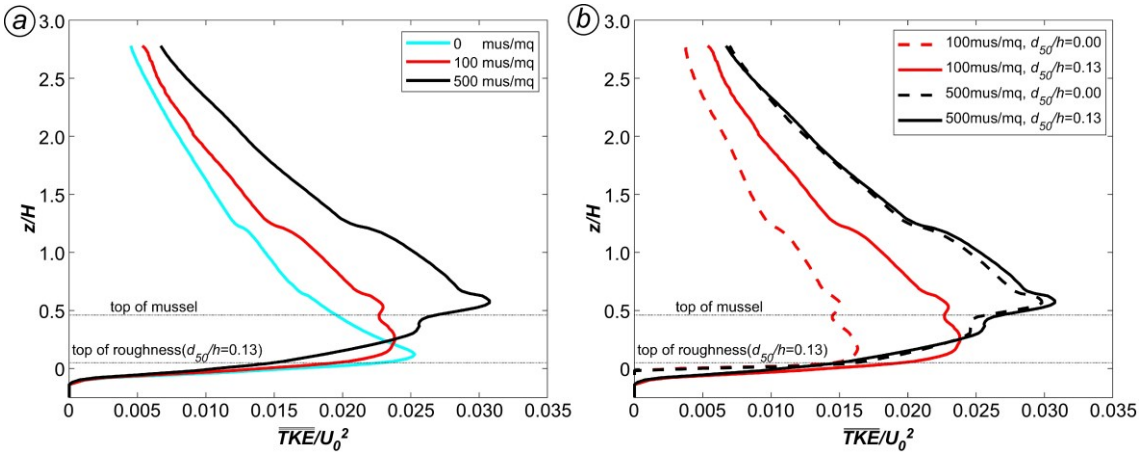

Figure 3-30. Vertical profiles of the double-averaged turbulent kinetic energy, $\overline{\overline{TKE}}/U_0^2$, as a function of: a) the mussel density (with d_{50}/h = 0.13, VR = 0.5), and b) the bed roughness (for two values of ρ_M, and with VR = 0.5)

3.4.6 Drag Forces

The stability of the mussels is connected to the drag forces acting on the emerged part of the shells (Dey, 2003; Diedericks et al., 2018; Witman and Suchanek, 1984). In Figure 3-31 mean drag forces on the streamwise (F_{dx}^{MEAN}, blue symbols) and the spanwise (F_{dy}^{MEAN}, red symbols) directions are compared for the different simulations (see also Table 3-3). All the values are non-dimensionalized using the water density, ρ, the section-averaged flow velocity, U_0, and the height of the mussel, H, which are constant for all simulations. Besides the mean values (filled symbols), the RMS fluctuations are also reported (empty symbols) to characterize temporal variations. All the values reported in Figure 3-31 (both mean and RMS fluctuations) are averaged on all the mussels in the bed.

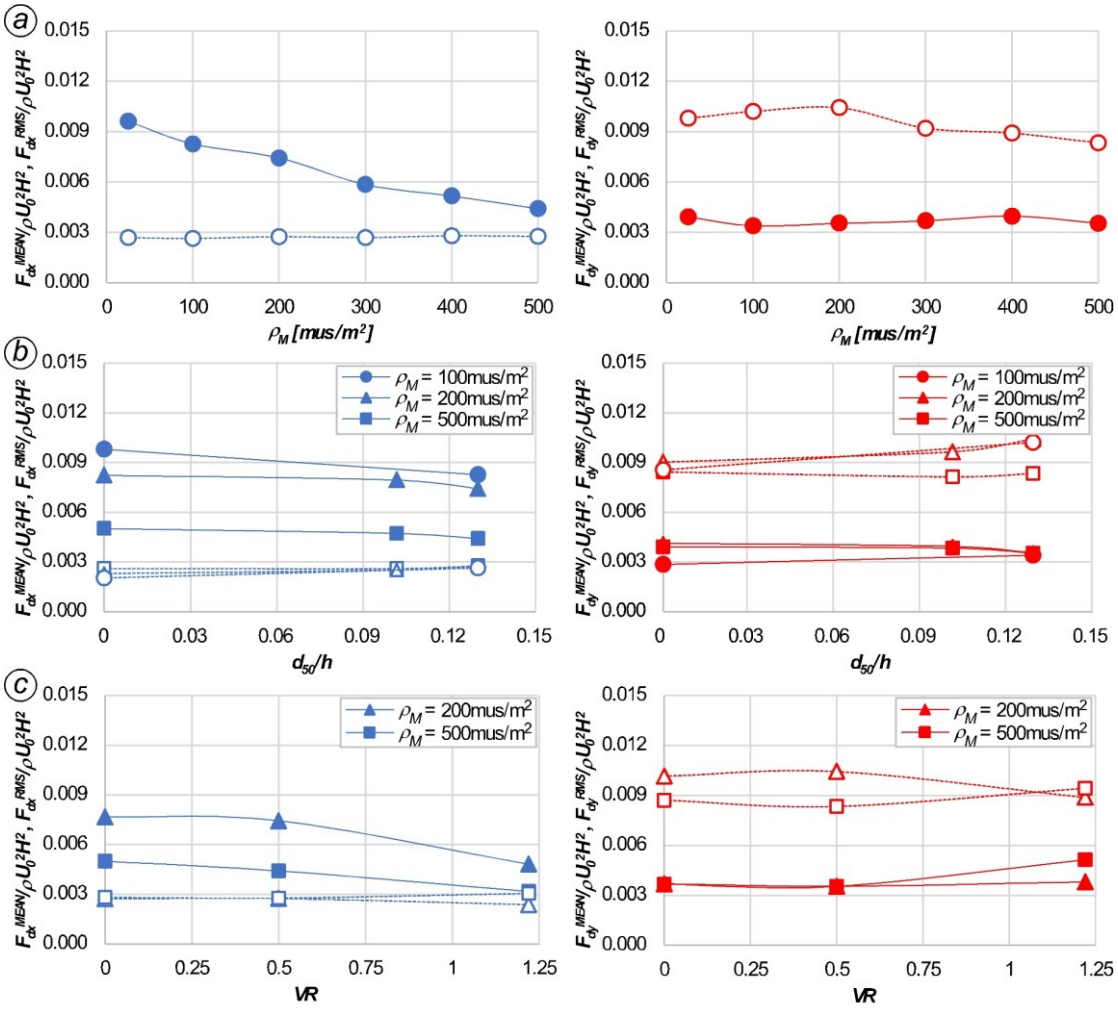

Figure 3-31. Mean (filled symbols) and RMS fluctuations (empty symbols) of non-dimensional mean drag forces (blue symbols refer to the x-direction, left; red symbols to the y-direction, right) as a function of a) mussel density ρ_M, b) bed roughness d_{50}/h (for three values of ρ_M), c) exhaling velocity ratio VR (for two values of ρ_M).

In the case of a low-density cluster of mussels (i.e., $\rho_M \leq 26$ mussel/m^2), the mean drag force in the streamwise direction, F_{dx}^{MEAN}, is similar to the value obtained for an isolated mollusk in Section 3.3 (Lazzarin et al., 2023a). F_{dx}^{MEAN} then decreases with increasing mussel density (Figure 3-31a). The average RMS fluctuations are roughly constant with the mussel density, and can be as high as 63% of the mean drag force for $\rho_M = 500$ mussel/m^2. In the spanwise direction, both the mean values and the RMS fluctuations are almost independent of the mussel density; interestingly, the spanwise averaged RMS fluctuations are nearly three times higher than both the mean values in the spanwise direction and the RMS fluctuations in the streamwise direction. This is an effect of the presence of neighboring shells influencing flow and turbulence in the roughness layer.

For a fixed value of mussel density, the bed roughness influences the drag forces slightly (Figure 3-31b). While F_{dy}^{MEAN} values are poorly influenced by bed roughness, small decrease of F_{dx}^{MEAN} are observed with increasing roughness. The average RMS fluctuations, both in x- and in y-directions, are observed to slightly increase with increasing roughness, probably due to the additional turbulence induced by the gravel bed.

When increasing the filtering velocity ratio, VR, the mean streamwise force, F_{dx}^{MEAN}, decreases. In particular, the rate of decrease is higher for high values of VR, in agreement to what observed for an isolated mussel in Sect. 3.3.6. The spanwise force, F_{dy}^{MEAN}, instead, slightly increase when increasing VR. No relevant variation as a function of VR are observed for the average RMS fluctuations.

The mean drag coefficient in the streamwise direction, for a single mussel of the cluster, is defined as $C_{dx}^{MEAN,i} = 2F_{dx}^{MEAN,i}/(\rho U_0^2 A_x^i)$, where $F_{dx}^{MEAN,i}$ is the mean drag force in the streamwise direction for the i-th mussel and A_x^i is the projected area of the emerged part of its shell (when a rough bed is considered, it depends on the topography around each single mussel). The value of the mean drag coefficient averaged on the number of mussels, C_{dx}^{MEAN}, follows the same trend observed for F_{dx}^{MEAN}, i.e., it strongly decreases with increasing ρ_M and it slightly decreases when increasing d_{50}/h or VR (Figure 3-32, filled symbols in left frames). The average RMS fluctuations of the drag coefficient, C_{dx}^{RMS}, are basically independent of the parameters here analyzed (Figure 3-32, open symbols in left frames).

Considering that the streamwise velocity in the lower part of the water column is generally reduced by the presence of increasingly denser mussel clusters, we computed the mean value of the streamwise velocity in the $z < h$ region, U_{inner} (Table 3-3). U_{inner} decreases with increasing mussel density, whereas it is roughly constant when varying d_{50}/h or VR. The streamwise drag coefficient C^*_{dx} has been computed replacing U_0 with U_{inner}. This expression for the drag coefficient can be more useful to compare the different cases as U_{inner} represents the real mean velocity approaching the shells. $C^*_{dx}{}^{MEAN}$ still decreases with increasing ρ_M, although at a lower rate if compared to the variation of C_{dx}^{MEAN} with mussel density (Figure 3-32a, filled symbols). $C^*_{dx}{}^{RMS}$, instead, increases with increasing mussel density (Figure 3-32a, empty symbols). When changing d_{50}/h or VR, $C^*_{dx}{}^{MEAN}$ and $C^*_{dx}{}^{RMS}$ exhibit the same trends as C_{dx}^{MEAN} and C_{dx}^{RMS} (Figure 3-32b,c).

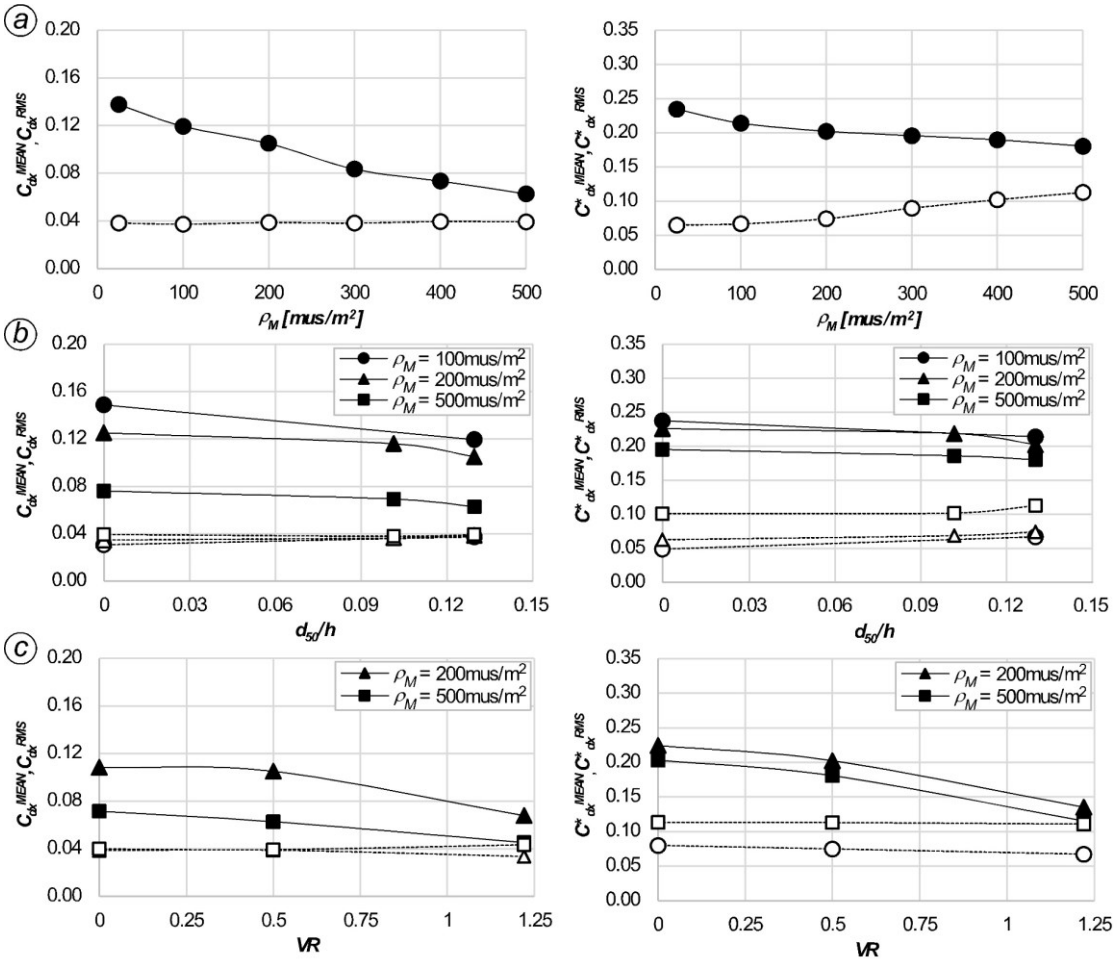

Figure 3-32. Mean (filled symbols) and RMS fluctuations (empty symbols) of the drag coefficient in the *x*-direction considering the mean velocity in the entire (C_{dx}, left) or in the inner region (C^*_{dx}, right), as a function of a) mussel density ρ_M, b) bed roughness d_{50}/h (for three values of ρ_M), c) exhaling velocity ratio VR (for two values of ρ_M).

The values of forces and of drag coefficients shown in in Figure 3-31 and in Figure 3-32, respectively, are averaged values for the whole mussel bed. However, strong variations of the forces are observed for the various mussels, as a function of their position in the array and of their relative sheltering. These variations of the drag forces correlate with strong spatial variations of the pressure fields on the mussels (see e.g., Figure 3-22).

Figure 3-33 describes the variability of the time-averaged drag coefficient in the x-direction, $C_{dx}^{MEAN,i}$, for four cases. It compares results for smooth (frames a,c) and rough (frames b,d) bed cases and results for a sparse (100 mussel/m², frames a,b) and for a dense (500 mussel/m², frames c,d) cluster of mussels. The drag coefficients for the individual mussels are grouped in bins and results are plotted in the form of a histogram showing the distribution of the drag coefficients for the mussels forming the cluster.

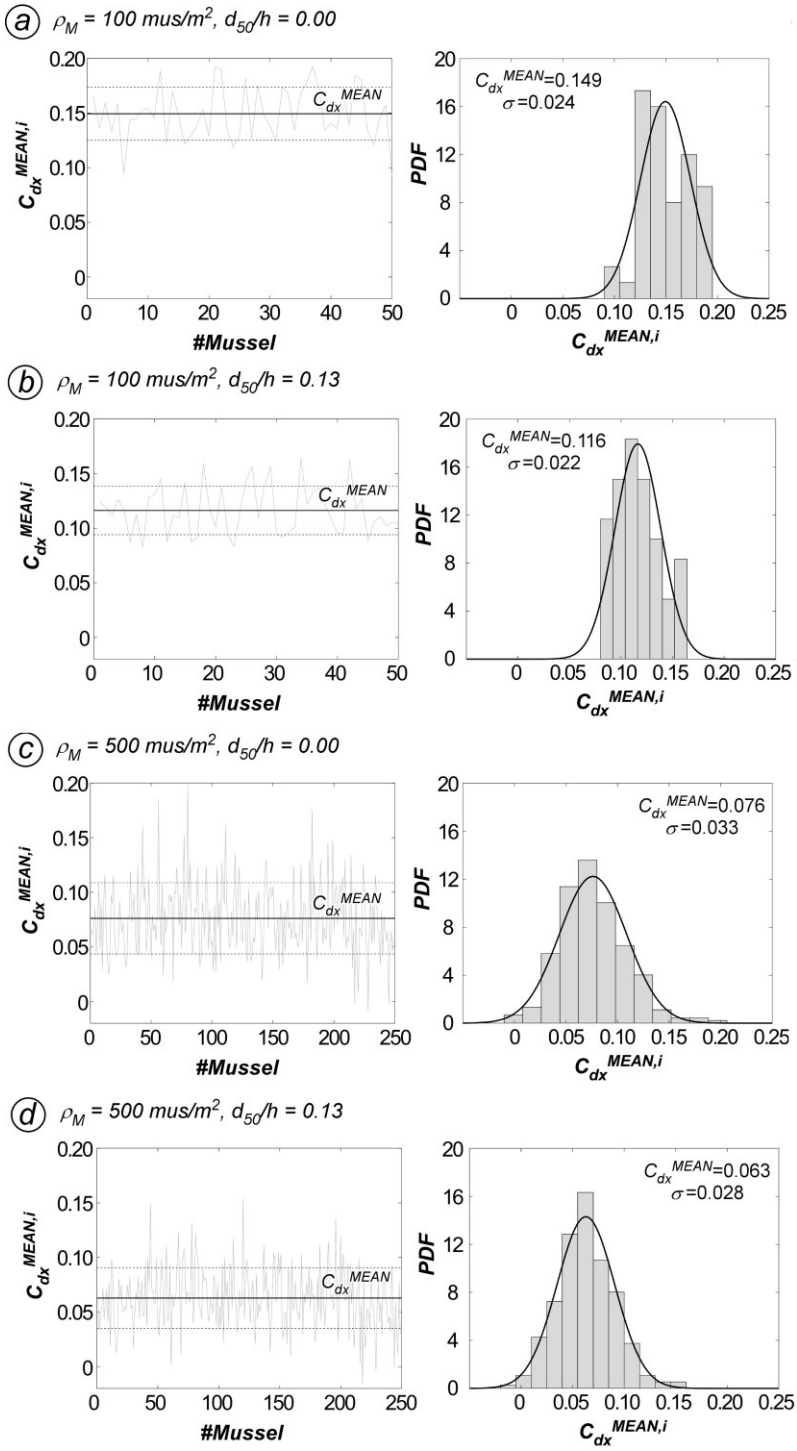

Figure 3-33. Streamwise (time-averaged) drag coefficients for the individual mussels forming the mussel bed for different simulations (a-d) with $VR = 0.5$. Also shown are the mean (cluster averaged) value and RMS fluctuations for the mussels in the cluster (left), the histogram of the drag coefficient for the mussels forming the cluster and comparison with the normal distribution (right).

For dense clusters, the histogram's shape is close to that of a Gaussian (symmetrical) distribution. For sparse clusters, the distribution is more irregular. The standard deviation increases with the mussel bed density and slightly decreases in the cases with a rough bed compared to the corresponding smooth-bed cases. In the case of dense cluster (ρ_m = 500 mussel/m²) and smooth bed (Figure 3-33c), $C_{dx}^{MEAN,i}$ ranges from 0.00 to 0.20. The larger variability observed for denser clusters is due to the increased mussel-to-mussel interactions, which produce an increased sheltering for some of the mussels forming the clusters. Indeed, when increasing the mussel density from 100 mussel/m² to 500 mussel/m² (see Figure 3-33), the maximum values of the drag coefficients remain almost the same, but the distribution shifts to the left, indicating that there is an increased number of mussels that experience a reduced drag compared to the sparser cluster. Increasing the bed roughness reduces the drag on the most exposed (i.e., less sheltered) mussels, thus reducing both the average drag and the standard deviation.

Though averaged values of the mean drag forces can be used to characterize the global effect of the flow on the mussel shells, these values do not offer a full characterization of the capacity of the individual mussels to resist dislocation from the substrate. Rather, the stability of each mussel in the array is controlled by the (maximum) instantaneous forces acting on its shell. DES simulations showed that these forces can be much higher than the cluster- and time-averaged values of drag forces because of *i)* a more exposed position within the array (i.e., mean force on the individual shell is significantly higher than the average value for the whole array), and *ii)* instantaneous large peaks induced by high RMS fluctuations on top of the mean drag value.

3.4.7 Bed Shear Stresses and Sediment Entrainment Capacity

Local scour in the vicinity of the shells is another factor that influences mussel stability, since the increased area exposed to the flow induces more severe drag forces on the shell that, along with a reduced anchoring within the bed, increases the probability of dislocation. The entrainment of bed particles is directly related to the shear stress acting on the bottom, which has been recognized to be among the key parameters controlling mussels abundance in natural streams (Daraio et al., 2010; French and Ackerman, 2014; Layzer and Madison, 1995).

In the case of gravel beds, particles entrainment is mostly driven by pressure forces acting on them. This requires to simulate hyporheic flow and to include more than just particles in contact with the overflow (e.g., Fang et al., 2018; Lian et al., 2019; Rosti et al., 2018), which is beyond the scope of the present study. However, for flat bed cases, one can study effect of mussels on entrainment from the bed based on bed shear stress distributions in mean and instantaneous flow (Cheng et al., 2018; Cheng and Constantinescu, 2022; Koken et al., 2013).

Figure 3-34 shows the instantaneous and the mean distributions of bed shear stresses for different mussel densities in case of a flat bed, scaled by the mean bed shear stress acting on the flatbed without mussels, τ_0. Regions of high bed shear stress are observed especially at the side of mussels because of the flow acceleration. A second region of high bed shear stresses is observed downstream of the mussels, approximatively at a distance

of $2H$ from the centre of the shell, just after the flow reattaches. For ρ_M = 100 mussel/m², the former region is visible for all the mussels; the latter region, instead, is visible only if the downstream neighbouring mussels are sufficiently spaced to let the flow reattach. For ρ_M = 500 mussel/m², both these regions are strongly reduced, and only small regions of high shear stresses are observed at the side of mussels. Hence, the mussel density has relevant implications on the value of the shear stress on the river bed.

To obtain an overall picture of the erosive capacity of the flow with varying mussel density for the flat bed cases, when the bed shear stress distribution can be easily calculated, the (peak) sediment entrainment potential is estimated using the sediment entrainment flux given by the empirical pick-up formula of van Rijn (1984):

$$E_\tau(t) = \frac{1}{A'}\int_{A'} \frac{(\tau - \tau_C)^{1.5}}{\rho^{1.5}\, U_0^3} dA \tag{3-4}$$

in which τ_c is the critical shear stress computed in the flat-bed simulations, (τ-τ_c) is the excess of bed shear stress, and A' is the net bed area (i.e., the portion of the bed without considering the mussel shells).

A rigorous application of such a formulation is limited to relatively large spatial scales with average stress values, thus it cannot be applied to the gravel-bed computations. Though τ_c is generally estimated with the Shields diagram as a function of the sediment size, here one has assumed $\tau_c = 0.0024\rho U_0^2$, i.e., slightly higher than τ_0.

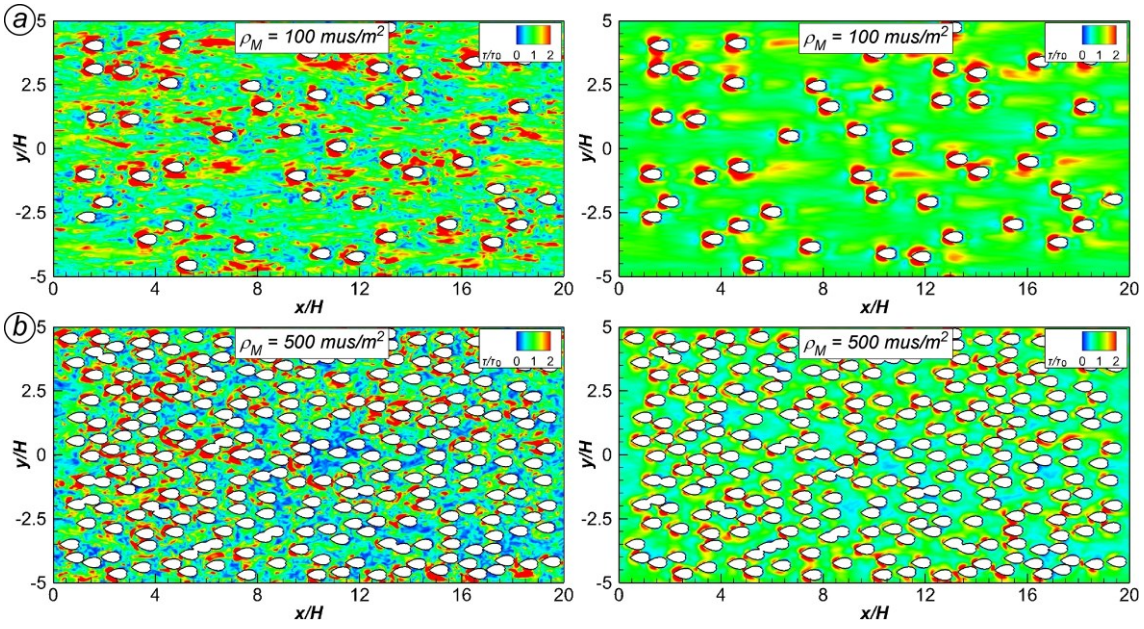

Figure 3-34. Instantaneous (left frame) and mean (right frame) bed shear stress, τ/τ_0, for the simulations with $d_{50}/h = 0$, $VR = 0.5$ and with ρ_M = 100 mussel/m² (a) and ρ_M = 500 mussel/m² (b).

As shown in Figure 3-35, the volumetric flux of entrained sediment, E_τ^{MEAN}, obtained by averaging in time the instantaneous values of the flux of entrained sediment, increases with the mussel bed density from 100 to 200 mussel/m². One should notice that E_τ^{MEAN} is smaller for 500 mussel/m² compared to 200 mussel/m², so one expects E_τ^{MEAN} will decrease with increasing ρ_M for very large mussel bed densities. The initial increase of E_τ^{MEAN} with ρ_M is associated with the larger number of mussels (i.e., each mussel generates a region of high bed shear stress on its sides while the stress magnitude remains nearly independent of the mussel density). For very high mussel densities, E_τ^{MEAN} decreases mainly because of the decay of the bed shear stresses at the sides of the mussels (Figure 3-34). When mussels are very close to each other, regions of high shear stress are rarely forming at both sides of each mussel (Figure 3-34), and a number of mussels are surrounded by regions with $\tau/\tau_0 < 1$. This explains why high-density clusters of mussels have a stabilizing effect for the river bed.

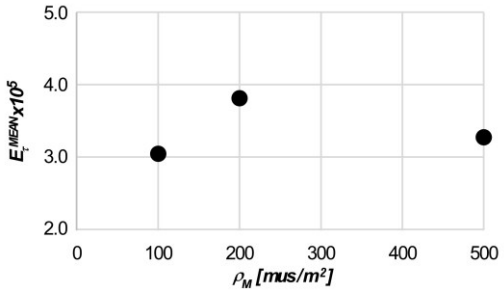

Figure 3-35. Time averaged volumetric flux of entrained sediment per unit bed area, E_τ^{MEAN}, as a function of the mussel density, ρ_M (with $d_{50}/h = 0$, $VR = 0.5$ and $\tau_c = 0.0024\rho U_0^2$)

3.4.8 Mixing between the water filtered by the mussels and the overflow

The transport of nutrients in the water flow is essential for mussel life. Water rich in nutrients is acquired from the inhaling siphon located in the upstream part of the mussel and depleted by the jet exiting from the excurrent siphon. For an isolated mussel, the amount of phytoplankton inside the water column depends on the external water flow and on the filtering activity, which in turn depends on the dynamics of the excurrent jet and its mixing with the overflow, and on the filtering velocity ratio. In the case of a mussel bed, the excurrent jet dynamics and mixing are further complicated because of mutual interactions with the other excurrent jets, especially for denser arrays. In a fully developed flow, the filtered water ejected by the mussels accumulates along the channel to form a boundary layer; this was the focus of previous experimental studies (e.g., Butman et al., 1994; O'Riordan et al., 1995).

The "inverse concentration" approach is here used to study the transport of nutrients and the distribution of clean water. This is the standard method used to study phytoplankton distribution in both laboratory and numerical investigations of flow over mussels (Crimaldi et al., 2007; Monismith et al., 1990; Wu et al., 2020). A concentration $C_0 = 1$ is prescribed at the exhaling siphon to represent clean, filtered water. At the channel inlet, C is set equal to zero to represent water containing nutrients and

phytoplankton. As the distance from the leading edge of the mussel bed increases, in the concentration of nutrients decreases and mussels inhale part of water that was already filtered by upstream mussels. According to the "inverse concentration" approach, in these simulations the passive scalar concentration increases with the x-coordinate and the refiltration fraction at the incurrent siphon, which measures the nutrient availability for each mussel (O'Riordan et al., 1993), is defined as $n = 1 - C$.

As another peculiarity of the present study, the simulations use periodic boundary conditions in the streamwise direction. Accordingly, the 1 m long domain represents an infinitely long channel in which the velocity field is statistically steady and (on average) uniform. However, the scalar concentration within the computational domain increases linearly with time because the passive scalar that exits at the downstream boundary re-enters the domain at the upstream section. This means that the change in time of the scalar concentration observed in the simulations represents how the concentration increases along a sufficiently long mussel bed. With this caution, the results from the numerical simulations can be used to infer qualitative trends in the changes of the scalar concentration profiles due to the variation of the different controlling variables (e.g., mussel array density, filtering velocity ratio).

Figure 3-36 shows the instantaneous concentration of the passive scalar, C/C_0, for a high-density array of mussels (ρ_M = 500 mussel/m²) in the $z/D \leq 2/3$ region. Jets of filtered water ($C/C_0 > 0$) are injected vertically in the water column by each excurrent siphon. At some distance streamwise, above the top of the mussels, the jets become aligned with the incoming flow (Figure 3-36a), similarly to the case of a single mussel in Section 3.3 (Lazzarin et al., 2023a). In the transversal sections of Figure 3-36b, the jets generated by the mussels located upstream of the plane are well visible.

The bed roughness has minor effect on the concentration fields (Lazzarin et al., 2023a), which become negligible for the higher mussel densities because the effect of the protruding parts of the shells prevails on that of the gravel particles at the bed. The results also show the different dynamics of jets depending on the exhaling velocity ratio, VR. As noticed in Section 3.3 (Lazzarin et al., 2023a), when increasing VR, the increased momentum of the jet implies a jet penetration to higher elevations and a longer distance needed to re-align with the incoming flow

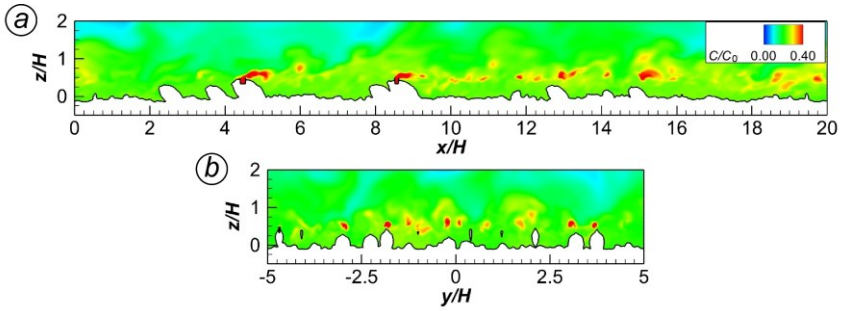

Figure 3-36. Instantaneous concentration of the passive scalar, C/C_0, at $t \cdot U^0/D$ = 50.3 in the y/H = -0.7 plane (a) and in the x/H = 10 plane (b) for the simulation with d_{50}/h = 0.13, VR = 0.5, ρ_M = 500 mussel/m².

The removal efficiency, R, is evaluated as the ratio of phytoplankton concentration at the incurrent siphon to that in the incoming flow. For a bed with N mussels with equal filtering discharge Q_i (= Q_{in} = Q_{ex}), and a water discharge Q, it is:

$$R = \frac{Q_i \sum_{i=1}^{N} (1-n)_i}{Q} \tag{3-5}$$

This value should be compared with an ideal removal efficiency, R_{ideal}, which does not account for refiltration and is defined as $R_{ideal} = NQ_i/Q$. For mussels situated in the downstream part of the channel, the water inhaled at their incurrent siphons is less rich in nutrient and phytoplankton (i.e., the concentration C is higher). So, the "filtering efficiency" of the downstream mussels is less compared to that of the upstream mussels. In the present simulations, the temporal decay of R inside the computational domain represents the streamwise decay of $R(x)$, computed between the leading edge of the mussel bed and the cross-section at the x coordinate.

The removal efficiency R increases with the mussel array density and with the filtering discharge (or equivalently, VR), as shown in Figure 3-37 and in Table 3-4. No appreciable differences are noticed when varying the bed roughness. The removal efficiency decreases with the distance because an increase in the refiltration, n (Figure 3-37). Data for the removal efficiency R obtained from the simulations has been interpolated using the following equation, which depends on R_{ideal} and on a calibrating coefficient p_C (see values in Table 3-4):

$$R\left(\frac{tU_0}{D}\right) = R_{ideal}\, e^{-p_C \frac{tU_0}{D}} \tag{3-6}$$

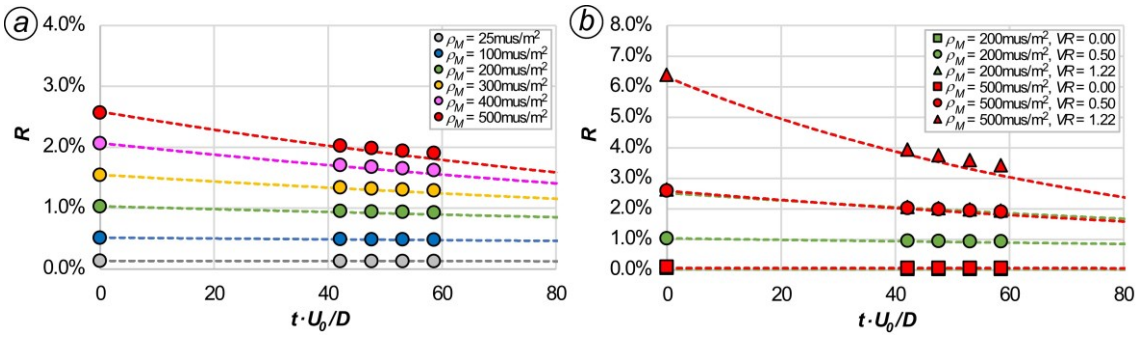

Figure 3-37. Values of the removal efficiency R at different times for different mussel densities, ρ_M (a), and exhaling velocity ratios, VR (b). Dashed lines are obtained using interpolating equation (3-6) with values of R_{ideal} and p_C given in Table 3-4. Time here is a proxy for the x-coordinate in a long channel, even though a precise relationship cannot be established because the development of the boundary layer is neglected.

Table 3-4. Characterization of the temporal evolution of the removal efficiency. Q_i is the filtering discharge (which is equal to the discharge through the inhaling siphon Q_{in} and through the exhaling siphon Q_{ex}), R is the removal efficiency (as a function of the length from the leading edge of the mussel bed, represented here through the non-dimensional time $t \cdot U_0/D$), R_{ideal} is the ideal removal efficiency, p_C is the calibration coefficient introduced in Eq. (3-6).

N	ρ_M	VR	$Q_i = Q_{in} = Q_{ex}$	R $(t \cdot U_0/D=42.1)$	R $(t \cdot U_0/D=47.6)$	R $(t \cdot U_0/D=53.1)$	R $(t \cdot U_0/D=58.6)$	R_{ideal}	p_C
13	26	0.5	1.3E-06	0.13%	0.13%	0.13%	0.13%	0.13%	0.0004
50	100	0.5	1.3E-06	0.49%	0.49%	0.49%	0.49%	0.52%	0.0013
100	200	0.5	1.3E-06	0.95%	0.95%	0.94%	0.93%	1.04%	0.0024
150	300	0.5	1.3E-06	1.34%	1.33%	1.31%	1.29%	1.55%	0.0037
200	400	0.5	1.3E-06	1.71%	1.68%	1.65%	1.63%	2.07%	0.0048
250	500	0.5	1.3E-06	2.03%	1.99%	1.94%	1.91%	2.59%	0.0061
100	200	0	3.3E-08	0.03%	0.03%	0.03%	0.03%	0.03%	0.0001
100	200	1.22	3.1E-06	2.06%	2.02%	1.98%	1.94%	2.53%	0.0051
250	500	0	3.3E-08	0.07%	0.07%	0.07%	0.07%	0.07%	0.0002
250	500	1.22	3.1E-06	3.94%	3.75%	3.59%	3.42%	6.32%	0.0122

For $t \cdot U_0/D = 0$, $R = R_{ideal}$ as all mussels inhale water rich in phytoplankton. When moving along the channel (i.e., as time passes in the periodic simulations), R decreases at a rate that is proportional to the number of mussels and to their filtering discharge. Table 3-4 shows that for $t \cdot U_0/D = 42 \div 58$ small differences are observed between R and R_{ideal} for low mussel densities and/or low filtering discharge. When increasing ρ_M or VR, differences increase. For example, in the simulation with $\rho_M = 500$ mussel/m² and $VR = 1.22$, R is 62÷54% of R_{ideal} in the analyzed interval.

3.5 Discussion and Conclusions

The present study used eddy-resolving numerical simulations to investigate the open channel flow and the turbulence structures over isolated specimens and arrays of freshwater mussels partially-burrowed on smooth and rough beds.

Mussels were partially buried in a gravel bed to provide a more accurate representation of the substrates in which they are typically buried in. This extends the study of Wu et al. (2020a) who focused on an isolated freshwater mussel of a different species placed on a horizontal, smooth bed. Since mussels are common in sand and gravel bed rivers, understanding the influence of varying bed roughness is of particular importance to characterize the interactions between the mussels and the flow at the organism level.

As mussels typically form aggregations of different density, understanding how the mussel-to-mussel interactions affect the near bed flow, the drag forces, the bed shear stress and the mixing of exhaling jet is also of particular importance to provide realistic descriptions to be used for preserving mussels in river systems. In this case, the analysis focused on the fully developed flow regime observed at large distances from the leading

edge of a long mussel bed, way downstream of the location where the internal boundary layer induced by the mussels reaches the free surface.

3.5.1 Isolated mussels

Results of the simulations with an isolated mussel showed that the bed roughness influences the structure of the vortices forming near the shells. In the case of a smooth bed a symmetric shedding prevails because of the streamlined shape of the *Unio Elongatulus* mussel and the downflow in the symmetry axis past the shell. When increasing bed roughness, the antisymmetric shedding mode gradually becomes dominant, because eddies induced by bed particles break the symmetry of vortices forming in the wake of the mussels, and reduce their coherence.

The simulations also showed that for constant filtering ratio and burrowing level, the mean streamwise drag coefficient increases with increasing bed roughness. This means that the stability of an exposed, isolated mussel decreases in case of a gravel bed. On the other hand, the volumetric flux of the excurrent jet increases with increasing bed roughness, thus enhancing the mixing of a passive scalar injected in the flow through the exhaling siphon.

The simulations with a flat bed and the comparisons with results of Wu et al. (2020a) also showed that the vortices forming at the mussels and their dynamics are strongly dependent on the shape of the emerged part of the shell and on its orientation. Differently from the case studied by Wu et al. (2020a), the present analysis on a *Unio Elongatulus* mussel showed that an elongated region of very strong downflow forms near the symmetry plane, that tip vortices form in the wake and that no horseshoe vortices form around the upstream base of the mussel. It can be concluded that the exposed part of the mussel shell controls the type and coherence of the streamwise vortices forming in the wake, which in turn determines what shedding mode is dominant in the wake.

The study considered also the effect of the filtering activity of the mussel, considering a large range of the velocity ratio between the excurrent siphon velocity and the mean velocity in the overflow ($0 \leq VR \leq 1.22$). The present investigation found that the streamwise drag force increases with increasing VR when the active filtering is turned on (e.g., for $0 < VR < 0.61$). However, the predicted values obtained in simulations conducted with $VR = 1.22$, suggest that the effect of increasing VR on C_{dx}^{MEAN} changes around $VR = 1$ and that mussels can reduce the drag force acting on them and the probability to be displaced by the overflow by increasing their filtering levels.

3.5.2 Musselbeds

Simulations of fully developed flow over musselbeds showed that increasing mussel bed density for constant level of mussel burrowing has notable consequences on the flow field and turbulence structure.

Besides the decrease of longitudinal velocity in the mussel region, in dense clusters of mussels the downflow observed at the back of the mussel for an isolated specimen is strongly reduced. The dynamics of the vortices have been also shown to be influenced

by the mussel density. While jets from the excurrent siphons are qualitatively similar to those observed for an isolated mussel, tip vortices developed at the back of the shells are strongly dampened by the presence of other shells. The effect of bed roughness, which has been shown to be significant for isolated specimens and for clusters with sparse shells, becomes progressively less important increasing the mussel density as the near-bed flow is controlled by the roughness associated with the protruding shells rather than by the bed particles. In case of the clusters with high densities considered in this study, bed roughness marginally affects the flow.

Increasing mussel density also reduces the average values of the mean drag forces on the shells, which is beneficial for the stability of the mussels. In any case, large variations of the mean drag force on the individual shells have been observed as a function of the mussel position in the array, as some of the shells showed mean forces as high as twice the array-averaged values. Simulations with smooth beds also showed that clusters with very high mussel density reduce bed shear stress. While in sparse cluster the sediment entrainment potential of the flow increases with increasing number of mussels, it decays at higher densities when mussels are very close to each other. Both the reduced drag forces and the reduced entrainment potential highlight that sufficiently dense cluster of mussels can be of help for mussel stability and conservation. The present study, in which all mussels were aligned with the incoming flow, showed also that the spanwise drag forces and the associated fluctuations can be significant, especially for large mussel bed densities where the flow approaching each mussel can be not aligned with the shell because of mussel sheltering. For ρ_M = 500 mussel/m², the mean drag forces have been observed to become comparable in the streamwise and spanwise directions, and the RMS fluctuations of the drag force larger along the spanwise direction.

Values of the drag coefficients obtained from the present simulations can be used in reduced-order models to characterize the averaged roughness of mussel beds through extra drag terms in the momentum equations within the roughness layer, interpreted as a porous layer. These simplified approaches, known as momentum forcing approaches, are computationally less expensive as they account for the presence of musselbeds without the need of explicitly solving the flow around the shells, similarly to what proposed for vegetation (e.g., Etminan et al., 2017; Kim and Stoesser, 2011).

The dynamics of the excurrent jets was found to be relatively similar for different mussel densities. However, the availability of nutrients, represented by the passive scalar concentration, can be highly reduced by the presence of other mussels in the cluster. In particular, the removal efficiency decreases with the streamwise distance at a higher rate for higher mussel density or high filtering activity of the mollusks.

3.5.3 Limitations and future goals

The present work considered relatively high submergence ratios and impermeable substrates, neglecting the hyporheic flow. Further research is needed to understand how flow and turbulent structures, as well as drag forces, change when the free surface is strongly deformed by the presence of the shells, or when mussels start interacting with the free surface. Simulations conducted with a permeable bed can also be of help to

assess the role of the hyporheic flow, and to understand to what extent it affects the flow approaching the mussels.

The present work considered only mussel beds composed by specimens all equal each other, whereas in natural streams heterogeneous and dynamic conditions are observed (i.e., beds with live mussels of different dimensions, orientation, burrowing height, filtering activity, etc.). Further research on these topics is need also to investigate more complex case to understanding how the flow physics and the drag forces acting on the individual shells forming the musselbed change. This should be complemented also by experiment measurement, to understand the threshold of mussel dislocation for a given shape of the shell and a given material of the substrate. This information is critical to predict how flow conditions can affect the stability of the mussels.

3.6 References

Allen, D.C., Vaughn, C.C., 2009. Burrowing behavior of freshwater mussels in experimentally manipulated communities. J. North Am. Benthol. Soc. 28, 93–100. https://doi.org/10.1899/07-170.1

Atkinson, C.L., Vaughn, C.C., 2015. Biogeochemical hotspots: temporal and spatial scaling of the impact of freshwater mussels on ecosystem function. Freshw. Biol. 60, 563–574. https://doi.org/10.1111/fwb.12498

Blettler, M., Sukhodolov, A., Tockner, K., 2010. Hydraulic conditions over bed forms control the benthic fauna distribution in a lowland river (Spree River, Germany). River Flow 2010 1463–1468.

Bunt, C.M., Maclsaac, H.J., Sprules, W.G., 1993. Pumping Rates and Projected Filtering Impacts of Juvenile Zebra Mussels (Dreissena polymorpha) in Western Lake Erie. Can. J. Fish. Aquat. Sci. 50, 1017–1022. https://doi.org/10.1139/f93-117

Butman, C.A., Fréchette, M., Geyer, W.R., Starczak, V.R., 1994. Flume experiments on food supply to the blue mussel Mytilus edulis L. as a function of boundary-layer flow. Limnol. Oceanogr. 39, 1755–1768. https://doi.org/10.4319/lo.1994.39.7.1755

Chang, K., Constantinescu, G., 2013. Coherent structures in flow over two-dimensional dunes. Water Resour. Res. 49, 2446–2460. https://doi.org/10.1002/wrcr.20239

Chang, K., Constantinescu, G., Park, S.-O., 2007a. Assessment of Predictive Capabilities of Detached Eddy Simulation to Simulate Flow and Mass Transport Past Open Cavities. J. Fluids Eng. 129, 1372–1383. https://doi.org/10.1115/1.2786529

Chang, K., Constantinescu, G., Park, S.-O., 2007b. Purging of a Neutrally Buoyant or a Dense Miscible Contaminant from a Rectangular Cavity. II: Case of an Incoming Fully Turbulent Overflow. J. Hydraul. Eng. 133, 373–385. https://doi.org/10.1061/(ASCE)0733-9429(2007)133:4(373)

Chang, W.-Y., Constantinescu, G., Tsai, W.-F., 2020. Effect of array submergence on flow and coherent structures through and around a circular array of rigid vertical cylinders. Phys. Fluids 32, 035110. https://doi.org/10.1063/1.5138604

Chen, Y., DiBiase, R.A., McCarroll, N., Liu, X., 2019. Quantifying flow resistance in mountain streams using computational fluid dynamics modeling over structure-from-motion photogrammetry-derived microtopography. Earth Surf. Process. Landf. 44, 1973–1987. https://doi.org/10.1002/esp.4624

Cheng, Z., Constantinescu, G., 2022. Shallow mixing interfaces between parallel streams of unequal densities. J. Fluid Mech. 945, A2. https://doi.org/10.1017/jfm.2022.505

Cheng, Z., Koken, M., Constantinescu, G., 2018. Approximate methodology to account for effects of coherent structures on sediment entrainment in RANS simulations with a movable bed and applications to pier scour. Adv. Water Resour. 120, 65–82. https://doi.org/10.1016/j.advwatres.2017.05.019

Constantinescu, G., 2014. LE of shallow mixing interfaces: A review. Environ. Fluid Mech. 14, 971–996. https://doi.org/10.1007/s10652-013-9303-6

Constantinescu, G., Chapelet, M., Squires, K., 2003. Turbulence Modeling Applied to Flow over a Sphere. AIAA J. 41, 1733–1742. https://doi.org/10.2514/2.7291

Constantinescu, G., Miyawaki, S., Liao, Q., 2013. Flow and Turbulence Structure past a Cluster of Freshwater Mussels. J. Hydraul. Eng. 139, 347–358. https://doi.org/10.1061/(ASCE)HY.1943-7900.0000692

Constantinescu, G., Squires, K.D., 2003. LES and DES Investigations of Turbulent Flow over a Sphere at Re = 10,000. Flow Turbul. Combust. 70, 267–298. https://doi.org/10.1023/B:APPL.0000004937.34078.71

Crimaldi, J.P., Koseff, J.R., Monismith, S.G., 2007. Structure of mass and momentum fields over a model aggregation of benthic filter feeders. Biogeosciences 4, 269–282. https://doi.org/10.5194/bg-4-269-2007

Crimaldi, J.P., Thompson, J.K., Rosman, J.H., Lowe, R.J., Koseff, J.R., 2002. Hydrodynamics of larval settlement: The influence of turbulent stress events at potential recruitment sites. Limnol. Oceanogr. 47, 1137–1151. https://doi.org/10.4319/lo.2002.47.4.1137

Daraio, J.A., Weber, L.J., Newton, T.J., 2010. Hydrodynamic modeling of juvenile mussel dispersal in a large river: the potential effects of bed shear stress and other parameters. J. North Am. Benthol. Soc. 29, 838–851. https://doi.org/10.1899/09-118.1

Dey, S., 2003. Incipient Motion of Bivalve Shells on Sand Beds under Flowing Water. J. Eng. Mech. 129, 232–240. https://doi.org/10.1061/(ASCE)0733-9399(2003)129:2(232)

Di Maio, J., Corkum, L.D., 1997. Patterns of orientation in unionids as a function of rivers with differing hydrological variability. J. Molluscan Stud. 63, 531–539. https://doi.org/10.1093/mollus/63.4.531

Diedericks, G.P.J., Troch, C.N.A., Smit, G.J.F., 2018. Incipient Motion of Shells and Shell Gravel. J. Hydraul. Eng. 144, 06017030. https://doi.org/10.1061/(ASCE)HY.1943-7900.0001421

Doucet, C.V., Labaj, A.L., Kurek, J., 2021. Microfiber Content in Freshwater Mussels from Rural Tributaries of the Saint John River, Canada. Water. Air. Soil Pollut. 232, 32. https://doi.org/10.1007/s11270-020-04958-4

Engelhardt, C., Krüger, A., Sukhodolov, A., Nicklisch, A., 2004. A study of phytoplankton spatial distributions, flow structure and characteristics of mixing in a river reach with groynes. J. Plankton Res. 26, 1351–1366. https://doi.org/10.1093/plankt/fbh125

Etminan, V., Lowe, R.J., Ghisalberti, M., 2017. A new model for predicting the drag exerted by vegetation canopies. Water Resour. Res. 53, 3179–3196. https://doi.org/10.1002/2016WR020090

Fang, H., Han, X., He, G., Dey, S., 2018. Influence of permeable beds on hydraulically macro-rough flow. J. Fluid Mech. 847, 552–590. https://doi.org/10.1017/jfm.2018.314

Ferreira-Rodríguez, N., Akiyama, Y.B., Aksenova, O.V., Araujo, R., Christopher Barnhart, M., Bespalaya, Y.V., Bogan, A.E., Bolotov, I.N., Budha, P.B., Clavijo, C., Clearwater, S.J., Darrigran, G., Do, V.T., Douda, K., Froufe, E., Gumpinger, C., Henrikson, L., Humphrey, C.L., Johnson, N.A., Klishko, O., Klunzinger, M.W., Kovitvadhi, S., Kovitvadhi, U., Lajtner, J., Lopes-Lima, M., Moorkens, E.A., Nagayama, S., Nagel, K.-O., Nakano, M., Negishi, J.N., Ondina, P., Oulasvirta, P., Prié, V., Riccardi, N., Rudzīte, M., Sheldon, F., Sousa, R., Strayer, D.L., Takeuchi, M., Taskinen, J., Teixeira, A., Tiemann, J.S., Urbańska, M., Varandas, S., Vinarski, M.V., Wicklow, B.J., Zając, T., Vaughn, C.C., 2019. Research priorities for freshwater mussel conservation assessment. Biol. Conserv. 231, 77–87. https://doi.org/10.1016/j.biocon.2019.01.002

French, S.K., Ackerman, J.D., 2014. Responses of newly settled juvenile mussels to bed shear stress: implications for dispersal. Freshw. Sci. 33, 46–55. https://doi.org/10.1086/674983

Froufe, E., Lopes-Lima, M., Riccardi, N., Zaccara, S., Vanetti, I., Lajtner, J., Teixeira, A., Varandas, S., Prié, V., Zieritz, A., Sousa, R., Bogan, A.E., 2017. Lifting the curtain on the freshwater mussel diversity of the Italian Peninsula and Croatian Adriatic coast. Biodivers. Conserv. 26, 3255–3274. https://doi.org/10.1007/s10531-017-1403-z

Gutiérrez, J.L., Jones, C.G., Strayer, D.L., Iribarne, O.O., 2003. Mollusks as ecosystem engineers: the role of shell production in aquatic habitats. Oikos 101, 79–90. https://doi.org/10.1034/j.1600-0706.2003.12322.x

Haag, W.R., 2012. North American freshwater mussels: natural history, ecology, and conservation, Cambridge University Press. ed.

Hajimirzaie, S.M., Buchholz, J.H.J., 2013. Flow dynamics in the wakes of low-aspect-ratio wall-mounted obstacles. Exp. Fluids 54, 1616. https://doi.org/10.1007/s00348-013-1616-1

Hajimirzaie, S.M., Wojcik, C.J., Buchholz, J.H.J., 2012. The role of shape and relative submergence on the structure of wakes of low-aspect-ratio wall-mounted bodies. Exp. Fluids 53, 1943–1962. https://doi.org/10.1007/s00348-012-1406-1

Hajisafarali, M., Aaltonen, S., Pulkkinen, K., Taskinen, J., 2022. Does the freshwater mussel Anodonta anatina remove the fish pathogen Flavobacterium columnare from water? Hydrobiologia 849, 1067–1081. https://doi.org/10.1007/s10750-021-04769-6

Heinz, S., 2020. A review of hybrid RANS-LES methods for turbulent flows: Concepts and applications. Prog. Aerosp. Sci. 114, 100597. https://doi.org/10.1016/j.paerosci.2019.100597

Horna-Munoz, D., Constantinescu, G., 2018. A fully 3-D numerical model to predict flood wave propagation and assess efficiency of flood protection measures. Adv. Water Resour. 122, 148–165. https://doi.org/10.1016/j.advwatres.2018.10.014

Howard, J.K., Cufey, K.M., 2006. The functional role of native freshwater mussels in the fluvial benthic environment. Freshw. Biol. 51, 460–474. https://doi.org/10.1111/j.1365-2427.2005.01507.x

Keylock, C.J., Constantinescu, G., Hardy, R.J., 2012. The application of computational fluid dynamics to natural river channels: Eddy resolving versus mean flow approaches. Geomorphology 179, 1–20. https://doi.org/10.1016/j.geomorph.2012.09.006

Keylock, C.J., Hardy, R.J., Parsons, D.R., Ferguson, R.I., Lane, S.N., Richards, K.S., 2005. The theoretical foundations and potential for large-eddy simulation (LES) in fluvial geomorphic and sedimentological research. Earth-Sci. Rev. 71, 271–304. https://doi.org/10.1016/j.earscirev.2005.03.001

Kim, S.J., Stoesser, T., 2011. Closure modeling and direct simulation of vegetation drag in flow through emergent vegetation. Water Resour. Res. 47. https://doi.org/10.1029/2011WR010561

Kirkil, G., Constantinescu, G., 2009. Nature of flow and turbulence structure around an in-stream vertical plate in a shallow channel and the implications for sediment erosion. Water Resour. Res. 45. https://doi.org/10.1029/2008WR007363

Koken, M., Constantinescu, G., 2021. Flow structure inside and around a rectangular array of rigid emerged cylinders located at the sidewall of an open channel. J. Fluid Mech. 910, A2. https://doi.org/10.1017/jfm.2020.900

Koken, M., Constantinescu, G., 2009. An investigation of the dynamics of coherent structures in a turbulent channel flow with a vertical sidewall obstruction. Phys. Fluids 21, 085104. https://doi.org/10.1063/1.3207859

Koken, M., Constantinescu, G., Blanckaert, K., 2013. Hydrodynamic processes, sediment erosion mechanisms, and Reynolds-number-induced scale effects in an open channel bend of strong curvature with flat bathymetry. J. Geophys. Res. Earth Surf. 118, 2308–2324. https://doi.org/10.1002/2013JF002760

Kreeger, D.A., Gatenby, C.M., Bergstrom, P.W., 2018. Restoration Potential of Several Native Species of Bivalve Molluscs for Water Quality Improvement in Mid-Atlantic Watersheds. J. Shellfish Res. 37, 1121–1157. https://doi.org/10.2983/035.037.0524

Kryger, J., Riisgård, H.U., 1988. Filtration rate capacities in 6 species of European freshwater bivalves. Oecologia 77, 34–38. https://doi.org/10.1007/BF00380921

Kumar, S.S., Kozarek, J., Hornbach, D., Hondzo, M., Hong, J., 2019. Experimental investigation of turbulent flow over live mussels. Environ. Fluid Mech. 19, 1417–1430. https://doi.org/10.1007/s10652-019-09664-2

Lacey, R.W.J., Rennie, C.D., 2012. Laboratory Investigation of Turbulent Flow Structure around a Bed-Mounted Cube at Multiple Flow Stages. J. Hydraul. Eng. 138, 71–84. https://doi.org/10.1061/(ASCE)HY.1943-7900.0000476

Layzer, J.B., Madison, L.M., 1995. Microhabitat use by freshwater mussels and recommendations for determining their instream flow needs. Regul. Rivers Res. Manag. 10, 329–345. https://doi.org/10.1002/rrr.3450100225

Lazzarin, T., Constantinescu, G., Di Micco, L., Wu, H., Lavignani, F., Lo Brutto, M., Termini, D., Viero, D.P., 2023a. Influence of bed roughness on flow and turbulence structure around a 2 partially-buried, isolated freshwater mussel. Water Resour. Res. 59, e2022WR034151. https://doi.org/10.1029/2022WR034151

Lazzarin, T., Viero, D.P., Defina, A., Cozzolino, L., 2023b. Flow under vertical sluice gates: Flow stability at large gate opening and disambiguation of partial dam-break multiple solutions. Phys. Fluids 35, 024114. https://doi.org/10.1063/5.0131953

Lian, Y.P., Dallmann, J., Sonin, B., Roche, K.R., Liu, W.K., Packman, A.I., Wagner, G.J., 2019. Large eddy simulation of turbulent flow over and through a rough permeable bed. Comput. Fluids 180, 128–138. https://doi.org/10.1016/j.compfluid.2018.12.015

Lohrer, A.M., Thrush, S.F., Gibbs, M.M., 2004. Bioturbators enhance ecosystem function through complex biogeochemical interactions. Nature 431, 1092–1095. https://doi.org/10.1038/nature03042

Lopes-Lima, M., Sousa, R., Geist, J., Aldridge, D.C., Araujo, R., Bergengren, J., Bespalaya, Y., Bódis, E., Burlakova, L., Van Damme, D., Douda, K., Froufe, E., Georgiev, D., Gumpinger, C., Karatayev, A., Kebapçi, Ü., Killeen, I., Lajtner, J., Larsen, B.M., Lauceri, R., Legakis, A., Lois, S., Lundberg, S., Moorkens, E., Motte, G., Nagel, K.-O., Ondina, P., Outeiro, A., Paunovic, M., Prié, V., von Proschwitz, T., Riccardi, N., Rudzīte, M., Rudzītis, M., Scheder, C., Seddon, M., Şereflişan, H., Simić, V., Sokolova, S., Stoeckl, K., Taskinen, J., Teixeira, A., Thielen, F., Trichkova, T., Varandas, S., Vicentini, H., Zajac, K., Zajac, T., Zogaris, S., 2017. Conservation status of freshwater mussels in Europe: state of the art and future challenges. Biol. Rev. 92, 572–607. https://doi.org/10.1111/brv.12244

Lopez, J.W., DuBose, T.P., Franzen, A.J., Atkinson, C.L., Vaughn, C.C., 2022. Long-term monitoring shows that drought sensitivity and riparian land use change coincide with freshwater mussel declines. Aquat. Conserv. Mar. Freshw. Ecosyst. 32, 1571–1583. https://doi.org/10.1002/aqc.3884

Lopez, J.W., Vaughn, C.C., 2021. A review and evaluation of the effects of hydrodynamic variables on freshwater mussel communities. Freshw. Biol. 66, 1665–1679. https://doi.org/10.1111/fwb.13784

Lydeard, C., Cowie, R.H., Ponder, W.F., Bogan, A.E., Bouchet, P., Clark, S.A., Cummings, K.S., Frest, T.J., Gargominy, O., Herbert, D.G., Hershler, R., Perez, K.E., Roth, B., Seddon, M., Strong, E.E., Thompson, F.G., 2004. The Global Decline of Nonmarine Mollusks. BioScience 54, 321–330. https://doi.org/10.1641/0006-3568(2004)054[0321:TGDONM]2.0.CO;2

Mahesh, K., 2013. The Interaction of Jets with Crossflow. Annu. Rev. Fluid Mech. 45, 379–407. https://doi.org/10.1146/annurev-fluid-120710-101115

Marion, A., Nikora, V., Puijalon, S., Bouma, T., Koll, K., Ballio, F., Tait, S., Zaramella, M., Sukhodolov, A., O'Hare, M., Wharton, G., Aberle, J., Tregnaghi, M., Davies, P., Nepf, H., Parker, G., Statzner, B., 2014. Aquatic interfaces: a hydrodynamic and ecological perspective. J. Hydraul. Res. 52, 744–758. https://doi.org/10.1080/00221686.2014.968887

Marrone, F., Gianbattista, N., Cianfanelli, S., Govedic, M., Barra, S., Arculeo, M., Bodon, M., 2019. Diversity and taxonomy of the genus Unio Philipsson in Italy, with the designation of a neotype for Unio elongatulus C. Pfeiffer (Mollusca, Bivalvia, Unionidae). Zootaxa 4545, 339–374. https://doi.org/10.11646/zootaxa.4545.3.2

McCoy, A., Constantinescu, G., Weber, L., 2007. A numerical investigation of coherent structures and mass exchange processes in channel flow with two lateral submerged groynes. Water Resour. Res. 43. https://doi.org/10.1029/2006WR005267

Menter, F., 1994. Two-equation eddy-viscosity turbulence models for engineering applications. AIAA J. 32, 1598–1605. https://doi.org/10.2514/3.12149

Menter, F., Hüppe, A., Matyushenko, A., Kolmogorov, D., 2021. An Overview of Hybrid RANS–LES Models Developed for Industrial CFD. Appl. Sci. 11. https://doi.org/10.3390/app11062459

Menter, F., Kuntz, M., Langtry, R., 2003. Ten years of industrial experience with the SST turbulence model. Heat Mass Transf. 625–632.

Modesto, V., Tosato, L., Pilbala, A., Benistati, N., Fraccarollo, L., Termini, D., Manca, D., Moramarco, T., Sousa, R., Riccardi, N., 2023. Mussel behaviour as a tool to measure the impact of hydrodynamic stressors. Hydrobiologia 850, 807–820. https://doi.org/10.1007/s10750-022-05126-x

Monismith, S.G., Koseff, J.R., Thompson, J.K., O'Riordan, C.A., Nepf, H.M., 1990. A study of model bivalve siphonal currents. Limnol. Oceanogr. 35, 680–696. https://doi.org/10.4319/lo.1990.35.3.0680

Morales, Y., Weber, L.J., Mynett, A.E., Newton, T.J., 2006. Effects of substrate and hydrodynamic conditions on the formation of mussel beds in a large river. J. North Am. Benthol. Soc. 25, 664–676. https://doi.org/10.1899/0887-3593(2006)25[664:EOSAHC]2.0.CO;2

Nakato, T., Christensen, J., Schonhoff, B., 2007. Freshwater mussel survey in pool 16, the mississippi river, near fairport, Iowa: Rm 463.5-rm 464.1, approximately. IIHR Technical Report 464, The University of Iowa, IIHR-Hydroscience ….

Newton, T.J., Woolnough, D.A., Strayer, D.L., 2008. Using landscape ecology to understand and manage freshwater mussel populations. J. North Am. Benthol. Soc. 27, 424–439. https://doi.org/10.1899/07-076.1

Nikora, V., 2010. Hydrodynamics of aquatic ecosystems: An interface between ecology, biomechanics and environmental fluid mechanics. River Res. Appl. 26, 367–384. https://doi.org/10.1002/rra.1291

Nikora, V., Green, M., Thrush, S., Hume, T., Goring, D., 2002. Structure of the internal boundary layer over a patch of horse mussels (Atrina zelandica) in an estuary. J. Mar. Res. 60, 121–150. https://doi.org/10.1357/002224002762341276

Nishizaki, M., Ackerman, J.D., 2017. Mussels blow rings: Jet behavior affects local mixing. Limnol. Oceanogr. 62, 125–136. https://doi.org/10.1002/lno.10380

O'Riordan, C.A., Monismith, S.G., Koseff, J.R., 1995. The effect of bivalve excurrent jet dynamics on mass transfer in a benthic boundary layer. Limnol. Oceanogr. 40, 330–344. https://doi.org/10.4319/lo.1995.40.2.0330

O'Riordan, C.A., Monismith, S.G., koseff, J.R., 1993. A study of concentration boundary-layer formation over a bed of model bivalves. Limnol. Oceanogr. 38, 1712–1729. https://doi.org/10.4319/lo.1993.38.8.1712

Papanicolaou, A.N. (Thanos), Tsakiris, A.G., Wyssmann, M.A., Kramer, C.M., 2018. Boulder Array Effects on Bedload Pulses and Depositional Patches. J. Geophys. Res. Earth Surf. 123, 2925–2953. https://doi.org/10.1029/2018JF004753

Patankar, S.V., Spalding, D.B., 1972. A calculation procedure for heat, mass and momentum transfer in three-dimensional parabolic flows. Int. J. Heat Mass Transf. 15, 1787–1806. https://doi.org/10.1016/0017-9310(72)90054-3

Perles, S.J., Christian, A.D., Berg, D.J., 2003. Vertical migration, orientation, aggregation, and fecundity of the freshwater mussel Lampsilis siliquoidea. Ohio J. Sci. 103, 73–78.

Polvi, L.E., Sarneel, J.M., 2018. Ecosystem engineers in rivers: An introduction to how and where organisms create positive biogeomorphic feedbacks. WIREs Water 5, e1271. https://doi.org/10.1002/wat2.1271

Qin, J., Pan, H., Rahman, M.M., Tian, X., Zhu, Z., 2021. Introducing compressibility with SIMPLE algorithm. Math. Comput. Simul. 180, 328–353. https://doi.org/10.1016/j.matcom.2020.09.010

Rehmann, C.R., Stoeckel, J.A., Schneider, D.W., 2003. Effect of turbulence on the mortality of zebra mussel veligers. Can. J. Zool. 81, 1063–1069. https://doi.org/10.1139/z03-090

Rosti, M.E., Brandt, L., Pinelli, A., 2018. Turbulent channel flow over an anisotropic porous wall – drag increase and reduction. J. Fluid Mech. 842, 381–394. https://doi.org/10.1017/jfm.2018.152

Sadeque, F.M., Rajaratnam, N., Loewen, M.R., 2009. Shallow turbulent wakes behind bed-mounted cylinders in open channels. J. Hydraul. Res. 47, 727–743. https://doi.org/10.3826/jhr.2009.3464

Sadeque, M.A., Rajaratnam, N., Loewen, M.R., 2008. Flow around Cylinders in Open Channels. J. Eng. Mech. 134, 60–71. https://doi.org/10.1061/(ASCE)0733-9399(2008)134:1(60)

Sansom, B.J., Atkinson, J.F., Bennett, S.J., 2018. Modulation of near-bed hydrodynamics by freshwater mussels in an experimental channel. Hydrobiologia 810, 449–463. https://doi.org/10.1007/s10750-017-3172-9

Sansom, B.J., Bennett, S.J., Atkinson, J.F., 2022. Freshwater mussel burrow position and its relation to streambed roughness. Freshw. Sci. 41, 315–326. https://doi.org/10.1086/719993

Sansom, B.J., Bennett, S.J., Atkinson, J.F., Vaughn, C.C., 2020. Emergent Hydrodynamics and Skimming Flow Over Mussel Covered Beds in Rivers. Water Resour. Res. 56, e2019WR026252. https://doi.org/10.1029/2019WR026252

Shamloo, H., Rajaratnam, N., Katopodis, C., 2001. Hydraulics of simple habitat structures. J. Hydraul. Res. 39, 351–366. https://doi.org/10.1080/00221680109499840

Simeone, D., Tagliaro, C.H., Beasley, C.R., 2021. Amazonian freshwater mussel density: A useful indicator of macroinvertebrate assemblage and habitat quality. Ecol. Indic. 122, 107300. https://doi.org/10.1016/j.ecolind.2020.107300

Singh, S.K., Raushan, P.K., Debnath, K., 2019. Role of multiple flow stages over submerged structure. Ocean Eng. 181, 59–70. https://doi.org/10.1016/j.oceaneng.2019.03.048

Strayer, D., 2008. Freshwater Mussel Ecology. University of California Press. https://doi.org/10.1525/california/9780520255265.001.0001

Strayer, D.L., 1999. Use of Flow Refuges by Unionid Mussels in Rivers. J. North Am. Benthol. Soc. 18, 468–476. https://doi.org/10.2307/1468379

Strayer, D.L., Downing, J.A., Haag, W.R., King, T.L., Layzer, J.B., Newton, T.J., Nichols, J.S., 2004. Changing Perspectives on Pearly Mussels, North America's Most Imperiled Animals. BioScience 54, 429–439. https://doi.org/10.1641/0006-3568(2004)054[0429:CPOPMN]2.0.CO;2

Strayer, D.L., Hunter, D.C., Smith, L.C., Borg, C.K., 1994. Distribution, abundance, and roles of freshwater clams (Bivalvia, Unionidae) in the freshwater tidal Hudson River. Freshw. Biol. 31, 239–248. https://doi.org/10.1111/j.1365-2427.1994.tb00858.x

Sullivan, K.T., Woolnough, D.A., 2021. Water depth, flow variability, and size class influence the movement behavior of freshwater mussels (Unionida) in Great Lakes river drainages. Freshw. Sci. 40, 328–339. https://doi.org/10.1086/714412

Termini, D., Lavignani, F., Benistati, N., 2022. Flow Velocity and Turbulence Structure in gravel-bed rivers: experimental investigation in a straight laboratory flume. Proceedings of the 39th IAHR World Congress 19–24 June 2022, Granada, Spain https://doi.org/10.3850/IAHR-39WC2521711920221082.

van de Koppel, J., Gascoigne, J.C., Theraulaz, G., Rietkerk, M., Mooij, W.M., Herman, P.M.J., 2008. Experimental Evidence for Spatial Self-Organization and Its Emergent Effects in Mussel Bed Ecosystems. Science 322, 739–742. https://doi.org/10.1126/science.1163952

van Duren, L.A., Herman, P.M.J., Sandee, A.J.J., Heip, C.H.R., 2006. Effects of mussel filtering activity on boundary layer structure. Exch. Process. Sediment-Water Interface 55, 3–14. https://doi.org/10.1016/j.seares.2005.08.001

Vaughn, C.C., 2018. Ecosystem services provided by freshwater mussels. Hydrobiologia 810, 15–27. https://doi.org/10.1007/s10750-017-3139-x

Vaughn, C.C., Gido, K.B., Spooner, D.E., 2004. Ecosystem Processes Performed by Unionid Mussels in Stream Mesocosms: Species Roles and Effects of Abundance. Hydrobiologia 527, 35–47. https://doi.org/10.1023/B:HYDR.0000043180.30420.00

Vaughn, C.C., Nichols, S.J., Spooner, D.E., 2008. Community and foodweb ecology of freshwater mussels. J. North Am. Benthol. Soc. 27, 409–423. https://doi.org/10.1899/07-058.1

Witman, J., Suchanek, T., 1984. Mussels in flow: Drag and dislodgement by epizoans. Mar. Ecol. - Prog. Ser. 16, 259–268. https://doi.org/10.3354/meps016259

Wu, H., Constantinescu, G., 2022. Effect of angle of attack on flow past a partially-burrowed, isolated freshwater mussel. Adv. Water Resour. 168, 104302. https://doi.org/10.1016/j.advwatres.2022.104302

Wu, H., Constantinescu, G., Zeng, J., 2020. Flow and Entrainment Mechanisms Around a Freshwater Mussel Aligned with the Incoming Flow. Water Resour. Res. 56, e2020WR027983. https://doi.org/10.1029/2020WR027983

Wu, H., Zeng, J., Constantinescu, G., 2021. A multi-parameter design formula for riprap size selection at wing-wall abutments. J. Hydraul. Res. 59, 651–661. https://doi.org/10.1080/00221686.2020.1818310

Xu, Q., Li, R., Xu, M., 2022. High-performance Implementation of Parallel Semi-Implicit Method for Pressure Linked Equations Solver on CPU+GPU Platform. Int. J. Heat Mass Transf. 182, 121976. https://doi.org/10.1016/j.ijheatmasstransfer.2021.121976

Zigler, S.J., Newton, T.J., Steuer, J.J., Bartsch, M.R., Sauer, J.S., 2008. Importance of physical and hydraulic characteristics to unionid mussels: a retrospective analysis in a reach of large river. Hydrobiologia 598, 343–360. https://doi.org/10.1007/s10750-007-9167-1

4 CFD analysis of turbulent flow and bed shear stresses at a bridge for different flow regimes

This Chapter reports the content of a manuscript submitted for possible publication in Advances in Water Resources[4]. It presents the results of the CFD analysis of flow and bed shear stresses at a realistic, full-scale bridge with multiple piers over a natural river bathymetry. The analysis highlights the dependence on the flow regime (i.e., free-surface or pressure flow with deck overtopping) and on the presence of piers.

Since severe scours around piers and abutments are among the most common causes for bridge failures, understanding how the flow and the scouring processes are affected by the bridge structures is of great importance to obtain indications for preventing their collapse. To this end, simulations with the DES approach, conducted with a deformable free surface, are used to simulate the flow and to evaluate the dynamics of the coherent structures in a realistic case study based on a bridge over the Po River.

The comparison of different simulated scenarios allows to indirectly assess how the presence of the piers and the transition to a pressure-flow regime with bridge deck overtopping increase the potential for erosion of sediments at the bridge site. In addition, the predictions obtained by DES and RANS models are compared to each other to evaluate the ability of the RANS model in estimating the flow field and the bed shear stresses at the bridge site in case of the pressure-flow regime.

[4] Lazzarin, T., Constantinescu, G., Viero, D.P. A numerical investigation of flow field and bed stresses at a river bridge: the effects of piers and of pressure-flow with deck overtopping. Submitted for publication in Adv. Water Resour.

4.1 Introduction

Understanding how flow in rivers is affected by the presence of bridge structures is of great importance to predict the flow behavior in case of floods and to prevent the bridge damaging or collapse. The triggering causes of bridge failures are often related to bed erosion during flooding events (Montalvo et al., 2020; Wardhana and Hadipriono, 2003; Zhang et al., 2022). Severe scours around the piers and abutments of bridges are among the most common causes for their collapse (Ballio et al., 2018; Cook et al., 2015; Deng et al., 2016; Flint et al., 2017). Other factors include the hydrodynamic forces on the structure, and the actions induced by transported material (e.g., log jams), especially at sites with partial obstruction of the bridge openings (Chen et al., 2009; De Cicco et al., 2020; Muñoz Diaz et al., 2009).

Local scour induced by the flow acceleration around in-stream structures, by the formation of horseshoe vortices around the upstream face of the piers and by the turbulent wakes is generally the main driving factor for sediment erosion around bridge piers and abutments (Breusers et al., 1977; Ettema et al., 2017; Melville and Sutherland, 1988; Wang et al., 2017). A second driving mechanism for bed erosion at bridges is contraction scour which is associated with supplementary flow acceleration around an in-stream structure due to its vicinity with other structures (Bui and Rodi, 2008; Dey and Raikar, 2005; Raikar et al., 2016). Finally, pressure-flow scouring occurs once the flow at the bridge site becomes pressurized (Carnacina et al., 2019; Majid and Tripathi, 2021; Umbrell et al., 1998). In this case, the flow accelerates in between the bed and the bridge deck, with the core of high velocities moving closer to the bed, and separation and recirculation regions forming below and downstream of the bridge (Kara et al., 2015b; Pregnolato et al., 2022).

These driving mechanisms of bed scouring are often interlaced with each other in real applications, hence assessing the influence of each of them is challenging. While physical processes driving local scour around bridge piers and abutments are fairly well understood (e.g., Kirkil et al., 2009; Koken & Constantinescu, 2014; Melville & Coleman, 2000), less attention has been paid to the other scour mechanisms and how changes in the flow associated with the transition to a pressure-flow regime and with proximity of other piers or abutments affect the velocity and the bed shear stresses in the vicinity of the structure being analyzed. The use of computer simulations to investigate flow structure around bridge piers and abutments in such cases has the particular advantage that it provides the full three-dimensional (3-D) flow fields containing the main vortices and the bed shear stress distributions (e.g., Kirkil and Constantinescu, 2010). Such information is generally not available from experimental investigations. Given the strongly three-dimensionality of the flow and the complex vortical structures generated around such in-stream structures, 3-D numerical models are required to obtain reliable information (Ettema et al., 2017).

Most 3-D simulations of flow in natural river reaches with and without hydraulic structures are performed using the Reynolds Averaged Navier Stokes (RANS) approach, which allows predicting 3-D turbulent flows over large domains and also performing

unsteady simulations over long periods of time (e.g., Roulund et al., 2005; Zeng et al., 2008; Mannini et al., 2010; Horna-Munoz & Constantinescu, 2018, 2020; Wu et al., 2021). Such RANS simulations are generally not very accurate in predicting the redistribution of momentum inside the regions where the flow accelerates as it passes the structure and the coherence of the main vortices forming around in-stream structure. This is mainly because of the difficulties of RANS models to predict flows where strong adverse pressure gradients and massive flow separations are present and flows where highly unsteady coherent structures form (e.g., horseshoe vortices, vortices generated in the wake of the pier, abutment or of the submerged bridge deck). These aspects, which are of a fundamental importance to understand the physics of the flow at bridge sites under different flow regimes and the sediment entrainment potential of the flow around piers and abutments supporting the bridge, may be not well captured using steady and unsteady RANS simulations (Bressan et al., 2011; Cheng et al., 2018; Ge and Sotiropoulos, 2005; Paik et al., 2004). Moreover, RANS-based predictions of sediment entrainment are generally underpredicted because RANS simulations do not capture the temporal variations in the local bed shear stresses associated with unsteadiness of the large-scale near-bed coherent structures and the other turbulent eddies present near the bed surface (Cheng et al., 2018). Capturing the coherence and the unsteady dynamics of the energetically important eddies in the near bed region and being able to accurately predict the bed shear stresses require the use of more advanced turbulence models that directly resolve the large-scale coherent structures generated by the different in-stream structures and at the channel banks (Kang et al., 2011; Keylock et al., 2012; Teruzzi et al., 2009). Such models are based on the Large Eddy Simulation (LES) approach. LES was successfully used to study flow fields and bed shear stress distributions around in-stream structures in open channels and river reaches (Kang et al., 2011; Kara et al., 2015a; Khosronejad et al., 2016; McCoy et al., 2008). Though the use of classical LES at high Reynolds number is possible using wall functions, hybrid RANS-LES models (Fröhlich and von Terzi, 2008; Heinz, 2020; Menter et al., 2021) using a more sophisticated RANS model near the solid surfaces require less computational resources with an accuracy that is comparable to LES with wall functions. The most popular model in this category is called Detached Eddy Simulations (DES).

Although numerical simulations based on RANS, LES, and DES were widely used to study flow fields around hydraulic structures placed in channels, these studies generally focused on isolated structures in open channel free surface flow regimes, typically in quite idealized configurations. The most common types of hydraulic structures investigated in such numerical studies include surface-mounted emerged cylinders of different shapes and bridge piers (Aghaee-Shalmani and Hakimzadeh, 2022; Alemi and Maia, 2018; Chang et al., 2013, 2011; Cheng et al., 2018; Khosronejad et al., 2012; Kim et al., 2014; Kirkil et al., 2009, 2008; Kirkil and Constantinescu, 2015, 2012, 2010, 2009; Roulund et al., 2005; Xiong et al., 2016; Zeng and Constantinescu, 2017), bridge abutments and isolated spur dikes (Chrisohoides et al., 2003; Kara et al., 2015a; Koken and Constantinescu, 2014, 2011; Teruzzi et al., 2009; Wu et al., 2021) and river groynes (McCoy et al., 2008; Pourshahbaz et al., 2022). Other two important classes of numerical studies relevant for the present investigation are numerical simulations of flow in curved

open channels with natural bathymetry at laboratory and field scale conditions (e.g., Constantinescu et al., 2013; Ge & Sotiropoulos, 2005; Kang et al., 2011; Koken et al., 2013) and numerical investigations of flow in open channels with a submerged bridge deck (e.g., Horna-Munoz & Constantinescu, 2020; Kara, Stoesser, et al., 2015).

Quite often bridges are situated in meandering or irregular reaches. Even if the angle of attack of the piers is generally negligible at low flow conditions, this is not always the case at high flow conditions when the interaction between the flow over the floodplains and inside the main channel and the curvature effects may induce a fairly significant transversal velocity, which results in a non-zero angle of attack for some of the bridge piers (Akhlaghi et al., 2020; Larsen et al., 2011). Other factors generally affecting flow patterns near the bridge include large-scale deposition and erosion patterns and secondary flow induced by channel curvature, bank protrusions and the presence of other hydraulic structures like river groynes upstream of the bridge (Constantinescu et al., 2013; Kitanidis and Kennedy, 1984; Lazzarin and Viero, 2023; Zeng et al., 2008). The proximity of other piers may also affect flow patterns and how the angle of attack changes with increasing flow depth at the pier being analyzed (Malik and Setia, 2019; Zhou et al., 2020). All these effects, which are neglected or only partially considered in laboratory experiments and simulations conducted for idealized conditions, can substantially modify the flow approaching a bridge placed in a natural stream, its interaction with its piers and, ultimately, its capacity to erode the bed around the bridge structure.

This motivates the present work in which DES simulations are used to investigate how different flow conditions and the bridge geometry affect the turbulent flow field and the bed shear stresses, which are important to assess the structural stability and the hydraulic compatibility of bridges. The simulations are performed with the natural, deformed bathymetry of the channel bed and of active floodplains and include the bridge structure (i.e., multiple piers of complex shape and bridge deck).

A first goal of the present study is to characterize the change in the flow structure at the bridge site when passing from a free-surface regime to a pressure-flow regime with deck overtopping. A second goal is to understand to what extent the erosive capacity of the flow changes due to the change in the flow regime. Also, the work aims at understanding the interactions and the mutual feedbacks associated with the presence of multiple piers and different flow regimes.

To the best knowledge of the authors this is the first study using DES with a deformable free surface to study the flow, the turbulence structures and the erosive capacity of the flow at a real bridge with multiple piers on a natural river. The analysis also investigates the capability of RANS to accurately predict the mean flow, turbulence statistics and bed shear stresses at the bridge site by means of the comparison with results of the DES simulations. This is important given that for engineering purposes RANS is mostly used to simulate the flow in river reaches with bridge structures.

The Chapter is organized as follows. Section 4.3 describes the case study, the numerical model, and the details of the simulation set-up. The section also discusses the methodology used to estimate the sediment flux entrained by the flow which is used to

approximatively quantify the erosional capacity of the flow at the bridge site. Section 4.3 shows the model results and discusses the flow fields and the sediment entrainment capacity for the different cases (free-surface vs. pressure-flow regime, with or without bridge piers and bridge deck, DES vs. RANS). Section 4.4 summarizes the main findings and provides some conclusions.

4.2 Case study, numerical model and methodology to estimate the entrained sediment flux

4.2.1 Case Study

The bridge geometry considered in the present numerical study is inspired by a real bridge located in the terminal reach of the Po River (Italy), near the town of Occhiobello (Figure 4-1a). The Po is the largest river in Italy with a length of about 650 km flowing from the western Alps to the Adriatic Sea. The average river discharge is 1,470 m^3/s, and it can exceed 10,000 m^3/s during floods. In the terminal reach, the Po River has a meandering pattern. The bridge is located downstream of a series of low-curvature bends and just upstream of a larger bend, at a section where the main channel is 320 m wide (Figure 4-1b).

The bridge is part of the A13 highway, which has two lanes in each direction. The total length of the bridge is 1.8 km. The bridge is supported by a total of 41 piers. Four piers (i.e., P1 to P4) fall within the main channel, and are spaced from each other by 70 m (Figure 4-1c-d). The other piers are located on the floodplain and are spaced 56.5 m apart. The piers have a rectangular footprint, with round edges; they are 2.8 m wide and 21.3 m long in the upper part and 3.6 m wide and 23.3 m long in the lower part, with rounded edges at their upstream and downstream ends (Figure 4-1e-f). The foundation of each pier is made of a block of reinforced concrete 9.6 m wide, 23.3 m long and 10 m high. This block is supported by 8 piles buried into the ground. Each of the two beams composing the deck has a π−shaped cross section 9.8 m wide and 3.7 m high. At both extremities, Jersey barriers 1 m high are used to prevent vehicles falling from the bridge.

In the simulations, the bridge deck is taken 6.5 m lower than in the real case to assess the effects of pressure-flow regime with reasonable values of the flow discharge. Thus, the distance between the bottom of the bridge deck and the channel bed varies from 7 m to 17 m due to the presence of relatively large scour holes around piers P1 and P2.

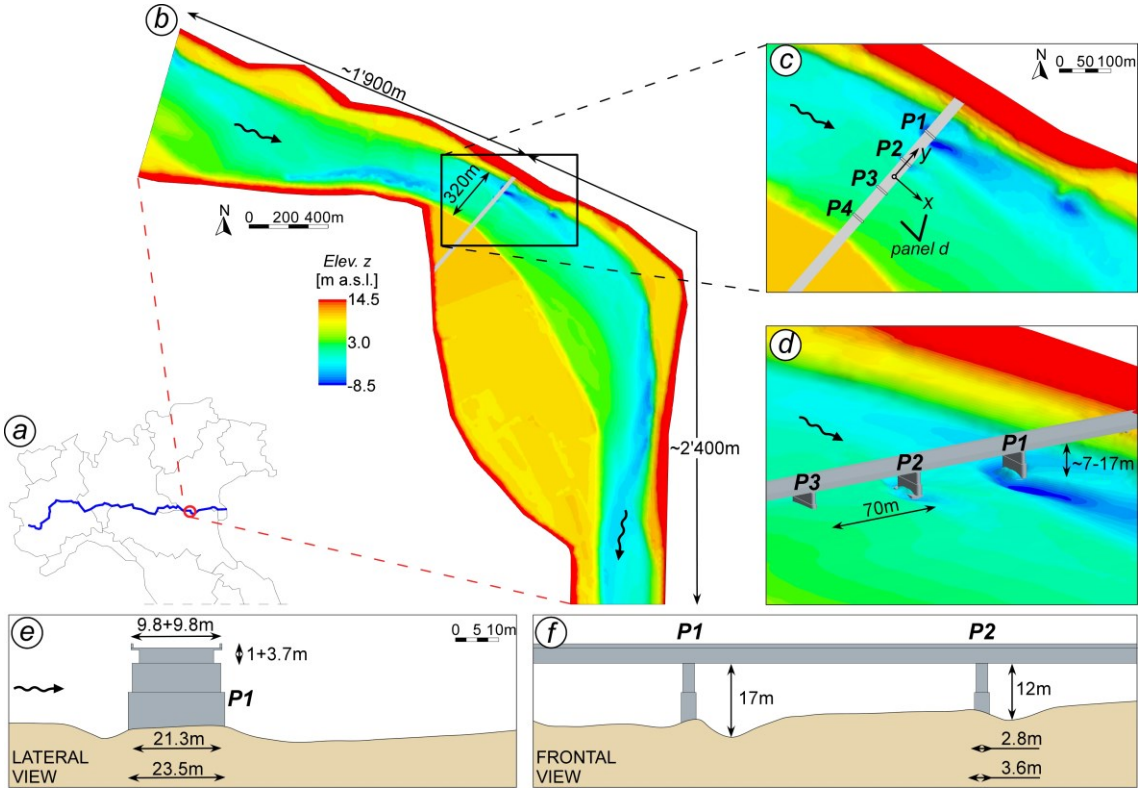

Figure 4-1. Computational domain and bridge geometry. a) location of the bridge site along the Po River; b) and c) 2-D views of the bridge and bathymetry; d) 3-D view of the bridge and the scour holes looking from downstream; e) lateral view of the pier P1; f) frontal view of the piers P1 and P2. Also shown are the main geometrical dimensions.

4.2.2 Test Cases

Table 4-1 summarizes the main flow and geometrical conditions including the flow regime at the bridge site for the different test cases (an overview of the main geometric features is provided in Figure 4-2). Most of the simulations are performed using DES. Case 2 is also computed using RANS (this simulation is denoted 2R in Table 1). Both a low discharge (Q = 4,470 m³/s, 1-year return period) and a high discharge (Q = 14,485 m³/s, 500-years return period) are considered (Table 4-2). Given that the bottom of the bridge deck is situated at an elevation of 10.3 m above the sea level (a.s.l.), and the water level at the bridge site is 9.0 m in the low discharge cases (Q = 4,470 m³/s), a free surface regime (*FS*) establishes in the low discharge simulations of Cases 1 and 5 (see Table 1 and Figure 4-2), with no need of including the bridge deck in the computational domain. In the high discharge simulations (Q = 14,485 m³/s for Cases 2 and 4) the water level at the bridge is 14.6 m a.s.l., which generates a pressurized flow beneath the bridge deck (pressure-flow regime, *PF*). For comparison purposes, the bridge deck is not included in Case 3, which thus represents the free-surface counterpart of the high discharge *PF* Case 2. The four piers in the main channel, P1 to P4, are removed in Case 4, whereas only pier P1 is included in Case 5. All simulations are performed

using the surveyed bathymetry. For the Case 5, which does not include piers P2 to P4, the bathymetry is artificially modified by filling the scour holes around these missing piers.

Comparison of Cases 1 and 2 allows investigating the differences associated with changes in the flow regime at the bridge site when passing from a low-discharge, *FS* regime, to a thigh-discharge, *PF* regime. To be able of making a direct comparison, one needs to compare cases with same discharge and water stage in the flow approaching the bridge site. The difference between simulations of Cases 2 and 3 is a direct consequence of the flow becoming pressurized at the bridge and serves as an indirect measure of pressure-scour effects.

Another important question is whether the presence of the pier results in significant differences in terms of flow fields and sediment entrainment potential. This is investigated by comparing Case 2 where the bridge deck and the piers are part of the computational domain with Case 4 where only the bridge deck is present.

Comparison of the results of simulations when all piers are present (Case 2) and when only one pier is present and thus contraction scour effects are absent (Case 5) allows to investigate the effect of the presence of neighbouring piers. This comparison allows estimating the importance of contraction scour effects for a case where the flow at the bridge site is in the *FS* regime.

Table 4-1. Matrix of test cases. *Q* denotes the discharge; *FS* and *PF* stand for free-surface flow and pressure-flow regime, respectively.

Case	Model	Piers	Discharge	Regime	Bed
1	DES	All Piers	Low *Q*	*FS* (free surface)	Natural bathimetry
2	DES	All Piers	High *Q*	*PF* (pressure-flow)	Natural bathimetry
2R	RANS	All Piers	High *Q*	*PF* (pressure-flow)	Natural bathimetry
3	DES	All Piers	High *Q*	*FS* (free surface)	Natural bathimetry
4	DES	No Piers	High *Q*	*PF* (pressure-flow)	Natural bathimetry
5	DES	Pier P1	Low *Q*	*FS* (free surface)	Natural bathymetry but with filled scour holes for piers P2, P3 and P4

Table 4-2. Flow conditions for the low and the high discharge simulations.

	Q [m³/s]	Water level *h* [m a.s.l.]	Froude number *F* [-]	Reynolds number *Re* [-]	Bridge deck elev. [m a.s.l.]	Return Period T_R [years]
Low Q	4'470	9	0.172	14'580'000	10.3-15.0	1
High Q	14'485	14.6	0.224	39'128'000	10.3-15.0	500

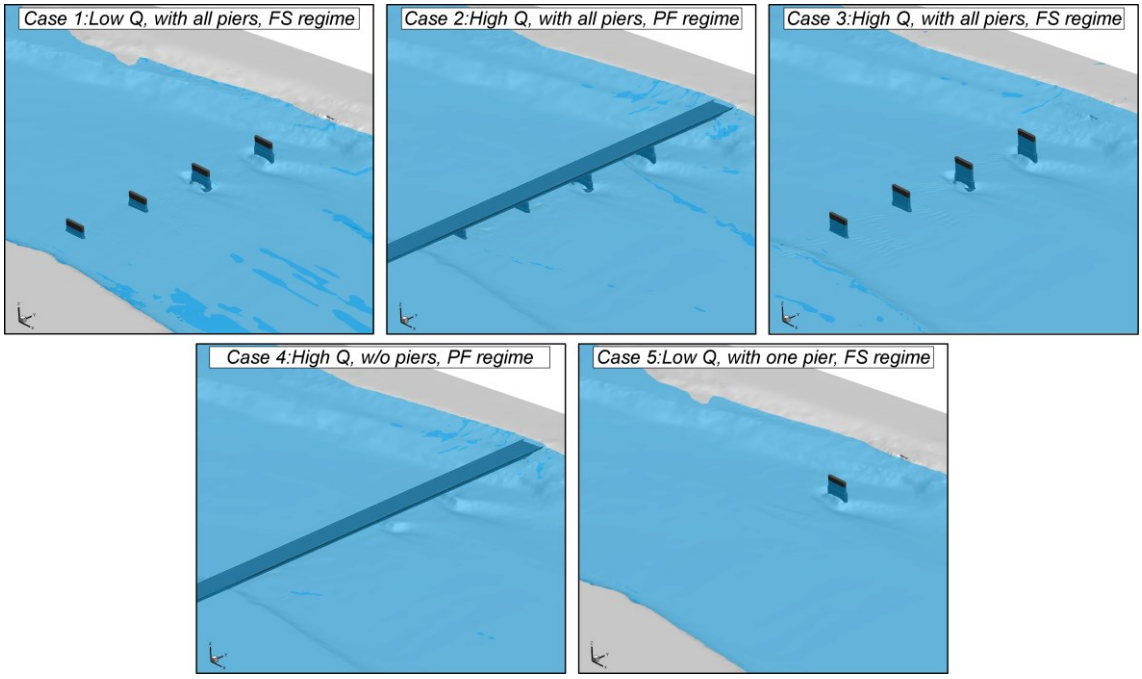

Figure 4-2. Overview of the geometrical configuration of the test cases, with the bathymetry (light grey surfaces), the bridge structure (dark grey surfaces), and the water free surface (light blue).

4.2.3 Numerical Model

The viscous flows solver in the commercial code STAR-CCM+ is used to perform both DES and RANS simulations. The discretized Navier-Stokes equations are solved on unstructured grids using a finite-volume method. In the present work, the SIMPLE algorithm was used to solve continuity and momentum equations (Patankar and Spalding, 1972). In the predictor step the momentum equations are solved without the pressure gradient terms; a pressure correction is then used in the corrector step to modify the velocity vectors to exactly satisfy continuity. The Hybrid-BCD scheme, which combines an upwind scheme with a bounded central difference scheme, is used to discretize the convective terms. The viscous and pressure gradient terms are discretized using a second-order, central-difference scheme. The equations are advanced in time using an implicit second-order scheme.

The two-phase Volume of Fluid (VoF) method is used to track the free surface deformations (Hirt and Nichols, 1981). The method assumes that the air and water phases are immiscible and the computational grid is capable of resolving the interface. A standard advection equation is solved for the volume fraction. To maintain a sharp interface, a high-resolution interface capturing scheme (HRIC) is employed. In the present work, the sharpening factor was set equal to 1.

In the RANS simulations, the SST k-ω turbulence model is used (Menter et al., 2003) to conduct the RANS simulations. The turbulent kinetic energy, k, and the specific dissipation rate, ω, are estimated by solving two transport equations. Previous studies

have confirmed the accuracy of this model to predict water flow and passive-scalar transport in natural open channels with complex bathymetry and surface roughness (e.g., Wu et al., 2021). The SST RANS model is also used as base model in the DES simulations reported in the present analysis.

The STAR-CCM+ solver has been extensively used and validated to predict steady and unsteady flows in natural river channels containing hydraulic structures (e.g., Horna-Munoz & Constantinescu, 2018, 2020; Lazzarin et al., 2023; Shinneeb et al., 2021). Applications of direct relevance for the present investigation include those of flow past arrays of cylinders with flat and naturally deformed bed (e.g., Chang et al., 2017) and of flow in open channels containing piers and abutments (e.g., Cheng et al., 2018; Edwards et al., 2013; Tulimilli et al., 2011).

4.2.4 Computational domain, boundary conditions and mesh

The computational domain represents a 4,300 m long reach of the Po River. The bridge is located at about 1,900 m downstream of the inlet section (Figure 4-1b). On its lateral sides, the domain is delimited by the main levees which have an elevation of about 16.0 m. The domain includes the main river channel and its adjacent floodplains. The ground elevation is derived from a LiDAR survey with 1 m resolution. The riverbed bathymetry is derived from a 2 m resolution multi-beam survey performed in 2004.
The values of water levels prescribed at the outlet section, which are kept fixed for each simulation, are derived from a set of preliminary simulations performed on a longer river stretch with the 2-D depth-averaged '2DEF' model (Defina, 2003, 2000; Lazzarin et al., 2023a; Mel et al., 2020; Viero et al., 2019, 2013). At the inlet section, the air velocity is set to zero and a logarithmic profile is specified for the streamwise velocity inside the water domain. A hydrostatic pressure distribution is imposed at the outlet section. A roughness height k_s = 0.1 m was specified at the riverbed to account for small dunes and ripples not included in the bathymetric survey, thus not explicitly resolved in the present simulations. In STAR-CCM+, when the flow is solved up to the viscous sublayer using the k-ω turbulence model, the effect of the roughness is modelled by imposing a specific value of the dissipation rate ω on the cells next to the rough wall as $\omega = 2{,}500\ \nu\ k_s^{-2}$ with ν the kinematic viscosity (Wilcox, 1998). The surfaces of the piers and bridge deck are assumed to be smooth. At the top (air) boundary of the computational domain, atmospheric pressure is assumed, and the air velocity is set to zero. At the beginning of each simulation, the water elevation was linearly interpolated along the streamwise direction from the inlet to the outlet section.

The computational mesh is generated using the grid generator in the STAR-CCM+ package (Figure 4-3). The unstructured mesh generator allows using nested-like grids with cell cutting near boundaries of complex shape. Hexahedral Cartesian-like meshes are used, and various controls are used to refine the mesh in critical parts of the domain (e.g., near the piers, the bridge deck, and the free-surface). Trimmed cells are added near these surfaces to ensure a smooth transition between elements of different size.

The average cell size in the horizontal directions is of 10.0 m away from the bridge site, and 5.0 m in a 200 m long region situated in the vicinity of the bridge. Close to solid

surfaces, the cell size progressively decreased to 0.6 m. The same resolution is used for the 100 m long and 30 m wide regions surrounding each pier. To set the cell size in the vertical direction, an aspect ratio of 1:2.5 was used away from the bridge. The aspect ratio was progressively increased to 1:1 closer to the bridge. A vertical resolution of 0.6 m was used in the 5.0 m thick region where the free-surface is expected to be situated. The vertical resolution was decreased to about 4.0 m in the upper part of the computational domain containing air. To resolve the attached boundary layers, the prism layer meshing function of STAR-CCM+ was used to refine the mesh close to all solid surfaces. Between 7 and 9 prism layers were used for the riverbed surface. The first cell at the solid surface was 13 mm high in the wall-normal direction. For the deck and the piers, 6 prism layers were used to reduce the size of the first cell to 7 mm in the wall-normal direction.

The computational grids generated according to the above rules and controls contained 14 to 19 million cells. The larger number of cells was required for cases where the flow was pressurized at the bridge. The time step in the simulations was set to 0.2 s. Simulations were performed for a total time of 5,000s (~830 D/U, with D the average water depth and U the average flow velocity in the high flow cases). 3,000s (~500 D/U) were needed to reach quasi-steady conditions; the mean flow and the associated statistics were computed over 2,000 s (~330 D/U).

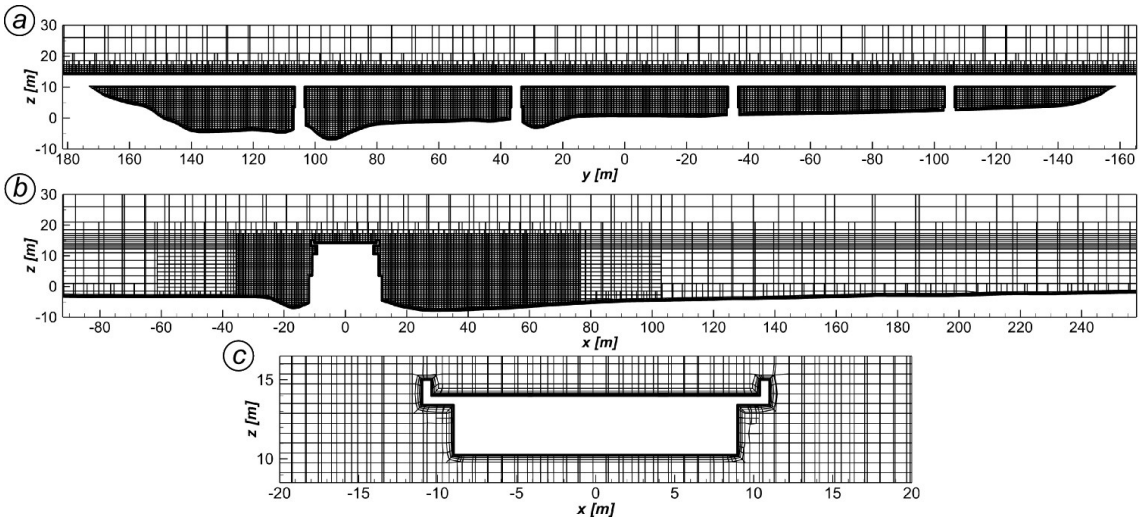

Figure 4-3. Computational mesh in a transversal (a) and in a longitudinal section (b), with detail (c), at the bridge for the simulation of Case 2.

4.2.5 Bed Shear Stress and Flux of Entrained Sediment

In this study, the bed shear stress predictions are used to estimate the flux of entrained sediment in a region close to the bridge. In turbulent flows, velocity fluctuations and large-scale turbulence affect the sediment entrainment capacity of the flow, as the entrainment of sediment particles primarily correlates with the instantaneous bed shear stress magnitude rather than the mean bed shear stress. The bed shear stress fluctuations can be explicitly predicted by DES simulations. By contrast, unsteady RANS simulations

can only represent very large-scale unsteadiness (see Section 4.3.5 for a comparison). The proper representation of velocity fluctuations induced by large-scale turbulence is thus a key advantage of DES simulations, particularly when trying to estimate the bed shear stresses and the entrainment of bed particles close to geometrical singularities (e.g., piers, abutments), which complicate the structure of the turbulent flow field.

In DES, the flux of entrained sediment can be estimated using both the instantaneous and the time-averaged (mean) bed shear stress magnitude. The difference between these two values gives an indication on the effect of large-scale turbulence on the sediment entrainment capacity of the flow. Typically, as the flow unsteadiness and the coherence of turbulent eddies in the near-bed region increase, so does the difference between the entrainment flux computed based on the mean and the instantaneous bed shear stresses (see e.g., Hofland & Battjes, 2006; Schmeeckle & Nelson, 2003; Chang et al., 2011). For turbulent flows, the distribution of the mean bed shear stress, $\bar{\tau}_b$, gives only an incomplete picture of the erosive action exerted by the flow on the bed particles (Nelson et al., 1995; Schmeeckle and Nelson, 2003; Sterling et al., 2008; Sumer et al., 2003). When available, the standard deviation of the bed shear stress, τ_b^{SD}, should be used to approximatively account for the increase in the sediment entrainment capacity of the flow due to the intermittent increase of the instantaneous bed shear stress at a given location (Chang et al., 2013, 2011). In the present work, since the mesh is not sufficiently refined at the bottom to resolve the viscous sublayer, the bed shear stresses are estimated using the law of the wall.

The approach proposed by Cheng et al. (2018) is used to identify the contribution of turbulence and flow unsteadiness to the total flux of entrained sediment. The total entrainment flux per unit area (A), E, is estimated as:

$$E = \frac{1}{A}\iint_A (\rho_S P) dA \tag{4-1}$$

where ρ_S is the density of bed particles and P is the sediment pick up formula proposed by van Rijn (1984):

$$P = 0.00033\left(\frac{\tau_b - \tau_{b,c}}{\tau_{b,c}}\right)^{1.5} \frac{\Delta^{0.6} g^{0.6} d_{50}^{0.8}}{\nu^{0.2}} \tag{4-2}$$

with $\Delta = (\rho_S - \rho)/\rho$, where ρ is the density of water, ν is the molecular viscosity of water, and d_{50} is the mean sediment diameter. τ_b and $\tau_{b,c}$ are the (instantaneous) bed shear stress magnitude and the critical shear stress, respectively. Equation (4-2) is applied to estimate P only at locations where $\tau_b > \tau_{b,c}$, otherwise $P = 0$.

Correcting the critical shear stress by accounting for the local bed slope is fundamental when studying the potential bed erosion for domains with deformed bathymetry. For example, gravitational effects reduce the capacity of the horseshoe vortex to entrain particles inside the scour hole forming around the upstream face of each pier. To account for the bed slope effects, $\tau_{b,c}$ in Eq. (4-2) is computed as:

$$\tau_{b,c} = \frac{\sin(\gamma + \phi)}{\sin(\phi)} \tau_{b,c,0} \tag{4-3}$$

where $\tau_{b,c,0}$ is the critical shear stress computed using Shields' diagram for a given value of d_{50}, γ is the angle of the bed relative to the horizontal evaluated along the local flow direction, and ϕ is the repose angle of the bed particles (ϕ = 33°).

Given that Δ, g, d_{50}, ν and ρ_S are all constant in the present simulations, Eq. (4-1) can be rewritten as:

$$E = \frac{\beta}{A} \iint_A \left(\frac{\tau_b - \tau_{b,c}}{\tau_{b,c}} \right)^{1.5} dA = \frac{\beta}{A} \iint_A \mathrm{T}^{1.5} dA \tag{4-4}$$

where β is a dimensional constant and T is the nondimensional excess bed shear stress. The mean flux of sediment entrainment from the bed is then computed as:

$$\bar{E}_1 = \frac{\beta}{A} \overline{\iint_A \mathrm{T}^{1.5} dA} \tag{4-5}$$

Given that β and $\tau_{b,c}$ are constant in the present simulations, the entrainment flux can be analyzed in terms of its nondimensional value $\bar{E}_1' = \frac{1}{A} \overline{\iint_A \mathrm{T}^{1.5} dA}$.

4.3 Results

4.3.1 Changes in Flow Structure Associated with Transition from the FS to the PF Regime

Figure 4-4 shows the longitudinal free-surface profile along the centerline of the reach of the Po River for Case 1 (low flow, *FS*), Case 2 (high flow, *PF*), and Case 3 (high flow with no deck, *FS*). The total discharge in Case 2 is 14,485 m³/s, of which 215 m³/s are advected over the bridge deck.

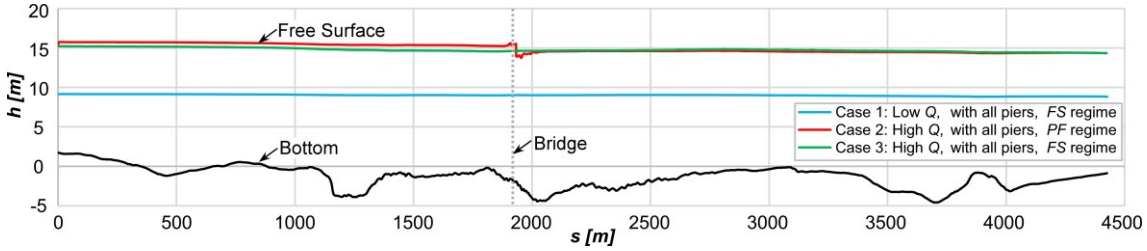

Figure 4-4. Longitudinal free-surface profiles for some of the DES simulations.

The 2-D free surface profiles are very different in the *FS* and *PF* regimes (see also Figure 4-2). In the *FS* regime (Cases 1 and 3), the water surface profile remains almost flat across the bridge section, with only minor disturbances due to the presence of the

bridge piers. In Case 2 (*PF* regime), the bridge causes a clear backwater effect (~0.5 m increase in water level) due to increased resistance induced by the interaction of flow with the bridge deck. The water level drops at the bridge section and some small undulations form downstream of it, with an amplitude of about 0.02 *D* (*D* is the water depth). This value is smaller than the amplitude observed by Kara, Stoesser, et al. (2015), which was close to 0.1 *D*, although the Froude numbers are comparable in the two cases. This can be explained by the lower water head on the bridge in the present Case 2 simulation (~0.03 *D* versus ~0.36 *D* in the experiment of Kara, Stoesser, et al., 2015).

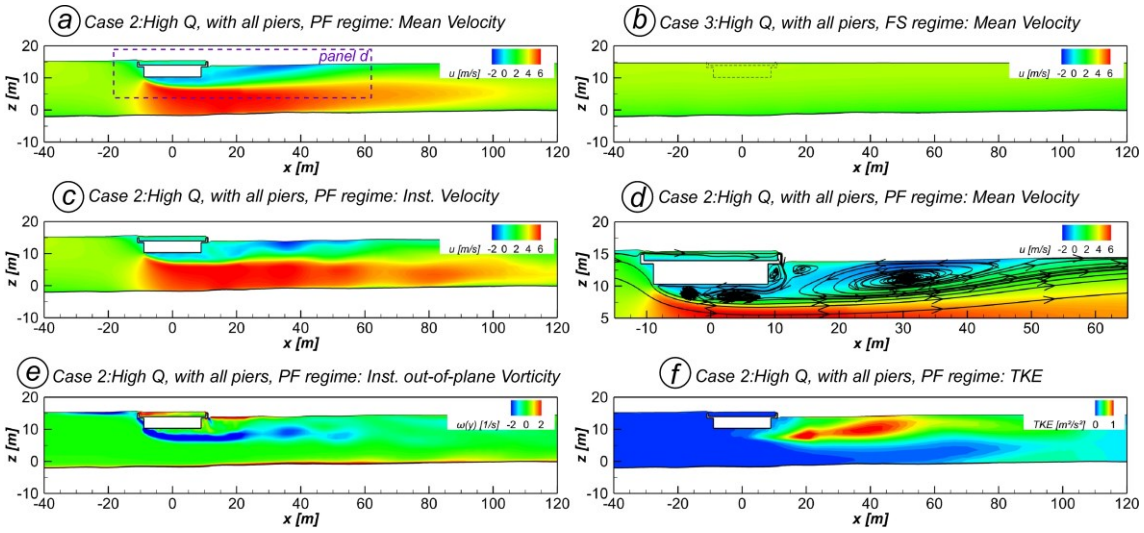

Figure 4-5. Flow structure in a streamwise vertical section in between piers P1 and P2 (y = 70 m). Mean streamwise velocity component for Case 2 (a) and for Case 3 (b). For Case 2, instantaneous streamwise velocity component (c), mean streamwise velocity component with 2-D streamlines (d), instantaneous out-of-plane vorticity (e), and *TKE* (f).

A main effect of *PF* conditions at the bridge site is to induce a strong downward velocity component that conveys the flow below the deck, where the flow is strongly accelerated. Here, the streamwise velocity is roughly two times larger than in an equivalent simulation with no bridge deck (Case 3, *FS* regime) as observed from comparing Figure 4-5a and Figure 4-5b. The high-velocity core moves toward the bed in Case 2 compared to Case 3. This is expected to have a large effect on the bed shear stress and the capacity of the flow to entrain particles at the bed (see Sect. 4.3.2).

Upstream of the bridge, the effect of the flow being pressurized at the bridge site is limited an increase in the water elevation. Downstream of the bridge, the high-velocity region extends for a long distance. For an average velocity U = 2.5 m/s and depth D = 15 m, the region with streamwise velocity u > 4 m/s (≈1.5U) extends for about 100 m in Case 2, which corresponds to 6.7 *D* (Figure 4-5a).

The high-velocity core in Case 2 is unsteady in time. The instantaneous flow velocity (Figure 4-5c) shows large-scale waviness, especially in the downstream leg of the orifice

flow region. Strong fluctuations of the velocity are observed below the deck and in the wake of the piers.

For *PF* conditions at the bridge site, recirculation regions form below and downstream of the deck, as shown by the streamlines in Figure 4-5d. Below the deck, the recirculation region is separated from the high-velocity core by a relatively steady shear layer, as shown by the instantaneous out-of-plane vorticity field in Figure 4-5e. Downstream of the bridge, the recirculation region extends for about 60 m (~4 *D*); the separated shear layer becomes unstable (see instantaneous vorticity in Figure 4-5e), which explains the presence of patches of negative vorticity that are advected downstream. Other smaller unsteady flow structures form immediately downstream of the deck, close to the free-surface, where the overflow plunges and reenters the main current (Figure 4-5c). Inside the recirculation regions, the *TKE* is also amplified (Figure 4-5f), which is consistent to what was observed by Kara, Stoesser, et al., (2015) in their experiment. *TKE* values are higher downstream of the bridge, which is consistent with the high unsteadiness observed inside these recirculation regions.

Figure 4-6a shows that in Case 2 (*PF* regime) the streamwise velocity is nearly uniform in the spanwise direction, apart from singularities that are generated close to the piers. The asymmetrical behavior of the flow at the sides of piers is a consequence of the misalignment of the axes of the piers with respect to the main current.

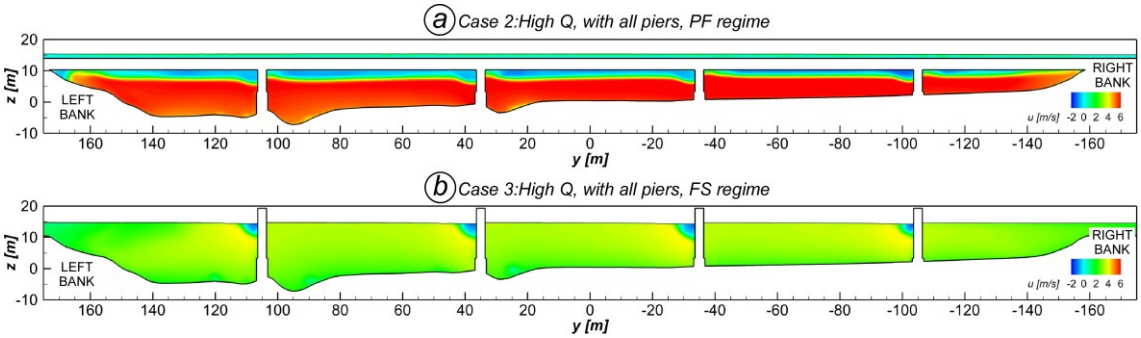

Figure 4-6. Mean streamwise velocity, u, in the bridge cross-section ($x = 0$) for Case 2 (a) and Case 3 (b).

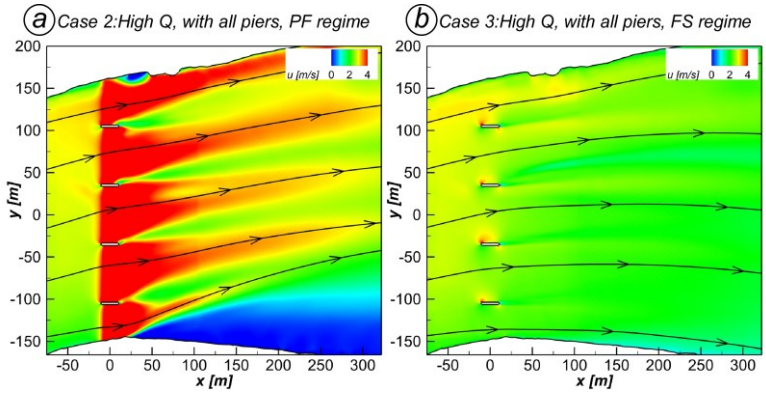

Figure 4-7. Mean streamwise velocity, u, in a horizontal plane at $z = 5$ m, with streamlines, for Case 2 (a) and for Case 3 (b).

As illustrated by 2-D streamlines in Figure 4-7, the flow approaches the piers with a certain angle of attack, which is of about 17° for the simulations conducted with the lower discharge, and 14° for those conducted with the higher discharge. As a result, recirculation regions form on the left-hand side of each pier. In Case 3 (*FS* regime), the recirculation regions are confined near the free surface (Figure 4-6b). This differs from what was observed by Chang et al. (2011) who considered the flow past a rectangular plate with a non-zero angle of attack. They found that the recirculation region on the side of the structure extended over the entire depth. However, Chang et al. (2011) performed their simulations with a rigid lid treatment of the free surface at lower Reynolds numbers and using a flat channel bottom. In case of *PF* of Figure 4-6a, the corresponding low-velocity recirculation regions are weaker due to the flow acceleration dictated by the orifice-flow condition. In Case 2 (*PF* regime), the influence of the piers becomes particularly relevant downstream of the bridge, where long unsteady wakes form (Figure 4-7). These wakes separate regions of strong flow acceleration.

Another difference between cases where the flow at the bridge site is in the *FS* and, respectively, in the *PF* regime regards the large-scale recirculation region that forms downstream of the bridge at the right side of the main channel (see the dark blue region in Figure 4-7a). This low-velocity region acts as a channel contraction when the *PF* regime is present, which increases the mean velocity downstream of the piers.

As expected, horseshoe vortices (HVs) form around the upstream side of the piers with their legs oriented parallel to the approaching mean flow direction. The size and strength (e.g., circulation) of the HVs forming around isolated piers depend on the Reynolds number (e.g., Kirkil & Constantinescu, 2015), on the pier shape (e.g., Kirkil & Constantinescu, 2009), and on the pier orientation with respect to the incoming velocity (e.g., Chang et al., 2011). The size and strength of the HVs typically increase as scour develops and the scour hole grows mainly because the longitudinal velocity of the incoming flow is reduced and the counter-rotating flow can fully develop if larger scour holes are present (Dey and Raikar, 2007; Muzzammil and Gangadhariah, 2003). These aspects enforce the need of representing the details of the real geometry at a given bridge site (e.g., in terms of deformed bathymetry, geometry of piers) to obtain a reliable and precise description of the local flow field. Figure 4-8 shows the HVs for some of the simulations. HVs are well-developed only at piers P1 and P2, around which deep scour holes are present. No HVs are observed around piers P3 and P4. Figure 4-9 shows the out-of-plane vorticity, $\omega(y)$, and the 2-D streamlines in the symmetry plane of piers P1 and P2. The comparison of Case 1 and Case 3 (panels a and c in Figure 4-9) shows that the primary HVs have a similar shape in the corresponding low and high discharge cases. The circulation of the vortex at pier P1, $\Gamma_{T,P1}$, is estimated as the integral of out-of-plane vorticity in the symmetry plane over the core of the vortex. The circulation of the primary HV increases with the discharge (see nondimensional $\Gamma_{T,P1}$ values in Table 4-3 scaled using the mean velocity in the channel for the low discharge condition, $U_{0,LQ}$), mainly due to the higher incoming velocity in Case 3. When nondimensionalizing $\Gamma_{T,P1}$ using the upstream average flow velocity in the channel, U_0, the circulation values are comparable (Table 4-3), though still slightly higher for the higher discharge simulation.

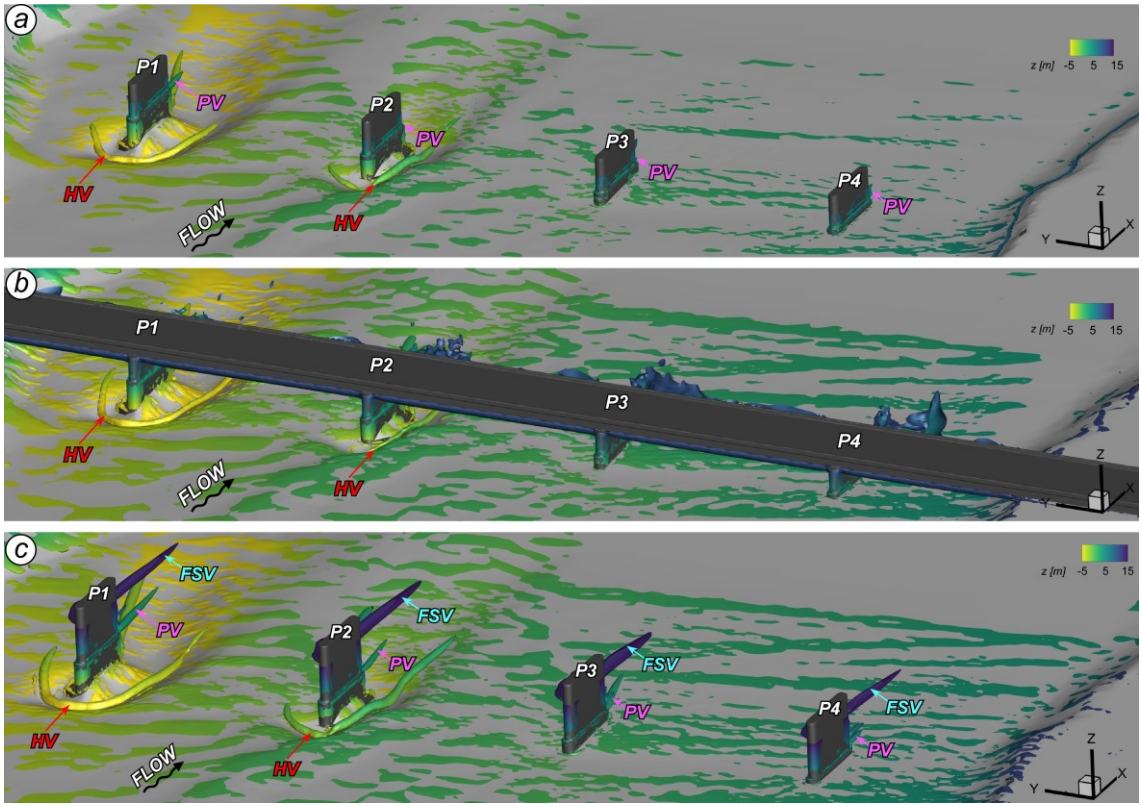

Figure 4-8. Coherent structures visualized from upstream using the Q criterion, for (a) Case 1 (low Q, with all piers, *FS* regime), (b) Case 2 (high Q, with all piers, *PF* regime), and (c) Case 3 (high Q, with all piers, *FS* regime). The red arrows point to the horseshoe vortices (HVs). The pink arrows point to the vortices forming where the pier width changes abruptly (PVs). The cyan arrows point to the vortices forming just below free surface at the left/back side of piers (FSVs).

Table 4-3. Main variables for the different simulations: $\Gamma_{T,P1}$ is the circulation of the horseshoe vortex at pier P1, d_s is the scour depth, U_0 is the mean velocity in the channel, $U_{0,LQ}$ is the mean velocity in the channel for the low Q condition, $\bar{E}_1'$ is the nondimensional mean flux of entrained sediment estimated in a 90,000 m² area around the bridge .

Case	Details of the simulation	$\Gamma_{T,P1}$ ($d_s U_{0,LQ}$)	$\Gamma_{T,P1}$ ($d_s U_0$)	$\bar{E}_1'$
1	low Q, with all piers, *FS* regime	1.057	1.057	0.0034
2	high Q, with all piers, *PF* regime	2.490	1.505	1.7009
2R	high Q, with all piers, *PF* regime, RANS	2.347	1.419	1.7567
3	high Q, with all piers, *FS* regime	1.913	1.156	0.0383
4	high Q, w/o piers, *PF* regime	-	-	1.6843
5	low Q, with one pier, *FS* regime	1.022	1.022	-

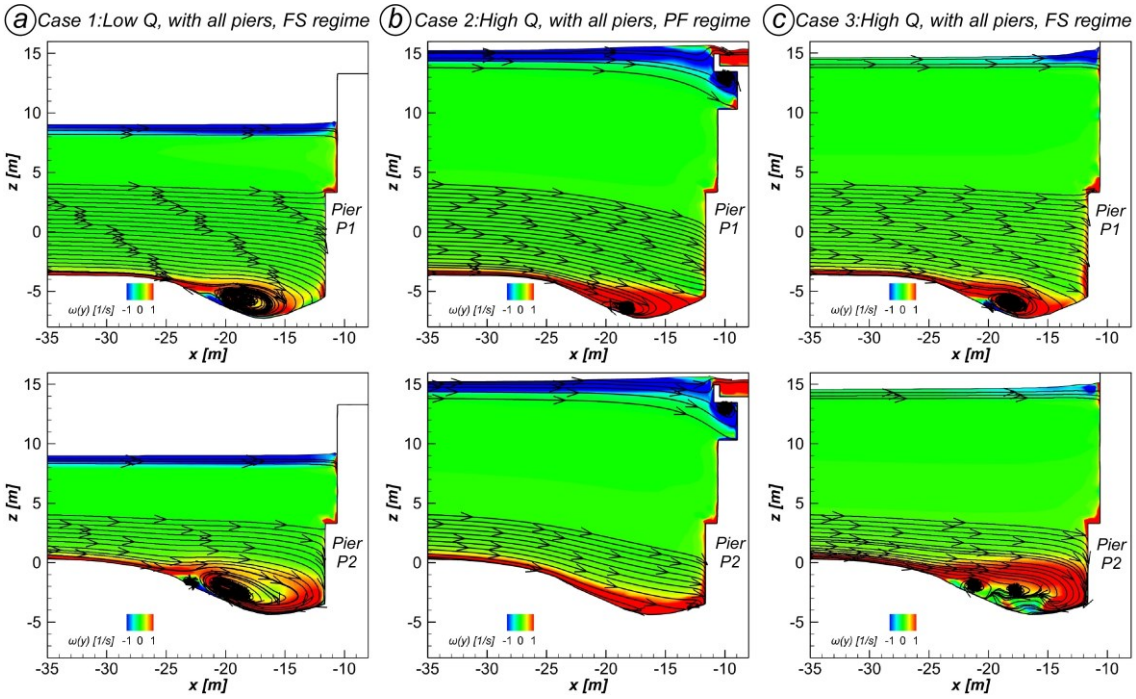

Figure 4-9. Out-of-plane mean vorticity, $\omega(y)$, and 2-D streamlines visualizing the horseshoe vortex system in a vertical plane cutting through the symmetry plane of pier P1 (top) and pier P2 (bottom). a) Case 1; b Case 2; c) Case 3.

Figure 4-9b shows that HVs also form in the simulations where the *PF* regime is present at the bridge site. The strong vertical acceleration imposed by the bridge deck limits their vertical development compared to the corresponding *FS* case (Figure 4-9c). At pier P1, the presence of pressurized flow beneath the deck reduces the HV height, but increases its circulation (see results for Cases 2 and 3 in Table 4-3). This is expected to further enhance the potential for the development of local scour in Case 2. At pier P2, the downflow associated to the orifice-flow conditions keeps the streamlines parallel to the bottom. No HV is present in the symmetry plane at pier P2 in Case 2. Interestingly, a large structure resembling the leg of a HV is present inside the scour hole of pier P2 (see Case 2 results in Figure 4-8b). This is consistent with the HV observed around pier P2 in Case 1 whose right leg is much more coherent than its right leg (see Case 1 results in Figure 4-8a). So, the transition to the *PF* regime may act toward reducing the coherence of the HV at some piers and increasing the asymmetry of this vortex with respect to the axis of the pier.

Figure 4-10 shows the coherent structures in the wake of piers P1 and P2 for some of the simulations. The turbulent structures visualized in Figure 4-10 correspond to the patches of high vorticity magnitude in the cross-sections shown in Figure 4-11. The legs of the primary HV are also visible in Figure 4-11. Because of the angle of attack of the approaching flow relative to the axis of the pier, free surface vortices (FSVs) develop at the left-hand-side of piers, whereas the flow remains attached to the right-hand side of piers P1 and P2. The FSV is a low-velocity region extending over the entire length of the pier and further downstream, where a significant increase of the *TKE* is also observed.

As the width of this detached region decreases rapidly with increasing distance from the free surface, the flow remains almost attached to the lateral face of the pier near the channel bottom.

A second coherent structure forms at the junction between the lower (3.6 m wide) and the upper (2.8 m wide) part of the pier. Being strictly connected with the geometrical shape of the pier, it is labelled as pier vortex (PV) in Figure 4-10 and Figure 4-11. A third coherent structure develops inside the scour hole (scour vortex, SV). The strength of SV is higher for pier P1, suggesting a direct dependence of the coherence of this vortical structure on the depth of the scour hole which is larger for P1 than for P2. At piers P3 and P4, where the bathymetry does not show well-developed scour holes, SV vortices are not observed, while the FSV and PV vortices are still present (Figure 4-8). FSV are not present or very weak in low-discharge simulations where the *FS* regime is present at the bridge site. SV and PV vortices are present, though their coherence is low (see results for Case 1 in Figure 4-10b). The SV and PV vortices form at piers P1 and P2 regardless of the flow regime at the bridge site (see also Figure 4-10), whereas in the *PF* regime the large-scale recirculation regions forming below and downstream the deck suppress the formation of the FSV vortex.

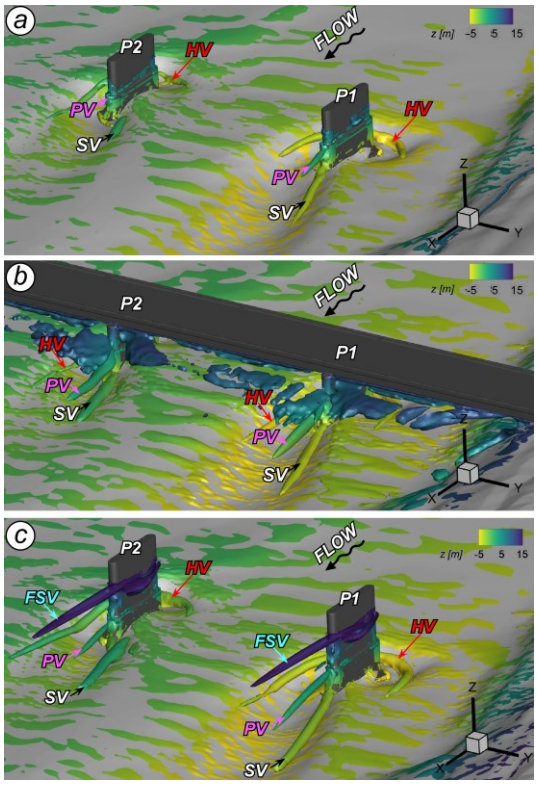

Figure 4-10. Coherent structures visualized using the Q criterion for (a) Case 1 (low Q, with all piers, *FS* regime), (b) Case 2 (high Q, with all piers, *PF* regime), and (c) Case 3 (high Q, with all piers, *FS* regime), view from downstream. Red arrows point to the horseshoe vortices (HVs), pink arrows to the vortices forming where the pier width changes abruptly (PVs), cyan arrows to the free surface vortices at the back side of the piers, beneath the free surface (FSVs), and black arrows to the streamwise-oriented vortices inside the scour hole (SVs).

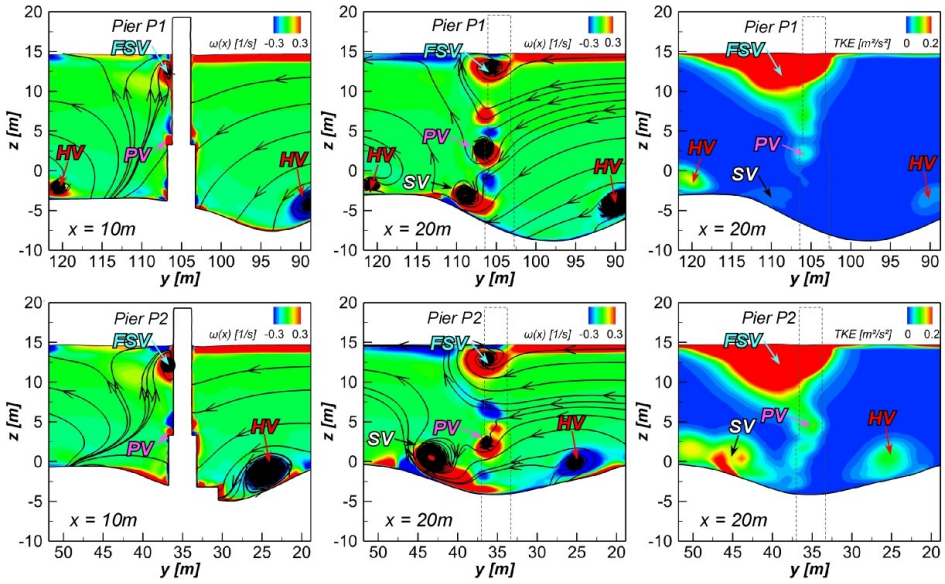

Figure 4-11. Vertical-spanwise planes downstream of piers P1 (upper frames) and P2 (lower frames) showing, for Case 3, the mean out-of-plane vorticity, $\omega(x)$, and 2-D streamline patterns at $x = 10$ m (left panels) and at $x = 20$ m (center panels), and the *TKE* at $x = 20$ m (right panels). The vortices are defined in the caption of Figure 4-10.

The large-scale vortex structures generated by the piers induce regions of high turbulence intensity. Figure 4-12 shows the *TKE* distribution upstream of pier P1 for some of the simulations. All the cases in Figure 4-12 show a large *TKE* amplification inside the HV region. The high *TKE* values are due to oscillations in the position of the vortex core, such that the *TKE* peaks inside the core of the primary HVs (Figure 4-9), as also observed by Kirkil et al. (2008) for isolated piers. Similar to the trends observed for the circulation of these vortices, the *TKE* inside the core of these vortices increases with the discharge and for the same discharge the circulation is larger in the *PF* regime than in the *FS* regime.

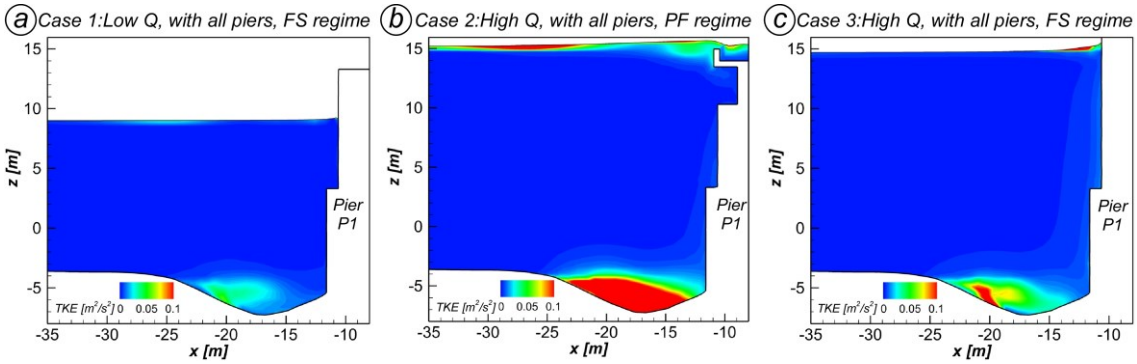

Figure 4-12. *TKE* in a vertical plane cutting through the symmetry plane of pier P1 showing the amplification of the turbulence inside the horseshoe vortex system. a) Case 1; b Case 2; c) Case 3.

4.3.2 Changes in the erosive capability of the flow associated with transition from *FS* to *PF* regime

A reliable and precise estimation of bed shear stresses at bridge sites is important for several reasons. For example, the design of the riprap apron to protect piers against erosion requires prediction of the peak bed shear stresses over the riprap region. Figure 4-13 compares the distributions of the mean bed shear stress magnitude, $\bar{\tau}_b$, around the bridge for the different simulations where either the *FS* or the *PF* regime is present. As a result of the deformed bathymetry, the spatial distribution of $\bar{\tau}_b$ is generally less regular than the typical distributions presented in studies that considered flat-bed conditions (e.g., Chang et al., 2013; Kirkil & Constantinescu, 2015). For Case 1 (*FS* regime), regions of high bed shear stress are observed at the sides of piers due to the flow acceleration; this effect is particularly clear for piers P3 and P4 where no scour hole forms. It should be also noted that the regions of high bed shear stress are not symmetric with respect to the main axis of the pier because of the irregular bathymetry and, above all, the pier orientation with respect to the approaching flow. Even modest angles of attack have been shown to strongly amplify the bed shear stresses and to increase the scour depth (Chang et al., 2011; Yu and Zhu, 2020).

In case of severe flooding, when the flow becomes pressurized at the bridge site, the distribution of bed shear stresses is strongly altered. Results for Case 2 (Figure 4-13b) show that a large region of high bed shear stresses is present below the deck due to the strong acceleration of the flow. Inside this region, high values are observed both inside and outside the scour holes at piers P1 and P2. The average magnitude of the bed shear stresses strongly decays fast past the bridge location even if regions with relatively high bed shear stresses starting in between the piers are present. The decay of the bed shear stress inside these regions follows the same trend observed for the mean streamwise velocity (see Figure 4-7a). This confirms that in the cases where the *PF* regime is present, the strong increase of the bed shear stresses beneath and downstream of the bridge deck is essentially induced by the strong acceleration of the flow passing beneath the deck. In the simulations where the *FS* regime is observed at the bridge site, the distribution of the bed shear stresses remains similar as the discharge increases (see Figure 4-13a and Figure 4-13d). One should also note that for same discharge and water stage in the incoming flow, the maximum values of $\bar{\tau}_b$ in the simulation where the *FS* regime is present are less than half compared to ones in the corresponding simulation where the *PF* regime is present.

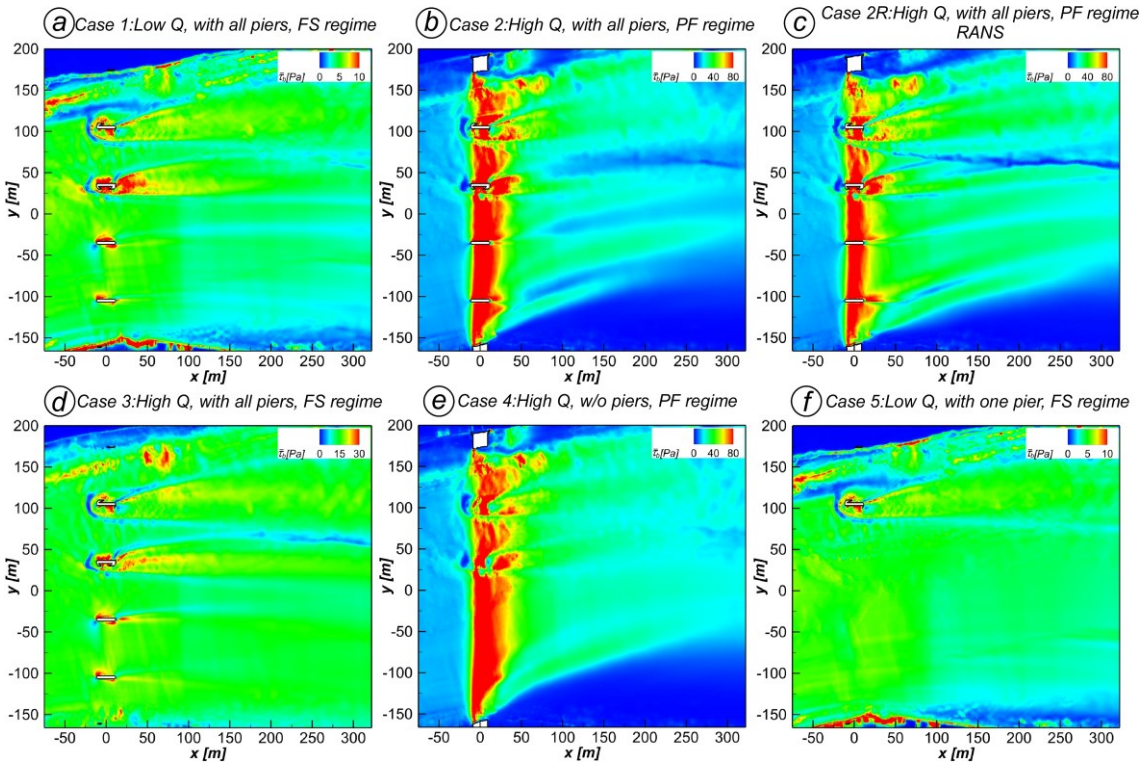

Figure 4-13. Mean bed shear stress, $\bar{\boldsymbol{\tau}}_{\boldsymbol{b}}$, over the region where the entrained flux of sediment is evaluated. Frames (a) to (f) refer to the different simulations. Note that the color scale is different in the frames.

The distributions of the standard deviation of bed shear stress magnitude, τ_b^{SD}, provide information on the temporal variability of τ_b (Figure 4-14). In the simulations where the *FS* regime is present at the bridge site, high values of τ_b^{SD} are observed inside the scour holes and in the wakes of the piers wakes due to the presence and/or passage of large-scale coherent structures close to the bed surface. As expected, τ_b^{SD}increases with increasing flow discharge (see Figure 4-14a and Figure 4-14d). In the simulation where the flow is pressurized at the bridge site, strong fluctuations are observed downstream of the bridge and, especially, in the pier wakes (Figure 4-14b). The region below the deck is characterized by high values of $\bar{\tau}_b$ but fairly low values of τ_b^{SD}. This is due the relative steadiness of the high-velocity core forming beneath the bridge deck. The largest values of τ_b^{SD} are predicted just downstream of the bridge where the thickness of the core of high velocities is the smallest. The variation in the thickness of this region is controlled by the shear layer and associated recirculation regions generated at the leading edge of the bridge deck (e.g., see Figure 4-5c-e). For same discharge and water stage in the incoming flow, the average τ_b^{SD} values are larger in the simulation where the *PF* regime is present. For example, peak τ_b^{SD} values are about 3 times larger in Case 2 (Figure 4-14b) compared to Case 3 (Figure 4-14d). This further enhances the sediment erosive capacity of the flow in cases when the *PF* regime is present.

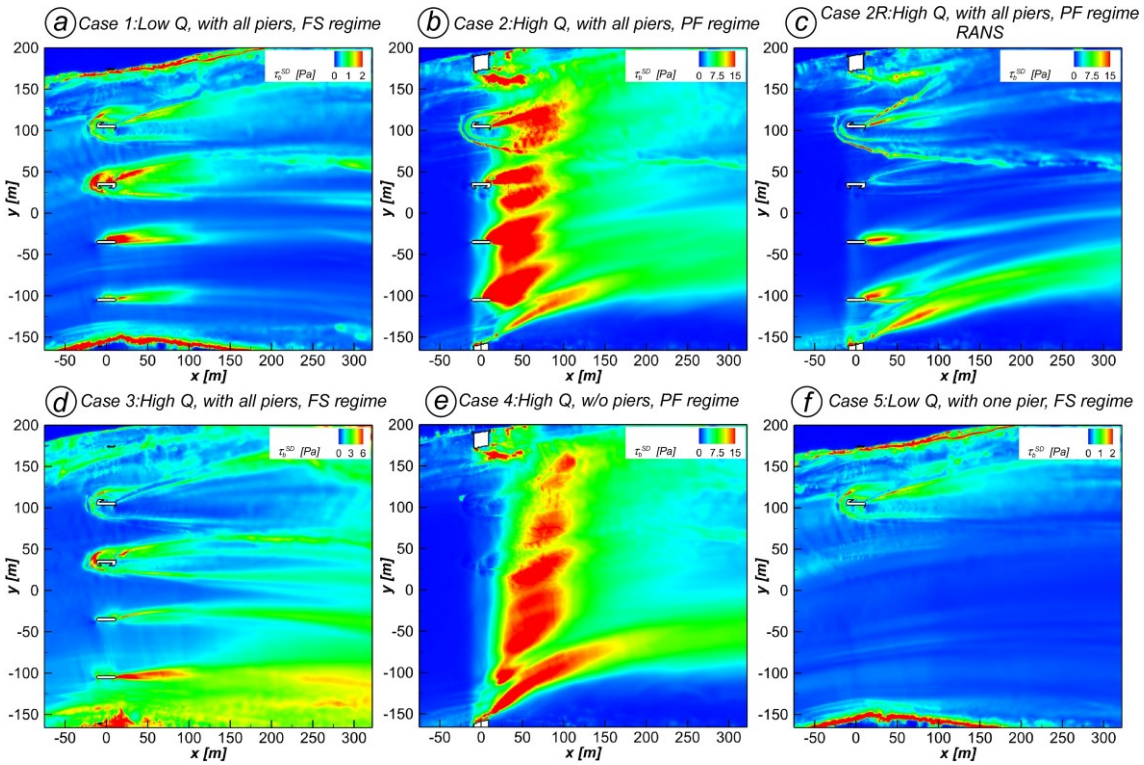

Figure 4-14. Standard deviation of the bed shear stress, τ_b^{SD}, over the region where the entrained flux of sediment is evaluated. Frames (a) to (f) refer to the different simulations. Note that the color scale is different in the frames.

The area used for estimating the total flux of entrained sediment in the bridge region extends from x = -50 m to x = 250 m, and is limited to the active riverbed (i.e., z < 3 m). This surface has an area of about 90,000 m². The critical bed shear stress used in Eq. (5) was $\tau_{b,c}$ = 15.21 Pa, which corresponds to a mean sediment diameter d_{50} = 20 mm based on the Shields diagram. In the *FS* regime, the total flux of entrained sediment increases with increasing flow discharge. For example, $\bar{E}_1'$ increases by a factor of 10 between Case 1 and Case 3 for which the discharge increases only by a factor of 3 (Table 3). The highest values of the bed shear stress are recorded close to the piers and inside the scour holes.

One of the most critical aspects associated with the change from the *FS* to the *PF* regime is the increase of the bed shear stresses around the region where the bridge is situated, which results in an increased potential of the flow to entrain sediment. The increased erosion induced by the flow becoming pressurized at the bridge site is associated with pressure scour effects. Severe pressure scour effects are a major risk for the structure, especially considering that usually only limited areas around the base of piers and abutments are adequately protected against scouring (e.g., with riprap stones or using armoring). Comparison of the flux of sediment entrained from the bed in Case 2 and Case 3 can be used to approximatively estimate the increase in the sediment entrainment capacity of the flow associated with a change from the *FS* regime to the *PF* regime for a given elevation of the bridge deck, water stage and discharge in the incoming flow. The estimated flux of entrained sediments for Case 2 (*PF* regime) is 50

times larger than the value estimated for the same flow conditions but assuming *FS* regime at the bridge site. This enforces the need of preventing transition to *PF* conditions at bridges to preserve the bed integrity.

4.3.3 Effects of pier proximity in the *PF* regime

As discussed in Sections 4.3.1 and 4.3.2, once the pressure-flow (*PF*) regime occurs, the erosive capacity of the flow around the bridge section increases significantly. To be able to estimate the relative contribution of the piers (which induce local and contraction scour) on the sediment entrainment capacity of the flow, an additional simulation (Case 4) was performed with the same discharge, water stage and bridge deck elevation as in Case 2 but with the piers removed. The capacity of the flow to erode the bed in Case 4 is due only to the pressurized flow forming beneath the bridge deck. So, the difference between the total flux of entrained sediment in Case 2 and Case 4 can be used to estimate the contribution of the piers for cases where the *PF* regime is present at the bridge site.

The flow field in streamwise-vertical planes in Case 4 (Figure 4-15) is qualitatively and quantitatively similar to that observed in Case 2 at sections situated not very close to the piers (Figure 4-5). This indicates that the vertical contraction induced by the deck is controlling the acceleration of the flow beneath the bridge deck. This is somewhat expected given that the piers are relatively thin at the analysed bridge site. The recirculation regions originating below and downstream of the deck are also qualitatively similar for Case 2 and Case 4. The main difference is the absence of the pier wakes and HVs in Case 4.

The distributions of mean bed shear stresses also reveal very small differences between Case 2 (Figure 4-13b) and Case 4 (Figure 4-13e). This is because the high-velocity core forming below the deck in the *PF* regime is the driving factor for sediment erosion. The increase of the mean bed shear stress due to local acceleration of the flow around the sides of the piers and the HVs is quite small compared to the average values in the same regions predicted in the simulation with no piers. The standard deviation of the bed shear stress also shows only small variations between the cases with and without piers (Figure 4-14b and Figure 4-14e). For *PF* conditions at the bridge, the shedding of vortices in the wake of the piers does not induce large fluctuations in the bed shear stresses. This differs from the cases where the flow at the bridge site is in the *FS* regime where vortex shedding in the wake of the piers can induce relatively high values of τ_b^{SD}.

Consistent with the previous comparison of the bed shear stress quantities, the volumetric fluxes of entrained sediment, $\bar{E}_1'$, for Case 2 and Case 4 (Table 4-3) are close to each other. The estimated value is 1% higher for Case 2 which shows that the added entrainment due to the acceleration of the flow close to the piers and the formation of HVs is negligible for high bridge submergence where the bed shear stress amplification near the bridge is driven by pressurized flow effects.

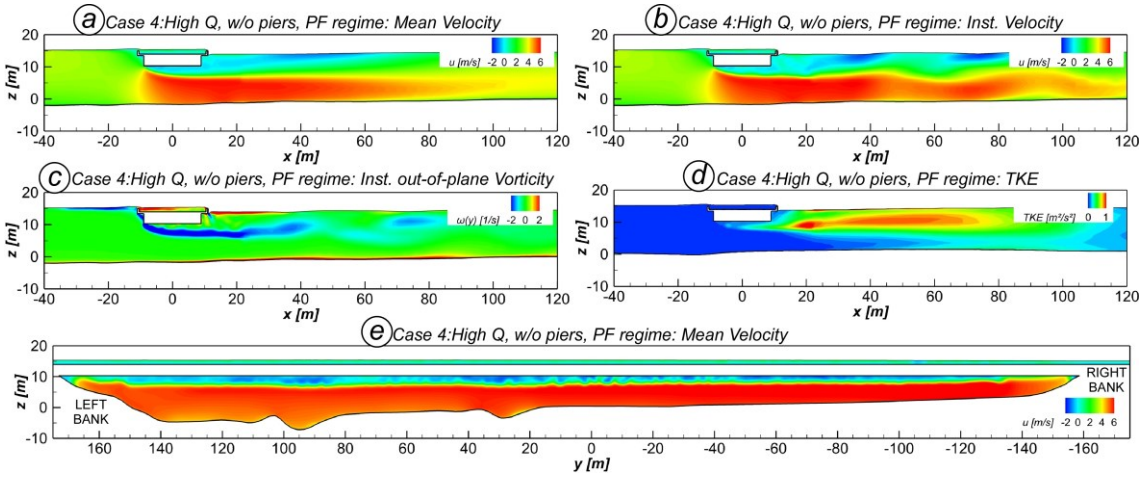

Figure 4-15. Flow structure for the Case 4 simulation. In the longitudinal-vertical section at $y = 70$m: a) mean streamwise velocity; b) instantaneous streamwise velocity; c) instantaneous out-of-plane vorticity, $\omega(y)$; d) *TKE*. In the transversal section at the bridge ($x = 0$): e) mean streamwise velocity.

4.3.4 Effects of pier proximity in the FS regime

Contraction scour is another driving mechanisms for bed erosion at bridges (Ballio et al., 2009; Dey and Raikar, 2005; Singh et al., 2020). To approximatively estimate the contribution of contraction scour if the *FS* regime is present at the bridge site, an additional simulation (Case 5) was performed. Case 1 and Case 5 conditions are identical except that only pier P1 is present in Case 5. The scour holes at the removed piers were also eliminated. Assuming an erodible bed, both local scour and contraction scour effects are present at pier P1 in Case 1, while only local scour effects are present at pier P1 in Case 5.

The flow around pier P1 is similar in the two cases (Figure 4-16), which indicates that the contraction of the flow due to the presence of pier P2 has a small overall effect on the flow fields. The coherent structures generated around pier P1 are also similar in Case 1 and Case 5. In fact, the circulation of the HV in the symmetry plane differs by less than 3% between the two simulations (Table 3). One should also mention that the contraction ratio associated with piers P1 and P2 is only about 4%, which explains the low influence of the lateral flow contraction on the flow field at the bridge analyzed in the present work.

The distributions of mean bed shear stress (Figure 4-13f) and of its standard deviation (Figure 4-14f), show also negligible variations around pier P1. Though in Case 1 all piers are included, sediment entrainment occurs mostly around pier P1 if $\tau_{b,c} = 15.21$ Pa. The total nondimensional sediment entrainment flux in a 4,000 m² area around pier P1 is $4.56 \cdot 10^{-3}$ in Case 1 and $4.05 \cdot 10^{-3}$ in Case 5, which means an increase of 12% due to the presence of pier P2. This indicates that for the case analyzed the contraction of the flow near P1 due to the presence of P2 does not significantly increase the capacity of the flow to entrain sediment.

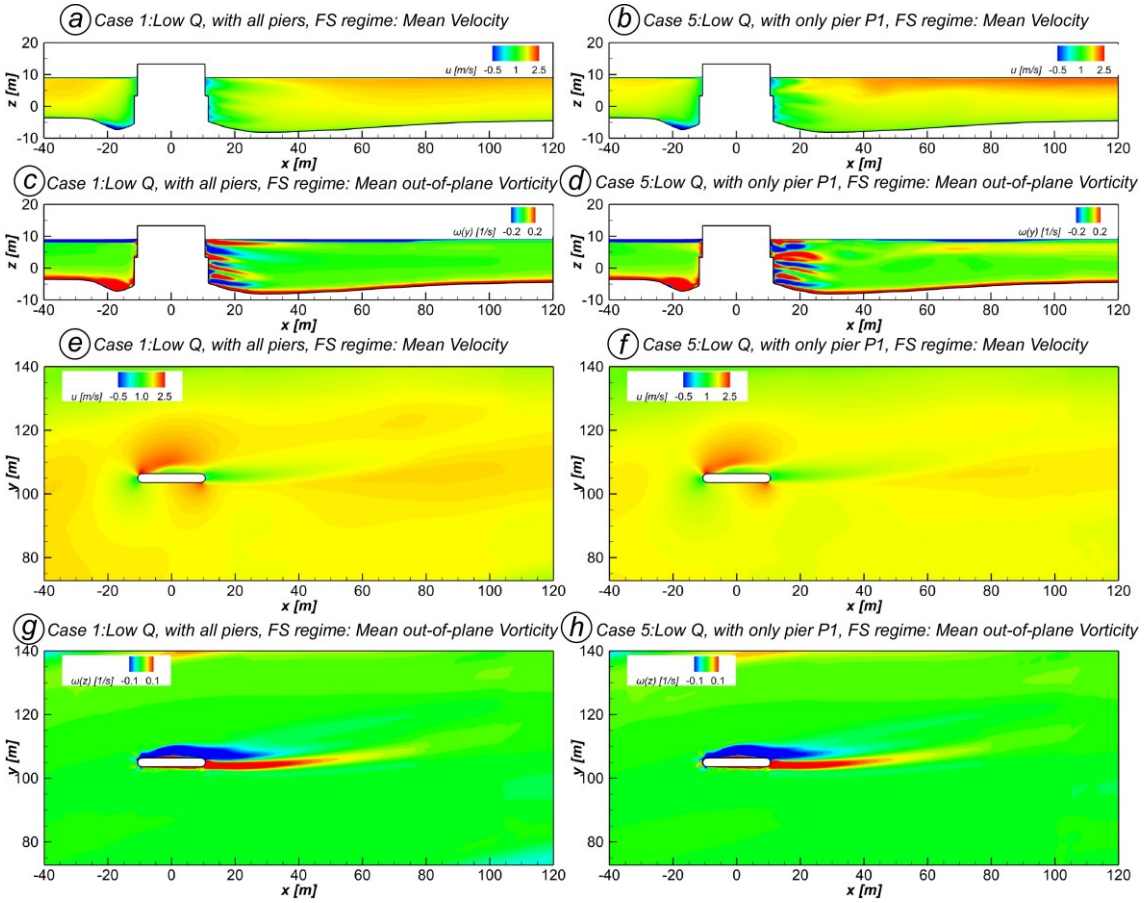

Figure 4-16. Comparison of flow structure for simulations of Case 1 (with all the piers, left) and Case 5 (with only pier P1, right). Longitudinal-vertical section at pier P1 (y = 105m): a,b) mean streamwise velocity; c,d) mean instantaneous out-of-plane vorticity, $\omega(y)$. Horizontal plane at pier P1 (z = 5 m): e,f) mean streamwise velocity; g,h) mean instantaneous out-of-plane vorticity, $\omega(z)$.

4.3.5 RANS vs. DES modelling

Previous studies have shown that eddy resolving simulations are more accurate than RANS simulations in predicting complex turbulent flows with strong adverse pressure gradients, including flow past isolated piers of various geometries and in channels with naturally-deformed bathymetry (see e.g., Constantinescu et al., 2011; Ettema et al., 2017; Kang et al., 2011). This section tries to establish the accuracy of unsteady RANS for a more complex case in which the flow at the bridge deck is pressurized and multiple piers are present at the bridge site. In principle, this is a tougher test case for RANS models. The study is performed for the geometry and conditions of Case 2. The unsteady RANS simulation is denoted Case 2R. The mean flow and statistics predicted by DES are used as a numerical experiment with respect to which the predictive capabilities of RANS are evaluated. As the unsteady RANS simulation was performed using the same mesh as in DES, differences between RANS and DES cannot be attributed to under resolution of the

flow in RANS (commonly, RANS is performed on quite coarser meshes) but only to the turbulence model.

A first important observation is that the unsteady RANS solution is quasi steady with some unsteadiness mainly present in the wake of the piers and inside the separated shear layers. Despite the fine mesh, the large eddy viscosity predicted by RANS in critical regions where energetic coherent structures are present is too large to allow the formation of wake vortices, oscillating HVs or to capture the breakup of the shear layers into smaller-scale eddies (e.g. see Figure 4-17). Despite these shortcomings, the mean velocity field predicted by RANS is surprisingly close to the mean flow calculated using the instantaneous DES flow fields.

The results confirm that the flow field, either time-averaged or instantaneous, predicted by solving the RANS equations is very similar to the time-averaged flow field solved by DES (compare Figure 4-18 with Figure 4-5 and Figure 4-6a). In particular RANS correctly captures the position and sizes of the recirculation regions forming below and downstream of the bridge deck but overpredicts the *TKE* in the recirculation regions forming downstream of the deck. RANS also underpredicts *TKE* levels in the pier wakes which is expected given that it does not generate unsteady eddies in between the separated shear layers.

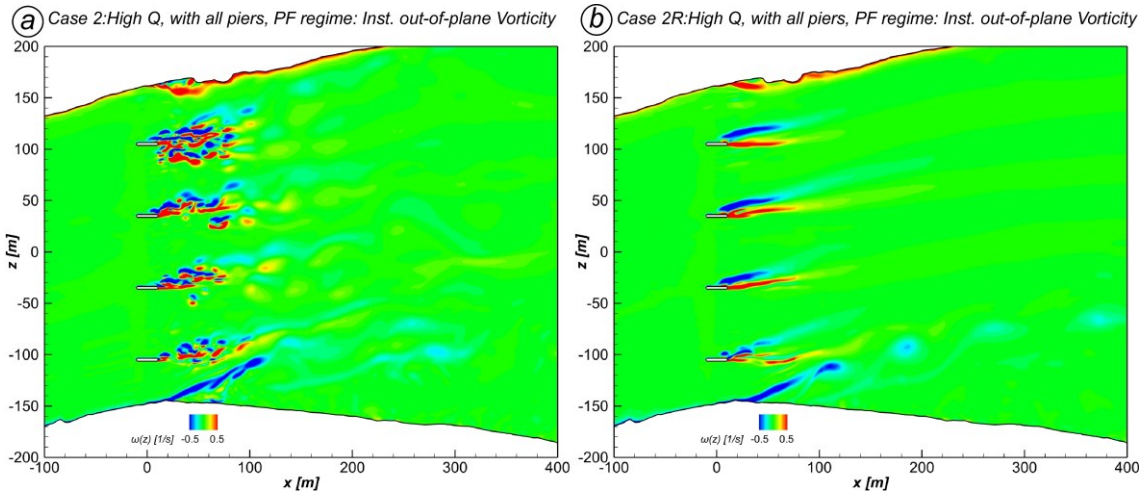

Figure 4-17. Comparison of flow structure for simulations of Case 2 (DES, a) and Case 2R (RANS, b). Instantaneous out-of-plane vorticity, $\omega(z)$, in the horizontal plane at z = 5 m.

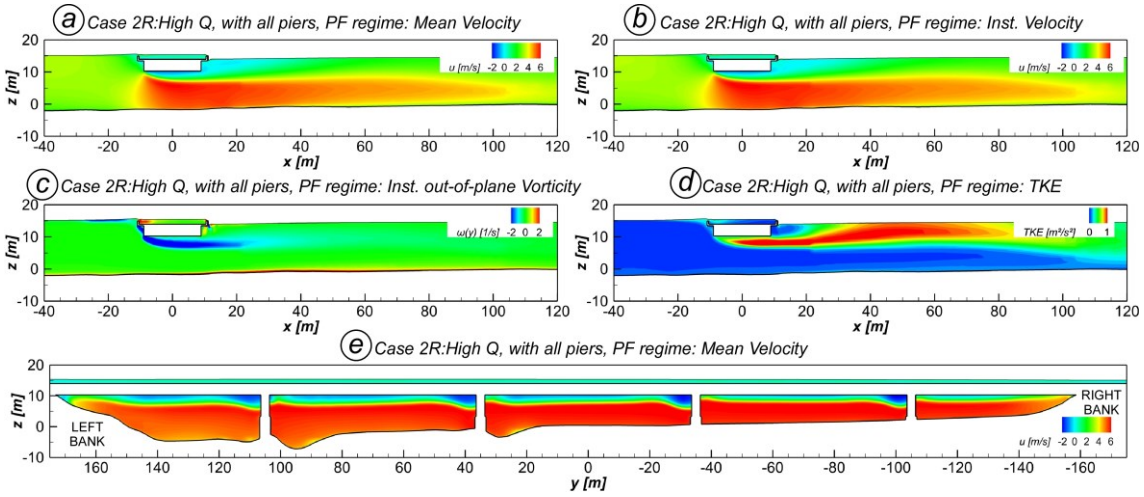

Figure 4-18. Flow structure for simulation of Case 2R. Longitudinal-vertical section situated in between piers P1 and P2 (y = 70m): a) mean streamwise velocity, u; b) instantaneous streamwise velocity, u; c) instantaneous out-of-plane vorticity, $\omega(y)$; d) *TKE*. Transversal section at the bridge (x = 0): e) mean streamwise velocity, u.

In the case of pier P1, the 2-D streamlines inside the scour hole (see Figure 4-19) show that the RANS simulation captures the formation of the HV, but the overall shape of the vortex is different from that predicted by DES (Figure 4-9b). Still the circulation of the vortex in RANS is within less than 10% of that predicted by DES (Table 3). The *TKE* levels are lower in the RANS simulation, as the unsteady RANS essentially predicts a steady HV, which is not the case in DES where the coherence of the vortex changes significantly over time. These findings are fairly consistent with that of other studies that compared the abilities of RANS and LES/DES to predict mean flow and turbulence structure at isolated piers (e.g., Constantinescu et al., 2004).

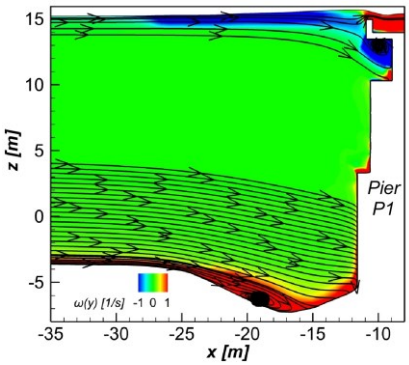

Figure 4-19. Case 2R, solved with RANS equations: out-of-plane mean vorticity, $\omega(y)$, and 2-D streamlines visualizing the horseshoe vortex system in the vertical-longitudinal symmetry plane at pier P1.

The mean bed shear stresses predicted by the RANS simulation (Figure 4-13c) are qualitatively similar to those predicted by DES (Figure 4-13b). Still, the bed shear stresses are underpredicted by RANS in the region with highest values of $\bar{\tau}_b$ (i.e., below the deck). Meanwhile, $\bar{\tau}_b$ predicted by RANS is more uniform and generally higher downstream of the bridge deck. The patterns of the standard deviation of the bed shear stress are very different in RANS and DES with much lower levels predicted in RANS (see Figure 4-14b and Figure 4-14c). This result is fully expected given the aforementioned shortcomings of unsteady RANS to capture the shedding of wakes in the piers, the break-up of the separated shear layers and the unsteady dynamics of the other large-scale coherent structures in the flow.

Despite the fact that the unsteady RANS solution does not capture the dynamics of the large-scale turbulence, the total entrainment flux predicted by RANS is about 3% higher than that predicted by DES. This is different from calculations performed at piers for non-pressurized flow conditions where the sediment entrainment flux around the pier is generally significantly higher in DES. The explanation is that in the case of *PF* regime the main contributor to the total flux of entrained sediment are the mean bed shear stresses induced beneath the core of high streamwise velocity. As already discussed, RANS predicts slightly higher bed shear stresses beneath the core of high velocity, especially downstream of the bridge deck.

4.4 Conclusions

In the present work, DES simulations with a deformable free surface have been used to simulate the flow approaching a multi-pier bridge over a complex bed geometry. Different flow regimes, including the *PF* case, and different geometrical configurations (with or without piers and/or deck) have been considered. The resulting flow fields have been analyzed in terms of coherent structures, and of the distribution of bed shear stresses, that have also been used to estimate the capacity of the flow to entrain sediment in the vicinity of the bridge site. The present study shows that eddy-resolving techniques like DES can be successfully applied to study the flow physics and the erosive potential of the flow at complex bridge sites present in natural streams including for cases when the flow becomes pressurized due to deck overtopping. Such cases cannot be modeled using 2-D depth averaged models. Complex interactions among the natural river flow and the bridge structure were explicitly accounted for with a detail level and a richness of information that are far beyond the ones available from standard methods used for hydrodynamic assessment of real bridges. Moreover, the model can be easily extended to include other man-made hydraulic structures that may affect flow pattern and sediment entrainment capacity at the bridge site and to investigate a wide range of relevant flow scenarios.

Even for the simpler case when the flow is not pressurized at the bridge site, the angle of attack and the deformed bathymetry, typical of natural rivers, as well as the complex shape of real piers, have been shown to modify the bed shear stress distributions compared to the canonical cases investigated in literature. A *FS* regime simulation

containing only the pier at which local scour is the most severe predicted very similar bed shear stresses around that pier compared to the corresponding case where all piers were present. The fact that flow contraction effects were negligible at the present bridge site was not too surprising given that the piers were thin, and the pier-to-pier distance was relatively large which translated in a low flow blocking ratio at the bridge. However, that may not be the case at other bridges.

The transition to the *PF* regime was accompanied by a super elevation of the free surface upstream the bridge section and a high-velocity orifice flow beneath the deck. Regions of high velocity were also present downstream of the bridge, and recirculation regions formed below and downstream of the deck. Compared to a simulation conducted with the same discharge and stage in the incoming flow but without the deck (*FS* regime), the bed shear stress magnitudes were much higher both around and in-between the piers. So, for sufficiently high submergence of the bridge deck, flow acceleration around the piers and contraction of the flow in between the piers have a fairly small contribution to the total erosive capacity of the flow around the bridge site. This was confirmed by conducting a *PF* regime simulation where the bridge piers were eliminated. The erosive capacity of the flow around the bridge was shown to be very close to the one in the corresponding simulation containing the piers.

Several previous studies investigated the predictive capabilities of 3-D (unsteady) RANS with respect to that of eddy resolving techniques at isolated piers and bridge sites for the *FS* regime (e.g., Kirkil & Constantinescu, 2010). However, there is very little information about the case when the flow is pressurized at the bridge site. Such information is critical as in fact the most severe erosion events at a bridge site occur when the flow becomes pressurized and pressure scour effects dominate. A comparison of the mean flow fields showed that RANS and DES predictions were qualitatively similar. In particular RANS correctly predicted the formation and position of the core of high streamwise velocities forming beneath the deck downstream of its leading edge and extending past the deck. However, the velocity distribution inside the core showed some small differences in the two simulations and RANS overpredicted the length of the core downstream of the deck. This explained why, the value of the total sediment flux entrained in the bridge region was slightly larger than that predicted by DES. This is different of what is observed around piers placed in an open channel where scour is driven by the HVs and the eddies shed in the wake. For such cases RANS and unsteady RANS severely underpredict the total flux of entrained sediment compared to LES and DES (e.g., see Cheng et al., 2018). In fact, this is true also for the present case where the unsteady RANS solution predicts a close to steady HV and no shedding in the wake and separated shear layer. So, the contribution of the large-scale turbulence to the total flux of entrained sediment is also underpredicted for cases when the flow is pressurized at the bridge site. However, for sufficient deck submergence this contribution is fairly minor compared to that associated with the flow becoming pressurized beneath the bridge. Or, this dominant contributor to the total flux of entrained sediment is slightly overpredicted by RANS. So, for engineering purposes RANS and unsteady RANS can be used to study the sediment entrainment capacity of the flow in the *PF* regime and/or

for design of scour protection measures that require information on the maximum bed shear stress in the vicinity of the pier. This is important given that present design formulas (e.g., for riprap sizing at piers) are available only for the *FS* regime.

The present study only considered cases with a constant inflow discharge and flow stage. A direction for future work will be to apply a realistic hydrograph at the inlet. Of particular relevance will be to check if the maximum bed shear stresses under varying discharge conditions still occur at the time when the peak discharge and water levels are reached and how the total flux of entrained sediment compares with that from a corresponding steady inflow simulation conducted with the peak discharge and water stage. Moreover, the sediment entrainment capacity of the flow is expected to be subject to hysteresis effects. Only fixed-bed scenarios were considered in the present study, which constitutes a first step in understanding how the flow field affects sediment entrainment. Mobile-bed simulations are computationally much more expensive, because of the large time-scale needed to obtain an equilibrium bathymetry, especially at the real scale. However, such simulations can provide valuable information on the evolution of the scouring processes and will be part of future research. In the case the flow is pressurized at the bridge site, a good compromise to tackle such very complex simulations may be the use of 3-D RANS with a movable bed.

4.5 References

Aghaee-Shalmani, Y., Hakimzadeh, H., 2022. Large eddy simulation of flow around semi-conical piers vertically mounted on the bed. Environ. Fluid Mech. 22, 1211–1232. https://doi.org/10.1007/s10652-022-09886-x

Akhlaghi, E., Babarsad, M.S., Derikvand, E., Abedini, M., 2020. Assessment the Effects of Different Parameters to Rate Scour around Single Piers and Pile Groups: A Review. Arch. Comput. Methods Eng. 27, 183–197. https://doi.org/10.1007/s11831-018-09304-w

Alemi, M., Maia, R., 2018. Numerical Simulation of the Flow and Local Scour Process around Single and Complex Bridge Piers. Int. J. Civ. Eng. 16, 475–487. https://doi.org/10.1007/s40999-016-0137-8

Ballio, F., Ballio, G., Franzetti, S., Crotti, G., Solari, G., 2018. Actions monitoring as an alternative to structural rehabilitation: Case study of a river bridge. Struct. Control Health Monit. 25, e2250. https://doi.org/10.1002/stc.2250

Ballio, F., Teruzzi, A., Radice, A., 2009. Constriction Effects in Clear-Water Scour at Abutments. J. Hydraul. Eng. 135, 140–145. https://doi.org/10.1061/(ASCE)0733-9429(2009)135:2(140)

Bressan, F., Ballio, F., Armenio, V., 2011. Turbulence around a scoured bridge abutment. J. Turbul. 12, N3. https://doi.org/10.1080/14685248.2010.534797

Breusers, H.N.C., Nicollet, G., Shen, H.W., 1977. Local Scour Around Cylindrical Piers. J. Hydraul. Res. 15, 211–252. https://doi.org/10.1080/00221687709499645

Bui, M.D., Rodi, W., 2008. Numerical Simulation of Contraction Scour in an Open Laboratory Channel. J. Hydraul. Eng. 134, 367–377. https://doi.org/10.1061/(ASCE)0733-9429(2008)134:4(367)

Carnacina, I., Pagliara, S., Leonardi, N., 2019. Bridge pier scour under pressure flow conditions. River Res. Appl. 35, 844–854. https://doi.org/10.1002/rra.3451

Chang, W.-Y., Constantinescu, G., Lien, H.-C., Tsai, W.-F., Lai, J.-S., Loh, C.-H., 2013. Flow Structure around Bridge Piers of Varying Geometrical Complexity. J. Hydraul. Eng. 139, 812–826. https://doi.org/10.1061/(ASCE)HY.1943-7900.0000742

Chang, W.-Y., Constantinescu, G., Tsai, W.F., 2017. On the flow and coherent structures generated by a circular array of rigid emerged cylinders placed in an open channel with flat and deformed bed. J. Fluid Mech. 831, 1–40. https://doi.org/10.1017/jfm.2017.558

Chang, W.-Y., Constantinescu, G., Tsai, W.F., Lien, H.C., 2011. Coherent structure dynamics and sediment erosion mechanisms around an in-stream rectangular cylinder at low and moderate angles of attack. Water Resour. Res. 47. https://doi.org/10.1029/2011WR010586

Chen, Q., Wang, L., Zhao, H., 2009. Hydrodynamic Investigation of Coastal Bridge Collapse during Hurricane Katrina. J. Hydraul. Eng. 135, 175–186. https://doi.org/10.1061/(ASCE)0733-9429(2009)135:3(175)

Cheng, Z., Koken, M., Constantinescu, G., 2018. Approximate methodology to account for effects of coherent structures on sediment entrainment in RANS simulations with a movable bed and applications to pier scour. Adv. Water Resour. 120, 65–82. https://doi.org/10.1016/j.advwatres.2017.05.019

Chrisohoides, A., Sotiropoulos, F., Sturm, T.W., 2003. Coherent Structures in Flat-Bed Abutment Flow: Computational Fluid Dynamics Simulations and Experiments. J. Hydraul. Eng. 129, 177–186. https://doi.org/10.1061/(ASCE)0733-9429(2003)129:3(177)

Constantinescu, G., Ettema, R., Koken, M., Muste, M., 2004. An eddy-resolving technique to predict the unsteady horseshoe vortex and wake of a cylindrical pier, in: Proceedings 2nd International Conference on Scour and Erosion (ICSE-2). November 14.–17., 2004, Singapore.

Constantinescu, G., Kashyap, S., Tokyay, T., Rennie, C.D., Townsend, R.D., 2013. Hydrodynamic processes and sediment erosion mechanisms in an open channel bend of strong curvature with deformed bathymetry. J. Geophys. Res. Earth Surf. 118, 480–496. https://doi.org/10.1002/jgrf.20042

Constantinescu, G., Koken, M., Zeng, J., 2011. The structure of turbulent flow in an open channel bend of strong curvature with deformed bed: Insight provided by detached eddy simulation. Water Resour. Res. 47. https://doi.org/10.1029/2010WR010114

Cook, W., Barr, P.J., Halling, M.W., 2015. Bridge Failure Rate. J. Perform. Constr. Facil. 29, 04014080. https://doi.org/10.1061/(ASCE)CF.1943-5509.0000571

De Cicco, P.N., Paris, E., Solari, L., Ruiz-Villanueva, V., 2020. Bridge pier shape influence on wood accumulation: Outcomes from flume experiments and numerical modelling. J. Flood Risk Manag. 13, e12599. https://doi.org/10.1111/jfr3.12599

Defina, A., 2003. Numerical experiments on bar growth. Water Resour. Res. 39, 1092. https://doi.org/10.1029/2002WR001455

Defina, A., 2000. Two-dimensional shallow flow equations for partially dry areas. Water Resour. Res. 36, 3251–3264. https://doi.org/10.1029/2000WR900167

Deng, L., Wang, W., Yu, Y., 2016. State-of-the-Art Review on the Causes and Mechanisms of Bridge Collapse. J. Perform. Constr. Facil. 30, 04015005. https://doi.org/10.1061/(ASCE)CF.1943-5509.0000731

Dey, S., Raikar, R.V., 2007. Characteristics of Horseshoe Vortex in Developing Scour Holes at Piers. J. Hydraul. Eng. 133, 399–413. https://doi.org/10.1061/(ASCE)0733-9429(2007)133:4(399)

Dey, S., Raikar, R.V., 2005. Scour in Long Contractions. J. Hydraul. Eng. 131, 1036–1049. https://doi.org/10.1061/(ASCE)0733-9429(2005)131:12(1036)

Edwards, C., Lottes, S.A., Majumdar, P., 2013. Three-Dimensional Mesh Morphing Methodology for Scouring Around Bridge Piers Based on Computational Fluid Dynamic Solution, in: IMECE2013. Volume 7B: Fluids Engineering Systems and Technologies. https://doi.org/10.1115/IMECE2013-62278

Ettema, R., Constantinescu, G., Melville, B.W., 2017. Flow-Field Complexity and Design Estimation of Pier-Scour Depth: Sixty Years since Laursen and Toch. J. Hydraul. Eng. 143, 03117006. https://doi.org/10.1061/(ASCE)HY.1943-7900.0001330

Flint, M.M., Fringer, O., Billington, S.L., Freyberg, D., Diffenbaugh, N.S., 2017. Historical Analysis of Hydraulic Bridge Collapses in the Continental United States. J. Infrastruct. Syst. 23, 04017005. https://doi.org/10.1061/(ASCE)IS.1943-555X.0000354

Fröhlich, J., von Terzi, D., 2008. Hybrid LES/RANS methods for the simulation of turbulent flows. Prog. Aerosp. Sci. 44, 349–377. https://doi.org/10.1016/j.paerosci.2008.05.001

Ge, L., Sotiropoulos, F., 2005. 3D Unsteady RANS Modeling of Complex Hydraulic Engineering Flows. I: Numerical Model. J. Hydraul. Eng. 131, 800–808. https://doi.org/10.1061/(ASCE)0733-9429(2005)131:9(800)

Heinz, S., 2020. A review of hybrid RANS-LES methods for turbulent flows: Concepts and applications. Prog. Aerosp. Sci. 114, 100597. https://doi.org/10.1016/j.paerosci.2019.100597

Hirt, C.W., Nichols, B.D., 1981. Volume of fluid (VOF) method for the dynamics of free boundaries. J. Comput. Phys. 39, 201–225. https://doi.org/10.1016/0021-9991(81)90145-5

Hofland, B., Battjes, J.A., 2006. Probability Density Function of Instantaneous Drag Forces and Shear Stresses on a Bed. J. Hydraul. Eng. 132, 1169–1175. https://doi.org/10.1061/(ASCE)0733-9429(2006)132:11(1169)

Horna-Munoz, D., Constantinescu, G., 2020. 3-D dam break flow simulations in simplified and complex domains. Adv. Water Resour. 137, 103510. https://doi.org/10.1016/j.advwatres.2020.103510

Horna-Munoz, D., Constantinescu, G., 2018. A fully 3-D numerical model to predict flood wave propagation and assess efficiency of flood protection measures. Adv. Water Resour. 122, 148–165. https://doi.org/10.1016/j.advwatres.2018.10.014

Kang, S., Lightbody, A., Hill, C., Sotiropoulos, F., 2011. High-resolution numerical simulation of turbulence in natural waterways. Adv. Water Resour. 34, 98–113. https://doi.org/10.1016/j.advwatres.2010.09.018

Kara, S., Kara, M.C., Stoesser, T., Sturm, T.W., 2015a. Free-Surface versus Rigid-Lid LES Computations for Bridge-Abutment Flow. J. Hydraul. Eng. 141, 04015019. https://doi.org/10.1061/(ASCE)HY.1943-7900.0001028

Kara, S., Stoesser, T., Sturm, T.W., Mulahasan, S., 2015b. Flow dynamics through a submerged bridge opening with overtopping. J. Hydraul. Res. 53, 186–195. https://doi.org/10.1080/00221686.2014.967821

Keylock, C.J., Constantinescu, G., Hardy, R.J., 2012. The application of computational fluid dynamics to natural river channels: Eddy resolving versus mean flow approaches. Geomorphology 179, 1–20. https://doi.org/10.1016/j.geomorph.2012.09.006

Khosronejad, A., Kang, S., Sotiropoulos, F., 2012. Experimental and computational investigation of local scour around bridge piers. Adv. Water Resour. 37, 73–85. https://doi.org/10.1016/j.advwatres.2011.09.013

Khosronejad, A., Le, T., DeWall, P., Bartelt, N., Woldeamlak, S., Yang, X., Sotiropoulos, F., 2016. High-fidelity numerical modeling of the Upper Mississippi River under extreme flood condition. Adv. Water Resour. 98, 97–113. https://doi.org/10.1016/j.advwatres.2016.10.018

Kim, H.S., Nabi, M., Kimura, I., Shimizu, Y., 2014. Numerical investigation of local scour at two adjacent cylinders. Adv. Water Resour. 70, 131–147. https://doi.org/10.1016/j.advwatres.2014.04.018

Kirkil, G., Constantinescu, G., 2015. Effects of cylinder Reynolds number on the turbulent horseshoe vortex system and near wake of a surface-mounted circular cylinder. Phys. Fluids 27, 075102. https://doi.org/10.1063/1.4923063

Kirkil, G., Constantinescu, G., 2012. A numerical study of the laminar necklace vortex system and its effect on the wake for a circular cylinder. Phys. Fluids 24, 073602. https://doi.org/10.1063/1.4731291

Kirkil, G., Constantinescu, G., 2010. Flow and turbulence structure around an in-stream rectangular cylinder with scour hole. Water Resour. Res. 46. https://doi.org/10.1029/2010WR009336

Kirkil, G., Constantinescu, G., 2009. Nature of flow and turbulence structure around an in-stream vertical plate in a shallow channel and the implications for sediment erosion. Water Resour. Res. 45. https://doi.org/10.1029/2008WR007363

Kirkil, G., Constantinescu, G., Ettema, R., 2009. Detached Eddy Simulation Investigation of Turbulence at a Circular Pier with Scour Hole. J. Hydraul. Eng. 135, 888–901. https://doi.org/10.1061/(ASCE)HY.1943-7900.0000101

Kirkil, G., Constantinescu, S.G., Ettema, R., 2008. Coherent Structures in the Flow Field around a Circular Cylinder with Scour Hole. J. Hydraul. Eng. 134, 572–587. https://doi.org/10.1061/(ASCE)0733-9429(2008)134:5(572)

Kitanidis, P.K., Kennedy, J.F., 1984. Secondary current and river-meander formation. J. Fluid Mech. 144, 217–229. https://doi.org/10.1017/S0022112084001580

Koken, M., Constantinescu, G., 2014. Flow and Turbulence Structure around Abutments with Sloped Sidewalls. J. Hydraul. Eng. 140, 04014031. https://doi.org/10.1061/(ASCE)HY.1943-7900.0000876

Koken, M., Constantinescu, G., 2011. Flow and turbulence structure around a spur dike in a channel with a large scour hole. Water Resour. Res. 47. https://doi.org/10.1029/2011WR010710

Koken, M., Constantinescu, G., Blanckaert, K., 2013. Hydrodynamic processes, sediment erosion mechanisms, and Reynolds-number-induced scale effects in an open channel bend of strong

curvature with flat bathymetry. J. Geophys. Res. Earth Surf. 118, 2308–2324. https://doi.org/10.1002/2013JF002760

Larsen, R.J., Ting, F.C.K., Jones, A.L., 2011. Flow Velocity and Pier Scour Prediction in a Compound Channel: Big Sioux River Bridge at Flandreau, South Dakota. J. Hydraul. Eng. 137, 595–605. https://doi.org/10.1061/(ASCE)HY.1943-7900.0000334

Lazzarin, T., Defina, A., Viero, D.P., 2023a. Assessing 40 Years of Flood Risk Evolution at the Micro-Scale Using an Innovative Modeling Approach: The Effects of Urbanization and Land Planning. Geosciences 13. https://doi.org/10.3390/geosciences13040112

Lazzarin, T., Viero, D.P., 2023. Curvature-induced secondary flow in 2D depth-averaged hydro-morphodynamic models: An assessment of different approaches and key factors. Adv. Water Resour. 171, 104355. https://doi.org/10.1016/j.advwatres.2022.104355

Lazzarin, T., Viero, D.P., Defina, A., Cozzolino, L., 2023b. Flow under vertical sluice gates: Flow stability at large gate opening and disambiguation of partial dam-break multiple solutions. Phys. Fluids 35, 024114. https://doi.org/10.1063/5.0131953

Majid, S.A., Tripathi, S., 2021. Pressure-Flow Scour Due to Vertical Contraction: A Review. J. Hydraul. Eng. 147, 03121002. https://doi.org/10.1061/(ASCE)HY.1943-7900.0001943

Malik, R., Setia, B., 2019. Interference between pier models and its effects on scour depth. SN Appl. Sci. 2, 68. https://doi.org/10.1007/s42452-019-1868-3

Mannini, C., Šoda, A., Voß, R., Schewe, G., 2010. Unsteady RANS simulations of flow around a bridge section. J. Wind Eng. Ind. Aerodyn. 98, 742–753. https://doi.org/10.1016/j.jweia.2010.06.010

McCoy, A., Constantinescu, G., Weber, L.J., 2008. Numerical Investigation of Flow Hydrodynamics in a Channel with a Series of Groynes. J. Hydraul. Eng. 134, 157–172. https://doi.org/10.1061/(ASCE)0733-9429(2008)134:2(157)

Mel, R.A., Viero, D.P., Carniello, L., D'Alpaos, L., 2020. Optimal floodgate operation for river flood management: The case study of Padova (Italy). J. Hydrol. Reg. Stud. 30, 100702. https://doi.org/10.1016/j.ejrh.2020.100702

Melville, B.W., Coleman, S.E., 2000. Bridge scour, Water Resources Publications. ed. Littleton, Colorado.

Melville, B.W., Sutherland, A.J., 1988. Design Method for Local Scour at Bridge Piers. J. Hydraul. Eng. 114, 1210–1226. https://doi.org/10.1061/(ASCE)0733-9429(1988)114:10(1210)

Menter, F., 1994. Two-equation eddy-viscosity turbulence models for engineering applications. AIAA J. 32, 1598–1605. https://doi.org/10.2514/3.12149

Menter, F., Hüppe, A., Matyushenko, A., Kolmogorov, D., 2021. An Overview of Hybrid RANS–LES Models Developed for Industrial CFD. Appl. Sci. 11. https://doi.org/10.3390/app11062459

Menter, F., Kuntz, M., Langtry, R., 2003. Ten years of industrial experience with the SST turbulence model. Heat Mass Transf. 625–632.

Montalvo, C., Cook, W., Keeney, T., 2020. Retrospective Analysis of Hydraulic Bridge Collapse. J. Perform. Constr. Facil. 34, 04019111. https://doi.org/10.1061/(ASCE)CF.1943-5509.0001378

Muñoz Diaz, E.E., Moreno Núñez, F., Mohammadi, J., 2009. Investigation of Common Causes of Bridge Collapse in Colombia. Pract. Period. Struct. Des. Constr. 14, 194–200. https://doi.org/10.1061/(ASCE)SC.1943-5576.0000006

Muzzammil, M., Gangadhariah, T., 2003. The mean characteristics of horseshoe vortex at a cylindrical pier. J. Hydraul. Res. 41, 285–297. https://doi.org/10.1080/00221680309499973

Nelson, J.M., Shreve, R.L., McLean, S.R., Drake, T.G., 1995. Role of Near-Bed Turbulence Structure in Bed Load Transport and Bed Form Mechanics. Water Resour. Res. 31, 2071–2086. https://doi.org/10.1029/95WR00976

Paik, J., Ge, L., Sotiropoulos, F., 2004. Toward the simulation of complex 3D shear flows using unsteady statistical turbulence models. Turbul. Shear Flow Phenom. TSFP-3 25, 513–527. https://doi.org/10.1016/j.ijheatfluidflow.2004.02.002

Patankar, S.V., Spalding, D.B., 1972. A calculation procedure for heat, mass and momentum transfer in three-dimensional parabolic flows. Int. J. Heat Mass Transf. 15, 1787–1806. https://doi.org/10.1016/0017-9310(72)90054-3

Pourshahbaz, H., Abbasi, S., Pandey, M., Pu, J.H., Taghvaei, P., Tofangdar, N., 2022. Morphology and hydrodynamics numerical simulation around groynes. ISH J. Hydraul. Eng. 28, 53–61. https://doi.org/10.1080/09715010.2020.1830000

Pregnolato, M., Winter, A.O., Mascarenas, D., Sen, A.D., Bates, P., Motley, M.R., 2022. Assessing flooding impact to riverine bridges: an integrated analysis. Nat. Hazards Earth Syst. Sci. 22, 1559–1576. https://doi.org/10.5194/nhess-22-1559-2022

Raikar, R.V., Wang, C.-Y., Shih, H.-P., Hong, J.-H., 2016. Prediction of contraction scour using ANN and GA. Flow Meas. Instrum. 50, 26–34. https://doi.org/10.1016/j.flowmeasinst.2016.06.006

Roulund, A., Sumer, B.M., Fredsøe, J., Michelsen, J., 2005. Numerical and experimental investigation of flow and scour around a circular pile. J. Fluid Mech. 534, 351–401. https://doi.org/10.1017/S0022112005004507

Schmeeckle, M.W., Nelson, J.M., 2003. Direct numerical simulation of bedload transport using a local, dynamic boundary condition. Sedimentology 50, 279–301. https://doi.org/10.1046/j.1365-3091.2003.00555.x

Shinneeb, A.-M., Nasif, G., Balachandar, R., 2021. Effect of the aspect ratio on the velocity field of a straight open-channel flow. Phys. Fluids 33, 085110. https://doi.org/10.1063/5.0057343

Singh, R.K., Pandey, M., Pu, J.H., Pasupuleti, S., Villuri, V.G.K., 2020. Experimental study of clear-water contraction scour. Water Supply 20, 943–952. https://doi.org/10.2166/ws.2020.014

Sterling, M., Beaman, F., Morvan, H., Wright, N., 2008. Bed-Shear Stress Characteristics of a Simple, Prismatic, Rectangular Channel. J. Eng. Mech. 134, 1085–1094. https://doi.org/10.1061/(ASCE)0733-9399(2008)134:12(1085)

Sumer, B.M., Chua, L.H.C., Cheng, N.-S., Fredsøe, J., 2003. Influence of Turbulence on Bed Load Sediment Transport. J. Hydraul. Eng. 129, 585–596. https://doi.org/10.1061/(ASCE)0733-9429(2003)129:8(585)

Teruzzi, A., Ballio, F., Armenio, V., 2009. Turbulent Stresses at the Bottom Surface near an Abutment: Laboratory-Scale Numerical Experiment. J. Hydraul. Eng. 135, 106–117. https://doi.org/10.1061/(ASCE)0733-9429(2009)135:2(106)

Tulimilli, B.R., Lottes, S.A., Majumdar, P., Kostic, M., 2011. Three-Dimensional Scouring Analysis for Open Channel Pressure Flow Scour Under Flooded Bridge Decks, in: IMECE2011. Volume 6: Fluids and Thermal Systems; Advances for Process Industries, Parts A and B, pp. 975–981. https://doi.org/10.1115/IMECE2011-65529

Umbrell, E.R., Young, G.K., Stein, S.M., Sterling, J.J., 1998. Clear-Water Contraction Scour under Bridges in Pressure Flow. J. Hydraul. Eng. 124, 236–240. https://doi.org/10.1061/(ASCE)0733-9429(1998)124:2(236)

van Rijn, L.C., 1984. Sediment Pick-Up Functions. J. Hydraul. Eng. 110, 1494–1502. https://doi.org/10.1061/(ASCE)0733-9429(1984)110:10(1494)

Viero, D.P., D'Alpaos, A., Carniello, L., Defina, A., 2013. Mathematical modeling of flooding due to river bank failure. Adv. Water Resour. 59, 82–94. https://doi.org/10.1016/j.advwatres.2013.05.011

Viero, D.P., Roder, G., Matticchio, B., Defina, A., Tarolli, P., 2019. Floods, landscape modifications and population dynamics in anthropogenic coastal lowlands: The Polesine (northern Italy) case study. Sci. Total Environ. 651, 1435–1450. https://doi.org/10.1016/j.scitotenv.2018.09.121

Wang, C., Yu, X., Liang, F., 2017. A review of bridge scour: mechanism, estimation, monitoring and countermeasures. Nat. Hazards 87, 1881–1906. https://doi.org/10.1007/s11069-017-2842-2

Wardhana, K., Hadipriono, F.C., 2003. Analysis of Recent Bridge Failures in the United States. J. Perform. Constr. Facil. 17, 144–150. https://doi.org/10.1061/(ASCE)0887-3828(2003)17:3(144)

Wilcox, D.C., 1998. Turbulence Modeling for CFD. 2nd edition, DCW Industries, Inc.

Wu, H., Zeng, J., Constantinescu, G., 2021. A multi-parameter design formula for riprap size selection at wing-wall abutments. J. Hydraul. Res. 59, 651–661. https://doi.org/10.1080/00221686.2020.1818310

Xie, Q., Yang, J., Lundström, T.S., 2019. Field Studies and 3D Modelling of Morphodynamics in a Meandering River Reach Dominated by Tides and Suspended Load. Fluids 4. https://doi.org/10.3390/fluids4010015

Xiong, W., Cai, C.S., Kong, B., Kong, X., 2016. CFD Simulations and Analyses for Bridge-Scour Development Using a Dynamic-Mesh Updating Technique. J. Comput. Civ. Eng. 30, 04014121. https://doi.org/10.1061/(ASCE)CP.1943-5487.0000458

Yu, P., Zhu, L., 2020. Numerical simulation of local scour around bridge piers using novel inlet turbulent boundary conditions. Ocean Eng. 218, 108166. https://doi.org/10.1016/j.oceaneng.2020.108166

Zeng, J., Constantinescu, G., 2017. Flow and coherent structures around circular cylinders in shallow water. Phys. Fluids 29, 066601. https://doi.org/10.1063/1.4984926

Zeng, J., Constantinescu, G., Weber, L., 2008. A 3D non-hydrostatic model to predict flow and sediment transport in loose-bed channel bends. J. Hydraul. Res. 46, 356–372. https://doi.org/10.3826/jhr.2008.3328

Zhang, G., Liu, Y., Liu, J., Lan, S., Yang, J., 2022. Causes and statistical characteristics of bridge failures: A review. J. Traffic Transp. Eng. Engl. Ed. 9, 388–406. https://doi.org/10.1016/j.jtte.2021.12.003

Zhou, K., Duan, J.G., Bombardelli, F.A., 2020. Experimental and Theoretical Study of Local Scour around Three-Pier Group. J. Hydraul. Eng. 146, 04020069. https://doi.org/10.1061/(ASCE)HY.1943-7900.0001794

5 Conclusions

The present work dealt with advances in hydrodynamic and morphodynamic modelling, which developed along two main directions, namely the enhancement of 2D depth-averaged models to account for the effects of curvature-induced secondary currents, and the application of eddy resolving CFD schemes to describe turbulent open-channel flows in presence of macro-roughness and geometrical singularities.

In the first part of the research, the effects of the curvature-induced secondary currents were included in an existing 2D depth-averaged Finite Element hydrodynamic model. Different formulations previously proposed in the literature were recast in a unique form and implemented in the model by means of dispersive terms that can be computed with either a local and a transported approach, i.e., assuming an instantaneous or an inertial adaptation of the secondary flow. The present approach also included a novel, pure 2D parametrization of the non-linear saturation effect, which allows applying the model also to relatively sharp bends. The model for the secondary currents has been coupled with modules that solve for the transport of passive tracers and of bed particles. The applications to laboratory and real test cases, with both fixed and mobile beds, allowed validating the model and assessing the importance of considering secondary currents in different context. Results provided by the model also allowed to highlight some key factors in modelling river flows in bends using 2D models with proper parametrizations of the helical flow. Implementation strategies and modelling options have been also discussed with the purpose of providing a set of practical guidelines for an effective application of 2D depth-averaged models to river flow in bends.

In the second part of the research, a CFD suite was used to describe turbulent flows over large roughness elements and in the presence of in-stream structures. The eddy resolving Detached Eddy Simulation (DES) approach was used, given its ability in predicting separated turbulent flows generated by complex irregular geometries. A first DES application considered freshwater mussels that, living at the sediment-water interface, represent large roughness elements whose size largely exceeds that of bed particles. Analyzing the interactions between the turbulent flow and freshwater mussels, the destabilizing forces, and the mixing of nutrients, can have important implications for the survival of these mollusks and the sustainability of fluvial ecosystems. The analysis started from the case of an isolated partially-buried mussel, and focused on how the flow field changes depending on bed roughness, the burrowing ratio, and the filtering activity of the mussel. As mussels typically live in clusters, the analysis was extended to consider large arrays of mussels, so as to evaluate the effect of the mussel density. Results showed that increasing the bed roughness intensifies the interactions of the eddies induced by

the isolated mussel and by bed particles, with consequences on the forces exerted on the shell and on the mixing of a passive tracer injected from the excurrent siphon. The effect of bed roughness becomes less important when increasing the mussel density, and negligible in dense clusters, as the effect of the protruding shells prevails on the bed roughness. In dense array of mussels, the bed shear stresses and the hydrodynamic forces on the emerging parts of the shells are also reduced, thus favoring the mussel stability.

A second DES application considered the complex flow field generated by the presence of a multi-pier bridge located on the Po River (Italy), which is of interest because the failure of in-stream structures is often driven by hydraulic reasons, such as severe scour processes. The application of the DES approach to a large-scale real-world case study was challenging because of the large Reynolds number, the strict constraints on the mesh resolution, and the size of the domain. Flow, turbulent structures, and bed shear stresses, which are strictly connected with scouring phenomena, were analyzed depending on different flow regimes and geometrical configurations of the bridge. It was shown that the shift from the free-surface regime to the pressure-flow with deck overtopping produces a substantial change in the flow field and a dramatic increase in the bed shear stresses at the bridge, with an erosive potential that is far larger than that induced by the bridge piers alone. Furthermore, the slight channel contraction was shown to produce negligible effects in the analyzed case study. Interestingly, a comparison between the DES and the classic RANS approaches confirmed the advantage of DES in describing the time-variation of the bed shear stresses; this is an important aspect because the strong fluctuations of bed shear stress, generated by unsteady energetic eddies, are known to play a key role on the erosion of bed materials and thus on scouring processes close to in-stream structures.